Tailoring optoelectronic properties of anthanthrene through O-, S-, and N-doping

Thesis by

Cataldo VALENTINI

Under the supervision of Prof. Davide BONIFAZI

Presented to the School of Chemistry of Cardiff University in Partial

Fulfillment of the Requirements for the degree of Doctor of Philosophy

(Ph.D.) in Chemistry

Acknowledgments

I would like to start with a special thanks to my supervisor, Professor Dr. Davide Bonifazi. This work would not have been possible without his support. I am very grateful for the trust that he placed in me during this research project and I will never forget the scientific meetings with him.

Many thanks to Professor Dr. Jean-François Nierengarten and Dr. Louis Morrill for accepting the co-examination of this manuscript. I am also very grateful to Dr. Grazia Bezzu and Dr. Antoine Stopin for the proofreading of the thesis.

I would like to thank all the people involved in this work: Dr. Nicola Bonini and Duncan Gowland for the theoretical calculation; Dr. Benson Kariuki, Dr. Nicola Demitri, Nicolas Biot and Deborah Romito for their support on the X-ray diffraction analysis. I would thank all the staff of Cardiff University for the daily support. Thanks to Perrine Weber and Ines Boughdiri, who did their Erasmus experience under my supervision and collaborated with me in some projects.

A special thanks to all people I have met in this period in Bonifazi Group: *F*rancesco F. l'unica persona che conoscevo prima di arrivare a Cardiff con cui ho condiviso bellissimi momenti assieme; *Maria L* e la Doc *Tanja M* che con la loro semplicità e schiettezza hanno ravvivato le tristi serate di pioggia gallesi; *Adrea F*, *Claudio B*, *Andrea S* and *Davide M* per tutte le serate passate assieme; *Tommaso B*. e *Jacopo D* per interminabili partite a biliardo, le birre e tutti i momenti passati davanti all' "acquario"; *Rodolfo T* per I momenti passata assieme anche e soprattutto durante la stesura della tesi; Lou R and her crazy-funny moments; *Andrey B* for teaching me some lab tricks and for the Wednesday beers; Grazia B per i consigli che mi ha dato; *Deborah R* and *Melina S* per tutte le battute che ci facevamo in lab; Alex R for his "amazing" lab music; *Antoine S.* for all fruitful discussions about NMR and for all the moments in lab; *Oliwia M*. for all the nice chats in lunch time; *Nicolas B* for all the scientific discussions; Andre for commenting with me football matches; *Daniele M*, Matteo, Jack, Luka and *Alexandra* for all the moments together; and all the students Eleni, Francesco, Paolo, DM, Francois, Komal, Tooba.

Tutto questo non sarebbe stato possibile senza l'appoggio di mio padre e mia madre che hanno sempre creduto in me, e dei miei fratelli Marco, Fabrizio e Dario. Un pensiero particolare va ai miei nonni Cataldo, Antonietta e Nicola che purtroppo non possono più gioire con me di questo traguardo, ed a mia nonna Filomena che mi aiutava con i compiti quando ero bambino.

E poi c’è lei, Silvia, la mia ragazza che mi è stata vicina nei momenti difficili, riuscendo a risollevarmi il morale e a calmarmi. Lei, con cui ho condiviso le gioie di questo periodo. GRAZIE!

E poi ci sono loro i tuoi Amici quelli veri, quelli che pur lontano chilometri è come se fossero sempre li con te; la comitiva nel barese: Marco, Carlo, Tonio, Dario, Francesca. Luca, Paolo, Gabriele, Roberto, Simone, Mimmo, Anna, Angelo; e la comitiva nel tarantino; Paolo, Vincenzo, Graziano, Alessandro, Luca, Giulia e Silvia. GRAZIE!

List of abbreviation

Å	Angstrom
Aq	Aqueous
B3LYP	Becke, 3-parameter, Lee-Yang-Parr
°C	Degree Celsius (0 °C = 273.16 K)
calc.	Calculated
CV	Cyclic voltammetry
DDQ	2,3-Dichloro-5,6-dicyano-1,4-benzoquinone
DFT	Density Functional Theory
DMF	*N,N*-Dimethylformamide
EDTA	Ethylenediaminetetraacetic acid
EI	Electron ionization
ESI	Electrospray ionization
Et_2O	Diethyl Ether
EtOAc	Ethyl Acetate
EtOH	Ethanol
eV	Electronvolt (1eV = 1.602 x 10^{-19} J)
Fc	Ferrocene
h	Hour
HOMO	Highest occupied molecular orbital
HR	High resolution
IR	Infrared spectroscopy
LR	Low resolution
LUMO	Lowest unoccupied molecular orbital
M	Molar
MALDI	Matrix-assisted laser desorption/ionisation
m-CPBA	Meta-chloroperoxybenzoic acid
MeCN	Acetonitrile
MeOH	Methanol
min	Minute

m.p.	Melting point
MS	Mass spectrometry
m/z	Mass-to-charge ratio
NMI	1-Methylimidazole
NIR	Near infrared
nm	Nanometer
NMR	Nuclear magnetic resonance
OFET	Organic field-effect transistor
PAH	Polycyclic aromatic hydrocarbon
pH	Potential of hydrogen
ppm	Parts per million
Py	Pyridine
r.t.	Room temperature
SCE	Saturated colomel electrode
S_N2	Bimolecular nucleophilic substitution
T °*C*	Temperature
*t*Bu	*Tert*-butyl
TFAA	Trifluoroacetic anhydride
THF	Tetrahydrofurane
TLC	Thin layer chromatography
UV-Vis	Ultraviolet-visible
vs.	*Versus* (latin)- against
λ	Wavelength
ε	Molar extinction coefficient
τ	Fluorescence lifetimes

Abstract

Molecular graphenes, also known as Polycyclic Aromatic Hydrocarbons (PAHs), have been intensely studied for their application in organic electronics. However, large PAHs are poorly stable under ambient condition and, therefore, their functionalisation is crucial to obtain stable and highly efficient functional materials. Among all the possible functionalisation, the replacement of C_{sp^2}-H moiety with heteroatoms, such as oxygen, boron and nitrogen atoms, has been chosen to successfully synthesise extended PAHs. For instance, the oxygen-doped analogue of anthanthrene, named *peri*-xanthenoxanthene (PXX), has been studied by SONY as organic semi-conductor. In this context, the goal of our project is the synthesis and characterisation of oxygen-, nitrogen-, and sulphur-doped PXX. The opto-electronic properties of the new class of N-PXXs and S-PXX have been investigated and compared with the PXX properties. The energy band gap of N-PXX can be tuned depending upon nitrogen atoms' position. Moreover, the nitrogen position affects the solid-state self-assembly. The N-PXX have been further modified via *N*-alkylation to viologen-like molecules, which are visible-light absorber with high reduction potential. The S-PXX shows a narrower band gap as compared to PXX due to the presence of an internal charge transfer. In addition, S-PXX has a strong molecular dipole which drives the solid-state organization in a lamellar π-π stacking motifs. Due to their photo-physical and solid-state organisational features, N-PXX, *N*-alkylated N-PXX, and S-PXX can be considered as new promising materials for optoelectronics and organic photocatalysis.

Table of Contents

Chapter 1 Oxygen-doped molecular graphenes 11

1.1 General introduction about graphene and molecular graphenes 11

1.1.1 Description of PAHs periphery topology..... 12

1.1.2 PAHs edges reactivity 13

1.2. Oxygen doping of PAHs..... 15

1.2.1 General synthetic approach for the preparation of O-doped PAH. 16

1.3 Synthesis and characterisation of O-doped PAHs..... 18

1.3.1 Furan-like O-doped PAHs..... 18

1.3.2 Synthesis of pyran-rings..... 19

1.4. Aim and Outline of the dissertation..... 29

1.5 References 31

Chapter 2 Synthesis and Characterisation of N-Doped *peri*-Xanthenoxanthene 37

2.1 General introduction about N-doping of Polycyclic Aromatic Hydrocarbons 38

2.1.1 Optoelectronic properties of N-doped Polycyclic Aromatic Hydrocarbons.. 38

2.1.2 N-doped tailored PAHs solid-state self-assembly..... 41

2.2 PXX properties and aim of the project..... 43

2.2.1 Introduction about PXX properties 43

2.2.2 Aim of the project: N-doped *peri*-Xanthenoxanthene 44

2.3.1 Retrosynthetic approach. 46

2.3.2 Cu-mediated oxidative dimerisation 48

2.3.3 Oxidative dimerisation through Directed ortho Metalation 49

2.3.4 3,9-diN-PXX 2 synthesis 51

2.3.5 1,7-diN-PXX 4 synthesis 51

2.3.6 4,10-diN-PXX 6 synthesis 52

2.3.7 5,11-diN-PXX 11 synthesis..... 55

2.3.8 2,8-diN-PXX 15 synthesis 56

2.3.9 Conclusion about the synthesis..... 58

2.4 Photophysical characterization. 58

2.4.1 Photophysical characterization general remarks. 58

2.4.2 Photophysical characterization of N-doped PXX..... 61

2.4.3 Theoretical Calculation..... 63

2.4.4 Synthesis and characterization of 1,9-diN-PXX as proof of concept 65

2.4.5 Conclusion 68
2.5. Electrochemical Investigations. 68
2.5.1. Cyclic voltammetry general remarks 68
2.5.2 Cyclic voltammetry investigations. 71
2.5.3 Determination frontier orbital energies and redox potential of excited state. 72
2.6 Solid-state self-assembly investigation of NPXXs 74
2.6.1 PXX Solid-state self-assembly 74
2.6.2 1,7-diN-PXX 4 Solid-state self-assembly 75
2.6.3 3,9-diN-PXX 2 Solid-state self-assembly 76
2.6.4 4,10-diN-PXX 6 Solid-state self-assembly 78
2.7. NPXXs crystal engineering through halogen-bonding 79
2.7.1 General remarks about halogen-bonding 79
2.7.2 Solid-state self-assembly of 3,9-diN-PXX 2 and 1,4-diiodotetrafluorobenzene . 82
2.7.3 Solid-state self-assembly of 4,10-diN-PXX 6 and 1,4-diiodotetrafluorobenzene83
2.8 Conclusion and future work 84
2.9 References 85
4.1 General introduction about S-doping of Polycyclic Aromatic Hydrocarbons 114
4.1.1 Tailoring of optoelectronic properties via S-doping and sulphur oxidation. 114
4.1.2 S-doped induced PAH solid-state self-assembly 120
4.2 Aim of the project: S-doped *peri*-Xanthenoxanthene 120
4.3 Synthesis of mono S-doped *peri*-Xanthenoxanthene 122
4.3.1 Retrosynthetic approach 122
4.3.2 Metal-free C-C formation via interrupted Pummerer reaction 124
4.3.3 *peri*-Thioxanthenoxanthene synthesis: synthetic routes a and b 126
4.3.4 *peri*-Thioxanthenoxanthene synthesis: synthetic route c 130
4.3.5 Conclusion about the synthesis 131
4.4 Photophysical characterization 131
4.4.1 General remarks about intramolecular charge transfer 131
4.5. Electrochemical investigation 135
4.5.1 Cyclic voltammetry investigation. 135
4.5.2 Frontier orbital energies determination of molecules 29 and 38 137
4.6 Solid-state self-assembly investigation of PTXX-SO_2 140
4.6.1 Crystal structure and packing of PTXX-SO_2 140
4.7 Conclusion and future work 143

3.8 References 144
Chapter 5 149
Experimental Part 149
5.1 Instrumentation 149
5.2 Material and General Methods 151
5.3 Experimental Procedures 152
5.4 Lifetime measurements 172
5.5 Cyclic Voltammetry 173
5.6 Lippert Matanga plot for molecules 38, 29 and PXX. 182
5.7 X-ray Data 182
5.7 References 192
Appendix A 194

Chapter 1

Oxygen-doped molecular graphenes

1.1 General introduction about graphene and molecular graphenes

Carbon-based materials with an extended π-system have a key role for the development of high performing and cheap advanced functional materials, figure 1.1a.[1–3] Graphene, which is defined in IUPAC "Gold Book" as "*a single carbon layer of the graphite structure, describing its nature by analogy to a polycyclic aromatic hydrocarbon of quasi infinite size*",[4] is the most important carbon-based material. It attracted an enormous amount of interest in the area of optoelectronic and composite materials, due to its high mechanical, thermal, and chemical stability and excellent electronic properties.[5] Molecular graphenes, also known as Polycyclic Aromatic Hydrocarbons (PAHs) or polyacenes, can be considered as fragments of graphene with finite size that ranges from 1 to 5 nm, figure 1.1b.[6] Having a well-defined structure, PAHs can serve as good model compounds for understanding the fundamental electronic properties of graphene and graphene nanoribbons.

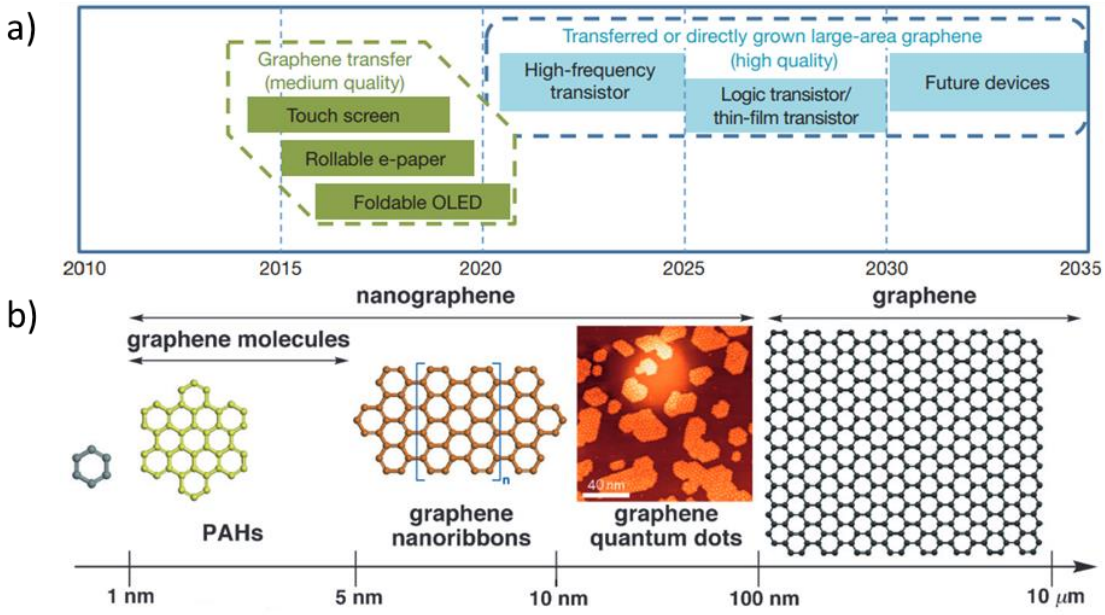

Figure 1.1. a) Display applications are shown in green; electronic applications are shown in blue. Possible application timeline based on projections of products requiring. b) Schematic representation of graphene terminology according to their size scale.

The preparation of PAHs can be performed following both bottom-up and top-down strategies.[7] The top-down protocols envisage the cutting of large graphene monolayers into small fragments by hydrothermal or lithographic etching, figure 1.2a.[8–10] The bottom up protocols provide access to monodisperse PAHs with controlled chemical structure, figure 1.2b.[6,11–13] The first PAHs synthesis was developed by Scholl and Clar, who used harsh reaction conditions that employed high temperature and strong oxidising agents.[14,15]

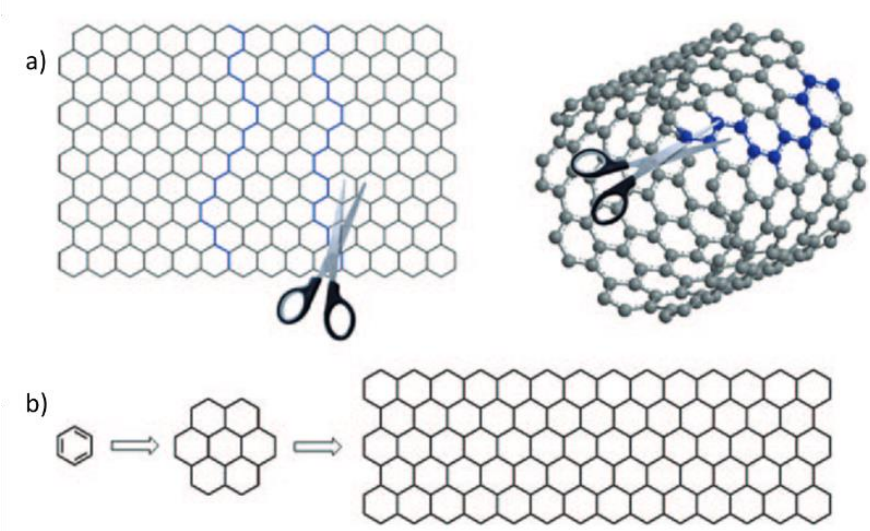

Figure 1.2. Schematic representation of the a) top-down and b) bottom-up fabrication of PAHs

1.1.1 Description of PAHs periphery topology

PAHs can have two basic edges shape, namely, armchair and zigzag edges, figure 1.3. The edges topology affects the π-electronic properties of PAH figure 1.3. [16–18] PAHs with zig-zag edges are especially interesting, because of their application in organic electronics as charge transporting material.[18–20]

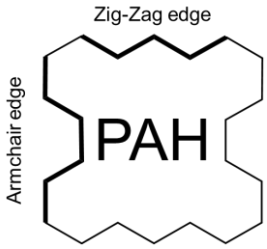

Figure 1.3. Zig-zag and armchair edges topology for a generic PAH.

Molecular graphenes can be linearly extended along the direction *n*, giving [*n*]acenes, figure 1.4.[21,22] The 2-dimensional *peri*-fusion of *m* number of [*n*]acenes in a rectangular motif with $\alpha = 90°$ gives [*n,m*]*peri*-acenes that have two zig-zag edges and two armchair edges, figure 1.3. The *peri*-fusion of *m* number of [*n*]acenes with $\alpha = 60°$ into a rhombic shape gives the [*n,m*]*peri*-acenoacenes that have only zig-zag edges, figure 1.4.[12,13]

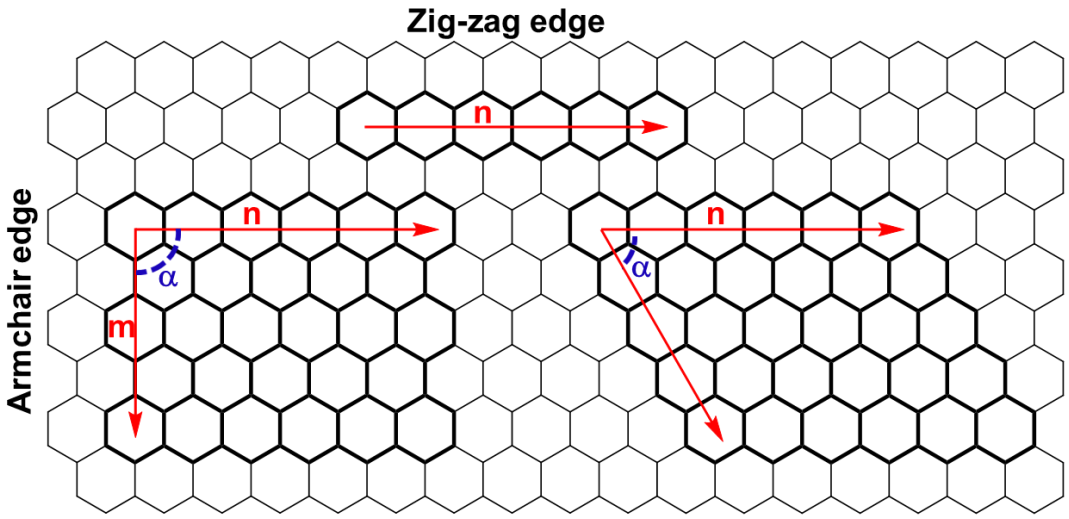

Figure 1.4. Linear acenes, *peri*-acenes and *peri*-acenoacenes.

1.1.2 PAHs edges reactivity

The reactivity and the stability of PAHs can be estimated qualitatively according to Clar's rule, which states that "*the most stable structure of annelated benzenes is the one possessing the maximal number of the aromatic sextets separated by the entirely "empty" six-membered rings"*.[16,17,23,24] For example, considering the two isomers triphenylene and anthracene, the first one is more stable because its structure has two additional aromatic sextet rings, figure 1.5. This rule is also valid for large PAH isomers, such as hexa-*peri*-hexabenzocoronene (HBC) and teranthene. The first is more stable as its structure has seven independents aromatic sextet versus the three sextets of teranthene, figure 1.5.

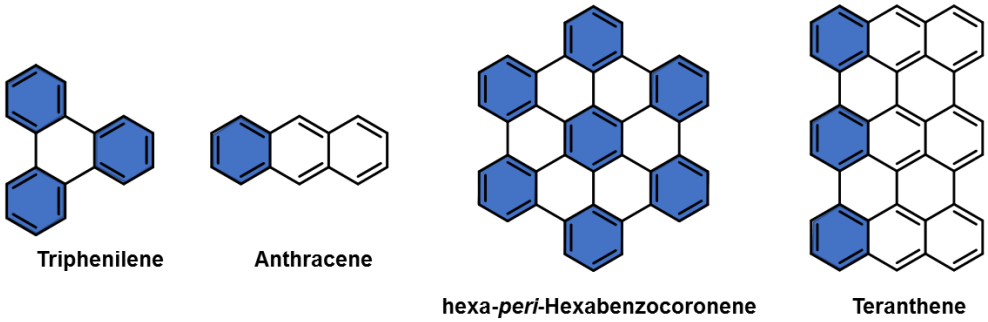

Figure 1.5. Clar's aromatic sextet drawing for thriphenilene, anthracene, hexabenzocoronene and teranthene.

The reactivity of molecular graphenes with high extended π-system and zig-zag edges is due to the increased radical character. These have more aromatic sextet rings in the corresponding resonance form than in the closed-shell form.[25–27] Kubo *et al.* observed the aromatic stabilisation of radical structures by studying anthene derivatives.[28] Considering the close-shell and the open-shell Kekule's resonance structures, the first one, which has one aromatic sextet per anthracene moiety, is less stable than the

second which, instead, has two aromatic sextets per anthracene moiety, figure 1.6. Therefore, they observed an enhancement of the radical character with increasing conjugation of PAHs.

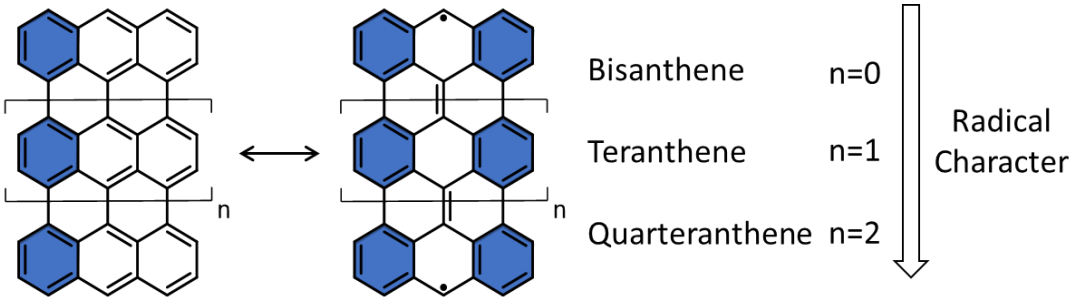

Figure 1.6. Bisanthene, teranthene and quarteranthene Kekule's resonance formulas.

The radical electrons are more localised on carbon atoms in zig-zag edges than in those in armchair edges. Therefore, zig-zag edges are the high reactive in radical cycloaddition and O_2 oxidation and, usually, the central rings are the most reactive.[29,30] The oxygen photooxidation and photo-dimerization of [n]acenes, such as anthracene, tetracene and pentacene, have been deeply investigated because they limit the practical applications of these molecules as active organic semiconductor in FETs.[31] For instance, both the oxygen photooxidation of [n]acenes to endoperoxide (EPO) in presence of O_2, scheme 1.7a,[32,33] and the [$4\pi_s$+$4\pi_s$] photo-dimerization of [n]acenes, scheme 1.7b, [34–37] are promoted by light.

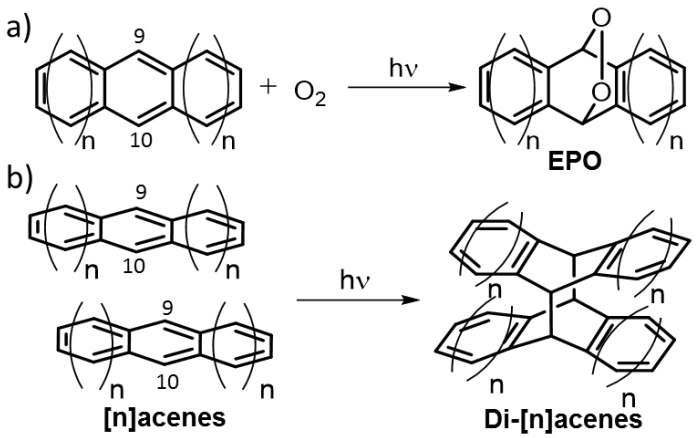

Scheme 1.1. a) Anthracene photo-oxidation; b) anthracenes photo-dimerisation

The functionalisation of specific positions, such as position 9 and 10 in anthracene, can enhance the stability by increasing their steric hindrance and extending their conjugation. For example, Maliakal *et al.* reported that alkynyl substituents on *peri*-positions of pentacene increases significantly the stability towards O_2 oxidation.[31,38] A further approach to enhance the stability of extended PAHs is represented by the heteroatoms doping.[19,39] It envisages the replacement of C_{sp^2}–H moieties with

heteroatoms such as oxygen,[39–42] nitrogen[43–45] or boron.[46–48] In addition, heteroatom doping is used to tailor the optoelectronic properties of PAHs. The inclusion of oxygen atoms in PAHs periphery will be thoroughly discussed in the following section.

1.2. Oxygen doping of PAHs

The O-doping in PAHs is emerging as a versatile functionalisation strategy to control the chemical stability, charge carrier and self-assembly behaviours of the corresponding molecules.[42,49–53] In polycyclic aromatic hydrocarbons, the atomic orbitals of the carbon atoms are hybridised sp^2 and therefore, they can bind three atoms. It is possible to define two different typologies of carbon atoms: *inner* carbons (C_i) and *peripheral* carbon (C_p). The C_i atoms bridge three different carbon atoms and the C_p atoms bridge two different carbon atoms and one hydrogen atom. Consequently, the introduction of oxygen atoms in a generic PAH scaffold is allowed only on the periphery replacing a C_{sp^2}-H moiety, figure 1.7.

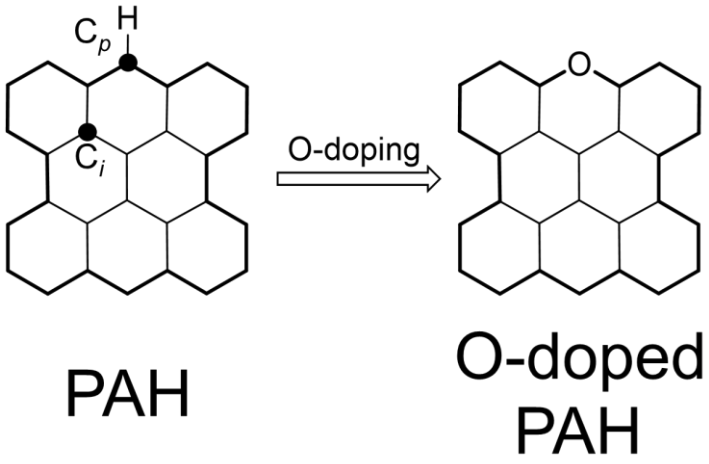

Figure 1.7. Oxygen doping scheme for a generic PAH.

The condition for the stability of an O-doped PAH is that all the electrons in the π-orbitals must be paired. To have the π-electrons paired, the number of electrons involved in π-delocalisation for a generic O-doped PAH with chemical formula $C_nH_xO_m$ must satisfy equation 1.1. Where *n* and *2m* are the number of electrons per carbon and oxygen atoms involved in the π-conjugation, respectively, and *k* is a generic natural number.

$$n + 2m = 2k \quad n, m, k = 1, 2, 3, \ldots.. \qquad \textbf{Equation 1.1}.$$

For instance, the mono O-doping of **1.A** in figure 1.8 leads to molecule **1.B** which is unstable since it does not satisfy equation 1.1 (15 electrons). Instead, the doping with two oxygen atoms leads to stable dibenzo dioxine **1.C** that has 16 π-electrons, figure

1.8. Furthermore, the doping of PAHs allows the synthesis of structures that do not have full-carbon analogous structures. For instance, PAHs **1.D** and **1.G** have 19 and 21 π-electrons and they are unstable, figure 1.8. The replacement of a C-sp^2-H moiety with an oxygen atom leads to stable molecules **1.E** and furan-like **1.H**. on the other hand, the preplacement of 2 C_{sp}^2-H **1.D** leads to molecule **1.F** which has 21 π-electrons and is not stable, figure 1.8.

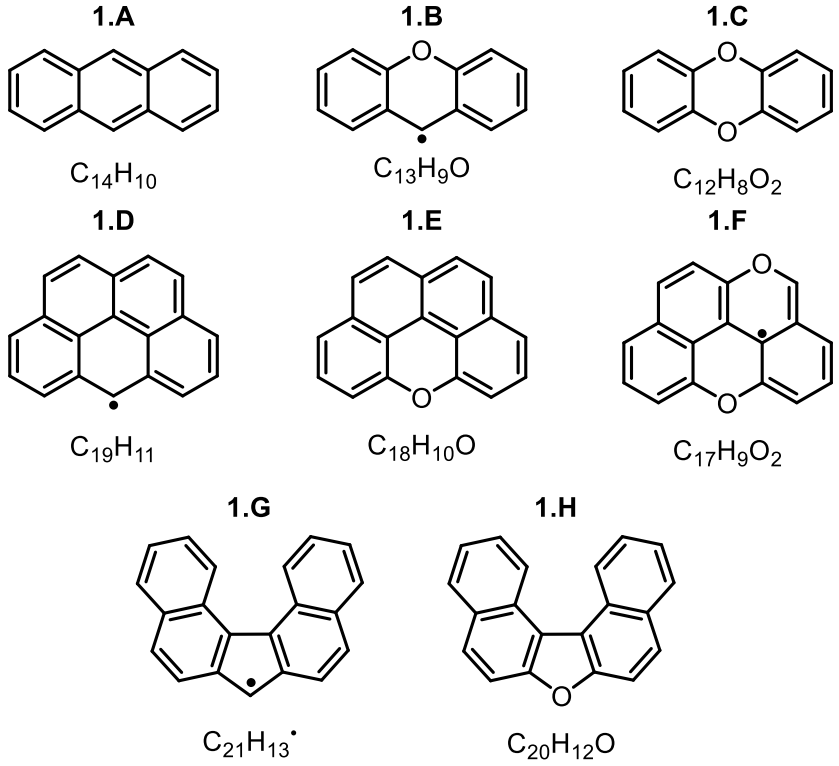

Figure 1.8. Mono and di-oxygen doping for different PAHs.

1.2.1 General synthetic approach for the preparation of O-doped PAH.

The synthesis of O-doped PAH envisages intramolecular cyclisation to form the pyran/furan ring. The cyclisation can be achieved through C_{sp}^2-O or C_{sp}^2-C_{sp}^2 bond formation, scheme 1.2.

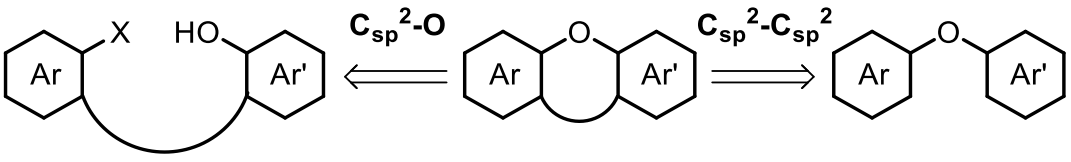

Scheme 1.2. Cyclisation patways

The C_{sp}^2-O bond formation can be achieved by reaction between a phenol moiety and a specific pre-functionalised C_{sp}^2 following different routes: a) transition-metal mediated

cross coupling, such as Buchwald–Hartwig, Ullmann, and Chan–Lam–Evans couplings, b) nucleophilic aromatic substitution (S_NAr) or c) C_{sp}^2-H activation through oxidants, scheme 1.3.[54–59]

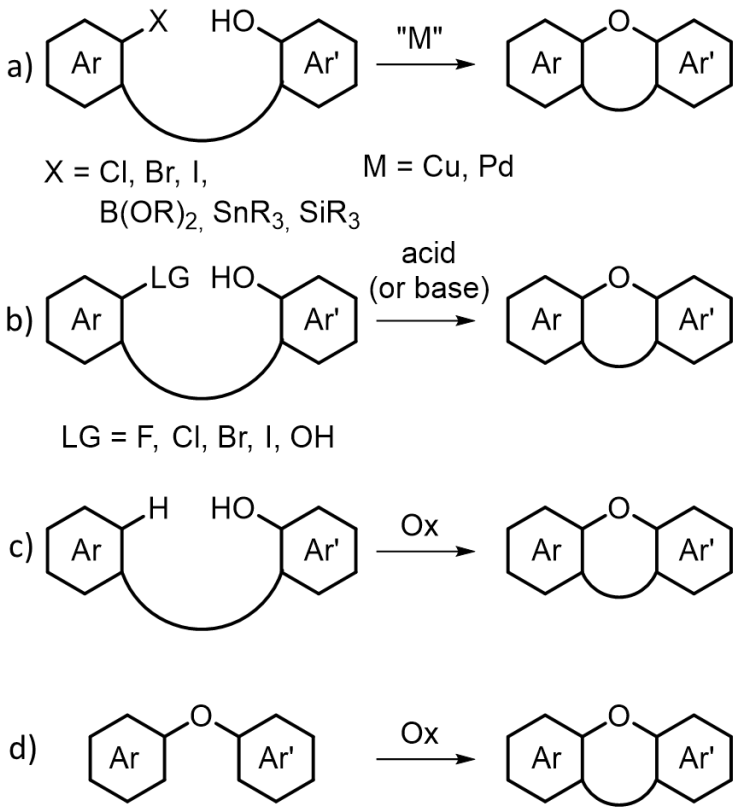

Scheme 1.3. General methodologies for preparing O-PAHs.

As mentioned above, the formation of the C_{sp}^2-O bond can be achieved by transition-metal mediated cross couplings, such as Ullmann and Buchwald–Hartwig reactions. Generally, these reactions are catalysed by Cu, Cu(I) and Pd, which allow the formation of C_{sp}^2-O bond between a phenol moiety and an aryl halide, scheme 1.3a.[54,55] The Chan-Lam-Evans involves Cu (II) as catalyst and the aryl-halide is replaced by boronic acids, stannanes or silanes, scheme 1.3a.[58] The S_NAr is a metal free reaction for the C_{sp}^2-O bond formation which envisages the reaction between a phenol moiety and a C_{sp}^2 bearing a leaving group (LG).[60] The cross-condensation reaction between two phenol groups promoted by strong acids is also a valuable route towards O-cyclisation reactions for substrates that are not sensitive to acidic conditions, scheme 1.3b.[42,61] In the last decades, the intramolecular C_{sp}^2-H activation route to form C_{sp}^2-O has also been deeply investigated because it does not require the pre-functionalisation of the aryl moiety, scheme 1.3c. The reaction is promoted by the presence of metallic oxidants, such as Pd(II), Cu(II), Cu(I), Ag(I) and Fe(III).[62–67]Therefore, this synthetic route is a functional shortcut for the preparation of aryl-ethers moieties.[40–42, 51,68] The

formation of C_{sp}^2-C_{sp}^2 bonds can also be achieved by diaryl ethers intramolecular oxidation with oxidants such as Fe (III) and DDQ, scheme 1.3d.[69]

1.3 Synthesis and characterisation of O-doped PAHs

1.3.1 Furan-like O-doped PAHs

Tsubaki *et al.* reported the incorporation of furan rings in a series of fan-shaped oligonaphthofurans.[70] The synthetic protocol consists in a two-step bottom up approach with the formation of a C_{sp}^2-C_{sp}^2 bond through Cu-mediated coupling to form oligonaphthols, that by subsequent acid mediated cyclisation form the corresponding oligonaphthofurans, scheme 1.4. The synthetic route allows the synthesis of oligomers with up to 8 repeating units, namely **2mer**, **3mer**, **4mer**, **6mer** and **8mer**.

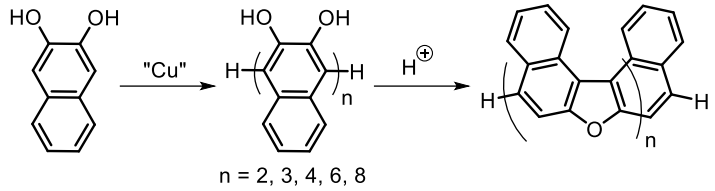

Scheme 1.4. Generic reaction scheme for the synthesis of fan-shaped oligonaphthofurans.

The UV-Vis absorption and emission spectra of the oligomers show a consistent red and hyperchromic shifts for **2mer**, **3mer** and **4mer** with unchanged spectra shapes, figures 1.9a and 1.9b. Instead, for **6mer** and **8mer**, while consistent red shifts were still observed, the spectra shape deviated from that of the smaller oligomers series, figure 1.9a. These observations indicated that the HOMO-LUMO energy gap decreased constantly with increasing π-system extension.

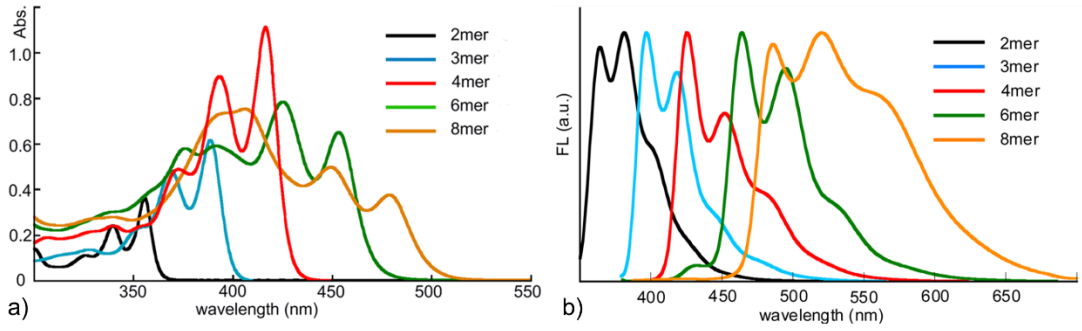

Figure 1.9. UV-Vis a) absorption and b) emission spectra for **2mer**, **3mer**, **4mer**, **6mer** and **8mer**.

Jux *et al.* reported the synthesis and characterization of a "superhelicene" PAH (**^{t}Bu-furan-HBC**) obtained from the condensation of two hexa-*peri*-hexabenzocoronene (HBC) molecules with a furan ring.[71] The authors synthesised **^{t}Bu-HBC**, **MeO-^{t}Bu-HBC** and **^{t}Bu-bisHBC** as refences to appreciate the O-doping effect on the optoelectronic properties, figure 1.10. The absorption spectra of

molecules **^{t}Bu-HBC**, **MeO-^{t}Bu-HBC** and **^{t}Bu-bisHBC** show similar outline with the lowest transition at 390 nm. The furanyl cyclisation extend the π-conjugation and the lowest transition of superhelicene **^{t}Bu-furan-HBC** is red-shifted by 125 nm with respect to **^{t}Bu-bisHBC**, figure 1.9a. **^{t}Bu-furan-HBC** shows a fluorescence emission at λ_{max} 525 nm, which is 42 nm red-shifted with respect to **^{t}Bu-HBC** and 60 nm with respect to **MeO-^{t}Bu-HBC** and **^{t}Bu-bisHBC**. Interestingly, the fluorescence quantum yield of **^{t}Bu-furan-HBC** is 83%, which is definitely higher than the quantum yield observed for **MeO-^{t}Bu-HBC** (4.1%) and **^{t}Bu-bisHBC** (6.9%). The shrinking of the optical band gap, from 2.80 eV for **^{t}Bu-HBC** to 2.29 eV for **^{t}Bu-furan-HBC**, is obtained through π-system extension.

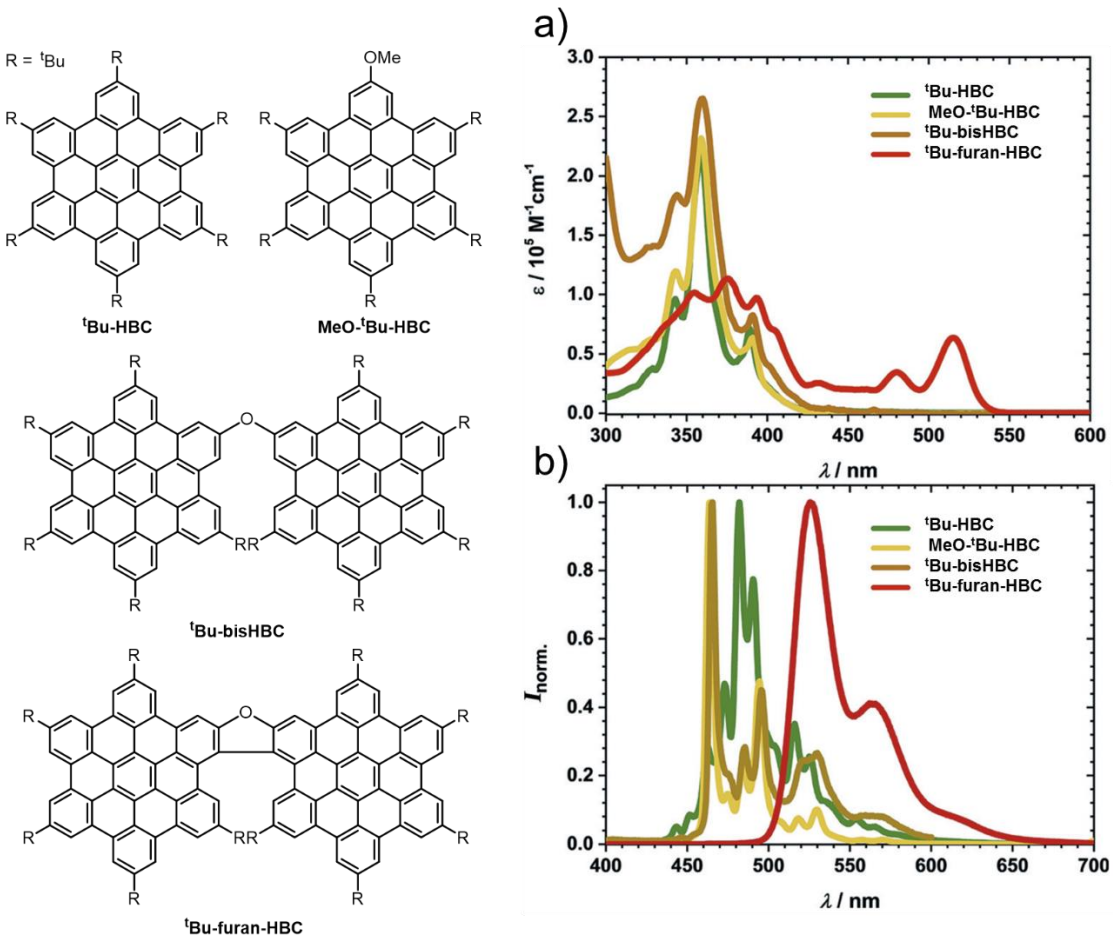

Figure 1.10. UV-Vis a) absorption and b) normalized fluorescence spectra of **^{t}Bu-HBC**, **MeO-^{t}Bu-HBC** and **^{t}Bu-bisHBC** in THF.

1.3.2 Synthesis of pyran-rings.

The introduction of pyran-like rings in PAHs with zig-zag edges, such as anthanthrene, pentacene and nonacene, increases remarkably their biradical character.[53,72] For instance, Chi *et al.* proposed the synthesis of di-oxygen doped nonacene and

decacenes (**ABA**, **ANA** and **ANA-TFA**), figure 1.11a.[73] Conversely to their full-carbon homologues, **ABA**, **ANA** and **ANA-TFA** do not have radical a character at room temperature.[74,75] However, variable-temperature (VT) EPR measurements of **ANA-TFA** shows that the intensity of the EPR signal and therefore the radical character increases as a function of temperature, figure 1.10b.[25,76,77]

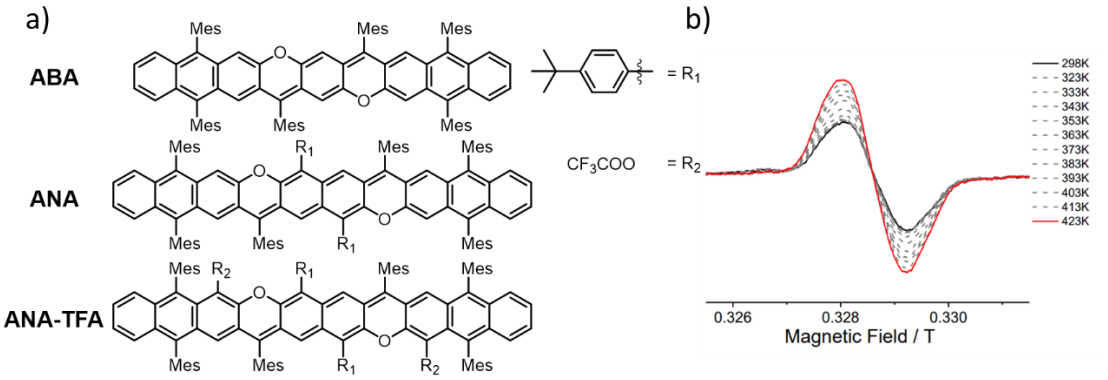

Figure 1.11. a) chemical structure of **ABA**, **ANA** and **ANA-TFA**; b) VT-ESP spectrum of **ANA-TFA**.

The cyclic voltammetry traces of **ABA** and **ANA-TFA** display two oxidation waves with $E_{1/2}^{ox}$ at 0.17 and 0.69 V for **ABA**, and 0.16 and 0.62 V for **ANA-TFA** (vs Fc/Fc^{+}), figure 1.12a. Two reduction waves are observed at $E_{1/2}^{red}$ at -1.85 and -2.14 V for **ABA**, and $E_{1/2}^{red}$ = -1.46 and -1.79 V for **ANA-TFA**, figure 1.12a. The spectroelectrochemistry of **ABA**$^{2+}$ and **ANA-TFA**$^{2+}$ exhibit a broad wavelength absorption with λ_{max} at 2109 and 1743 nm, respectively, figures 1.12b and 1.12c. Particularly, the dications are red-shifted compared with their radical cations (λ_{max} = 973 nm for **ABA**$^{\bullet+}$ and 1495 nm for **ANA-TFA**$^{\bullet+}$), figures 1.12b and 1.12c.

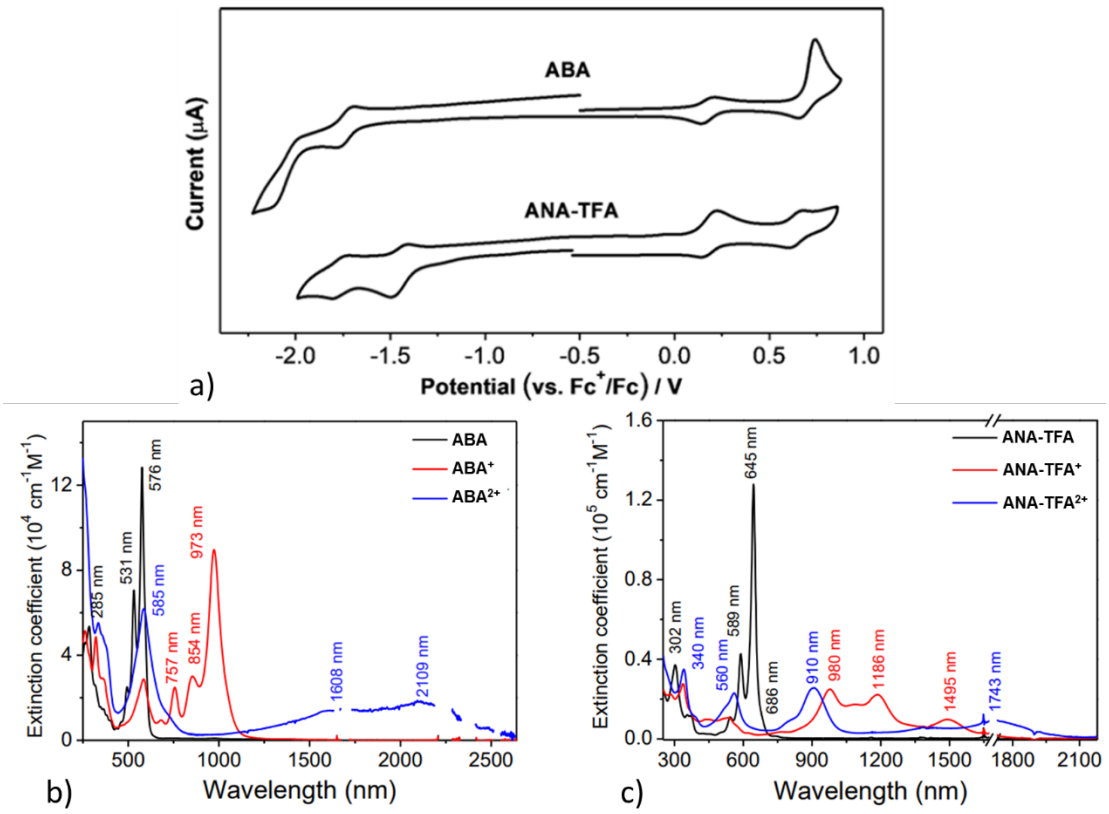

Figure 1.12. a) Cyclic voltammetry traces for **ABA** and **ANA-TFA**; b) absorption spectra of **ABA**, **ABA**$^{\cdot+}$ and **ABA**$^{2+}$; c) absorption spectra of **ANA-TFA**, **ANA-TFA**$^{\cdot+}$ and **ANA-TFA**$^{2+}$

Zeng *et al.* demonstrated that by increasing the oxygen-doping ratio, it is possible to enhance the chemical stability of the PAH considered. They reported the synthesis and photophysical characterisation of O-doped pentacene and nonacene, **P_2-OMe** and **N_2-OMe**, scheme 1.5.[53] Since, for molecules **P_2-OMe** and **N_2-OMe** no ESR signal was observed, it could be assumed that they have a close-shell character. The synthesis of O-pentacenes (**P_1-OH** and **P_2-OMe**) and O-nonaacenes (**N_1-OH** and **N_2-OMe**) was achieved by acid catalysed cross-condensation reaction which leads to the formation of C_{sp^2}–C_{sp^2} and C_{sp^2}-O bonds simultaneously, scheme 1.5.

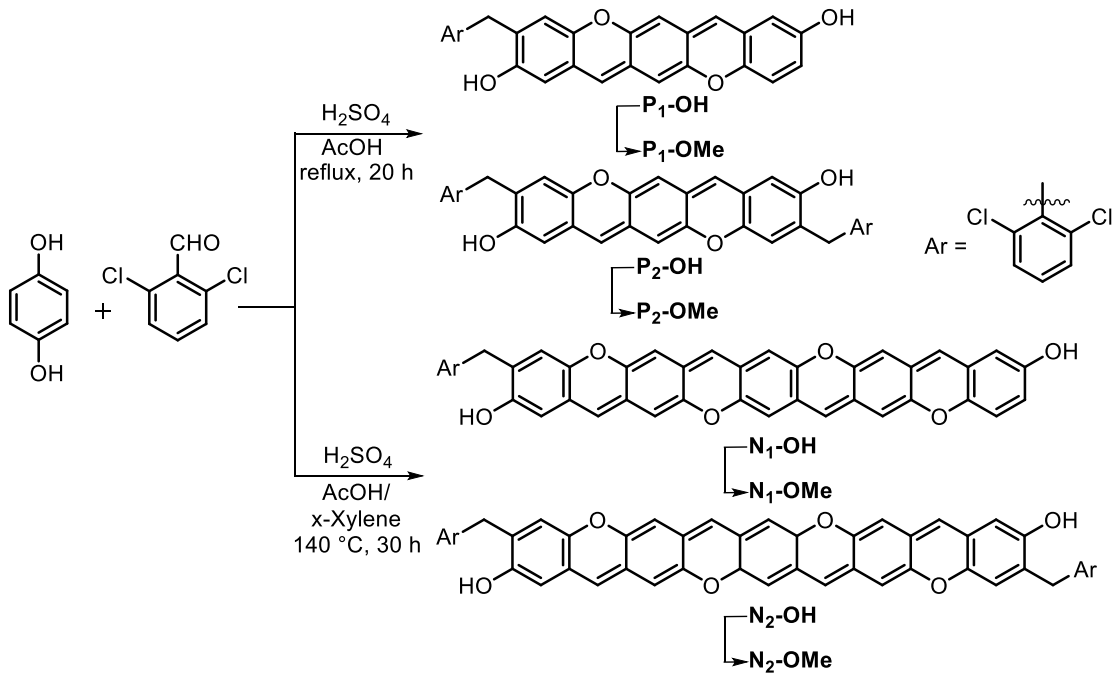

Scheme 1.5. Reaction schemes for the synthesis of O-doped pentacene and nonacene.

The UV−Vis absorption spectra of molecules **P_1-OH**, **P_1-OMe**, **N_1-OH** and **N_1-OMe** are shown in figure 1.13a. The spectra show a typical vibronic structure of polyacenes derivatives[78] and the methylation of the hydroxyl moiety of **P_1-OH** and **N_1-OH** does not affect the electronic transitions. The absorption maximum of **N_1-OMe** at 699 nm is 0.53 eV red-shifted with respect to the maximum for **P_1-OMe** (538 nm), figure 1.13a. The cyclic voltammetric trace of molecule **P1-OMe** shows two reversible oxidation waves with $E_{1/2}^{ox}$ at 0.03 and 0.61 V, and a *quasi*-reversible reduction wave $E_{1/2}^{red}$ at -1.87 V (vs Fc/Fc^{+}), figure 1.13b. In the cyclic voltammogram of molecule **N_2-OMe**, the two reversible reduction waves are observed at $E_{1/2}^{red}$ = -1.58 and -1.80 V,. figure 1.13b. It could be due to the extension of π-conjugation from a five member rings to a nine member rings. The UV−Vis-NIR spectroelectrochemistry of radical cation **N_1-OMe$^{\cdot+}$** shows an absorption band maximum centred at 1094 nm that is only 0.09 eV red-shifted with respect to the absorption band of **P_1-OMe$^{\cdot+}$** (1013 nm), figure 1.13c.

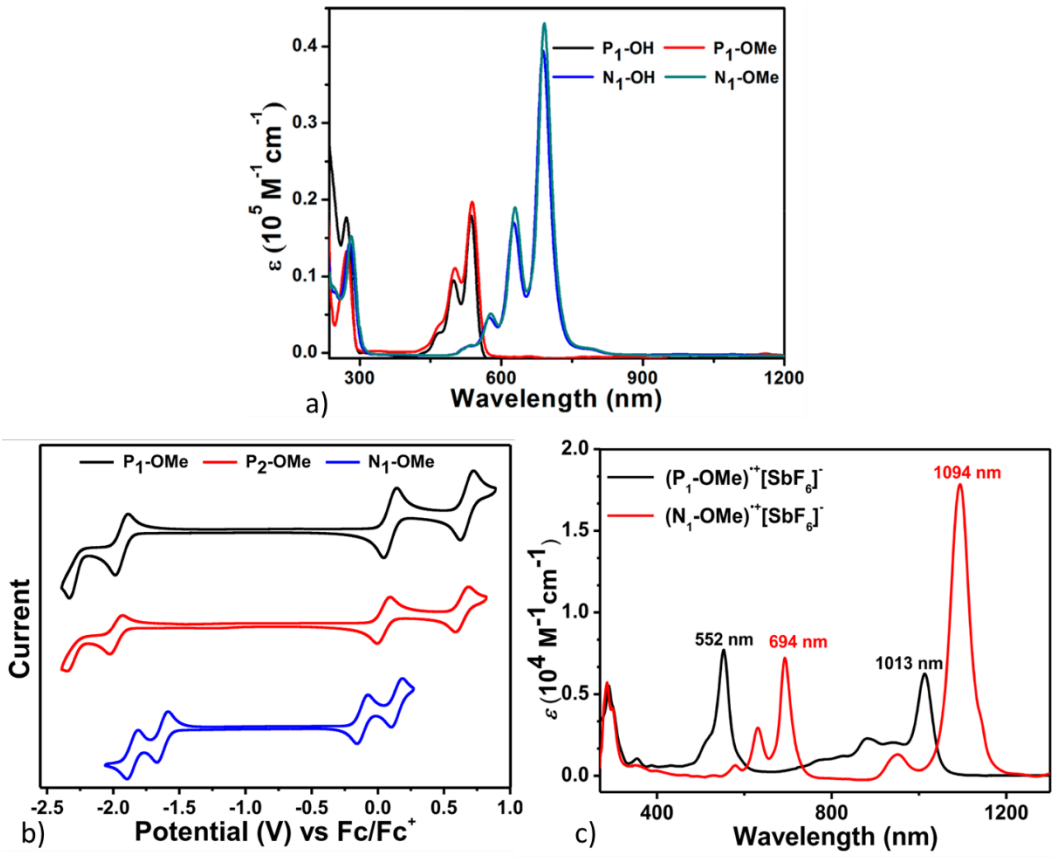

Figure 1.13. a) UV−Vis-NIR absorption spectra of **P₁-OH**, **N₁-OMe**, **N₁-OH** and **N₁-OMe** in CH_2Cl_2 (10^{-5} M); b) cyclic voltammetry traces of **P₁-OMe**, **P₂-OMe** and **N₁-OMe** (0.1 M n-$Bu_4N^+PF_6^-$ in CH_2Cl_2) at a scan rate of 50 mVs^{-1}; c) UV-Vis-NIR absorption spectra of (**P₁-OMe**)$^{\bullet+}$[**SbF₆**]$^-$ and (**N₁-OMe**)$^{\bullet+}$[**SbF₆**]$^-$ in CH_2Cl_2 (10^{-5} M).

Among the O-doped [n,m]acenes, *peri*-xanthenoxanthene (**PXX**) is one of the most studied, figure 1.14. Pummerer *et al.* were the first to report the synthesis of this molecule back in 1914. They obtained **PXX** by reacting 2-naphthol with Ag_2O.[79,80] The introduction of oxygen atoms in position 6 and 10 prevents the photoxidation due to $^1O_2$ typically observed for PAH with zig-zag edges.[33]

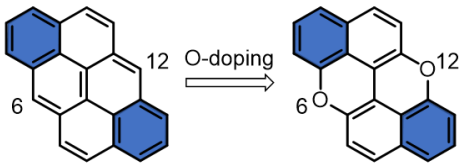

Figure 1.14. O-doping scheme for anthranthrene.

Moreover, the oxygen doping of anthanthrene changes the optoelectonic properties of the molecule. From the data reported in table 1.1, λ_{abs} and λ_{em} of **PXX** are 10 nm bathochromically shifted with respect to those of anthanthrene. A more significant enhancement is observed for **PXX** fluorescence quantum yield (QY_f), that is 0.62 compared to 0.24 for anthanthrene. Moreover, the cyclic voltammetry studies show a lower half-wave oxidation potential for PXX, $E_{1/2}^{ox}$ = 0.30 V, than that of anthanthrene,

$E_{1/2}^{ox}$ = 0.88 V. The introduction of oxygen atoms in the carbon periphery increases the energy of the HOMO orbital, decreasing the oxidation potential of 0.58 V. The presence of the oxygen atoms also affects also the reduction potential, lowering the reduction potential from -1.52 V for anthanthrene to -2.59 V for PXX.[51,81]

Table 1.1. Photophysical characterization of anthanthrene and PXX in CH_2Cl_2. The electrochemical measurements are referred against Fc/Fc^+.

	λ_{abs} (nm)	λ_{em} (nm)	QY_f (%)	$E_{1/2}^{ox}$ (V)	$E_{1/2}^{red}$ (V)
anthanthrene	433	437	24	0.88[a]	-1.52[a]
PXX	443	450	62	0.30[b]	-2.59[b, c]

[a] no reversible electrochemical process, [b] irreversible electrochemical process, [c] detectable only in CH_3CN.

Our research group has investigated different synthetic approaches to form various **PXX** derivatives, with the aim of modifying the optoelectronic properties through peripheral functionalisation and π-extension.[40–42,51,52] For instance, the functionalisation with electron withdrawing groups (EWGs) the on **PXX** periphery tunes the frontier orbitals energies.[51,52] Monoimide-PXX (**PXXMI**), diimide-PXX (**PXXDI**) and **PXXMI^{Per}** are examples of EWGs substituted **PXX**s and their synthesis can be achieved following three main different routes, scheme 1.6.[51] The synthetic route **a** leads to the symmetrically N-substituted **PXXDI**s or **PXXMI** via a three-steps synthesis: imidation, Suzuki and Pummerer-like reactions (ISP).[51] The instability of the boronate moiety on the imide-naphthyl derivative forces the in situ preparation of the boronate followed by C_{sp}^2-C_{sp}^2 bond formation. Therefore, this protocol can be used for the preparation of symmetric N-substituted **PXXDI**. On the other hand, it is possible to achieve **PXXMI** by using a naphthyl boronate derivative and the bromo imide derivative in the Suzuky coupling, scheme 1.6. Kamei *et al.* patented the synthetic pathway **b** which envisages the imidation as first step followed by the formation of C_{sp}^2-C_{sp}^2 and C_{sp}^2-O bonds through Cu-catalysed Pummerer-like reaction, **IP**, scheme 1.6.[82] However, this protocol leads to the formation of symmetrical N-substituted **PXXDI** only like for route **a**, scheme 1.6. The preparation of asymmetrical N-substituted **PXXDI** is achieved by following route **c**, scheme 1.6. The borylation of the dimethyl ester leads to the formation of a stable boronic ester derivative that can be used in asymmetric cross-coupling with a wide variety of halo derivative.[52]

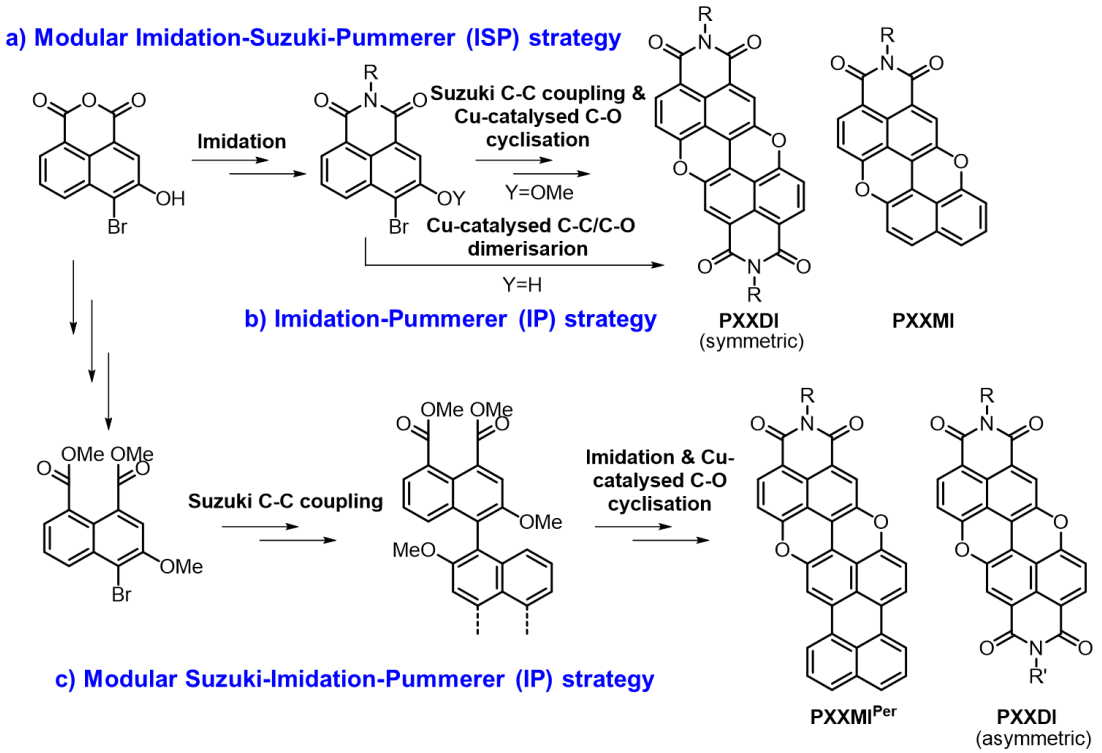

Scheme 1.6. Synthetic strategies a) ISP, b) IP and c) SIP.

The synthetic route **c** is also useful to extend the π-conjugation on the *peri* positions of **PXXMI**s, to further tune the optoelectronic properties of the deriving materials. The effect of the π-extension with a naphthyl moiety can be appreciated looking at the UV-Vis spectra of **PXXMI** and **PXXMI^{Per}**, figure 1.15. The absorption spectrum of **PXXMI** shows an absorption maximum at 525 nm that is red-shifted by 82 nm with respect to unfunctionalized **PXX**.[51] Moreover, the peripheral π-extension of **PXXMI** to **PXXMI^{Per}** shrinks the optical band gap and the absorption maximum of **PXXMI^{Per}** is red-shifted from 525 nm to 628 nm, figure 1.15.[52]

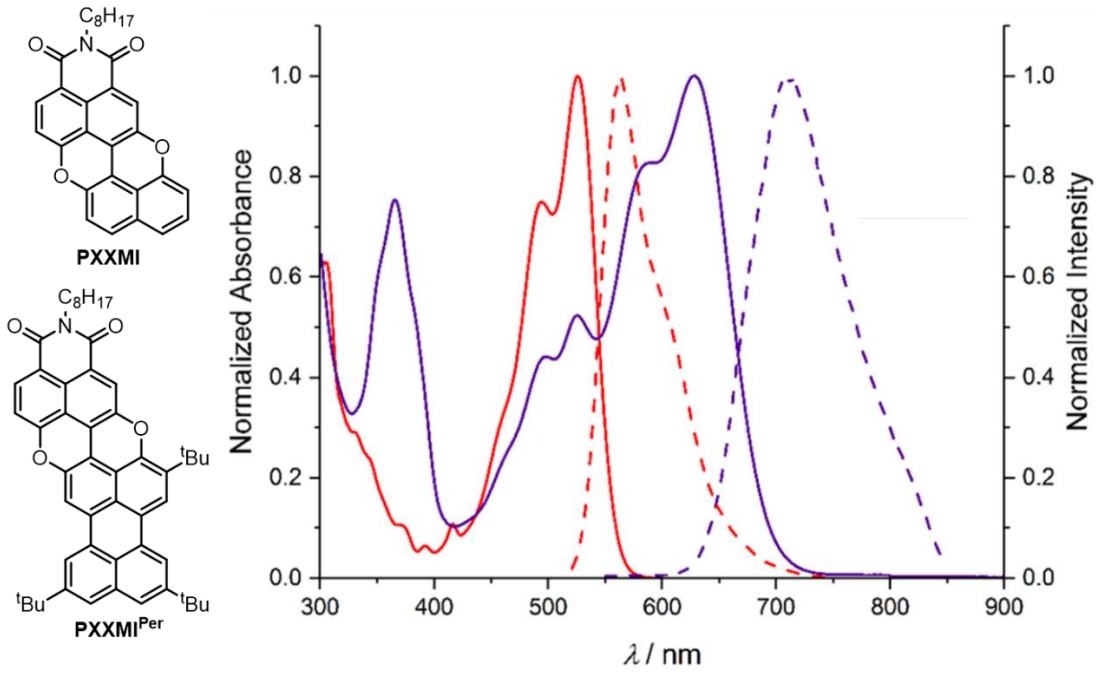

Figure 1.15. Absorption (solid lines) and emission (dashed lines) spectra of **PXXMI** (red) and **-PXXMI^{Per}** (purple) in CH_2Cl_2.

PXX can be considered as a useful molecular unit to include into extended PAHs with chemically stable zig-zag or armchair edges. For instance, the **PXX** π-conjugated system can be extended with naphthalene molecules following the synthetic pathway reported in scheme 1.7.[42] According to this strategy, **Perylen-OH** was dimerised through Cu-mediated oxidation giving **bis-Perylen-OH**. This was planarised in presence of Cu(I) to **bis-Napht-PXX,** according to the protocol that involves the Pummerer-like cyclisation. Interestingly, also **bis-Perylen-Fur,** which has a furan ring bridging the two perylene moieties, could be formed via acid catalysed reaction from **bis-Perylen-OH**.

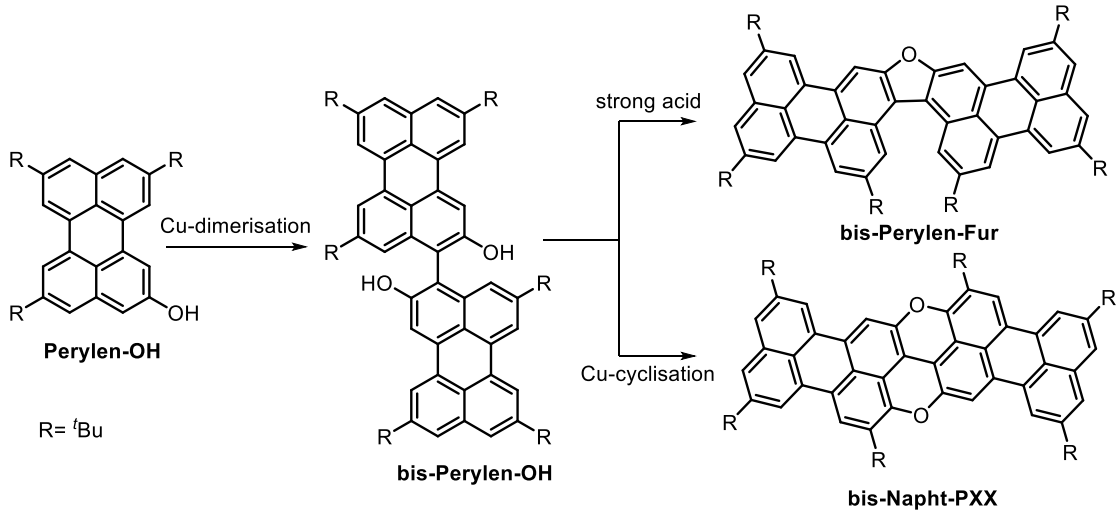

Scheme 1.7. Synthetic scheme for the preparation of **bis-Perylen-Fur** and **bis-Perylen-PXX**.

The two different cyclisations impart different photophysical behaviours to molecules **bis-Perylen-Fur** and **bis-Napht-PXX**. The absorption and emission spectra of **bis-Napht-PXX** are 100 nm bathochromically shifted with respect to **bis-Perylen-Fur**, figure 1.15a. The cyclic voltammetry traces of molecule **bis-Napht-PXX** and **bis-Perylen-Fur** show two very similar reversible reduction waves at about -2.15 V and -2.30 V (vs Fc^+/Fc), figure 1.16b and 1.16c. Conversely, the first oxidation potential of **bis-Napht-PXX** is 0.35 V lower than the first oxidation potential of **bis-Perylen-Fur**, figure 1.16b and 1.16c. This difference is due to the strong electron-donor character of the pyranopyranyl moiety compared to that of the furanyl ring.

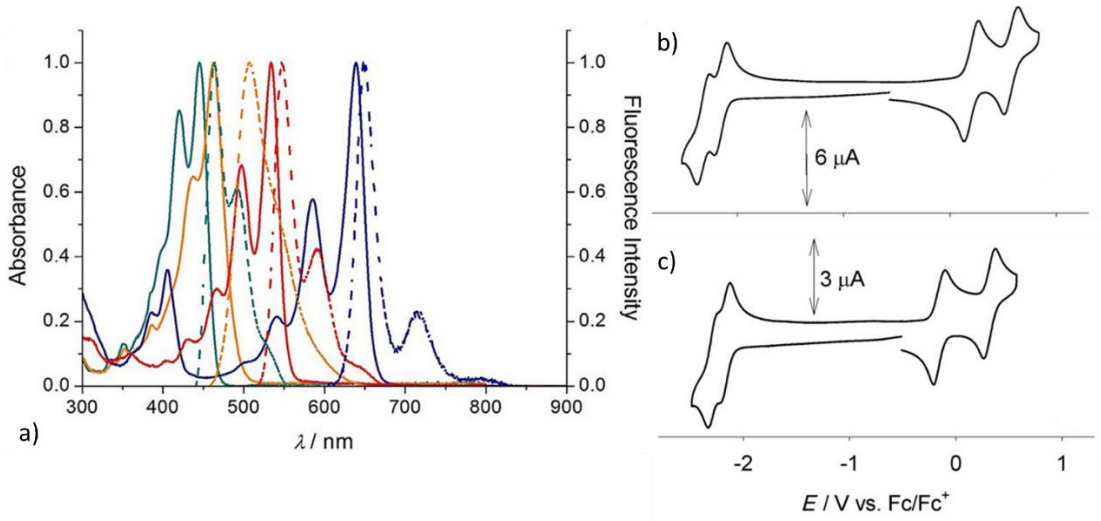

Figure 1.16. a) Normalized absorption (solid lines) and emission (dashed lines) spectra in toluene at r.t. of **Perylen-OH** (cyan), **bis-Perylen-OH** (orange), **bis-Perylen-Fur** (red), and **bis- Napht-PXX** (blue). Cyclic Voltammetry traces of b) **bis-Perylen-Fur** and c) **bis-Napht-PXX** in ODCB at scan rate 50 mV s^{-1} with $TBAF_6$ as supporting electrolyte.

The **PXX** structural motif can be extended to lead to O-PAHs with zig-zag or armchair edges as a function of the symmetry of the repeating units. For instance, the use of 2,3-dihydroxylnaphthalene leads to O-doped graphene nanoribbons with armchair edges, whereas, the use of 2,6-dihydroxyl naphthalene leads to O-doped graphene nanoribbons with zig-zag edges, scheme 1.8.[40,41]

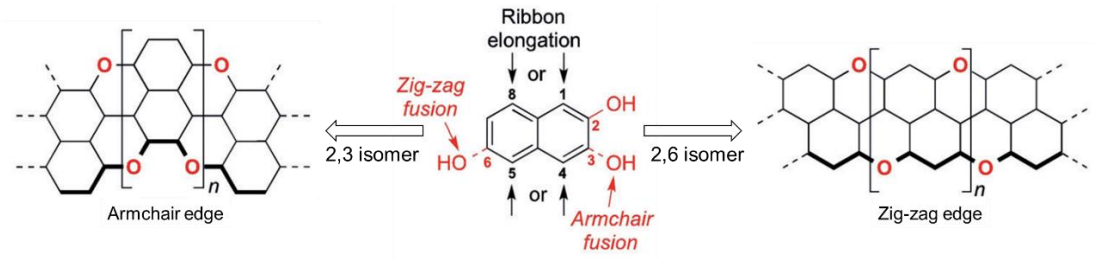

Scheme 1.8. Engineering O-doped peripheries with armchair and zig-zag topologies.

The synthesis of armchair and zig-zag extended **PXX**s has been achieved in our research group. The effect of different topologies on the photophysical properties of

these molecules can be evaluated through the spectroscopic characterisation.[40,41] For instance, this could be appreciated by the comparison of the UV-Vis steady-state absorption spectra of **PXX^{Ar}**, and that of the two **PXX^{Ar}** derivatives with armchair edges, **17.A^{X}** and **17.B^{X}**, figure 1.17.[41] While the spectrum of the **PXX^{Ar}** derivative features the typical lowest energy transitions at 449 nm, the spectra for molecules **17.A^{X}** and **17.B^{X}** are much broader. In particular, the absorption spectra of **17.A^{H}** and **17.A^{tBu}** show unstructured low-intensity red-shifted bands at 552 nm, whereas only a long absorption tail reaching 650 nm is observed for both **17.B^{H}** and **17.B^{tBu}**. The broadening of the electronic transitions is due to the molecular aggregation of the O-doped molecules.[41]

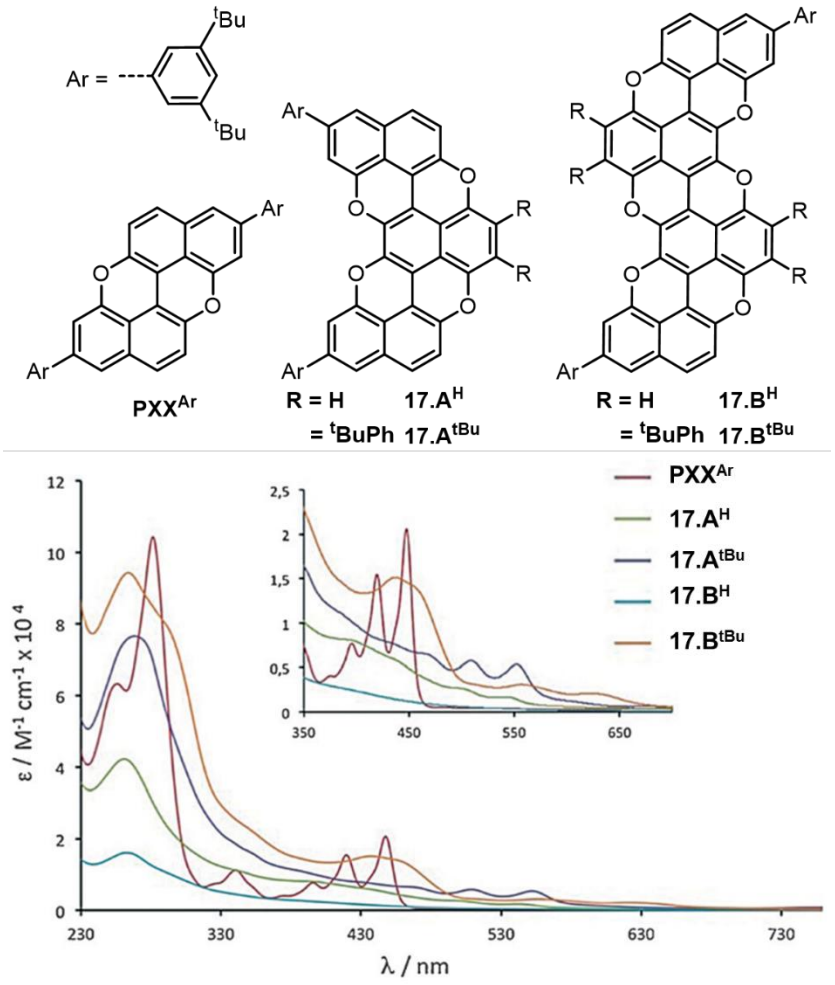

Figure 1.17. Absorption spectra of **PXX^{Ar}**, **17.A^{H}**, **17.A^{tBu}**, **17.B^{H}** and **17.B^{tBu}**.

UV/Vis absorption and emission properties of **18.C** molecules are displayed in Figure 1.18 with the specta of **18.A** and **18.B** used as references.[40] The lowest-energy electronic transition of **18.C** appears in the green region (523 nm) at a significantly lower energy than that of **18.B** (449 nm).

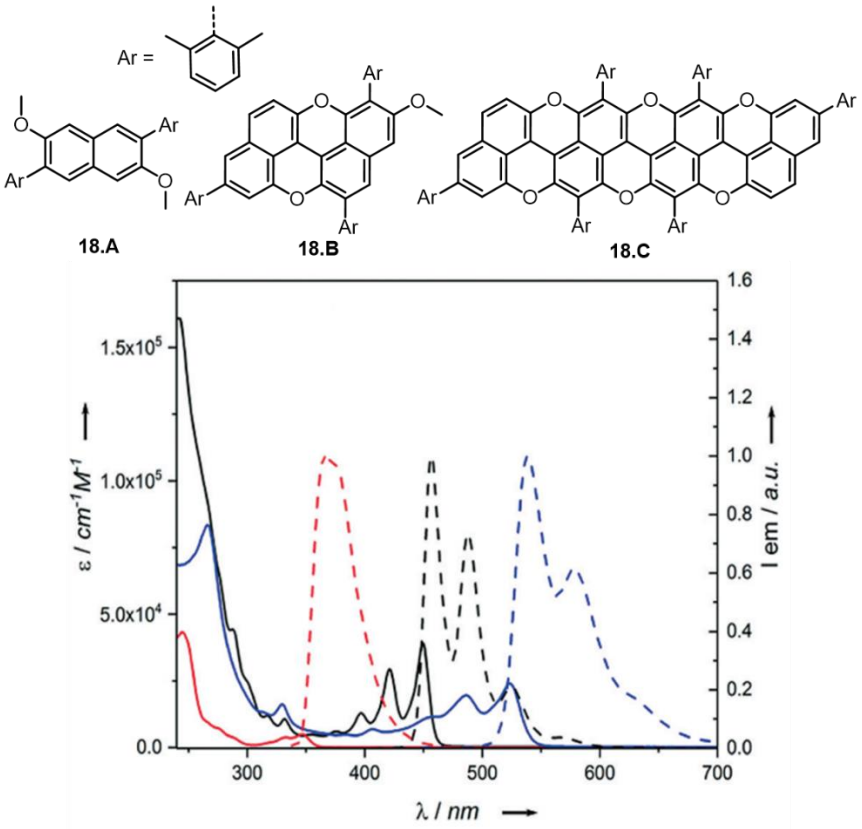

Figure 1.18. Absorption (solid lines) and emission (dashed lines) spectra of **18.A** (red), **18.B** (black) and **18.C** (blue).

In conclusion, the cases described above are clear examples on how oxygen doping in association with molecular modification by introducing EWGs or extending the π-conjugation in the *peri*-position are efficient methods to tune the optoelectronic properties of PAHs. Moreover, the optical band gap can be tuned as a function of the O-doped PAHs edges, as can be appreciated by comparing the absorption maxima in the spectra of **18.C,** which has only zig-zag edges, and of the isomer **17.B^{tBu}** , which has armchair edges, that are at 525 nm and ca. 650 nm, respectively.

1.4. Aim and Outline of the dissertation

In summary, PAHs have been deeply investigated for their application as electroactive materials. However, solution-based synthesis of large polyacenes has not been successful due to the poor chemical stability. In the attempt to improve their stability, the insertion of heteroatoms, such as oxygen, boron, and nitrogen atoms, in the carbon periphery is a feasible approach to prepare stable extended PAHs featuring zig-zag peripheries. The O-doping of PAHs is one of the most promising approach for the preparation of stable and highly efficient electroactive organic molecules. Particularly, the O-doped analogue of anthanthrene, PXX, can be considered as a building unit for engineering a new class of O-doped PAHs. However, the optoelectronic modification

has been achieved by introducing electron withdrawing groups on the periphery or extending the π-conjugation. In this doctoral work, our research activities were focused on the synthesis of novel PXX derivatives. Our aim was to study the effect of the PXX periphery heteroatom-doping, namely sulphur and nitrogen, on the optoelectronic properties. The different objectives of the thesis are: *i*) PXX optoelectronic properties modification through the insertion of nitrogen and sulphur atoms in PXX framework; *ii*) systematic study of the optoelectronic properties variation as a function of the position of nitrogen atoms; *iii*) *N*-methylation of nitrogen atoms in NPXXs and photophysical characterisation; *iv*) enhance the triplet population of PXX through mono sulphur doping and *v*) study the effect on the solid-state self-assembly due to the presence of heteroatoms. Accordingly, the work reported here is divided into three main chapters, figure 1.24.

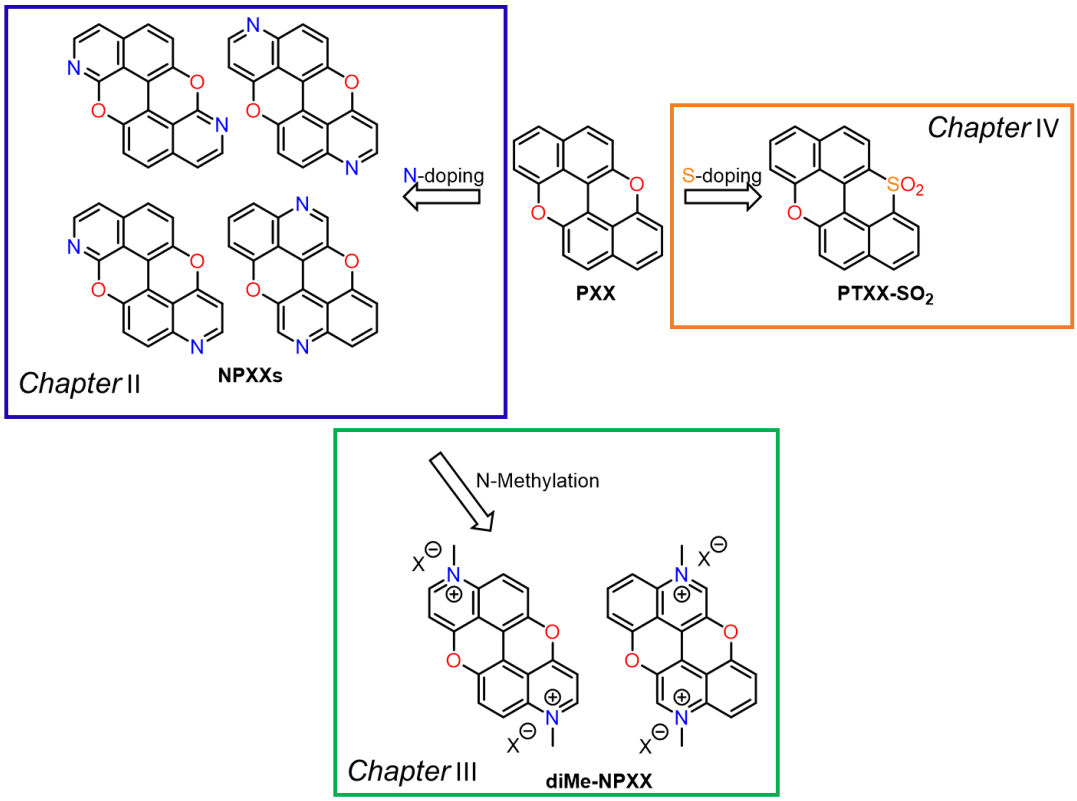

Figure 1.24. Schematic representation of the outline of this dissertation

Following this, the manuscript will be divided in three parts. *Chapter 2* will focus on the synthesis and characterisation of peripheral nitrogen-doping of PXX which leads to a new family of chromophores NPXXs. The effect of the doping will be also investigated as a function of the doping position. *Chapter 3* will focus on the synthesis and characterisation of N-methylated NPXXs, which can be considered as a new class of viologen-like molecules. *Chapter 4* will be dedicated to the synthesis and

characterisation of mono sulphur-doped PXX with the aim to enhance the triplet population of PXX-like molecule.

1.5 References

[1] K. S. Novoselov, A. K. Geim, S. V. Morozov, D. Jiang, Y. Zhang, S. V. Dubonos, I. V. Grigorieva, A. A. Firsov, *Science* **2004**, *36*, 666–669.

[2] K. S. Novoselov, V. I. Fal'Ko, L. Colombo, P. R. Gellert, M. G. Schwab, K. Kim, *Nature* **2012**, *490*, 192–200.

[3] M. J. Allen, V. C. Tung, R. B. Kaner, *Chem. Rev.* **2010**, *110*, 132–145.

[4] A. D. McNaught, A. Wilkinson, *IUPAC. Compendium of Chemical Terminology, 2nd Ed. (the "Gold Book")*, **1997**.

[5] A. Kuc, T. Heine, G. Seifert, *Phys. Rev. B: Condens. Matter Mater. Phys.* **2010**, *81*, 1–7.

[6] L. Chen, Y. Hernandez, X. Feng, K. Müllen, *Angew. Chem. Int. Ed.* **2012**, *51*, 7640–7654.

[7] L. Dössel, L. Gherghel, X. Feng, K. Müllen, *Angew. Chem. Int. Ed.* **2011**, *50*, 2540 –2543.

[8] D. Pan, J. Zhang, Z. Li, M. Wu, *Adv. Mater.* **2010**, *22*, 734–738.

[9] I. S. Byun, D. Yoon, J. S. Choi, I. Hwang, D. H. Lee, M. J. Lee, T. Kawai, Y. W. Son, Q. Jia, H. Cheong, and B. Ho Park., *ACS Nano* **2011**, *8*, 6417–6424.

[10] B. S. Jessen, L. Gammelgaard, M. R. Thomsen, D. M. A. Mackenzie, J. D. Thomsen, J. M. Caridad, E. Duegaard, K. Watanabe, T. Taniguchi, T. J. Booth, T. G. Pedersen, A. Jauho and P. Bøggild, *Nat. Nanotechnol.* **2019**, *14*, 340–346.

[11] K. Müllen, *ACS Nano* **2014**, *8*, 6531–6541.

[12] Y. Gu, X. Wu, T. Y. Gopalakrishna, H. Phan, J. Wu, *Angew. Chem. Int. Ed.* **2018**, *57*, 6541–6545.

[13] Y. Gu, Y. Gopalakrishna Tullimilli, J. Feng, H. Phan, W. Zeng, J. Wu, *Chem. Commun.* **2019**, *55*, 5567–5570.

[14] R. Scholl, C. Seer, *Justus Liebigs Ann. Chem.* **1912**, *394*, 111–177.

[15] E. Clar, *Ber. Dtsch. Chem. Ges.* **1929**, *62*, 1574–1582.

[16] K. Nakada, M. Fujita, G. Dresselhaus, M. S. Dresselhaus, *Phys. Rev. B: Condens. Matter Mater. Phys.* **1996**, *54*, 17954–17961.

[17] M. Fujita, K. Wakabayashi, K. Nakada, K. Kusakabe, *J. Phys. Soc. Jpn.* **1996**, *65*, 1920–1923.

[18] J. E. Anthony, *Angew. Chem. Int. Ed.* **2008**, *47*, 452–483.

[19] J. T. E. Quinn, J. Zhu, X. Li, J. Wang, Y. Li, *J. Mater. Chem. C* **2017**, *5*, 8654–8681.

[20] D. H. Kim, D. Y. Lee, H. S. Lee, W. H. Lee, Y. H. Kim, J. I. Han, K. Cho, *Adv. Mater.* **2007**, *19*, 678–682.

[21] K. Tanaka, K. Ohzeki, S. Nankai, T. Yamabe, H. Shirakawa, *J. Phys. Chem. Solids* **1983**, *44*, 1069–1075.

[22] A. Ciesielski, T. M. Krygowski, M. K. Cyrański, *J. Chem. Inf. Model.* **2008**, *48*, 1358–1366.

[23] R. Clar, E; Schoental, *Polycyclic Hydrocarbons, Vol. 2, Accademic Press: New York*, **1964**.

[24] C. H. Suresh, S. R. Gadre, *J. Org. Chem.* **1999**, *64*, 2505–2512.

[25] Z. Sun, Z. Zeng, J. Wu, *Acc. Chem. Res.* **2014**, *47*, 2582–2591.

[26] Z. Sun, S. Lee, K. H. Park, X. Zhu, W. Zhang, B. Zheng, P. Hu, Z. Zeng, S. Das, Y. Li, Y. Chunyan Chi, R. Li, K. Huang, J. Ding, D. Kim,J. Wu, *J. Am. Chem. Soc.* **2013**, *135*, 18229–18236.

[27] M. R. Ajayakumar, Y. Fu, J. Ma, F. Hennersdorf, H. Komber, J. J. Weigand, A. Alfonsov, A. A. Popov, R. Berger, J. Liu, et al., *J. Am. Chem. Soc.* **2018**, *140*, 6240–6244.

[28] T. Kubo, *Chem. Lett.* **2015**, *44*, 111–122.

[29] M. F. Cheng, W. K. Li, *Chem. Phys. Lett.* **2003**, *368*, 630–638.

[30] M. Bendikov, F. Wudl, D. F. Perepichka, *Chem. Rev.* **2004**, *104*, 4891–4954.

[31] A. Maliakal, K. Raghavachari, H. Katz, E. Chandross, T. Siegrist, *Chem. Mater.* **2004**, *16*, 4980–4986.

[32] W. Fudickar, T. Linker, *J. Am. Chem. Soc.* **2012**, *134*, 15071−15082.

[33] A. R. Reddy, M. Bendikov, *Chem. Commun.* **2006**, 1179–1181.

[34] R. B. Woodward, R. Hoffmann, *J. Am. Chem. Soc.* **1965**, *87*, 395–397.

[35] R. Hoffmann, R. B. Woodward, *Acc. Chem. Res.* **1968**, *1*, 17–22.

[36] R. B. Woodward, R. Hoffmann, *Angew. Chem. Int. Ed.* **1969**, *8*, 781–853.

[37] G. W. Breton, X. Vang, *J. Chem. Educ.* **1998**, *75*, 81–82.

[38] B. H. Northrop, K. N. Houk, A. Maliakal, *Photochem. Photobiol. Sci.* **2008**, *7*, 1463–1468.

[39] M. Stępień, E. Gońka, M. Żyła, N. Sprutta, *Chem. Rev.* **2017**, *117*, 3479–3716.

[40] A. Berezin, N. Biot, T. Battisti, D. Bonifazi, *Angew. Chem. Int. Ed.* **2018**, *57*, 8942–8946.

[41] D. Stassen, N. Demitri, D. Bonifazi, *Angew. Chem. Int. Ed.* **2016**, *55*, 5947–5951.

[42] T. Miletić, A. Fermi, I. Orfanos, A. Avramopoulos, F. De Leo, N. Demitri, G. Bergamini, P. Ceroni, M. G. Papadopoulos, S. Couris, D. Bonifazi., *Chem. - Eur. J.* **2017**, *23*, 2363–2378.

[43] R. Berger, A. Giannakopoulos, P. Ravat, M. Wagner, D. Beljonne, X. Feng, K. Müllen, *Angew. Chem. Int. Ed.* **2014**, *53*, 10520–10524.

[44] Y. S. Park, D. J. Dibble, J. Kim, R. C. Lopez, E. Vargas, A. A. Gorodetsky, *Angew. Chem. Int. Ed.* **2016**, *55*, 3352–3355.

[45] D. Cortizo-Lacalle, J. P. Mora-Fuentes, K. Strutyński, A. Saeki, M. Melle-Franco, A. Mateo-Alonso, *Angew. Chem. Int. Ed.* **2018**, *57*, 03 –708.

[46] T. Katayama, S. Nakatsuka, H. Hirai, N. Yasuda, J. Kumar, T. Kawai, T. Hatakeyama, *J. Am. Chem. Soc.* **2016**, *138*, 5210−5213.

[47] M. Fingerle, C. Maichle-Mössmer, S. Schundelmeier, B. Speiser, H. F. Bettinger, *Org. Lett.* **2017**, *19*, 4428–4431.

[48] M. Numano, N. Nagami, S. Nakatsuka, T. Katayama, K. Nakajima, S. Tatsumi, N. Yasuda, T. Hatakeyama, *Chem. - Eur. J.* **2016**, *22*, 11574–11577.

[49] N. Kobayashi, M. Sasaki, K. Nomoto, *Chem. Mater.* **2009**, *21*, 552–556.

[50] M. Noda, N. Kobayashi, M. Katsuhara, A. Yumoto, S. Ushikura, R. Yasuda, N.

Hirai, G. Yukawa, I. Yagi, K. Nomoto, T. Urabe, *Dig. Tech. Pap. - Soc. Inf. Disp. Int. Symp.* **2010**, *41*, 710–713.

[51] A. Sciutto, A. Fermi, A. Folli, T. Battisti, J. Beames, D. Murphy, D. Bonifazi, *Chem. - Eur. J.* **2018**, *24*, 4382–4389.

[52] A. Sciutto, A. Berezin, M. Lo Cicero, T. Miletić, A. Stopin, D. Bonifazi, *J. Org. Chem.* **2018**, *83*, 13787–13798.

[53] Y. Wang, S. Qiu, S. Xie, L. Zhou, Y. Hong, J. Chang, J. Wu, Z. Zeng, *J. Am. Chem. Soc.* **2019**, *141*, 2169−2176.

[54] A. Aranyos, D. W. Old, A. Kiyomori, J. P. Wolfe, J. P. Sadighi, S. L. Buchwald, *J. Am. Chem. Soc.* **1999**, *121*, 4369–4378.

[55] F. Ullmann, P. Sponagel, *Ber. Dtsch. Chem. Ges.* **1905**, *38*, 2211–2212.

[56] D. M. T. Chan, K. L. Monaco, R. P. Wang, M. P. Winters, *Tetrahedron Lett.* **1998**, *39*, 2933–2936.

[57] D. A. Evans, J. L. Katz, T. R. West, *Tetrahedron Lett.* **1998**, *39*, 2937–2940.

[58] P. Y. S. Lam, C. G. Clark, S. Saubern, J. Adams, M. P. Winters, D. M. T. Chan, A. Combs, *Tetrahedron Lett.* **1998**, *39*, 2941–2944.

[59] C. Sambiagio, S. P. Marsden, A. J. Blacker, P. C. McGowan, *Chem. Soc. Rev.* **2014**, *43*, 3525–3550.

[60] T. Rasmusson, L. J. P. Martyn, G. Chen, A. Lough, M. Oh, A. K. Yudin, *Angew. Chem. Int. Ed.* **2008**, *47*, 7009–7012.

[61] S. M. Elbert, M. Reinschmidt, K. Baumgärtner, F. Rominger, M. Mastalerz, *European J. Org. Chem.* **2018**, *2018*, 532–536.

[62] Y. Wei, N. Yoshikai, *Org. Lett.* **2011**, *13*, 5504–5507.

[63] B. Xiao, T. Gong, Z. Liu, J. Liu, D. Luo, J. Xu, L. Liu, *J. Am. Chem. Soc.* **2011**, *133*, 9250–9253.

[64] T. Asari, N. Kobayashi, T. Naito, T. Inabe, *Bull. Chem. Soc. Jpn.* **2001**, *74*, 53–58.

[65] J. Zhao, Y. Wang, Y. He, L. Liu, Q. Zhu, *Org. Lett.* **2012**, *14*, 1078–1081.

[66] J. Zhao, Y. Wang, Q. Zhu, *Synthesis (Stuttg).* **2012**, *44*, 1551–1555.

[67] J. Dai, W. Xu, Y. Wu, W. Zhang, Y. Gong, X. He, X. Zhang, H. Xu, *J. Org. Chem.* **2015**, 2–10.

[68] A. Rossignon, D. Bonifazi, *Synthesis (Stuttg).* **2019**, 10.1055/s-0037–1611892.

[69] D. Reger, P. Haines, F. W. Heinemann, D. M. Guldi, N. Jux, *Angew. Chem. Int. Ed.* **2018**, *57*, 5938–5942.

[70] K. Nakanishi, D. Fukatsu, K. Takaishi, T. Tsuji, K. Uenaka, K. Kuramochi, T. Kawabata, K. Tsubaki, *J. Am. Chem. Soc.* **2014**, *136*, 7101–7109.

[71] D. Reger, P. Haines, F. W. Heinemann, D. M. Guldi, N. Jux, *Angew. Chem. Int. Ed.* **2018**, *57*, 5938–5942.

[72] N. Kobayashi, M. Sasaki, K. Nomoto, *Chem. Mater.* **2009**, *21*, 552–556.

[73] S. Dong, T. Y. Gopalakrishna, Y. Han, H. Phan, T. Tao, Y. Ni, G. Liu, C. Chi, *J. Am. Chem. Soc.* **2019**, *141*, 62–66.

[74] H. F. Bettinger, *Pure Appl. Chem.* **2010**, *82*, 905–915.

[75] J. Hachmann, J. J. Dorando, M. Aviĺs, G. K. L. Chan, *J. Chem. Phys.* **2007**, *127*, 134309.

[76] Z. Sun, Q. Ye, C. Chi, J. Wu, *Chem. Soc. Rev.* **2012**, *41*, 7857–7889.

[77] T. Kubo, *Chem. Rec.* **2015**, *15*, 218–232.

[78] M. A. Wolak, B. Bin Jang, L. C. Palilis, Z. H. Kafafi, *J. Phys. Chem. B* **2004**, *108*, 5492–5499.

[79] A. R. Rudolf Pummerer, *Ber. Dtsch. Chem. Ges.* **1926**, *59*, 2159–2161.

[80] R. Pummerer, F. Frankfurter, *Ber. Dtsch. Chem. Ges.* **1914**, *47*, 1472–1493.

[81] B. K. Shah, D. C. Neckers, J. Shi, E. W. Forsythe, D. Morton, *J. Phys. Chem. A* **2005**, *109*, 7677–7681.

[82] T. Kamei, *JP 2018-39777 A 2018.3.15* **2018**, 1–104.

Chapter 2

Synthesis and Characterisation of N-Doped *peri*-Xanthenoxanthene

In this chapter, the design, synthesis and photophysical properties of a novel series of N-doped *peri*-xanthenoxanthene (PXX) are described. The first part addresses the retrosynthetic design and synthesis of different N-doped PXX regioisomers. The second part describes the investigation of the optoelectronics properties through spectroscopic and cyclic voltammetry measurements. The third part is focused on how the N-doping affects the solid-state organisation of these molecules.

The chapter is divided into seven main sections: *i) section 2.1*: general introduction on N-doped Polycyclic Aromatic Hydrocarbons (PAHs); *ii) section 2.2*: PXX properties description and aim of the project; *iii) section 2.3*: retrosynthetic approach and synthesis of the N-doped PXX molecules; i*v) section 2.4*: photophysical characterisation of the synthesised molecules and properties rationalisation via theoretical calculation; *v) section 2.5*: electrochemical characterisation via cyclic voltammetry; *vi) section 2.6*: solid-state characterisation through single crystal X-ray diffraction (XRD); *vii) section 2.7*: crystal engineering guided by halogen bonding; The X-ray analysis presented in this chapter were performed by *Dr. Nicola Demitri* (*Elettra-sincrotone, Trieste*), *Nicolas Biot* and *Deborah Romito* (*Cardiff University, School of Chemistry, Cardiff*) and TD-DFT calculation by Dr. *Nicola Bonini* and *Duncan Gowland* (*King's College, London*).

2.1 General introduction about N-doping of Polycyclic Aromatic Hydrocarbons

2.1.1 Optoelectronic properties of N-doped Polycyclic Aromatic Hydrocarbons.

N-Heteroacenes (or azaacenes) are nitrogen-doped (N-doped) homologues of acenes, where one or more than one C_{sp}^2−H moieties have been replaced by pyridine-like nitrogen atoms. This modification fine-tunes frontier molecular orbital energies by improving electron affinity and higher oxidative stability. Including nitrogen atoms into peripheral carbon framework is a goal as this induces a diversity of intermolecular interactions, which are essential to reach high-performance devices.[1] In this context, for instance, N-doped derivatives of perylene, which has been widely investigated due to its excellent optical and electronic properties,[2] have been studied.[3] In order to study the excited-state intramolecular proton transfer (ESPIT), 1-azaperylene was synthesized and functionalised with a hydroxyl-moiety by M. Gałezezowski *et al*, figure 2.1.[3] The absorption of 1-azaperylene **1.B** is bathochromic shifted by 1 nm with respect to the normal perylene **1.A**.[4] For the emission spectrum a Stokes shift of 4 nm and a quantum yield of 0.90 were observed. Nevertheless, the presence of the auxochrome hydroxyl-moiety in **1.C** shift the absorption maximum by 75 nm with respect to azaperylene B, table 2.1.

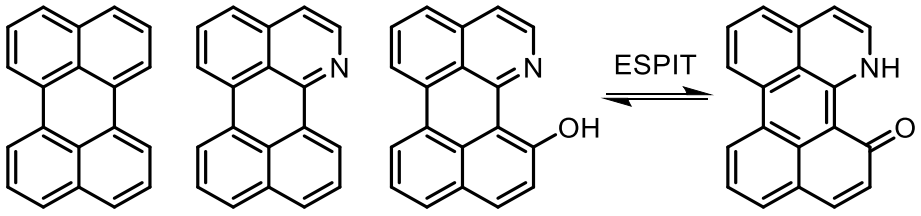

Figure 2.1. 1.A) perylene; **1.B**) 1-azaperylene; **1.C**) 12-hydroxy-1-azaperylene.

Table 2.1. Spectroscopic Properties of **1.A**, **1.B** and **1.C**.

	solvent	λ_{abs} (nm)	λ_{em} (nm)	QY_f (%)
1.A	Cyclohexane	435	436	0.94
	Acetonitrile	441	456	n.d.
1.B	Cyclohexane	444	448	90
	Ethanol	442	490	77
	Acetonitrile	516	524	n.d.
1.C	Cyclohexane	516	519	17
	Ethanol	516	523	26

The emission maximum of derivative **1.C** shows a red shift of 5 nm when the spectrum is measured in acetonitrile compared to that in cyclohexane, table 1.1. It is due to the favoured hydrogen bond between the hydroxyl group and the nitrogen in position 1. ESPIT was not observed for compound **1.C**. The calculated HOMO and LUMO energy levels difference for **c** and its relative keto-tautomer **c'** by TD-DFT are 2.79 eV and 2.73 eV. The authors assumed that the keto tautomer is not visible due to the close energy of emission with respect to irradiation, 0.06 eV.

Due to a wide use of OLEDs, organic thin film transistors and photovoltaic devices in the last decades, the N-heteroacenes chemistry has made significant progress and this class of compounds has been recognised as powerful n-type semiconductors. The general interest in azaacenes is witnessed by the constantly increasing number of research groups who work on these materials as novel functional and flexible species. Miao *et al*. reported a systematic study on peripheral N-doping of 6,13-bis(triisopropylsilylethynyl)pentacene (TIPS-PEN), a benchmark p-type organic semiconductor with high charge carrier mobility, figure 2.2.[5–9] In the absorption spectra, the longest-wavelength absorption of **2.B** and **2.D** shows a small bathochromic shift compared to that of TIPS-PEN, figure 2.2a. The HOMO and LUMO energy levels are lowered in **2.B** and **2.D** relatively to TIPS-PEN, figure 2.2b. As result of N-doping, molecule **2.D** shows electron mobility of up to 10 $cm^2V^{-1}s^{-1}$ changing the semiconductor nature of TIPS-PEN from p-type to n-type.

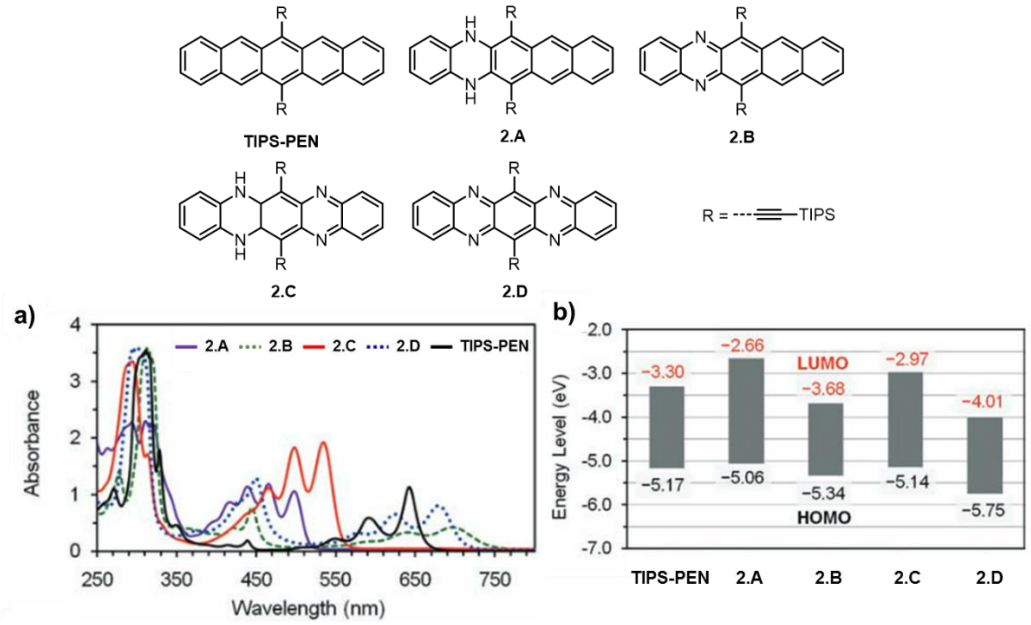

Figure 2.2. a) UV-vis absorption of 0.05 m M solutions of **2.A**, **2.B**, **2.C**, **2.D** and **TIPS-PEN** in CH_2Cl_2. b) HOMO and LUMO energy levels of **2.A**, **2.B**, **2.C**, **2.D** and **TIPS-PEN**.

Gong *et al.* focused their attention on the possibility to achieve an ambipolar material using the N-doping tool.[10] They doped with nitrogen atoms the already cited TIPS-PEN. In this work, they synthesised two different molecules: **1,8-diN-doped TIPS-PEN** and **1-diN-doped TIPS-PEN**, scheme 2.1.

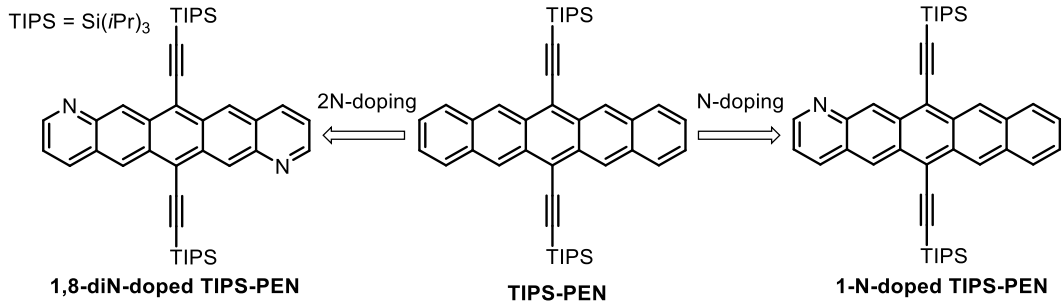

Scheme 2.1. TIPS-pentacene N-doping scheme.

As shown in table 2.2, TIPS-PEN and 1-N-doped TIPS-PEN have only p-type semiconductor properties with hole mobility μ_h = 0.4 $cm^2V^{-1}s^{-1}$ and μ_h = 0.22 $cm^2V^{-1}s^{-1}$, respectively. On the contrary, 1,8-diN-doped TIPS-PEN shows ambipolar semiconductor nature with hole charge mobility μ_h = 0.11 $cm^2V^{-1}s^{-1}$ and electron charge mobility μ_e = 0.15 $cm^2V^{-1}s^{-1}$.[11] The ambipolar behaviour of 1,8-diN TIPS-PEN was attributed to the presence of two nitrogen atoms which stabilised the formed anion after the electron injection in the LUMO orbital.

Table 2.2. Summary of μ_h and μ_e in top-contact OFETs fabricated for **TIPS-PEN**, **1,8-diN-TIPS-PEN** and **1-diN-TIPS-PEN** with Au electrodes.

	μ_h ($cm^2V^{-1}s^{-1}$)	μ_e ($cm^2V^{-1}s^{-1}$)
TIPS-PEN	0.4	-
1,8-diN TIPS-PEN	0.11	0.15
1-N TIPS-PEN	0.22	-

2.1.2 N-doped tailored PAHs solid-state self-assembly

Moreover, supramolecular organisation in the solid state is an important parameter to enhance organic semiconductors performance. N atoms in the periphery of PAHs influence the molecular packing in the solid state. For instance, the N-doping of 6,13-pentacenequinone induces the positive polarisation of the peripheral hydrogen atoms promoting weak hydrogen bonding between these hydrogen atoms and nitrogen or oxygen atoms, C-H···N, 3.47 Å, and C-H···O, 3.50 Å. The resulting crystal packing shows infinite one-dimensional stacks with a π-π distance of 3.39 Å. The unusual hydrogen bonding C-H···N/O present in the crystal structures may be applied as supramolecular recognition motif in crystal engineering.[12]

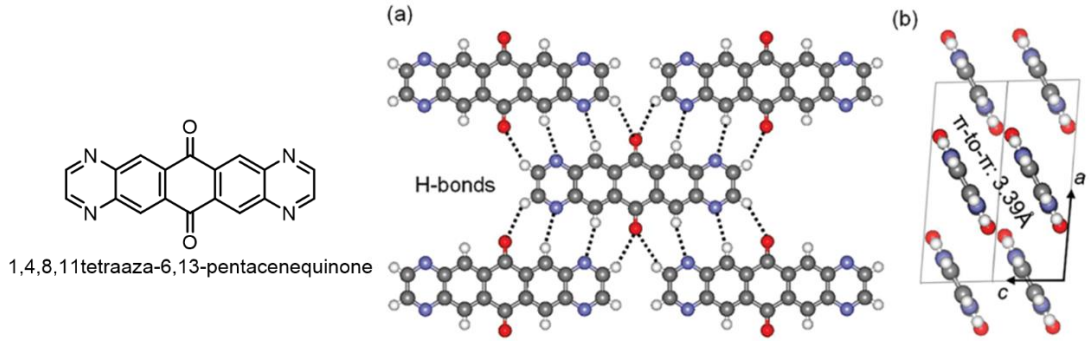

Figure 2.3. Crystal structure of 1,4,8,11-tetraaza-6,13-pentacenequinone: a) C-H···O/N hydrogen bonds as shown with dashed lines; b) π-π stacking as viewed along the b axis of unit cell.

Similarly, Sutter *et al.* demonstrated that it is possible to direct the hierarchical self-assembly of graphene nanoribbons (GNRs) into highly ordered structures through N-doping of the molecular precursor.[13] GNRs were prepared via surface assisted polymerisation or nickel mediated solution polymerisation, figure 2.4. GNRs are a category of carbon-based nanostructures with fascinating optoelectronic properties properties.[14] GNRs with armchair edges are predicted to be semiconductor materials with bandgaps that highly depend on the width of the ribbons.[15,16] The realisation of an extended crystalline GNR assembly could be an important starting point toward novel carbon-based semiconductors with widely tuneable properties.

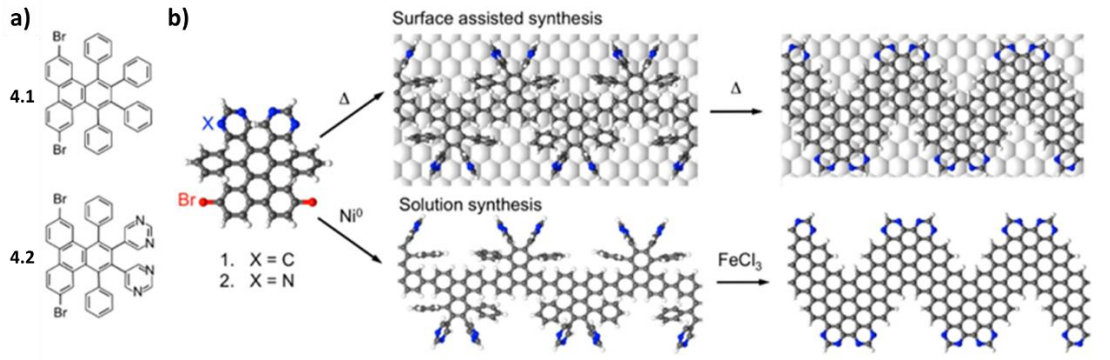

Figure 2.4. Atomically precise bottom-up synthesis of GNRs and 8N-GNRs on a surface and in solution. (a) Structure of the precursor monomers **4.1** and **4.2**. (b) Assembly into GNRs on an Au(111) surface (top) and in solution (bottom).

Undoped pristine P-GNRs prepared from **4.1** on surface form mainly isolated nanoribbons, typically 10−50 nm long, figure 2.5a. The synthesis of N-GNRs produces assemblies 10−20 nm long and STM analysis shows their organisation into a supramolecular motif where the N-doped edges of adjacent GNRs project toward each other, figure 2.5c and 2.5d. The observed arrangements are driven by weak hydrogen bonding between adjacent positively polarised C_{sp}^2−H and a nitrogen atom, figure 2.5f. In this work, the authors present an interesting tool for a possible highly precise assembly of N-doped GNRs in order to achieve 2-dimension conductive materials.

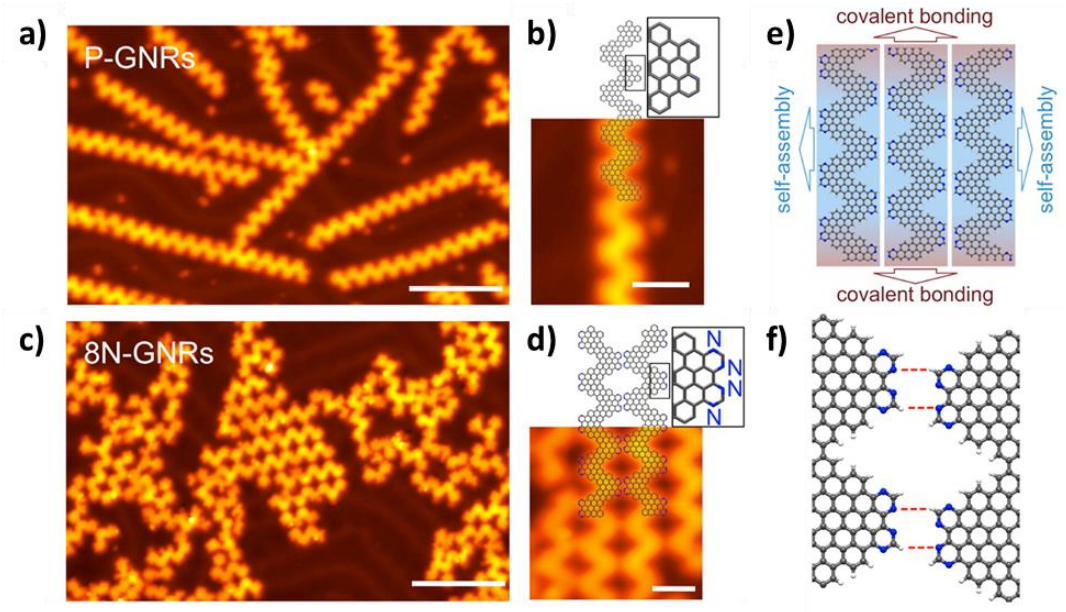

Figure 2.5. a) STM image of the morphology of pristine graphene nanoribbons (P-GNRs) on Au(111), after vacuum deposition of (1) followed by cyclo-dehydrogenation. Scale bar: 10 nm. V = 0.4 V, I = 0.1 nA; b) closeup view of one of the isolated P-GNRs. Scale bar: 2 nm; c) STM image of the morphology of N-doped 8N-GNRs on Au(111), synthesized by evaporation of (2) followed by cyclodehydrogenation. Scale bar: 10 nm. V = 0.4 V, I = 0.1 nA; d) close-up view of one of the 2D assemblies of 8N-GNRs. Scale bar: 2 nm; e) schematic representation of the 8N- GNR arrays; f) schematic structure of laterally coordinated 8N-GNRs.

2.2 PXX properties and aim of the project

2.2.1 Introduction about PXX properties

As discussed in Chapter 1, O-doping is a valid tool to improve the stability of PAH with unstable zig-zag edges such as tetracene, pentacene and anthanthrene. In particular, the oxygen doping of anthanthrene in the position 6 and 12 leads to the formation of the environmentally stable and excellent charge transport carrier *peri*-Xanthenoxanthene, PXX, which has been extensively investigated by Sony corporation as organic semiconductor, figure 2.6.[17,18]

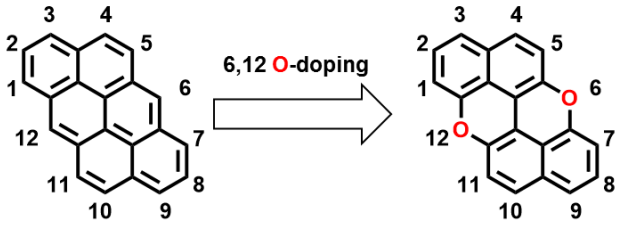

Figure 2.6. Anthanthrene O-doping scheme.

Looking at the supramolecular interactions in the solid state, PXX assembles in a herringbone motif driven by face to face interactions between the π planes and edge to face interactions between the partially negative π-cloud and the partially positive peripheral hydrogens, figure 2.7. Since the charge mobility is highly influenced by the supramolecular arrangement, this kind of packing is usually a limiting factor for the charge mobility inside the material.

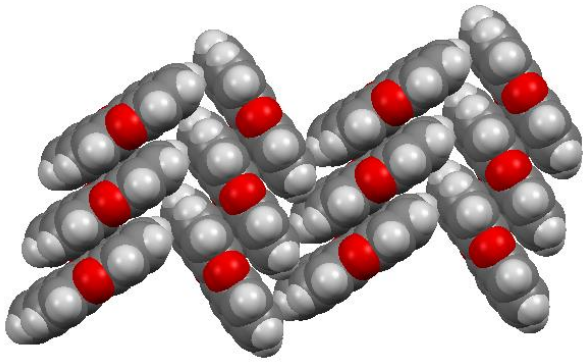

Figure 2.7. Side view PXX crystal packing. Space group Cc, R-factor 4.1%.

Functionalisation of the 3 and 9 positions of PXX with two phenyl rings enhances its chemical stability and solubility, as described by Kobayashi *et al*.[18] Moreover, this simple modification tunes the molecular self-assembly in a face-to-face stacking. The phenyl ring presence inhibits the edge-to-face interactions forcing the system to assemble into a graphite like structure, figure 2.8.

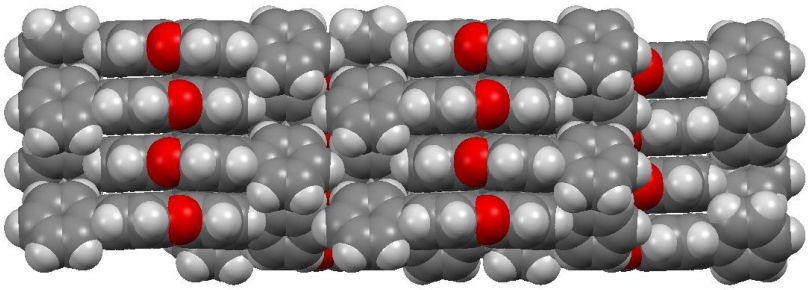

Figure 2.8. View perpendicular to face-to-face stacking column of Ph-PXX. Space group Pccn, R-factor 5.05%.

2.2.2 Aim of the project: N-doped *peri*-Xanthenoxanthene

The work objective shown in this chapter is the synthesis of N-doped PXX and the study of the optoelectronic properties variation as a function of the position of the nitrogen atoms. The replacement of a C_{sp^2}-H unit with its isoelectronic N_{sp^2} atom is a promising approach to tune the electronic properties keeping the extension of the π-conjugated framework unchanged. Moreover, the presence of the nitrogen atoms will modify the polarisation of the peripheral hydrogen atoms allowing weak hydrogen bond interactions, as discussed above, and possibly drive the solid-state arrangement of the molecules. According to the doping scheme depicted in the figure 2.9, it is possible to define two different naphthalene rings, blue and red, and each naphthalene has five available positions where the nitrogen atom can be placed. Therefore, considering all the possible combinations of doping between the naphthalene rings, it can be possible to synthesise fifteen different regioisomers.

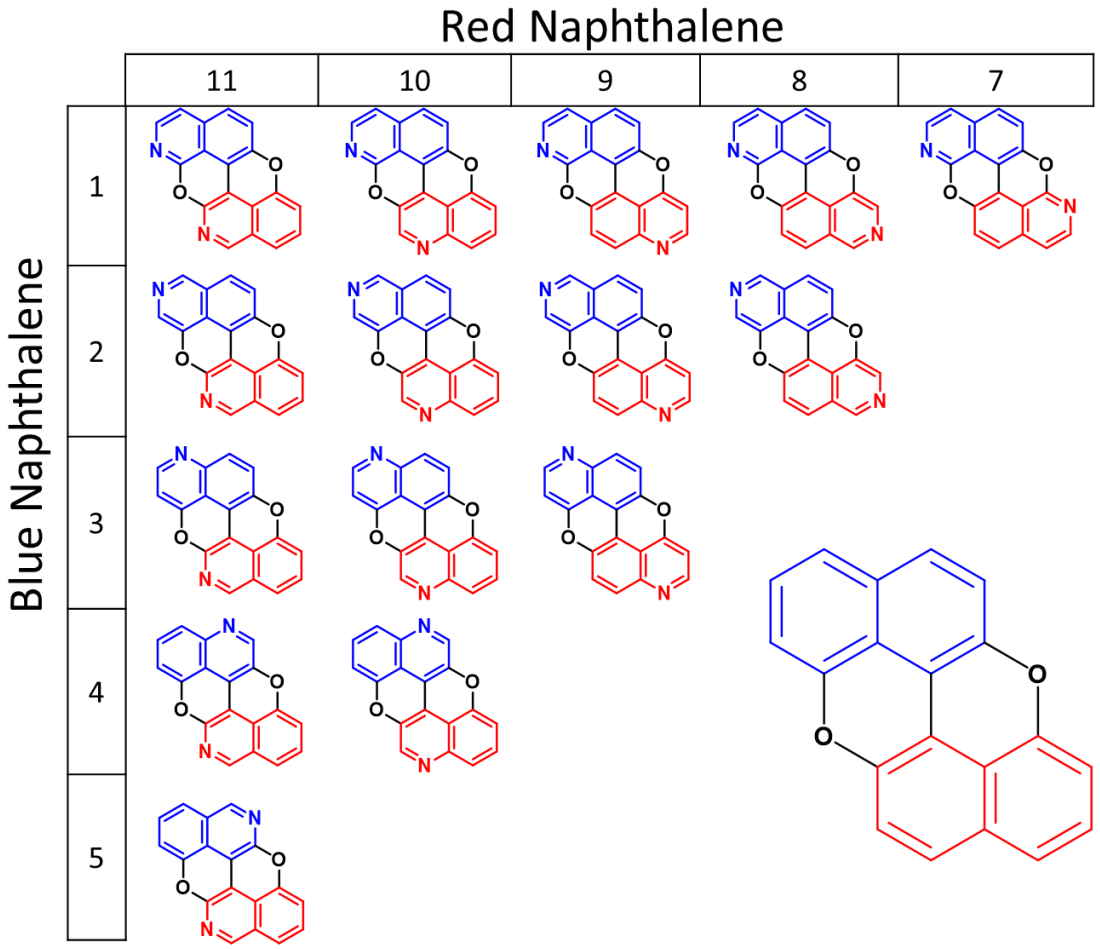

Figure 2.9. PXX N-doping strategy scheme.

This new family of compounds can be divided in asymmetrical dinitrogen doped PXX and symmetrical dinitrogen doped PXX, represented in the major diagonal of the figure 2.9. In order to investigate the chemical reactivity and the photophysical properties, it was decided to undertake, as first targets, the investigation of the symmetrical dinitrogen doped PXX, depicted in figure 2.10.

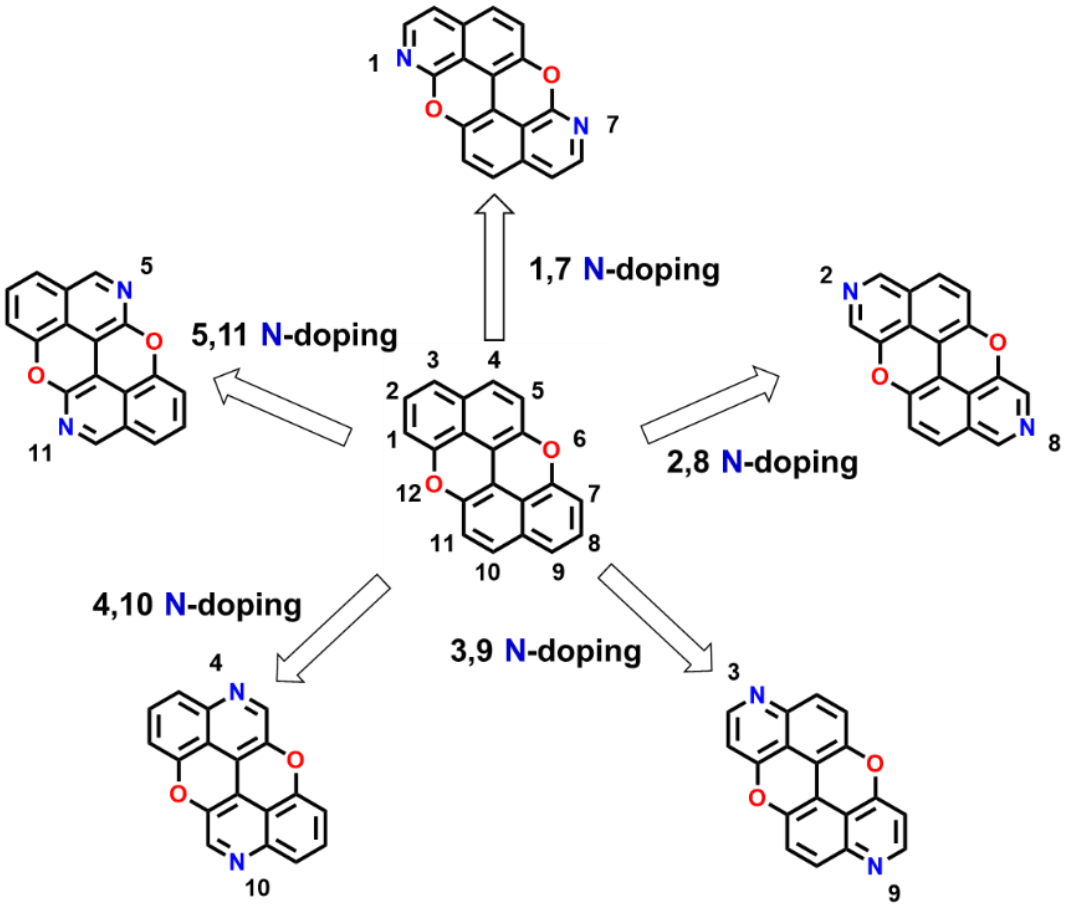

Figure 2.10. Symmetrical diN-doped PXXs.

.2.3 N-doped *peri*-Xanthenoxanthene: Synthesis

2.3.1 Retrosynthetic approach.

The synthetic plan towards the preparation of di-N-doped *peri*-xanthenoxanthene (diN-PXX) is guided by the literature on PXX synthesis.[17,19–23] The retrosynthetic pathway, shown in scheme 2.4, can be rationalised through the disconnection of two C_{sp}^2-O bonds and one C_{sp}^2-C_{sp}^2 bond, scheme 2.2.

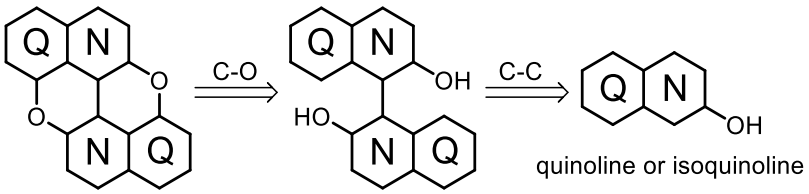

Scheme 2.2. NPXXs generic retrosynthetic pathway.

The C_{sp}^2-O bonds can be disconnected either in a homolytic or heterolytic way, figure 2.11. While the synthon a), which bears a positive charge on the oxygen atom, is difficult to obtain as a synthetic equivalent, the synthon b), which has a positive charge on the carbon atoms in *peri*-position, is easily achievable by halo-functionalisation of those carbons (analogous to e). On the other hand, halogenation of that position cannot

be highly selective because of the presence of the hydroxyl moiety that acts as *ortho*-orientating group for the halogenation via aromatic electrophilic substitution. The synthon c), instead, deriving from the homolytic disconnection, has carbon and oxygen radicals. The synthetic equivalent of this synthon is the relative bis-hydroxy-bisquinoline (BIQOL) f) which in presence of a specific oxidant can form C_{sp}^2-O bond via Single Electron Transfer (SET) mechanism. Taking this into consideration, it has been decided to follow the homolytic disconnection pathway. The literature about this C_{sp}^2-O oxidative annulation is extensive and, therefore, we limited our study to Cu-mediated C_{sp}^2-O oxidative annulation which is the most used for the PXX synthesis.

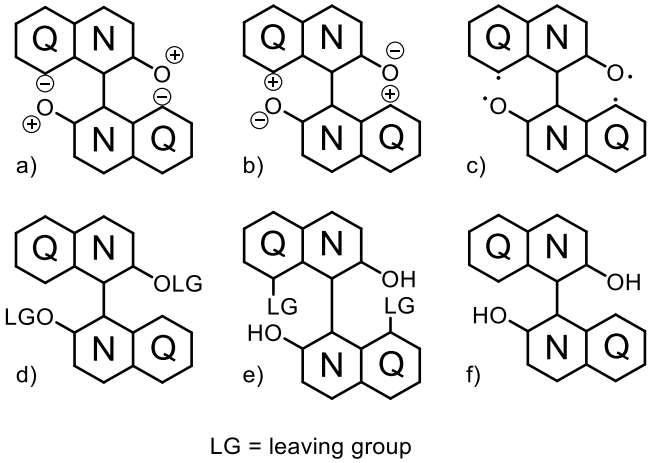

Figure 2.11. a) and b) Heterolytic disconnections, c) homolytic disconnection, d) and e) synthetic equivalent for heterolytic disconnections, f) synthetic equivalent for homolytic disconnection.

The C_{sp}^2-C_{sp}^2 bond disconnection leads to two polar synthons for the heterolysis and one radical synthon for the homolysis, figure 2.12a and 2.12b. The synthetic equivalents for the polar synthons are a halo-derivative for the cation and an organometallic species for the anion, figure 2.12c. This synthetic pathway has been used before for the synthesis of asymmetrically functionalised PXXs, such as PXX- monoimmide (PXXMI), asymmetric PXX-diimmide (PXXDI) and *peri-π-e*xtended PXXMI.[24,25] In our case, the homodimerization between two hydroxy(iso)quinoline molecules, figure 2.12d, appears as the most pratical synthetic approach due to the symmetry of the target molecules. Following this synthetic pathway, the functionalisation, either by halogenation or metalation of the starting material, is not required.[26]

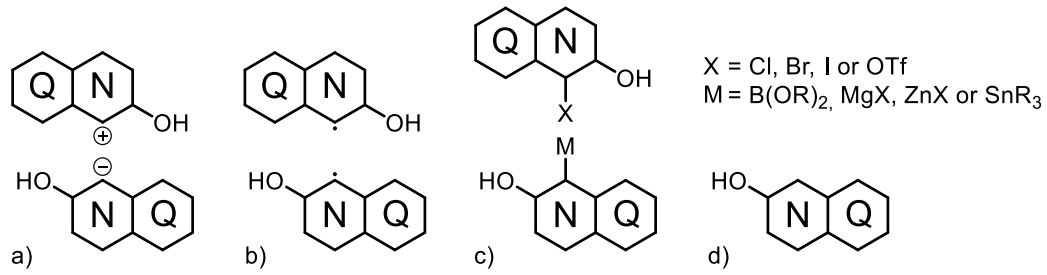

Figure 2.12. a) Heterolytic disconnections; b) homolytic disconnection; c) synthetic equivalent for heterolytic disconnection and d) synthetic equivalent for homolytic disconnection.

In the light of this, our synthetic plan envisaged an oxidative C_{sp^2}- C_{sp^2} bond formation followed by a second oxidation to form two C_{sp^2}-O bonds. Considering the literature, it was envisaged that the racemic BIQOL mixture could be synthesised by: 1) oxidative homo-dimerization of the (iso)quinoline derivative in the presence of a Cu as oxidant; 2) (iso)quinoline derivative Directed ortho Metalation (DoM) followed by oxidative dimerization.[27,28]

2.3.2 Cu-mediated oxidative dimerisation

The BIQOL has a similar skeleton to 1,1′-bi-2-naphthol (BINOL), except than one C_{sp^2}-H moiety per naphthyl group is replaced by one N_{sp^2}. For this reason, the synthetic protocols for the synthesis of BINOL can be adapt for BIQOL. Yi-Xin Chen *et al.* reported a successful route where the oxidative dimerization of the quinolin-6-ol is achieved with Cu-$BnNH_2$ complex generate *in situ* by stirring $CuCl_2$•$2H_2O$ and benzylamine in methanol at r.t., scheme 2.6. [29]

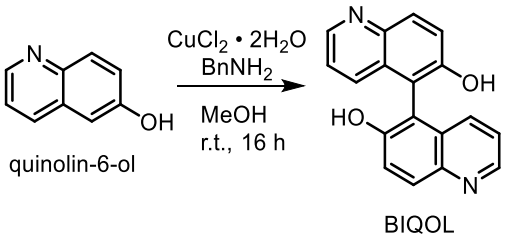

Scheme 2.3. BIQOL synthesis scheme form quinolin-6-ol via Cu-mediated oxidative dimerisation.

In accordance with the BINOL formation mechanism, the first step could be the oxidation of the quinolin-6-ol via single electron transfer (SET) in *ortho* position of the hydroxyl group to a radical species. In a second time, the formed radical could react with a second quinoline giving the dimer radical intermediate. The formed dimer is then oxidised again via SET to the diketo-form which tautomerises to the corresponding BIQOL, scheme 2.4.[30]

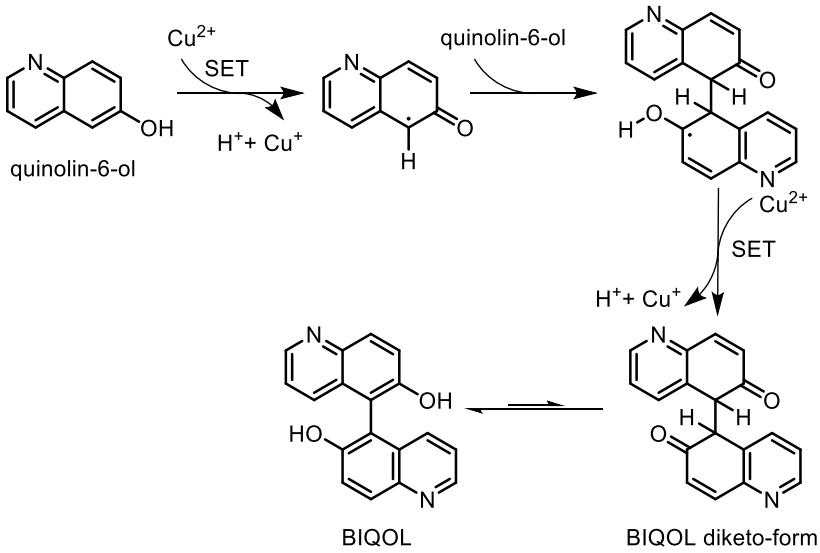

Scheme 2.4. Plausible reaction mechanism for BIQOL synthesis.

The discussed protocol offers the advantages of not being oxygen and water sensitive and does not require pre-functionalisation of hydroxyl-(iso)quinoline. Conversely, the successful outcome of the reaction is strictly related to the oxidation potential of the starting material. Thus, the reaction will not work for hydoxyquinolines with higher oxidation potential than Cu-$BnNH_2$ complex.

2.3.3 Oxidative dimerisation through Directed ortho Metalation

A second route for the synthesis of BIQOL has been reported by Milicevic *et al,* scheme 2.5.[28] It envisages a four step process: 1) *O*-acylation of hydroxyquinoline with carbamoyl chloride; 2) DoM on the carbamoyl (iso)quinoline derivative; 3) oxidative dimerisation promoted by $FeCl_3$; 4) carbamoyl deprotection. The DoM is an acid-base reaction and involves the deprotonation of an *ortho* C_{sp}^2-H bond to form the organolithium derivative with an organolithium reagent (RLi) used as strong base.[31] $FeCl_3$ acts as oxidising reagent to form the C_{sp}^2-C_{sp}^2 bond.

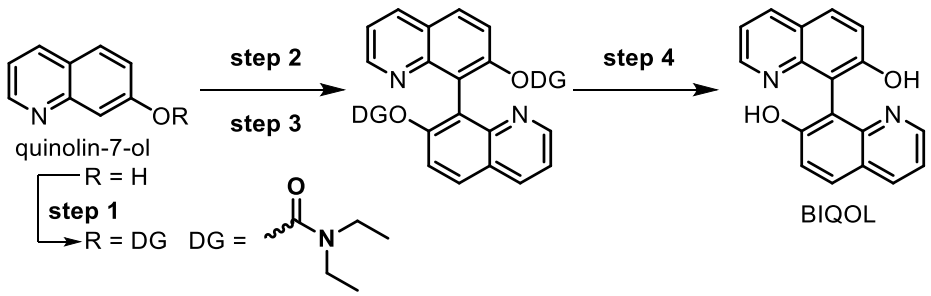

Scheme 2.5. BIQOL synthesis form quinolin-7-ol oxidative dimerisation through DoM.

The high regioselectivity of this reaction is due to the presence of a directing metalation group (DMG) which thermodynamically stabilises one of the possible metalation products. The DoM process could be rationalised as a two steps reaction, scheme 2.6:

step 1) coordination of the RLi aggregate to the DMG; step 2) *ortho*-deprotonation to give the coordinated lithiated species.

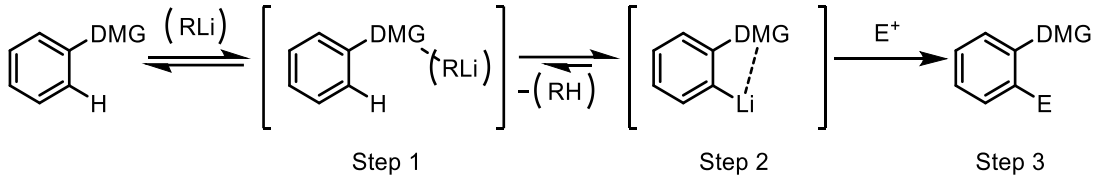

Scheme 2.6. Generic DoM reaction mechanism

The role of the DMG is crucial because it must be at the same time a good coordinating site for alkyl-lithium reagents and a poor electrophilic site to avoid nucleophilic attack by this base. The DMG must also have a heteroatom like nitrogen, oxygen and sulphur, able to coordinate and stabilise the organo-lithium intermediate. For aryl-hydroxy substrates ortho functionalisation, N,N-diethyl-O-carbamate group is one of the most common coordinating DMG, as it forms a stable six member ring complex within the organolithium compound, scheme 2.7a. Finally, the hydroxyl moiety can be easily acylated by carbamoyl chloride and, after DoM reaction, it can be simply deprotected by basic hydrolysis, scheme 2.7a and 2.7b.[28]

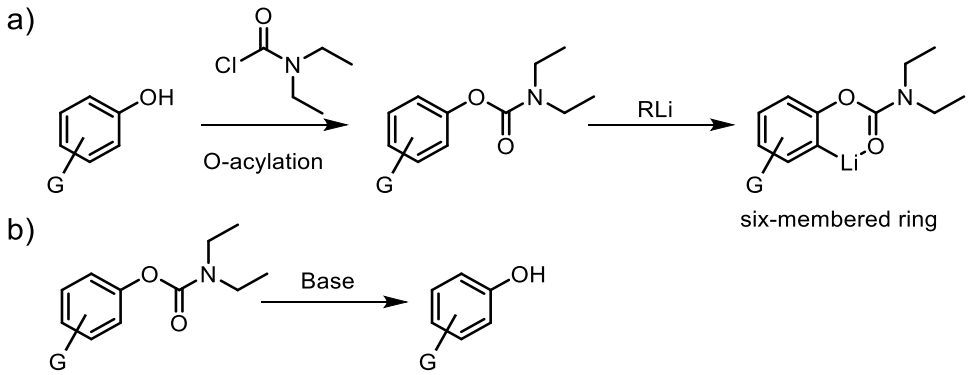

Scheme 2.7. a) hydroxyl moiety O-acylation and organo-lithium 6 stable six-member ring; b) basic deprotection of carbamoyl moiety.

Due to the electrophilicity of the α and γ carbon atoms in pyridine-like moieties, the choice of the organo-lithium base is very important. The lack of nucleophilic behaviour of lithium dialkyl amides (LDA) favours the metalation through deprotonation over the nucleophilic attack in this kind of molecules.[32] The advantage of this synthetic protocol is that the reaction outcome is independent of the oxidation potential of the hydroxylquinoline. It is due to because the $FeCl_3$ oxidises the lithiated quinoline which has lower oxidation potential than the normal quinoline. On the other hand, the reaction protocol requires two more synthetic steps: 1) the pre-functionalisation of the hydroxylquinoline with carbamoyl chloride to introduce the DMG and 2) the final deprotection of the hydroxyl moiety.

2.3.4 3,9-diN-PXX 2 synthesis

Molecule **1** has been prepared following the protocol reported by Kwong *et al*. Quinolin-6-ol was dimerised via oxidative coupling in presence of 2.4 equivalent of $CuCl_2$-$BnNH_2$ complex.[29] BIQOL **1** was collected as a brown solid precipitate in 55% yield. Product **1** and CuO were then suspended in $PhNO_2$ and refluxed at 210 °C for 16 hours. The purification of 3,9-diN-PXX **2** was achieved by chromatography on silica gel. Isolated product **2** was collected as a orange solid in 23% yield, scheme 2.8. Crystals of molecule **2** were obtained by slow evaporation of $CHCl_3$ and analysed by single crystal X-ray diffraction to confirm the molecular structure (essential crystal and refinement data are reported in *chapter 5*).

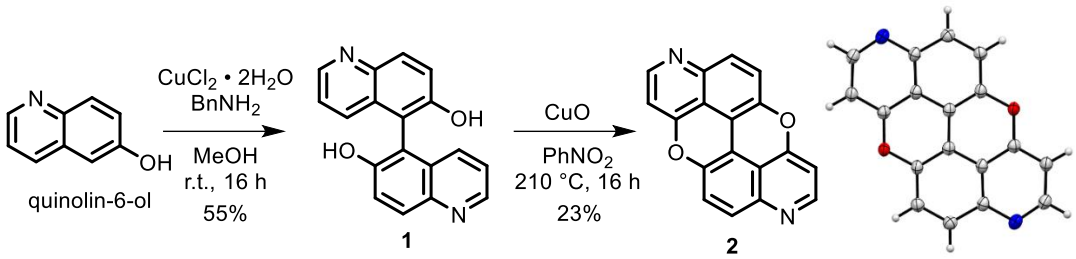

Scheme 2.8. Synthetic protocol for the preparation of 3,9-diN-PXX **2** and ORTEP representation of molecule **2** (50% probability ellipsoids), solvent for crystallisation: $CHCl_3$.

2.3.5 1,7-diN-PXX 4 synthesis

Following the same synthetic protocol used for the synthesis of 3,9-diN-PXX, isoquinolin-7-ol was dissolved in MeOH and treated with 2.4 equivalent of $CuCl_2$-$BnNH_2$ complex. BIQOL **3** was collected as brown precipitate and successively cyclised to 1,7-diN-PXX **4** via oxidative intermolecular $C_{sp}{}^2$-O formation. 1,7-diN-PXX **4** was purified by column chromatography and collected as a yellow solid in 52% yield, scheme 2.9. Crystals of molecule **4** were obtained by vapour diffusion of Et_2O in a toluene solution and analysed by single crystal X-ray diffraction to confirm the molecular structure (essential crystal and refinement data are reported in *chapter 5*).

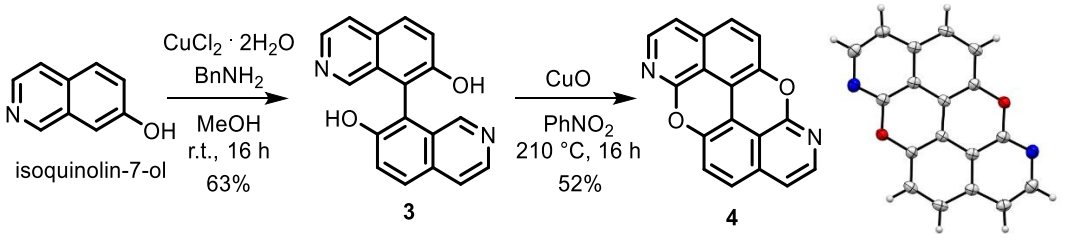

Scheme 2.9. Synthetic protocol for the preparation of 1,7-diN-PXX **4** and ORTEP representation of molecule **4** (50% probability ellipsoids), solvent for crystallisation: Toluene/Et_2O.

2.3.6 4,10-diN-PXX 6 synthesis

The synthesis of BIQOL **5** was attempted following the same protocol for the synthesis of BIQOLs **1** and **3**. However, the corresponding quinoline derivative did not yield the formation of the product and only the starting material was recovered, scheme 2.10. We think that the chemical inertia showed in the oxidative homo-dimerisation is due to the higher oxidation potential of quinolin-3-ol than the previously used (iso)quinolines.

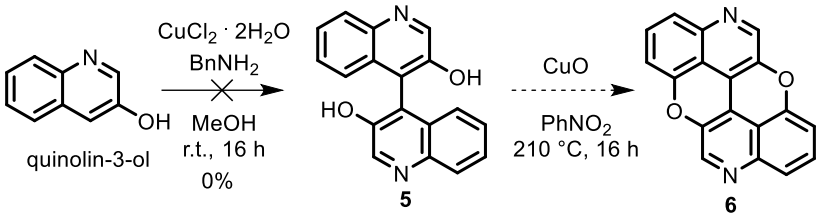

Scheme 2.10. Synthetic protocol for the preparation of BIQOL **5** with Cu-mediated oxidative dimerisation.

It has been decided to attempt the dimerisation of quinoline-3-ol using harsher conditions, such as CuCl in DMSO at 120 °C for 16 hours.[33] The reaction showed complete conversion of the starting material but, surprisingly, the only observed product was molecule **7** in 30% yield, scheme 2.11.

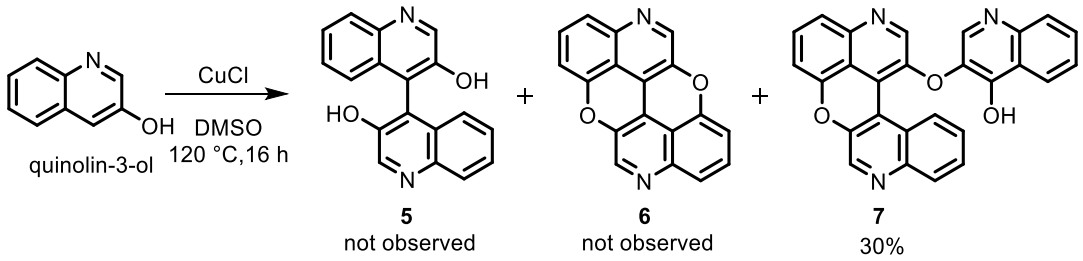

Scheme 2.11. Synthetic protocol for the preparation of BIQOL **5** with Cu-mediated oxidative dimerisation.

The structure assignment of **7** was given by single crystal X-ray diffraction, figure 2.13. The obtained product derives from an oxidative trimerization of quinoline-3-ol and it is composed of an helicoidal section and a further oxidised quinoline-3-ol. Due to the non-enantiospecificity of the reaction conditions, the achieved product is present in both enantiomeric forms. The crystal packing shows the presence of two helicoid enantiomers P (blue) and M (red), figure 2.13b, 2.13 c and 2.13d. The structure shows the formation of the desired C_{sp^2}-C_{sp^2} bond and one C_{sp^2}-O bond closing to form a pyran cycle. On the other side of the molecule, an ether bridge between its helicoidal part and the over oxidised quinoline is formed.

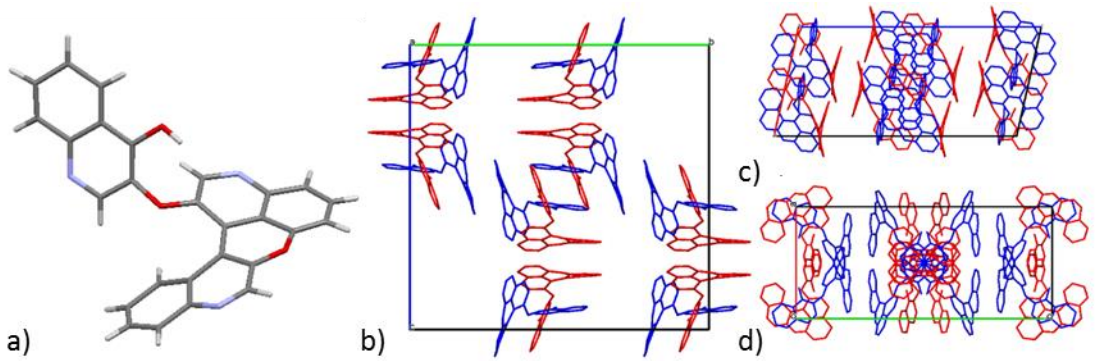

Figure 2.13. a) Capped stick representation of molecule **7**, solvent for crystallisation: MeOH. Coordinated solvent molecules omitted for clarity. b) Unit cell view along axis a, c) unit cell view along axis b, d) unit cell view along axis c. Enantiomer P in blue and enantiomer M in red.

In the light of the previously discussed homo-dimerisation mechanism, shown in scheme 2.4, a reasonable proposed mechanism for the formation of product **7** could consist of an oxidative dimerisation followed by condensation and further two oxidation steps, scheme 2.12. The first step is the oxidative homo-dimerization of quinolin-3-ol to form corresponding BIQOL **5**, which is followed by the formation of the ether bond with another hydroxyl quinoline. This derivative then undergoes an oxidation that leads to hemicyclised BIQOL followed by further oxidation in the last step to form molecule **7**.

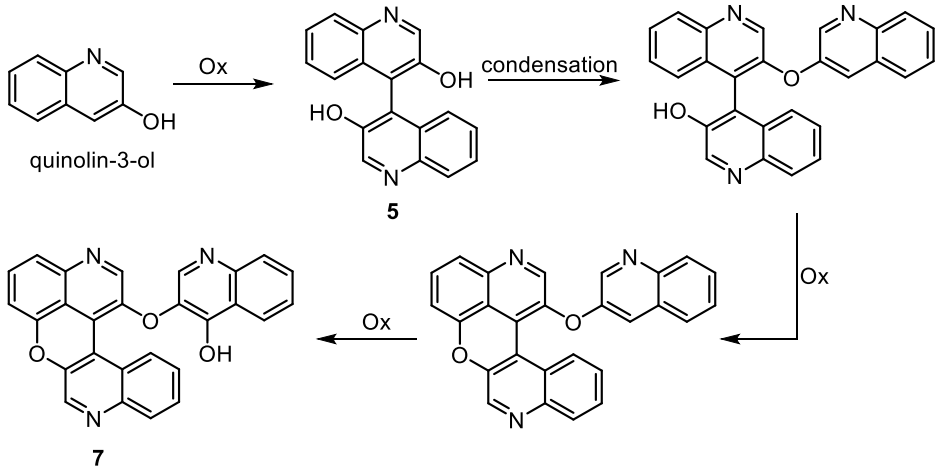

Scheme 2.12. Suggested reaction mechanism for the formation of molecule **7** formation.

In the light of this plausible reaction mechanism, it has been decided to investigate different reaction conditions for the purpose of stopping the reaction at the wanted BIQOL **5** step. Therefore, different ligands were employed in order to alter the redox potential of the Cu-complex. Furthermore, the reactions were performed both at 70 °C and 100 °C in order to investigate the influence of the temperature on the formation of the product, table 2.4. The reaction did not work at 70 °C and only starting material was

recovered independently of the ligand used. At 100 °C, the reactions showed only the formation of the helicene independently of the ligand.

Table 2.4. Reaction condition tested for BIQOL **5** synthesis using CuCl as oxidant.

Ligand	Temperature (°C)	**5** (%)	**6** (%)	**7** (%)	Conversion (%)
-	70	0	0	0	0
TMEDA	70	0	0	0	0
bipy	70	0	0	0	0
En	70	0	0	0	0
-	100	0	0	30	100
TMEDA	100	0	0	28	100
bipy	100	0	0	33	100
En	100	0	0	22	100

To overcome this synthetic issue, it has been decided to follow the DoM synthetic pathway, scheme 2.13. Quinolin-3-ol was dissolved in dry pyridine and treated with carbamoyl chloride giving product **8** as a yellow oil in 95% yield. The obtained product was dissolved in dry THF and the solution cooled down to -78 °C using a dry ice/acetone bath. The cold solution was firstly treated with LDA to form the lithiated compound and then with a suspension of anhydrous $FeCl_3$ to form biscarbamoyl BIQOL **9** as a colourless oil in 52% yield. The carbamoyl moieties of molecule **9** were hydrolysed with KOH in MeOH giving product **5** as a white solid in 98% yield. BIQOL **5** was then cyclised with CuO giving desired product **6** as an orange solid in 20% yield.

Crystals of molecule **6** were obtained by vapour diffusion of hexane in $CHCl_3$ and analysed by single crystal X-ray diffraction to confirm the molecular structure

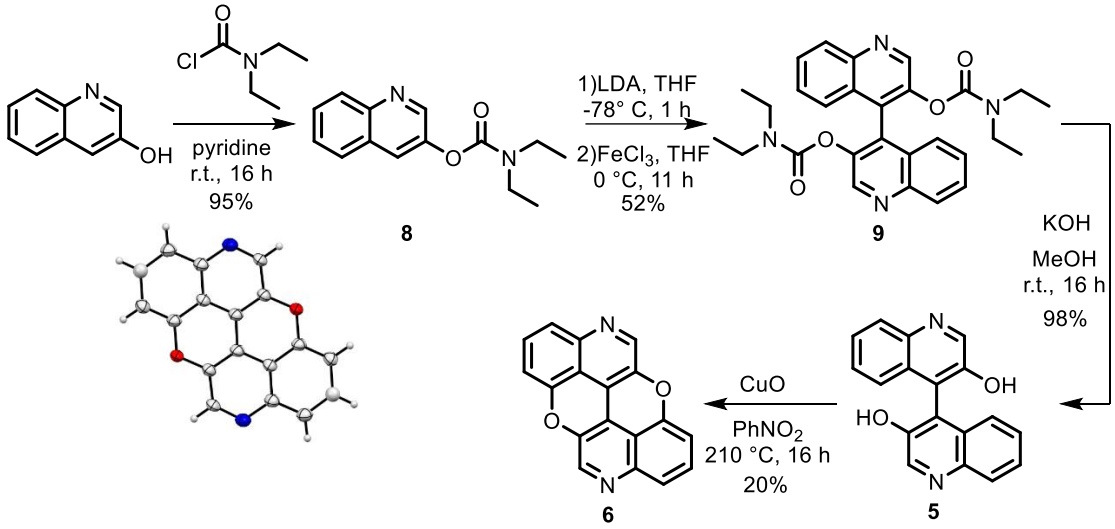

Scheme 2.13. Synthetic protocol for the preparation of 4,10-diN-PXX **6** and ORTEP representation of molecule **6** (50% probability ellipsoids), solvent for crystallisation: $CHCl_3$/Hexane.

2.3.7 5,11-diN-PXX 11 synthesis

Following the oxidative protocols performed for the attempted synthesis of BIQOL **5**, isoquinolin-3-ol was reacted with $CuCl_2$-$BnNH_2$ complex and with CuCl. The formation of desired BIQOL **9** was not observed in this case too, scheme 2.14 and table 2.5.

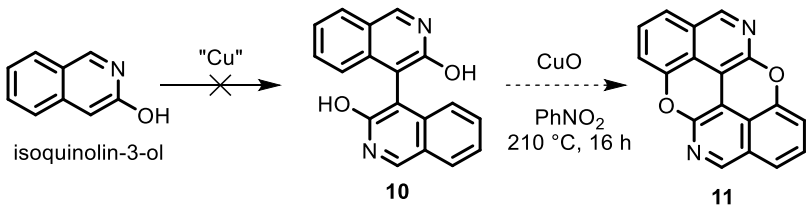

Scheme 2.14. Synthetic protocol for the preparation of BIQOL **10** with Cu-$BnNH_2$ and CuCl.

Table 2.5. Reaction condition tested for BIQOL **10** synthesis using Cu-$BnNH_2$ and CuCl as oxidant.

Reaction conditions	**10** (%)	Conversion (%)
$CuCl_2 \cdot 2H_2O$, $BnNH_2$, MeOH, r.t. 16 h	0	0
CuCl, DMSO, 120° C, 16 h	0	0

The C_{sp}^2-C_{sp}^2 bond formation promoted by DoM was attempted on isoquinolin-3-ol, scheme 2.15. The isoquinolin was treated with carbamoyl chloride in dry pyridine, yielding product **12** as a yellow oil in 35% yield. The lower reaction yield with respect to the O-acylation quinoline-3-ol could be explained considering that this molecule exists in two forms at equilibrium, the lactam and the lactim, with the latter only giving the desired product. Molecule **12** was than dimerised via DoM promoted oxidative

homo-coupling giving product **13** as a colourless oil in 12% yield. The carbamoyl moieties of molecule **13** were hydrolysed with KOH in MeOH yielding molecule **10** as a yellow solid in 92% yield. However, the C_{sp}^2-O annulation of molecule **10** did not give the formation of product **11** and only the decomposition of the starting material was observed.

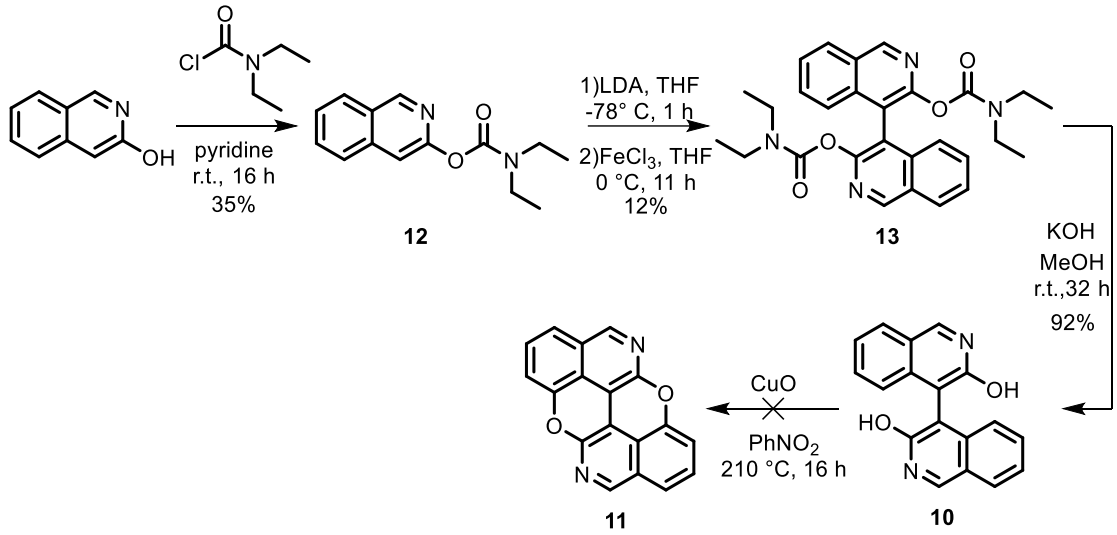

Scheme 2.15. Synthetic protocol for the preparation of 4,10-diN-PXX **11** via oxidative dimerisation through DoM.

2.3.8 2,8-diN-PXX 15 synthesis

Following the oxidative protocols performed for the synthesis of BIQOL **5**, isoquinolin-6-ol was reacted with $CuCl_2$-$BnNH_2$ complex and with CuCl. Again, the formation of desired BIQOL **14** was not observed, scheme 2.16 and table 2.6.

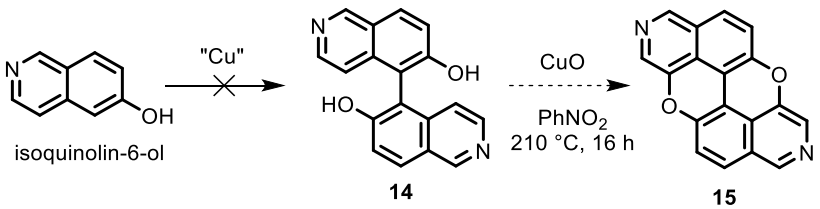

Scheme 2.16. Synthetic protocol for the preparation of BIQOL **14** with Cu-$BnNH_2$ and CuCl.

Table 2.6. Reaction condition tested for BIQOL **14** synthesis using Cu-$BnNH_2$ and CuCl as oxidant.

Reaction conditions	**14** (%)	Conversion (%)
$CuCl_2 \cdot 2H_2O$, $BnNH_2$, MeOH, r.t. 16 h	0	0
CuCl, DMSO, 120° C, 16 h	0	0

Isoquinolin-6-ol dimerisation was attempted following the oxidative homo-dimerisation mediated by DoM, scheme 2.17. The hydroxyisoquinoline was O-acylated with carbamoyl chloride in boiling pyridine for 16 hours giving molecule **16** as a yellowish oil in 95% yield. Molecule **16** was then dissolved in THF and lithiated with LDA at -78 °C. Molecule **16** was treated with $FeCl_3$ to form the C_{sp^2}-C_{sp^2}. Unexpectedly, the formation of the molecule **17** was not observed and **18** was the only product observed**.**

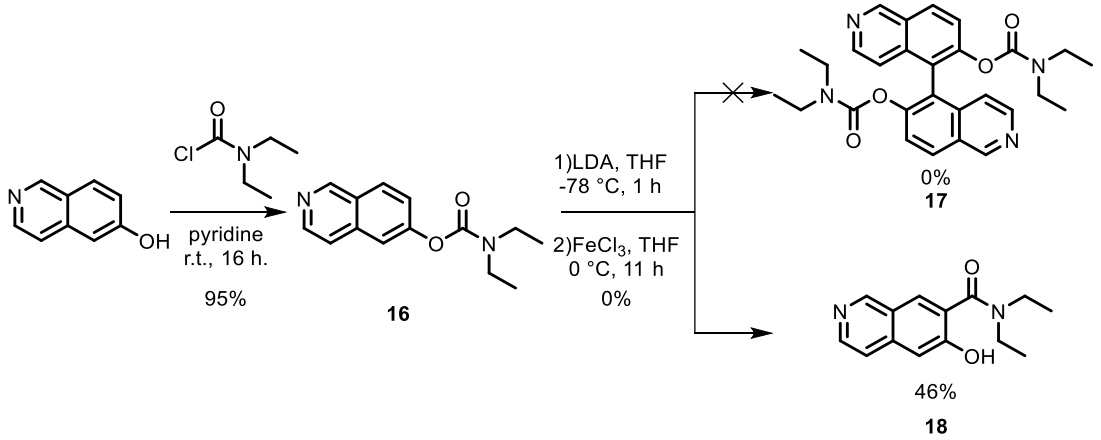

Scheme 2.17. Synthetic protocol for the preparation of 4,10-diN-PXX **11** via oxidative dimerisation through DoM.

Molecule **18** is the product of an anionic ortho-Fries rearrangement.[34] A possible explanation for this intramolecular carbamoyl transfer can be found in the equilibrium between the two possible organolithium products, α-Li quinoline and β-Li quinoline, scheme 2.18. As the temperature raises from -78 °C to 0 °C, the equilibrium favours the more stable β-Li quinoline, which then rearranges giving the transposition product.[28,35] As depicted in the scheme 2.18, the minor stability of α-Li quinoline is due to the repulsion between the hydrogen atom and the lithium in peri positions.[36]

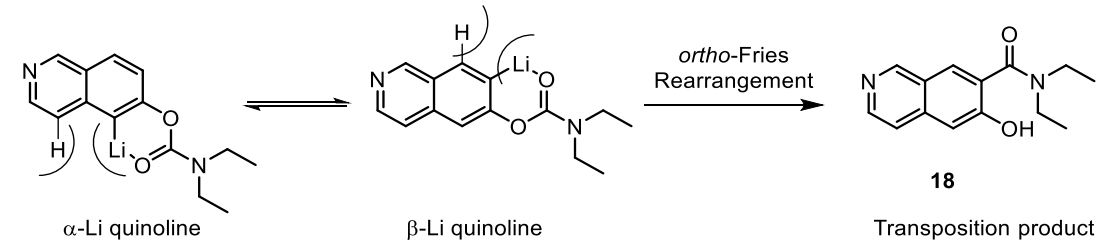

Scheme 2.18. Possible *ortho*-Fries rearrangement explanation

2.3.9 Conclusion about the synthesis

Summarising, three of the desired N-doped PXX, 3,9-diN-PXX **2**, 1,7-diN-PXX **4** and 4,10-diN-PXX **6**, were synthesised, figure 2.14. The first two have been obtained by using the typical PXX synthetic approach. This consists in the Cu-mediated oxidative dimerization of the respective hydroxyquinoline with $CuCl_2$-$BnNH_2$ complex followed by Cu-promoted pyranyl cyclisation with CuO. On the other hand, the same synthetic pathway did not allow the homo-dimerization of the remaining quinolin-3-ol, isoquinolin-3-ol and isoquinolin-6-ol, most probably because of their higher oxidation potential, and therefore 4,10-diN-PXX **6**, 5,11-diN-PXX **11** and 2,8-diN-PXX **15** synthesis could not be achieved following that synthetic pathway. Biquinolines **5** and **10** corresponding to the 4,10-NPXX **6** and 5,11-NPXX **11** were obtained via C_{sp}^2-C_{sp}^2 bond formation promoted by DoM. The C_{sp}^2-O oxidative annulation with CuO only worked for BIQOL **5** yielding molecule **6**. BIQOL **10** cyclisation did not yield the formation of desired NPXX **11,** owing to the low reactivity of the α-carbon in ortho position to the hydroxyl group. BIQOL **14** synthesis was not achieved with Cu-mediated oxidative dimerization neither with DoM pathway.

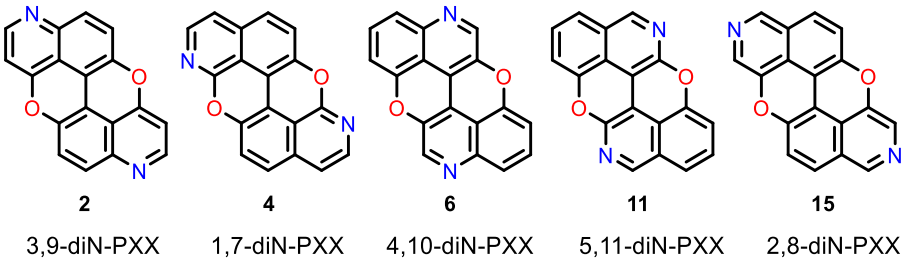

Figure 2.14. Symmetrical diN-doped PXXs.

2.4 Photophysical characterization.

2.4.1 Photophysical characterization general remarks.

This section presents a short overview of the fundamental principles involved in photophyshysical processes, with special emphasis on the photophysical features that are relevant for PAH chromophores.

The interaction of the light with molecules is generally an interaction between one molecule and one photon.[37] The absorbed energy can be released through three different pathways: luminescence (k_l), photoreaction (k_r) and thermal deactivation (k_t), figure 2.15. In this discussion, we are focusing more on the luminescence pathway in order to introduce the photophysical characterisation

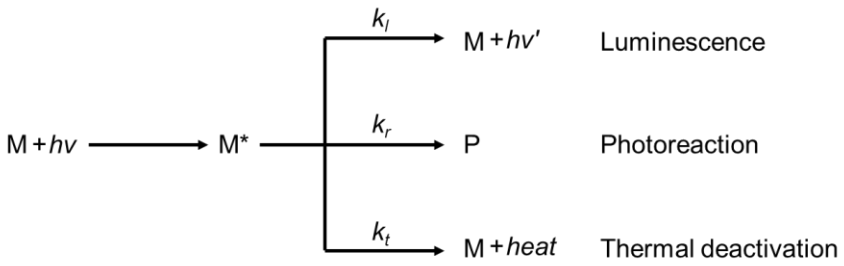

Figure 2.15. Light-matter interactions.

The luminescent pathway can be easily visualised using the Jablonski diagram, figure 2.16a. It represents three different electronic state, S_0, S_1 and T_1, with their relative vibrational states and spin multiplicity, figure 2.16b. The first transition in most Jablonski diagrams is the absorbance of a photon by the molecule, figure 2.16a, black arrows. Thanks to the photon absorption, an electron is excited from a lower energy level S_0 to a higher energy level, so called excite-state S_1. The absorbance of a photon is a very fast transition, on the order of 10^{-15} seconds. This transition will occur from the lowest vibrational state of S_0, which is the most populated at r.t., to a distribution of vibrational state of S_1. One pathway for molecules to release the absorbed energy is to emit a photon, figure 2.16b, red arrows. This phenomenon is called fluorescence. It is indicated on a Jablonski diagram as a straight line going down on the energy axis between electronic states. Fluorescence is a slower process than absorbance, on the order of 10^{-9} to 10^{-7} seconds. It is a permitted transition because S_1 has the same spin multiplicity as S_0. The photon energy emitted in fluorescence has the same energy as the difference between S_0 and S_1, however, the energy of fluorescent photons is always less than that of the exciting photons. This difference is due to the energy lost in vibrational relaxation. Due to the large number of vibrational levels of S_0 that can be coupled into the transition between electronic states, the measured emission is usually distributed over a range of wavelengths.

A third energy dissipation path is called intersystem crossing, *ISC*, figure 2.16a, waved arrow. In this process, the electrons change spin multiplicity from an excited singlet S_1 state to an excited triplet state (T_1). This is the slowest process in the Jablonski diagram, showing a lifetime in the order of 10^{-6} to 10^{-3} seconds. This slow transition is a forbidden transition. However, by coupling vibrational factors into the selection rules, the transition becomes weakly allowed and able to compete with the time scale of fluorescence. ISC leads to several interesting routes back to the ground electronic state. One direct transition is phosphorescence, where a radiative transition from an excited triplet state to a singlet ground state occurs, figure 2.16a, blue arrows.

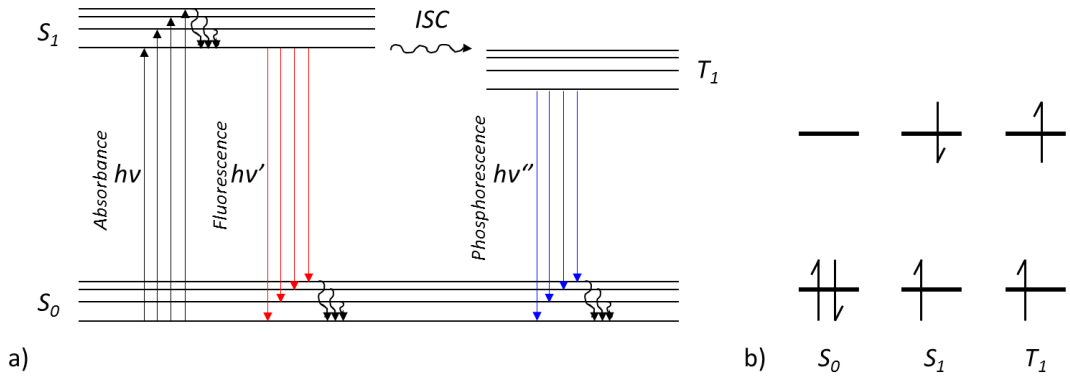

Figure 2.16. a) Jablonski Diagram; b) simplified representation of spin multiplicity for S_0, S_1 and T_1.

The quantitative aspects of the consequences of the deactivation of S_1 can be discussed considering the following equation 2.1. It is possible to define the *quantum yield,* Φ_i, for each i-th process starting with the absorption of a photon.

$$\Phi_i = \frac{number\ of\ molecules\ ungergoing\ the\ i\text{-}th\ process}{number\ of\ photons\ absorbed}$$

Equation 2.1. Quantum yield formula for i-th process.

Therefore, It is possible to define the quantum yield of fluorescence Φ_f for the radiative deactivation $S_1 \rightarrow S_0$, the quantum yield of ISC Φ_{ISC} for the non-radiative deactivation $S_1 \rightarrow T_1$ and the quantum yield of phosphorescence Φ_f for the radiative deactivation $T_1 \rightarrow S_0$. The energy difference between S_0 and S_1 is also called *energy gap* (E_g) and it is also the energy needed to move an electron from the Highest Occupied Molecular Orbital (HOMO) to the Lowest Unoccupied Molecular Orbital (LUMO). For the common chromophores based on a PAH structure, the main deactivation process is represented by the fluorescence phenomenon. Experimentally, it can be calculated following the method describe by Demas and Crosby. It is a relative measurement exploiting the know emission quantum yield ($\Phi_{em,S}$) of a standard, equation 2.2.[38]

$$\Phi_{em,X} = \Phi_{em,S} \times (A_s I_X / A_X I_S) \times (n_X / n_S)^2$$

Equation 2.2. Formula for emission quantum yield Φ_(em,X) determination via relative method..

Where $\Phi_{em,X}$ is the fluorescence quantum yield, *A* is the absorbance at the excitation wavelength, *I* is the integrated area of the fluorescence emission, and n is the refractive index of the solvents used. Subscripts *S* and *X* refer to the standard and to the unknown, respectively. In our case, $\Phi_{em,S}$ values are determined using coumarine-153 as reference, $\Phi_{em,S}$ = 0.53 in ethanol.[39]

For molecules with the same S_0 energy, the difference between the energy gaps is due to the variation of the excited-state S_1. Therefore, the optical band gap tuning can be

achieved by structural modification which can stabilise or destabilise the excited-state S_1. For example, considering a generic molecule M with an E_g in figure 2.17b, if the structural modification stabilises S_1 the resulting E^B is lower than E_g, figure 2.17c. On the contrary, if the structural modification destabilises S_1 the E^A is higher than E_g., figure, 2.17a.

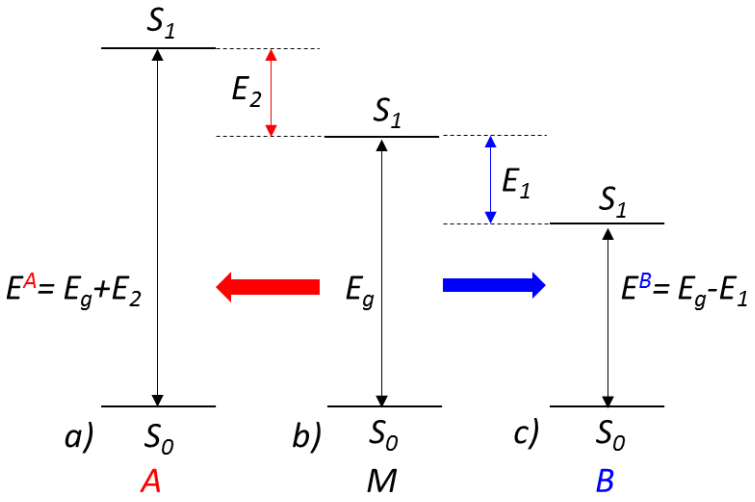

Figure 2.17. S_1 energy variation due to structural modification of a generic molecule M.

2.4.2 Photophysical characterization of N-doped PXX

In this section, the optoelectronic properties of previously synthesised 1,7-diN-PXX **4**, 3,9-diN-PXX **2** and 4,10-diN-PXX **6** are reported and compared with the normal PXX. The purpose of this investigation is to find a correlation between the optoelectronic properties and the position of the nitrogen doping atoms. The UV-Vis and emission measurements were carried out in toluene solution and depicted in figure 2.18. The absorption spectra show the same outline for all the diN-PXX regioisomers and PXX due to $\pi \rightarrow \pi^*$ transitions in the visible range of the spectrum. Looking at the absorption spectra of the synthesised regioisomers, the dependence of the peak positions on the heteroatom-doped position is clear. In comparison to normal PXX, the spectrum of 3,9-diN-PXX **2** spectrum is blue shifted by 30 nm, while that of 4,10-diN-PXX **6** is red shifted by 30 nm. A blue shift of only 6 nm is observed for 1,7-diN-PXX **4**, instead. The emission spectra show a radiative decay of the excited singlet state to the ground state with luminescence lifetimes corresponding with fluorescence phenomena, table 2.7.

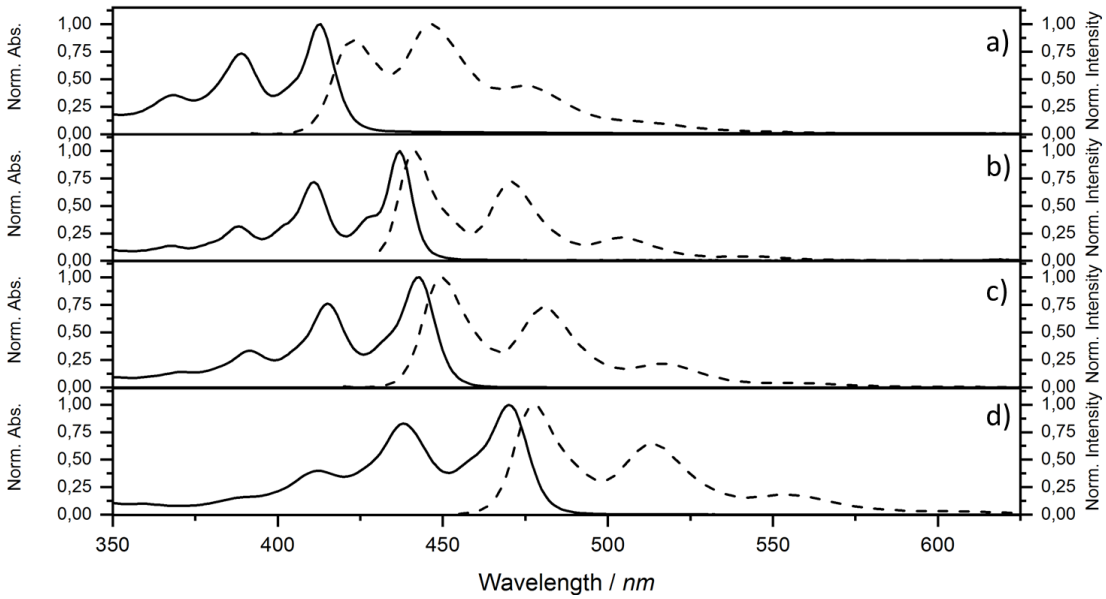

Figure 2.18. Normalised absorbance spectra (solid line) and normalised emission spectra (dashed line) recorded in toluene at r.t.; a) 3,9-diN-PXX **2**; b) 1,7-diN-PXX **4**; c) PXX and d) 4,10-diN-PXX **6**.

Table 2.7. Photophysical data for synthesised NPXXs and PXX in toluene at r.t..

	Absorbance		Emission			
	λ_{max} *(nm) [eV]*	ε *($M^{-1}cm^{-1}$)*	λ_{max} *(nm) [eV]*	τ *(ns)*	Φ_{em}[a] *(%)*	E_g^{opt}[b] *(eV)*
2	413 [3.00]	11838	423 [2.93]	6.6	75	2.93
4	437 [2.84]	26611	442 [2.80]	3.8	61	2.78
PXX	443 [2.80]	17560	450 [2.76]	5	61	2.74
6	470 [2.63]	7448	477 [2.60]	13.5	41	2.57

[a] Standard: Coumarin-153 in EtOH at r.t. (Φ_{em} = 0.53). [c] Energy (eV) calculated from normalized absorption spectrum edge λ_{edge}, exploiting the conversion nm to eV: E_g^{opt} = 1240/ λ_{edge}.[40]

The emission spectra are the mirror image of the absorption spectra discussed before, thus they show a direct dependence of the peak positions on the heteroatom-doped positions similarly to the absorbance spectra. The lowest energy transition into the absorption spectra and the highest energy transition in the emission spectra were converted from *nm* to *eV* in order to visualise their variation as function of the nitrogen-doping positions in the three different regioisomers, figure 2.19.

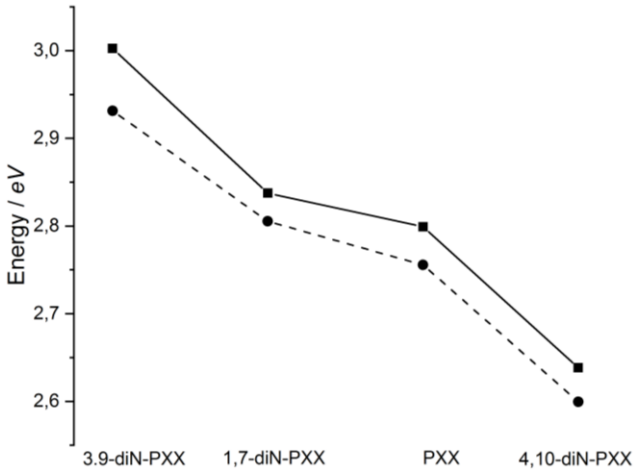

Figure 2.19. Black square absorption maximum energy; black spot emission maximum energy for NPXXs and PXX.

The fluorescence quantum yields, $\Phi_{em,X}$, were calculated using the method of Demas and Crosby from the emission spectra in toluene, table 2.20.[38] Even in this case, the results show the dependence of the fluorescence quantum yield on the position of the nitrogen atoms. 1,7-diN-PXX **4** has a quantum yield of 61% equal to PXX, while the quantum yield of 3,9-diN-PXX **2** (75%) is higher than PXX. Following the observed trend for the absorption and emission maxima, the 4,10-diN-PXX **6** has a fluorescence quantum yield lower than PXX (41%), figure 2.20.

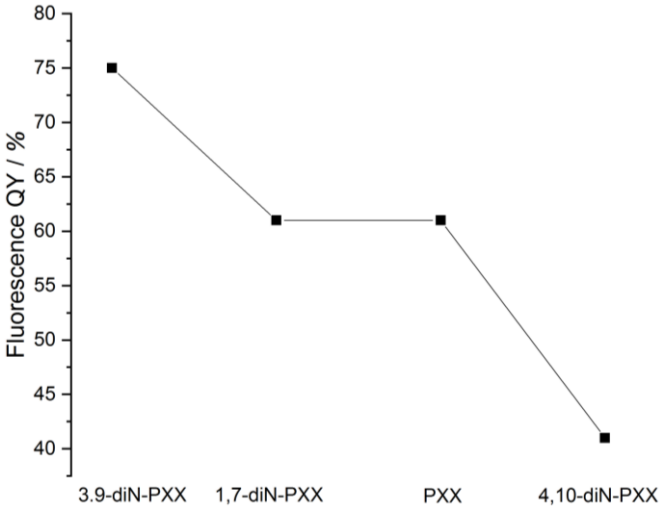

Figure 2.20. Black square fluorescence quantum yield for NPXXs and PXX.

2.4.3 Theoretical Calculation

In order to understand the nitrogen doping effects in the different positions of the PXX scaffold, we decided to investigate energy difference among the excited state and the ground states of the molecule using time-dependent Density Functional Theory (TD-DFT) with B3LYP/6-311+G* level with Gaussian 09E. The absorption transition

energy calculated with TD-DFT for all the 15 N-doped regioisomers *in vacuo* shows a good agreement with the experimentally measured ones, figure 2.21. Moreover, it is dependent from the position of the nitrogen atoms for all the 15 regioisomers is clear.

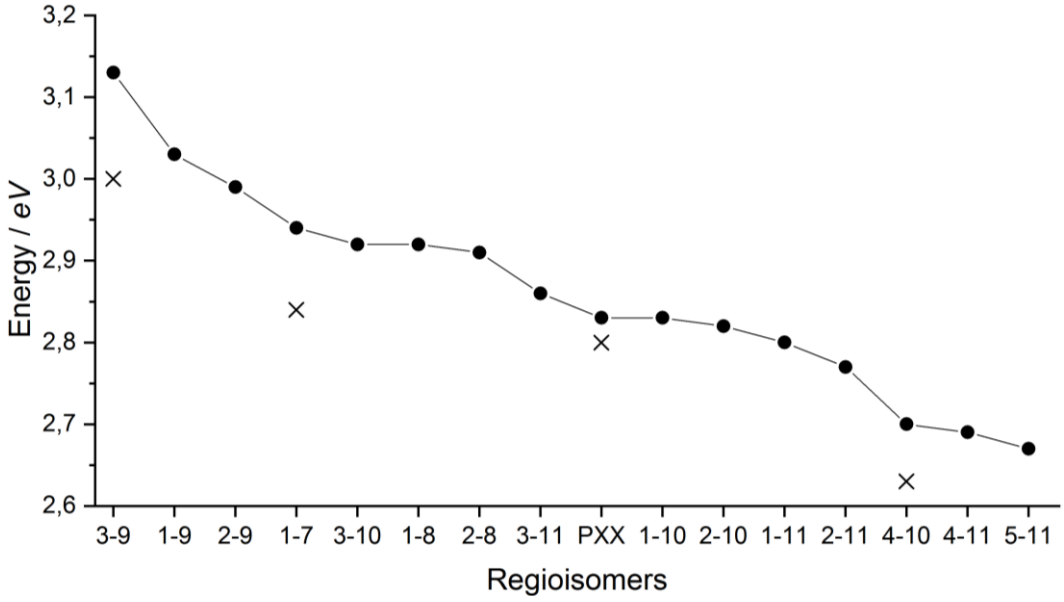

Figure 2.21. Black spots calculated absorption maxima, black cross experimental absorption maxima for NPXXs different regioisomers.

To establish the correlation among absorption transition energy and the position of the nitrogen atoms, it is useful to consider the charge distribution difference between the ground-state and the excited-state of PXX . On the charge distribution map of PXX, it is possible to observe two different regions, figure 2.22a: 1) electron poor in red on the positions 1, 3, 7 and 9; 2) electron rich in blue on the positions 2, 4, 5, 8, 10 and 11. Therefore, placing a more electron negative heteroatom than carbon, such as nitrogen, in the blue-zone stabilises the extra negative charge lowering the absorption transition energy compared to the undoped PXX. Conversely, the nitrogen atom in the red-zone increases the absorption transition energy with respect to undoped PXX.

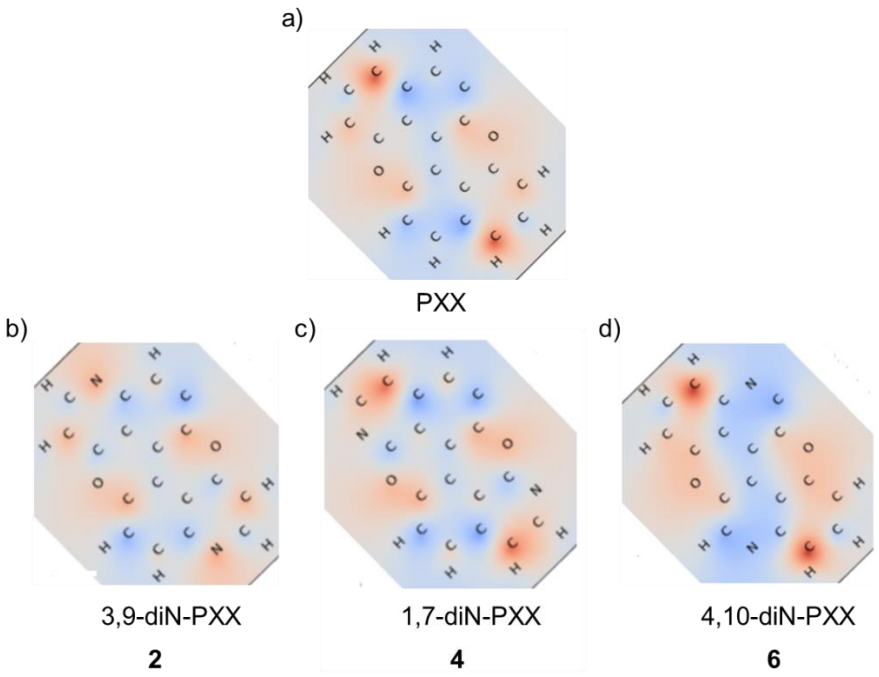

Figure 2.22. Excited-state CHELPG charges – ground-state CHELPG charges (radially interpolated over the atomic positions). The colour map ranges from +0.1 (red, donors) to -0.1 (blue, acceptors)

The three synthesised NPXXs, 3,9-diN-PXX **2**, 1,7-diN-PXX **4** and 4,10-diN-PXX **6**, seem to follow this rule. 3,9-diN-PXX **2** has 2 nitrogen atoms in the red-zone and as a result of that the absorption transition energy is hypsochromically shifted, figure 2.22b. Considering 4,10-diN-PXX **6**, the two nitrogen atoms are located in the blue-zone which leads to an absorption transition energy is bathochromically shifted. Interestingly, the nitrogen atoms in the 1,7-diN-PXX **4** are in the red-zone but the positions 1 and 7 are less electron poor than the positions 3 and 9, thus the absorption transition energy is higher than PXX but lower than 3,9-diN-PXX **2**.

2.4.4 Synthesis and characterization of 1,9-diN-PXX as proof of concept

Following our theory, the contribution of the nitrogen atoms in the optoelectronic property variation is strictly related to their positions. By placing the nitrogen atoms in the positions 1 and 9, the absorption transition energy for the 1,9-diN-PXX **20** has to be higher than 1,7-diN-PXX **4** but lower than 3,9-diN-PXX **2**. Therefore, we synthesised 1,9-diN-PXX in order to further prove the theory validity.

Taking into consideraton the chemical reactivity investigated during the synthesis of 1,7-diN-PXX **4** and 3,9-diN-PXX **2**, it was consequential to follow the Cu-mediated oxidative dimerisation pathway for the synthesis of 1,9-diN-PXX **20**. Isoquinolin-7-ol and quinolin-6-ol were dissolved in MeOH with $CuCl_2$ and $BnNH_2$ at r.t. for 16 hours.

The reaction mixture contained the three statistical BIQOL products which were not isolated because of their poor solubility. The BIQOLs mixture was then dissolved in $PhNO_2$ and oxidised with CuO in order to form the C_{sp}^2-O bonds. The reaction crude was purified by column chromatography yielding product **20** as a yellow solid in 3% yield.

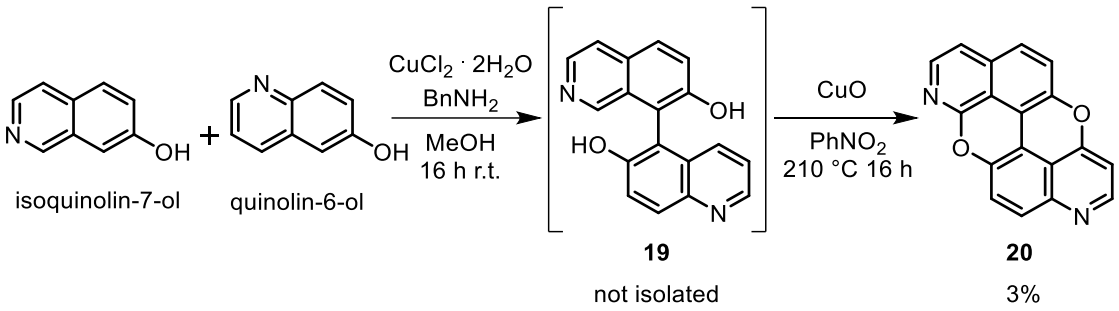

Scheme 2.20. Synthetic protocol for the preparation of 1,9-diN-PXX **20**.

The absorption and emission spectra of 1,9-diN-PXX **20** are in agreement with the theoretical prediction calculated with TD-DFT, figure 2.23, figure 2.24 and table 2.8. The lowest transition energy in the absorption spectrum of 1,9-diN-PXX **20** is at 427 nm which is between the observed values for 1,7-diN-PXX **4** (437 nm) and 3,9-diN-PXX **2** (413 nm). Following the same trend as the absorption spectra, the highest transition energy in the emission spectrum of 1,9-diN-PXX **20** is at 431 nm which is between the observed value for 1,7-diN-PXX **4** (442 nm) and 3,9-diN-PXX **2** (423 nm). The fluorescence quantum yield, 64 %, follows the same trend observed for the previously synthesised NPXXs.

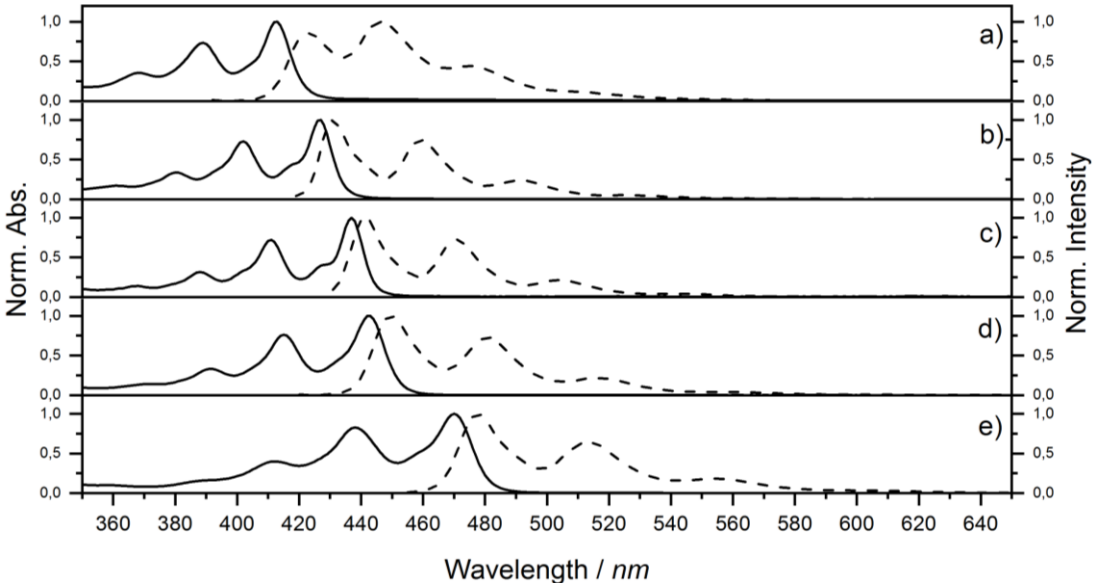

Figure 2.23. Normalised absorbance spectra (solid line) and normalised emission spectra (dashed line) recorded in toluene at r.t.; a) 3,9-diN-PXX **2**; b) 1,9-diN-PXX **20**; c) 1,7-diN-PXX **4**, d) PXX and e) 4,10-diN-PXX **6**.

Table 2.8. Photophysical data for synthesised NPXXs and PXX in toluene at r.t..

	Absorbance		Emission			
	λ_{max} (nm) [eV]	ε ($M^{-1}cm^{-1}$)	λ_{max} (nm) [eV]	τ [a] (ns)	Φ^{b}_{Fluo} (%)	$E_g^{opt\ c}$ (eV)
2	413 [3.00]	11838	423 [2.93]	6.6	75	2.93
20	427 [2.90]	16667	431 [2.88]	4.5	64	2,84
4	437 [2.84]	26611	442 [2.80]	3.8	61	2.78
PXX	443 [2.80]	17560	450 [2.76]	5.0	61	2.74
6	470 [2.63]	7448	477 [2.60]	13.5	41	2.57

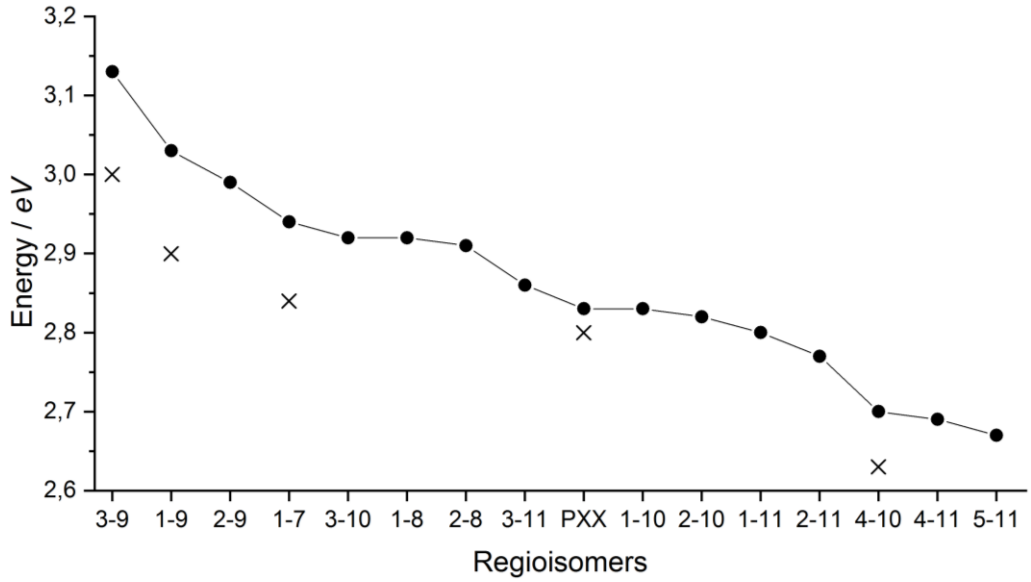

Figure 2.24. Black spots calculated absorption maxima, black cross experimental absorption maxima for NPXXs different regioisomers.

2.4.5 Conclusion

In conclusion, the photophysical properties of 3,9-diN-PXX **2**, 1,7-diN-PXX **4** and 4,10-diN-PXX **6** were characterised with spectroscopic measurements. A correlation between the doping position and the variation of the absorption and emission maxima was found and rationalised by investigation of the charge distribution difference between the S_0 and S_1 states. The theory validity was further demonstrated thanks to the synthesis of 1,9-diN-PXX **20**, that shows absorption and emission maxima between the 3,9-diN-PXX **2** and 1,7-diN-PXX **4**, as predicted by our theoretical calculation.

2.5. Electrochemical Investigations.

2.5.1. Cyclic voltammetry general remarks

Electrochemistry is a methodology broadly used to investigate quantitatively the electronic properties of organic molecules with extended conjugated π-systems. In particular, cyclic voltammetry (CV) is a kind of potentiodynamic measurement, where the working electrode increases the applied potential linearly as a function of time and then decreases the potential linearly in the opposite way, figure 2.24b. Since the electric potential is a relative value, all the electric potential variations are referred to standardised reference electrode such as Saturated Calomel Electrode (SCE), Ag/AgCl and Standard Hydrogen Electrode (SHE) or using an internal standard with a well-known redox potential such as the couple ferrocene /ferrocenium (Fc/Fc^+) . [41] The

oxidation potential ($E_{1/2}^{ox}$), for anodic scan, or the reduction potential ($E_{1/2}^{red}$), for cathodic scan, can be calculated with the following equations 2.3 for reversible processes:

$$E_{1/2}^{ox} = \frac{(E_a^{ox} + E_c^{ox})}{2} \qquad (a)$$

$$E_{1/2}^{red} = \frac{(E_a^{red} + E_c^{red})}{2} \qquad (b)$$

Equations 2.3. a) Equation for $E_{1/2}^{ox}$, b) equation for $E_{1/2}^{red}$.

By calculating the peak-to-peak separation (ΔE_{pp}) between the anodic peak and the cathodic peak, it is possible to discriminate mono-electron processes from multi-electrons processes. The ΔE_{pp} calculated for the molecules must be referred to Fc/Fc^+ ΔE_{pp} which is a mono-electron process. For CV performed in solution, the solvent quiescence is crucial and, in these conditions, the species concentration at the electrode surface is a function of chemical diffusion and electrochemical reaction on electrode surface. Considering the ferrocenium reversible reduction (Fc^+) to ferrocene (Fc), figure 2.25a, $Fc^+ + e^- \rightarrow Fc$, figure 2.25c, the cathodic peak is observed at potential C, and the current increase is due to the electrochemical reaction at the electrode interface. At potential D, figure 2.25a, the Fc^+ concentration at the electrode interface is zero and it is all converted to Fc, figure 2.25e. On the contrary during the anodic scan, the concentration of Fc decreases, and the anodic peak is observed at potential F. At potential G, the Fc species in proximity of the electrode is reconverted to Fc^+.

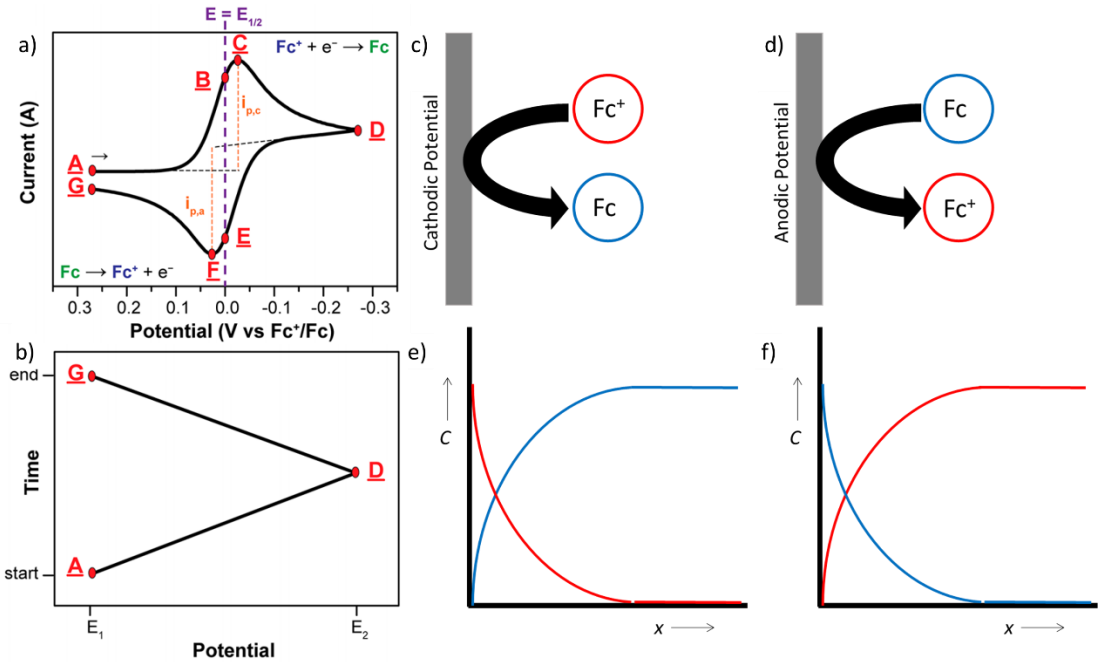

Figure 2.25. a) Voltammogram of the reversible reduction of a 1 mM Fc+ solution to Fc, at a scan rate of 100 mV s^{-1}; b) applied potential as a function of time for a generic cyclic voltammetry experiment, with the initial, switching, and end potentials represented, A, D, and G, respectively; c) reduction process; d)

oxidation process; e) Fc concentration during reduction process; f) Fc^+ concentration during oxidation. process

Generally, a cyclic voltammetry process is reversible if all the generated species at the interface of the working electrode are reconverted to the original species. It occurs if the generated species are not involved into side reactions. Conversely, if side reactions occur, the concentration of the generated species varies and the process is *quasi*-reversible or not reversible. The physical phenomenon could be rationalised by the Randles-Sevcik law, equation 2.4. It shows the dependence of the current peak, i_p, on the concentration of the chemical species involved in the electrochemical reaction, *C*, and potential scan rate, $v^{1/2}$. Moreover, it depends on different parameters considered constant such as the Faraday constant F, electrode area A, number of electrons involved in the electrochemical process n, gas constant R, temperature T and diffusion coefficient D, which depends on the solvent used.

$$i_p = 0.4463nFAC\left(\frac{nFvD}{RT}\right)^{1/2}$$

Equation 2.4. Randles-Sevcik equation.

The Randles-Sevcik equation is useful also to distinguish if an electrochemical process is reversible or irreversible. According to the equation 2.4, i_p is linearly dependent on $v^{1/2}$ when the concentration of the reacting species is constant. If the electrochemical process is not reversible the concentration of the species is modified by side reactions and the correlation between i_p and $v^{1/2}$ is not linear.

Cyclic voltammetry studies are used also to experimentally estimate the energy of the Highest Occupied Molecular Orbital (HOMO) and Lowest Unoccupied Molecular Orbital (LUMO). It is known that organic compounds shows a correlation between the energy required to add one electron to a molecule, Electron Affinity (EA), and the energy of the LUMO. Likewise, the energy required to remove an electron from a molecule, Ionisation Potential (IP), is correlated to the HOMO energy. Even though the EA and IP are energy values referred to processes in gas phase, the reduction potential and the oxidation potential can well approximate them for solution processes. Thus, the equation for the HOMO and LUMO energies calculation are represented in the equations 2.5a and 2.5b. $E_{1/2}^{ox}$ is the half-wave oxidation potential, $E_{1/2}^{red}$ is the half-wave reduction potential and 5.1 is the oxidation potential of Fc/Fc^+ against the vacuum.

$$E_{HOMO} = -\left(E_{1/2}^{ox} + 5.1\right)eV \quad (a)$$

$$E_{LUMO} = -\left(E_{1/2}^{red} + 5.1\right)eV \quad (b)$$

Equations 2.5. a) Equation for HOMO energy calculation from oxidation potential vs Fc/Fc^+, b) equation for LUMO energy calculation from oxidation potential vs Fc/Fc^+.

2.5.2 Cyclic voltammetry investigations.

The redox properties of the new molecules synthesised were studied by CV in *ortho*-dichlorobenzene (ODCB) with $TBAPF_6$ as electrolyte. All the measurements were calibrated against Fc/Fc^+, used as internal standard. The nitrogen doped PXX CV analyses are reported in table 2.9 and in figure 2.26.

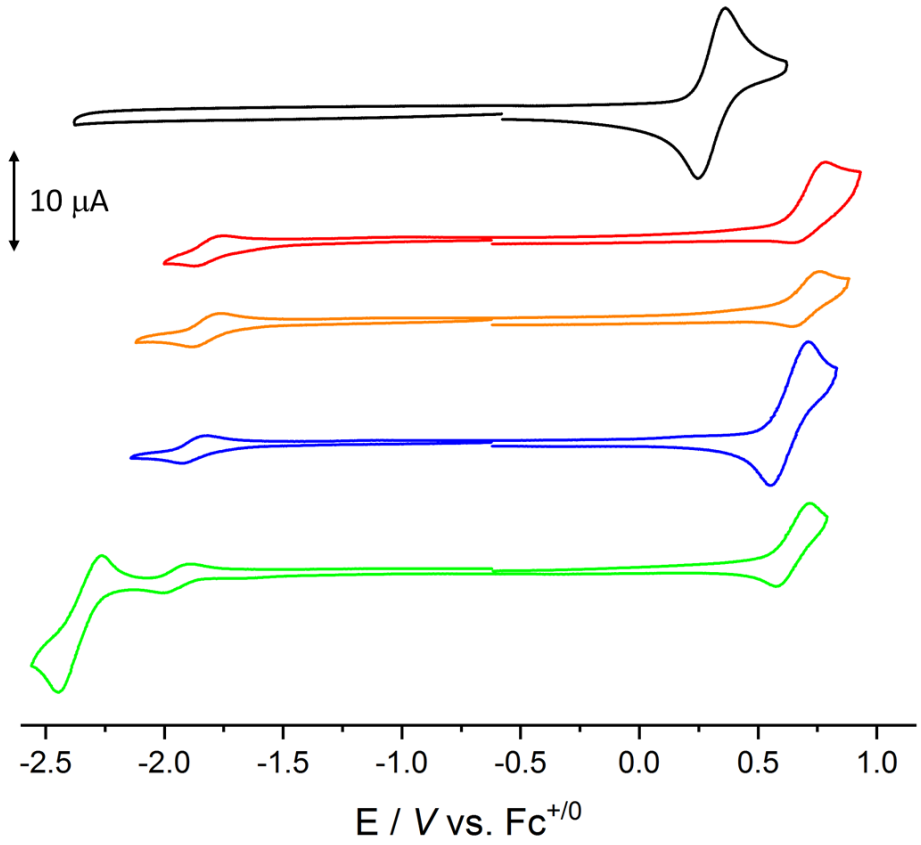

Figure 2.26. Cyclic voltammograms in ODCB at r.t. with electrolyte $TBAPF_6$ 63 mM. Black line PXX 0.75mM; red line 3,9-diN-PXX **2** 0.68 mM; orange line 1,9-diN-PXX **20** 0.65 mM; blue line1,7-diN-PXX **4** 0.67 mM; green line 4,10-diN-PXX**6** 0.63 mM.

The CV of PXX was performed in the same experimental conditions, in order to appreciate the effect of the peripheral nitrogen doping on the redox properties. The cyclic voltammetry trace of PXX in ODCB displays a reversible oxidation wave at $E_{1/2}^{ox}$ = 0.3 V and no reduction wave in the potential window scanned. It is known from the literature that the reduction wave of PXX can be detected in acetonitrile at $E_{1/2}^{red}$ = -2.59 V.[25] The cyclic voltammogram of 1,7-diN-PXX **4** shows a *quasi*-reversible

oxidation wave at approximately $E_{1/2}^{ox}$ = 0.63 V and a reversible reduction peak around $E_{1/2}^{red}$ = -1.87 V. For 3,9-diN-PXX **2**, the voltammetry behaviour retraces the same outline of 1,7-diN-PXX **4** with an irreversible oxidation peak at $E_{1/2}^{ox}$ = 0.71 V and a reversible reduction wave at $E_{1/2}^{red}$ = -1.81 V. Differently from the previously discussed NPXXs, the cyclic voltammetry trace of 4,10-diN-PXX **6** displays two reversible reduction waves at $E_{1/2}^{red}$ = -1.94 V and $E_{1/2}^{red}$ = -2.35 V, and a reversible oxidation at $E_{1/2}^{ox}$ = 0.65 V. The cyclic voltammetry trace of last synthesised 1,9-diN-PXX **20** shows a behaviour similar to 3,9-di-NPXX **2** with a *quasi*-irreversible oxidation peak at $E_{1/2}^{ox}$ = 0.71 V and a reversible reduction peak at $E_{1/2}^{red}$ = -1.83 V.

Table 2.9. Cyclic voltammetry data calculated vs Fc^+/Fc. in ODCB at r.t. with electrolyte $TBAPF_6$ 63 mM.

	$E_{1/2}^{ox}$ (V)	ΔE_{pp}^{ox} (mV)	$E_{1/2}^{red}$ (V)	ΔE_{pp}^{red} (mV)	$E_{1/2}^{red}$ [d] (V)	ΔE_{pp}^{red} (mV)	E_g^{CV} (eV)
PXX	0.30	119	-2.59[a]	-	n.d.	-	-
4	0.63	167	-1.87	97	n.d.	-	2.5
2	0.71	148	-1.81	116	n.d.		2.52
20	0.71	115	-1.83	125	n.d.	-	2.54
6	0.65	229	-1.94	108	-2.35	186	2.59

[a]detected in acetonitrile

Comparing the cyclic voltammogram of PXX with those of the discussed NPXXs, the presence of the reduction waves is due to presence of the two nitrogen atoms along the periphery, as expected from the literature survey.[1,42,43]

2.5.3 Determination frontier orbital energies and redox potential of excited state.

The frontier orbitals energies of NPXXs have been determined using the previously cited equations 2.5 and the values found do not show any significative difference between the four different regioisomers, figure 2.27. The introduction of two nitrogen atoms decreases the HOMO energy levels for the synthesised NPXXs by ca. 0.35 eV with respect to the PXX HOMO energy. The LUMO energy levels for all NPXXs is drastically lowered, by about 0.78 eV, compared to the PXX LUMO energy.

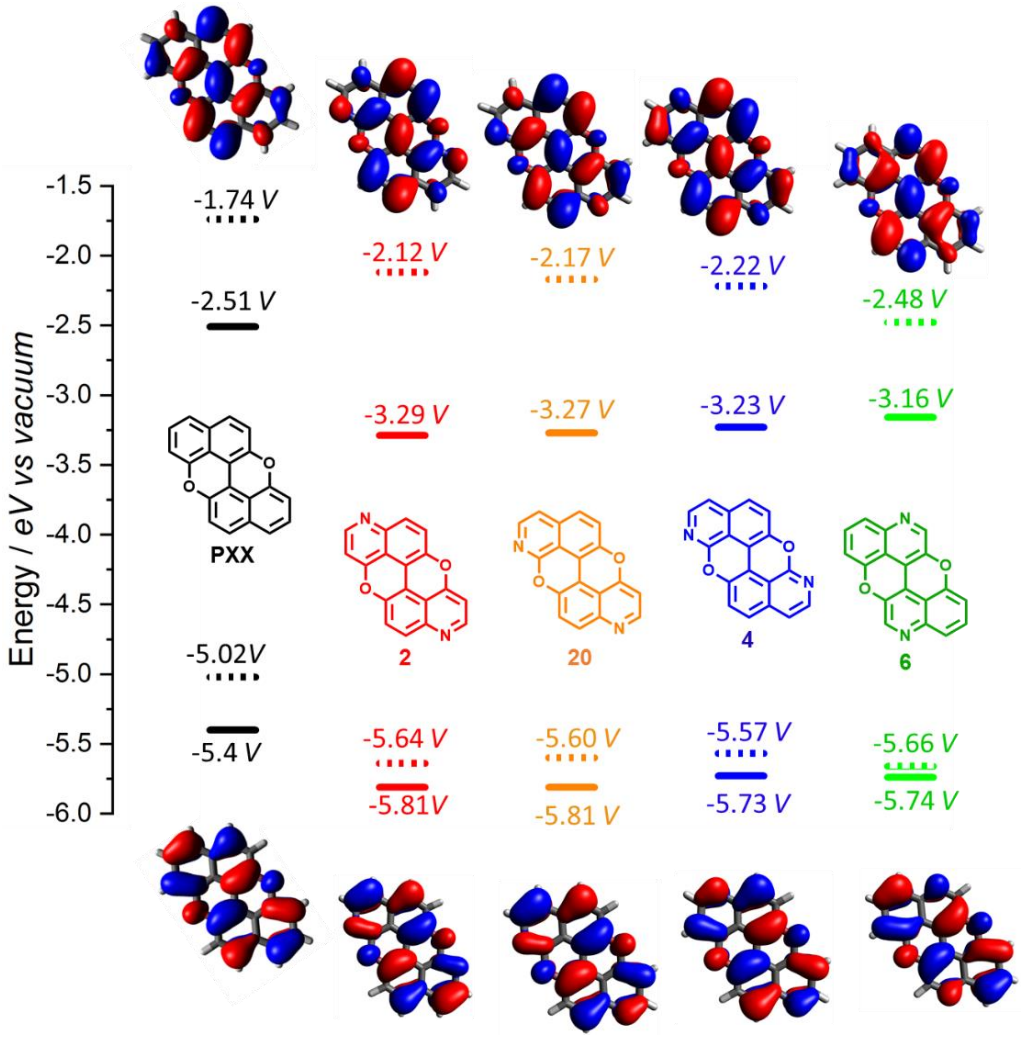

Figure 2.27. Experimental HOMO and LUMO energies (solid lines) and calculated (dashed lines).

By knowing the $E_{1/2}^{ox}$ and $E_{1/2}^{red}$ potentials and E_g^{opt} for the NPXXs and PXX, it is possible to calculate the redox potential of S_1 using the equations 2.6a and 2.6b.[44]

$$E_{ox}^{*} = E_{1/2}^{ox} - E_g^{opt} \quad a)$$

$$E_{red}^{*} = E_{1/2}^{red} + E_g^{opt} \quad b)$$

Equations 2.6. Equations for S_1 redox potential calculation. a) S_1 oxidation potential; b) S_1 reduction potential.

The resulting redox potentials for the NPXXs S_1 states are shifted with respect to the undoped PXX by nitrogen-doping effect, figure 2.28. Particularly, the E_{red}^{*} of the S_1 for NPXXs is higher than E_{red}^{*} for PXX, this mean that NPXXs in the excited state are better oxidants than the excited PXX. Moreover, since the E_g^{opt} is strictly related to the position of the nitrogen atoms in the PXX framework, the oxidative power of S_1 for the NPXXs can be fine-tuned as a function of the nitrogen atom position.

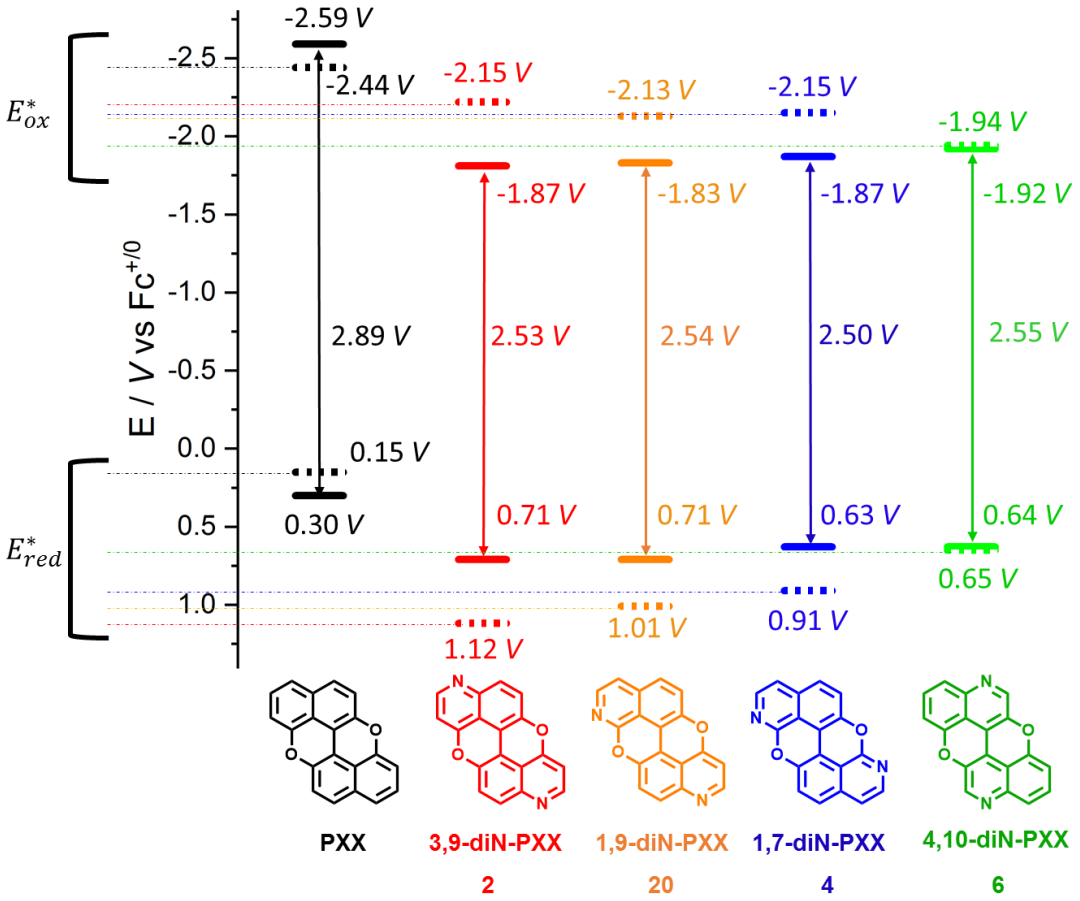

Figure 2.28. Solid line $E^{ox}_{1/2}$ and $E^{red}_{1/2}$ potentials in ODCB. Dashed lines E^*_{ox} and E^*_{red} potentials of the S_1 state.

2.6 Solid-state self-assembly investigation of NPXXs

In this section, the crystallographic analyses of 1,7-diN-PXX **4**, 3,9-diN-PXX **2** and 4,10-diN-PXX **6** are reported. Solid-state self-assemblies of NPXXs were studied via X-ray diffraction (XRD) of single crystals.

2.6.1 PXX Solid-state self-assembly

In order to appreciate the effect of the nitrogen doping on the solid-state self-assembly, it is useful to describe first the one of the undoped PXX. Inabe *et al*. crystallised PXX from vacuum sublimation obtaining yellow crystals.[45] It formed monoclinic crystals belonging to the Cc space group. The solid-state supramolecular packing in the lattice is guided by edge-to-face interactions between the hydrogen atoms in the peri positions of the naphthalene moiety and the electron-rich π-system, 3.64 Å, figure 2.29b. These interactions allow the supramolecular organisation in a herringbone type motif common in PAHs, figure 2.29e and 2.29c.[46] The interplanar distance between two parallel molecules of PXX is 3.39 Å, figure 2.29d.

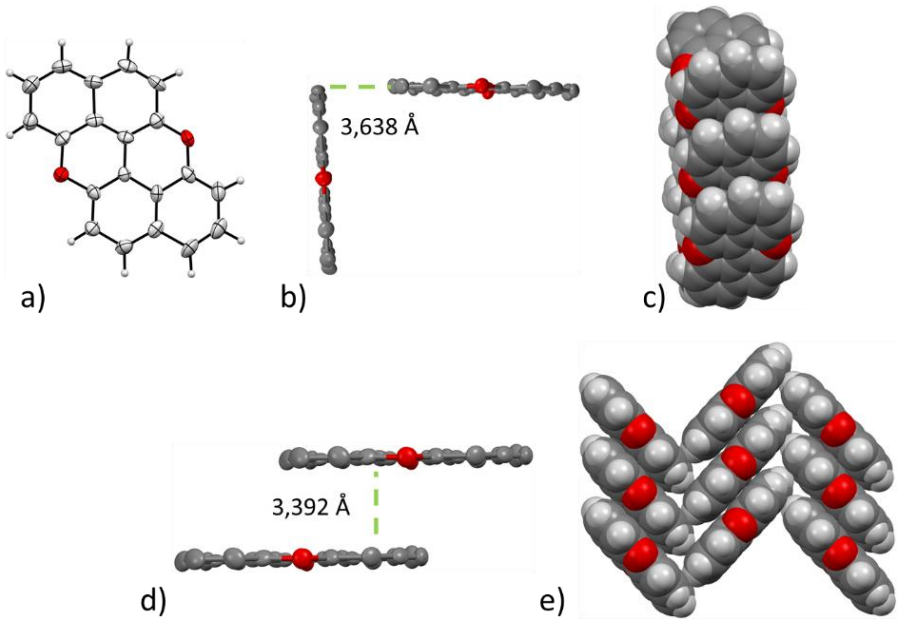

Figure 2.29. PXX crystal structure. A) ORTEP representation (50% probability ellipsoids); b) edge-to-face interaction; d) face-to-face interaction; c) crystal packing side view; e) crystal packing front view.

2.6.2 1,7-diN-PXX 4 Solid-state self-assembly

1,7-diN-PXX **4** was crystallised by slow vapour diffusion of diethyl ether into a toluene solution and from hot/cold toluene giving the same polymorphic form crystals with spatial group $P2_1/c$, R-factor 6.84%. The ORTEP representation of the 1,7-diN-PXX **4** is shown in figure 2.30a. The supramolecular self-assembly leads to the face-to-face interactions of the molecules, as showed in figure 2.30e. This spatial organization is driven by the weak hydrogen bonds between the two hydrogen atoms in the peri positions and the nitrogen-oxygen motif.[12] These hydrogen bond interactions prevent the typical herringbone packing observed for PAHs.[47] The distances between the carbon atoms carrying the protons involved in the hydrogen bonds and the nitrogen and the oxygen are 3.531 Å and 3.527 Å, respectively, figure 2.30b. These distances classify both these interactions as weak hydrogen bonding with a pure electrostatic nature.[48] The interplanar distance between the layered molecules is 3.330 Å, slightly lower than the interplanar distance between two parallel PXX molecules, 3.392 Å, and that of the graphite layers, 3.41 Å, figure 2.30d and figure 2.30d.[49]

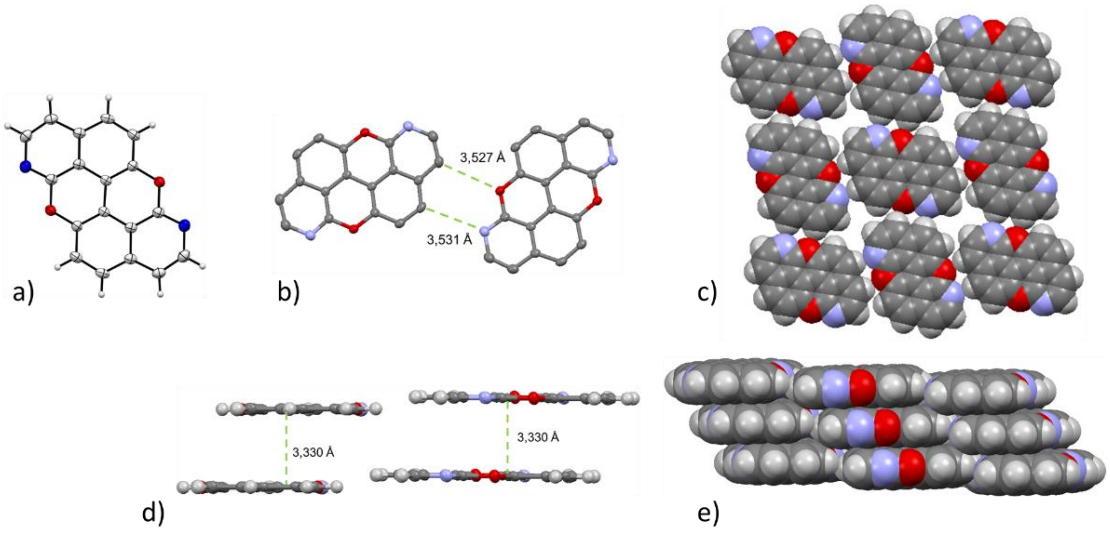

Figure 2.30. 1,7-diN-PXX **4** crystal structure. a) ORTEP representation (50% probability ellipsoids); b) double hydrogen bonding interaction; d) face-to-face interaction; c) crystal packing top view; e) crystal packing side view. Oxygen (red), carbon (grey), nitrogen (blue), hydrogen (white).

The hydrogen bonding interactions can be rationalised by taking into consideration the Electrostatic Surface Potential (ESP). In figure 2.31, the red part clearly highlights the hydrogen bond acceptor moieties corresponding to the nitrogen and the oxygen atoms, figure 2.31c. On the other hand, the *peri* positions show a partially positive polarisation of the hydrogen atoms which makes them weak hydrogen bond donors, figure 2.31b.

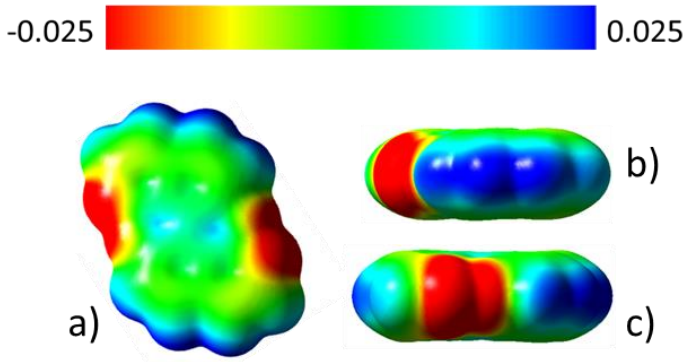

Figure 2.31. ESP for 1,7-diN-PXX **4** mapped on the vdW surface up to an electron density of 0.001 electron bohr^{-3}. a) Top view, b) side view1, c) side view2

2.6.3 3,9-diN-PXX 2 Solid-state self-assembly

Crystallisation of 3,9-diN-PXX **2** from slow evaporation of chloroform afforded monoclinic crystals belonging to the $P2_1/c$ space group (R-factor 7.06%). The molecule, which lacks the donor-acceptor hydrogen bonding motif present in the 1,7-diN-PXX **4**, crystallised hosting one molecule of water per molecule of N-doped PXX in the crystal packing, figure 2.32c and 2.32e. The hydrogen bonding between the

water molecules and the nitrogen atoms in the peri positions appear as the principal driving force directing the self-assembly. The molecules are spatially organised in columnar stackings and every NPXX molecule is bridged with two others, one per side, in the neighbouring columns by two molecules of water. The distance between the nitrogen of molecule **2** and the water is 2.858 Å, figure 2.32b. This suggests that this interaction is stronger than the hydrogen bonding showed in the 1,7-NPXX crystal.

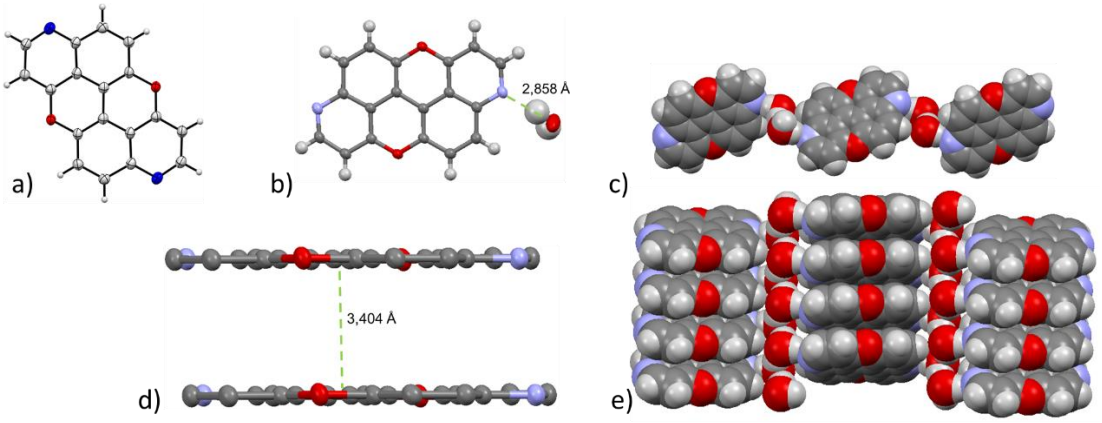

Figure 2.32. 3,9-diN-PXX **2** crystal structure. a) ORTEP view, b) hydrogen bonding interaction, d) π-π interaction, c) crystal packing top view and e) crystal packing side view. Oxygen (red), carbon (grey), nitrogen (blue), hydrogen (white).

From the ESP map, it is possible to observe the absence of a possible complementary homo-recognition motif guided by hydrogen bonding such as that observed for 1,7-diN-PXX **4**, figure 2.33. Instead, the nitrogen doped position shows a highly negative polarisation of the heteroatom which allow the hetero-recognition through hydrogen bonding between 3,9-diN-PXX **2** and a water molecule.

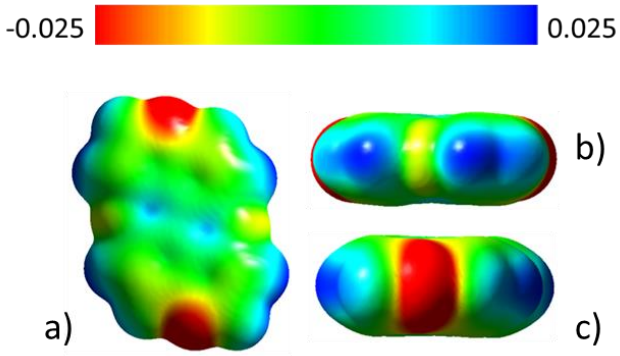

Figure 2.33. ESP for 3,9-diN-PXX **2** mapped on the vdW surface up to an electron density of 0.001 electron bohr^{-3}. a) Top view, b) side view1, c) side view2.

2.6.4 4,10-diN-PXX 6 Solid-state self-assembly

Crystals belonging to the space group P $2_1/c$, R-factor 6.84%, were obtained for 4,10-NPXX **6** by slow vapour diffusion of hexane into its chloroform solution. As depicted in the figure 2.34e and 2.34c, the supramolecular self-assembly leads the molecules to pack in columnar domains. Each NPXX molecule has a face-to-face π-interaction with two molecules in the same column with an interplanar distance of 3.406 Å. Intercolumnar interactions consist of weak hydrogen bonds between the oxygen atoms and a C-H motif.

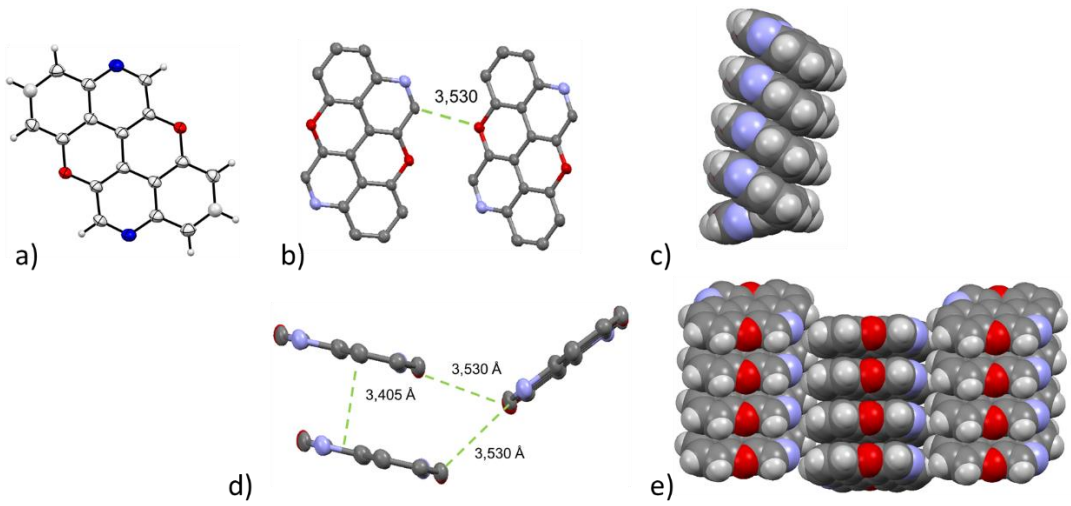

Figure 2.34. 4,10-diN-PXX **6** crystal structure. a) ORTEP view, b) hydrogen bonding interaction, d) π-π interaction, c) crystal packing top view and e) crystal packing side view. Oxygen (red), carbon (grey), nitrogen (blue), hydrogen (white).

As for 3,9-diN-PXX **2**, the ESP map shows the lack of sites that would induce intermolecular homo-recognition guided by hydrogen bonding, figure 2.35. The nitrogen doped positions show a negative polarisation but, in this case, water

molecules deriving from the non-anhydrous solvent of crystallisation were not trapped into the crystals.

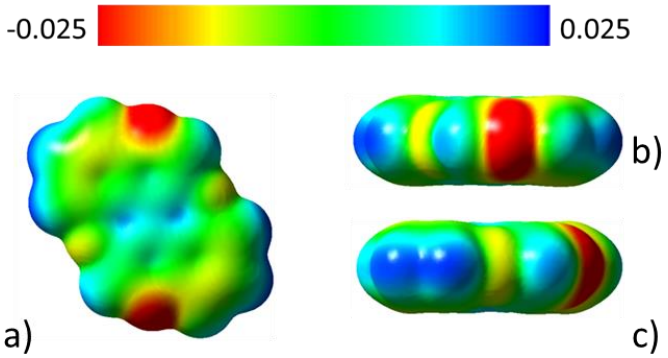

Figure 2.35. ESP for 4,10-diN-PXX **6** mapped on the vdW surface up to an electron density of 0.001 electron bohr^{-3}. a) Top view, b) side view1, c) side view2

2.7. NPXXs crystal engineering through halogen-bonding

In the previous section we have analysed the solid-state organisation of the 3,9-diN-PXX **2**, 1,7-diN-PXX **4** and 4,10-diN-PXX **6** and we rationalised their supramolecular organisation using ESP. Herein, we evaluate the possibility to use molecules **2** and **6** as halogen bonding acceptor for photoactive supramolecular crystal engineering.

2.7.1 General remarks about halogen-bonding

Halogen atoms in halogenated organic molecules are commonly classified as sites with high electron density due to their electronegativity. Nevertheless, the electron density surrounds the halogen anisotropically forming a belt orthogonal to the covalent bond between the halogen and the carbon atom, figure 2.36a. Along the covalent bond axis, it is possible to define a region with a charge depletion, namely a σ-hole, where the electrostatic potential is positive, figure 2.36b. The halogen bond interaction occurs between the positive σ-hole (halogen bond donor) and the electron rich moiety of a nucleophile (halogen bond acceptor), figure 2.36c.[50]

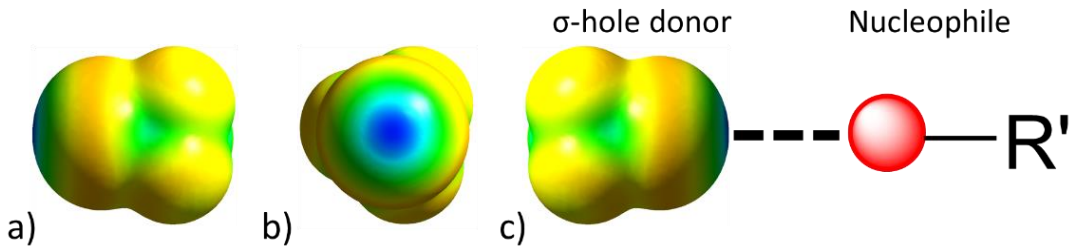

Figure 2.36. ESP of CH_3Br. a) side view; b) C-Br axial view; c) interaction between σ-hole and nucleophile.

The halogen bond is a particularly directional interaction, more than the hydrogen bond.[51] This peculiar character is a consequence, not only of the electrostatic attraction between the halogen σ-hole and the nucleophile, but of an orbital contribution to the interaction. The antibonding orbital of the carbon-halogen bond, σ^*, interacts with the non-bonding orbital of the nucleophile, n, figure 2.37a. This interaction depends on the energy difference and overlap of the orbitals involved. The maximum overlap with the σ* and n orbitals occurs when the nucleophile is oriented along the carbon-halogen bond, figure 2.37b, explaining the high directionality of the halogen bond.[52]

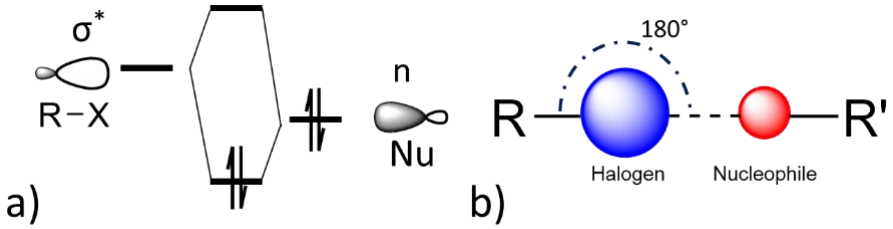

Figure 2.37. a) Constructive interaction between $\sigma^*$and n; b) schematic representation of axial halogen bonding interaction.

The halogen bond strength increases with polarizability of the halogen atom (F < Cl < Br < I). The halogen bond interaction can be tuned by structural modification of the substituent bonded on the halogen. Haloarenes are commonly used as halogen bond donors in crystal engineering and the dependence of the halogen bond strength on the number of fluorine atoms on the aryl ring has been demonstrated by Bruce *et., al.* figure 2.38a.[53] They studied the effect of the fluorine functionalisation on the iodobenzene. The presence of electron withdrawing group, such as fluorine atoms, increases the size and positive potential of the σ-hole on the halogen atom, figure 2.38b and 2.38c, increasing the strength of the halogen bond.

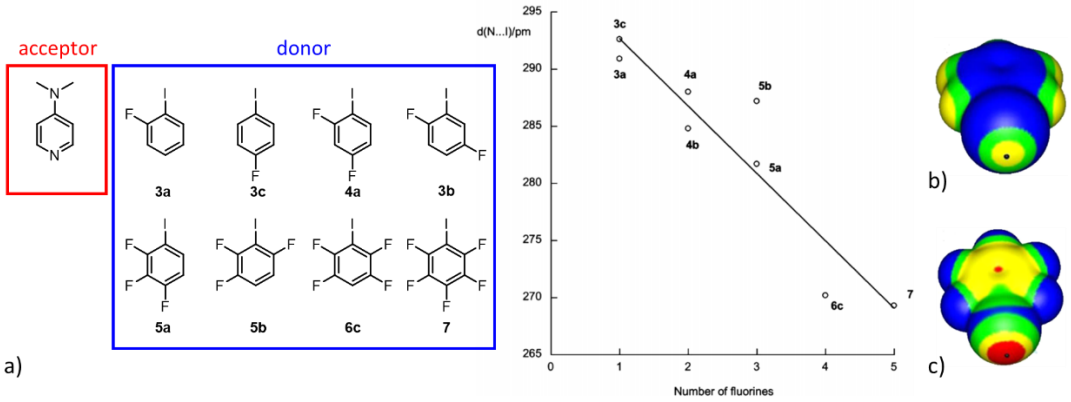

Figure 2.38. a) Halogen bond donors and acceptor; b) iodobenzene ESP and c) iodotetrafluorobenzene ESP. Color range (kcal/mol): red, greater than 20; yellow, between 20 and 10; green, between 10 and 0; blue, negative

In the light of these properties, iodine-based donors and nitrogen-based acceptors have been widely investigated as tools for geometry-based design for solid-state supramolecular organisation. For instance, Pennington *et. al.* investigated the halogen bonding interaction of bipyridine (bipy) with 1,4-diiodobenzene (DIB) and 1,4-diiodotetrafluorobenzene (F_4DIB) by single crystal XRD.[54] In both the cocrystal structure, the donors-acceptors couple form 1:1 linear chains in which both ends of the acceptors interact with both ends of the donors, figure 2.39. These chains loosely stack donor over donor and acceptor over acceptor.[54] The N···I distance of 3.032 Å in the bipy·DIB is considerably higher than the N···I distance in the bipy·F_6DIB, which is 2.871 Å, figure 2.39a and 2.39c. This is due to the stronger halogen bond donor character of F_6DIB with respect to DIB.

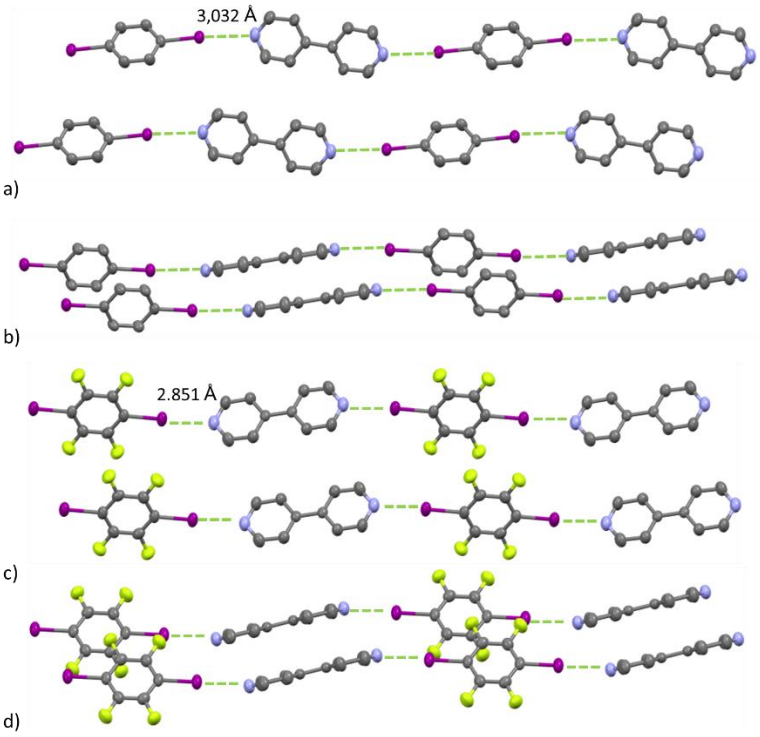

Figure 2.39. a) bipy·DIB crystal packing top view, b) bipy·DIB crystal packing side view, c) bipy·F_6DIB crystal packing top view, d) bipy·F_6DIB crystal packing top side. Fluorine (yellow), carbon (grey), nitrogen (blue), hydrogen (white), iodine (purple).

2.7.2 Solid-state self-assembly of 3,9-diN-PXX 2 and 1,4-diiodotetrafluorobenzene

3,9-diN-PXX **2** was co-crystallised with 1,4-diiodotetrafluorobenzene in a 1:1 stoichiometric ratio from slow evaporation of chloroform. The obtained cocrystals belong to the P-1 spatial group (R-factor 3.98%) and show a coplanar arrangement of the N-doped PXX and the diiodobenzene derivatives, which produces a graphite-like multilayer packing, figure 2.40e. The in-plane self-assembly is driven by halogen bonding between the nitrogen and the iodine atoms with a distance N···I of 2.871 Å. The binding angle of the halogen bonding interaction is 176° which is very close to the ideal binding angle of 180°, figure 2.40b. Moreover, two anti-parallel hydrogen bonding between two molecules of 3,9-diN-PXX **2** play an important role in assisting the formation of the coplanar system, C_{sp^2}-H···O of 3.467 Å, figure 2.40b. As expected, the nitrogen lone pair works as halogen bond acceptor interacting with the positive polarised σ-hole of the 1,4-diiodotetrafluorebenzene. The 1,4-diiodotetrafluorobenzene coplanarity is furtherly enforced by another intermolecular hydrogen bond among one negative fluorine and another positive polarised C_{sp^2}-H moiety, 3.206 Å, figure 2.40b.

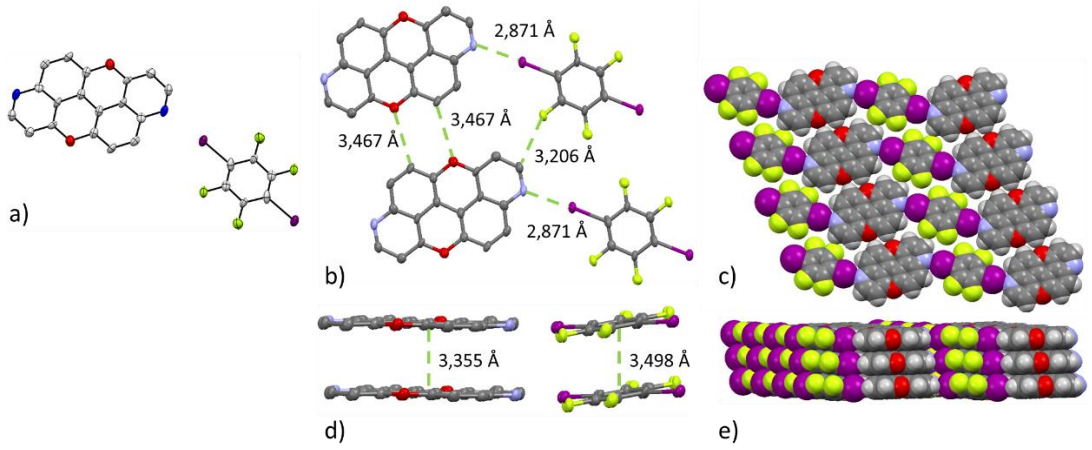

Figure 2.40. X-ray crystal structure of 3,9-diN-PXX **2** cocrystal. a) ORTEP view, b) halogen and hydrogen bonding interactions, d) π-π interactions, c) crystal packing top view and e) crystal packing side view. Oxygen (red), fluorine (yellow), carbon (grey), nitrogen (blue), hydrogen (white), iodine (purple).

2.7.3 Solid-state self-assembly of 4,10-diN-PXX 6 and 1,4-diiodotetrafluorobenzene

4,10-diN-PXX **6** was co-crystallised with 1,4-diiodotetrafluorobenzene in a 1:1 stoichiometric ratio from slow evaporation of chloroform. The cocrystals belong to the P-1 spatial group (R-factor 4.07%). The N-doped PXX and the diiodobenzene derivative are arranged in a non-coplanar organization, figure 2.41e, conversely to what was found for 3,9-diN-PXX **2** cocrystals. F_4DIB bridges two different NPXX molecules with two different interactions. The first is the halogen bond between the iodine atom and the peripheral nitrogen atom, which are 2.959 Å apart, figure 2.41b. This distance is higher than that found in the 3,9-diN-PXX **2** cocrystal, which was 2.871 Å. The second is the C_{sp^2}-H···F hydrogen bond between the fluorine atom of 1,4-diiodotetrafluorobenzene and a C_{sp^2}-H moiety of NPXX molecule, which are 3.333 Å distant, figure 2.41b. The angle between the 3,9-diN-PXX **2** plane and the F_4DIB plane is 45.87°. 4,10-diN-PXX **6** molecules have a coplanar arrangement is due to two C_{sp^2}-H···O anti-parallel hydrogen bonds, with a distance of 3.467 Å between the C_{sp^2} and the O atoms, figure 2.41b.

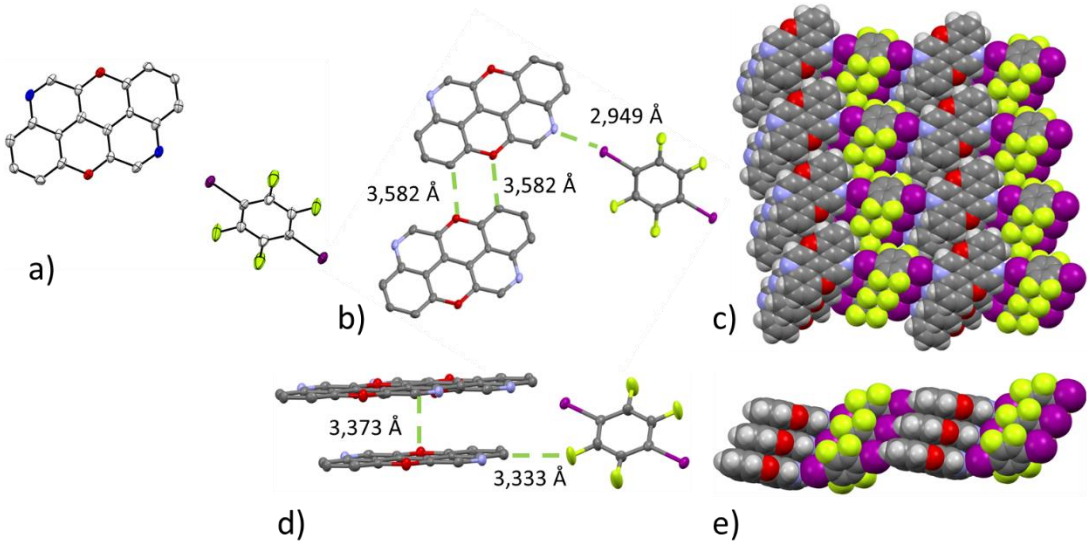

Figure 2.41. X-ray crystal structure of 4,10-diN-PXX **6** cocrystal. a) ORTEP view, b) halogen and hydrogen bonding interactions, d) π-π interactions, c) crystal packing top view and e) crystal packing side view. Oxygen (red), fluorine (yellow), carbon (grey), nitrogen (blue), hydrogen (white), iodine (purple).

2.8 Conclusion and future work

The work reported in this chapter concerned the synthesis of novel diN-doped *peri*-xanthenoxanthene (NPXXs). The chosen strategy involved the intermolecular $C_{sp}{}^2$-$C_{sp}{}^2$ bond formation through oxidative homo-dimerisation of the corresponding hydroxyl(iso)quinoline followed by the formation of two $C_{sp}{}^2$-O bonds yielding the desired NPXX. The synthesis of molecules **2**, **20**, **4** and **6**, was achieved by investigating two synthetic routes in order to address the different reactivity of the corresponding (iso)quinolines. Molecules **11** and **15** could not be obtained through the tested synthetic routes, figure 2.42.

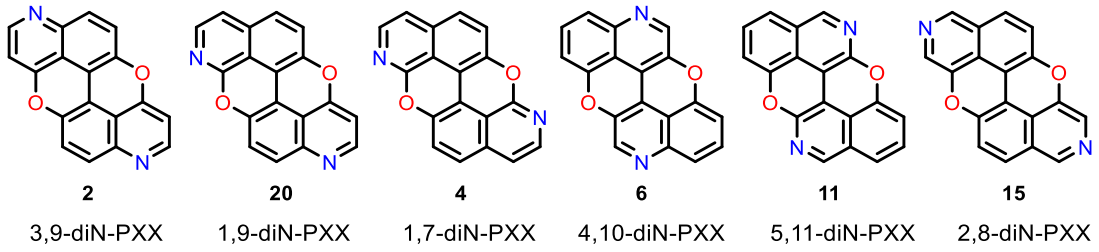

Figure 2.42. NPXXs target molecules

The molecules **2**, **20**, **4** and **6** were photophysically characterised and the correlation between the nitrogen atoms position in their scaffold and their absorption transition energy along with the difference between S_0 and S_1 rationalised via TD-DFT calculations. This study gives an interesting contribution to the fine tuning of the optoelectronic properties in electronically heteroatom-doped PAHs. X-ray diffraction of

molecules **2**, **4** and **6** showed how the presence of the nitrogen atom in the PXX scaffold changed completely the solid-state aggregation. Particularly, 1,7-diN-PXX **4** molecules interact at the solid-solid state via weak hydrogen bonding between the polarised hydrogen atoms in peri position and the nitrogen-oxygen motif, allowing a graphite-like coplanar self-assembly. Furthermore, molecules **2** and **6** were cocrystallised with a common halogen bonding donor, F_4DIB, in order to prove the suitability of this molecules as photoactive building block for crystal engineering.

In the near future, we have planned to investigate the synthesised molecules as charge transporting materials due to their supramolecular organisation in the solid state. Moreover, the materials should have ambipolar behaviour, p-type and n-type, due to the HOMO and LUMO energy levels position. For the redox properties in the excited state, NPXXs seem to be high promising molecules as organic photocatalyst in photooxidative processes.

2.9 References

[1] U. H. F. Bunz, J. U. Engelhart, B. D. Lindner, M. Schaffroth, *Angew. Chem. Int. Ed.* **2013**, *52*, 3810–3821.

[2] T. C. Werner, J. Chang, D. M. Hercules, *J. Am. Chem. Soc.* **1970**, *92*, 5560–5565.

[3] D. T. Gryko, J. Piechowska, M. Gałezezowski, *J. Org. Chem.* **2010**, *75*, 1297–1300.

[4] L.S.B., *Handbook of Fluorescence Spectra of Aromatic Molecules*, **1972**.

[5] D. H. Kim, D. Y. Lee, H. S. Lee, W. H. Lee, Y. H. Kim, J. I. Han, K. Cho, *Adv. Mater.* **2007**, *19*, 678–682.

[6] M. M. Payne, S. R. Parkin, J. E. Anthony, C. C. Kuo, T. N. Jackson, *J. Am. Chem. Soc.* **2005**, *127*, 4986–4987.

[7] T. Sakanoue, H. Sirringhaus, *Nat. Mater.* **2010**, *9*, 736–740.

[8] Z. Liang, Q. Tang, J. Xu, Q. Miao, *Adv. Mater.* **2011**, *23*, 1535–1539.

[9] X. Xu, Y. Yao, B. Shan, X. Gu, D. Liu, J. Liu, J. Xu, N. Zhao, W. Hu, Q. Miao, *Adv. Mater.* **2016**, *28*, 5276–5283.

[10] Y. Y. Liu, C. L. Song, W. J. Zeng, K. G. Zhou, Z. F. Shi, C. B. Ma, F. Yang, H. L. Zhang, X. Gong, *J. Am. Chem. Soc.* **2010**, *132*, 16349–16351.

[11] C. D. Sheraw, T. N. Jackson, D. L. Eaton, J. E. Anthony, *Adv. Mater.* **2003**, *15*, 2009–2011.

[12] G. R. Desiraju, T. Steiner, *The Weak Hydrogen Bond In Structural Chemistry and Biology (International Union of Crystallography, Monographs on Crystallography, 9)*, **1999**.

[13] T. H. Vo, U. G. E. Perera, M. Shekhirev, M. Mehdi Pour, D. A. Kunkel, H. Lu, A. Gruverman, E. Sutter, M. Cotlet, D. Nykypanchuk, P. Zahl, A. Enders, P. Sutter, *Nano Lett.* **2015**, *15*, 5770–5777.

[14] O. V. Yazyev, *Acc. Chem. Res.* **2013**, *46*, 2319–2328.

[15] V. Barone, O. Hod, G. E. Scuseria, *Nano Lett.* **2006**, *6*, 2748–2754.

[16] Y.-W. Son, M. L. Cohen, S. G. Louie, *Phys. Rev. Lett.* **2006**, *97*, 1–4.

[17] M. Noda, N. Kobayashi, M. Katsuhara, A. Yumoto, S. Ushikura, R. Yasuda, N. Hirai, G. Yukawa, I. Yagi, K. Nomoto, T. Urabe, *Dig. Tech. Pap. - Soc. Inf. Disp. Int. Symp.* **2010**, *41*, 710–713.

[18] N. Kobayashi, M. Sasaki, K. Nomoto, *Chem. Mater.* **2009**, *21*, 552–556.

[19] A. Berezin, N. Biot, T. Battisti, D. Bonifazi, *Angew. Chem. Int. Ed.* **2018**, *57*, 8942–8946.

[20] D. Stassen, N. Demitri, D. Bonifazi, *Angew. Chem. Int. Ed.* **2016**, *55*, 5947–5951.

[21] T. Miletić, A. Fermi, I. Orfanos, A. Avramopoulos, F. De Leo, N. Demitri, G. Bergamini, P. Ceroni, M. G. Papadopoulos, S. Couris, et al., *Chem. - Eur. J.* **2017**, *23*, 2363–2378.

[22] N. Kobayashi, M. Sasaki, K. Nomoto, *Chem. Mater.* **2009**, *21*, 552–556.

[23] T. Kamei, M. Uryu, T. Shimada, *Org. Lett.* **2017**, *19*, 2714–2717.

[24] A. Sciutto, A. Berezin, M. Lo Cicero, T. Miletić, A. Stopin, D. Bonifazi, *J. Org. Chem.* **2018**, *83*, 13787–13798.

[25] A. Sciutto, A. Fermi, A. Folli, T. Battisti, J. M. Beames, D. M. Murphy, D. Bonifazi, *Chem. - Eur. J.* **2018**, *24*, 4382–4389.

[26] K. Ding, Y. Wang, L. Zhang, Y. Wu, *Tetrahedron* **1996**, *52*, 1005–1010.

[27] C. Wang, D. M. Flanigan, L. N. Zakharov, P. R. Blakemore, *Org. Lett.* **2011**, *13*, 4024–4027.

[28] P. R. Blakemore, C. Kilner, S. D. Milicevic, *J. Org. Chem.* **2005**, *70*, 373–376.

[29] Y. X. Chen, L. W. Yang, Y. M. Li, Z. Y. Zhou, K. H. Lam, a S. Chan, H. L. Kwong, *Chirality* **2000**, *12*, 510–513.

[30] T. Matsuno, Y. Koyama, S. Hiroto, J. Kumar, T. Kawai, H. Shinokubo, *Chem. Commun.* **2015**, *51*, 4607–4610.

[31] V. Snieckus, *Chem. Rev.* **1990**, *90*, 879–933.

[32] E. J. Queguiner Guy, Marsais Fancis, Snieckus Victor, *Adv. Heterocycl. Chem.* **1991**, *52*, 187–304.

[33] T. Kamei, *JP 2018-39777 A 2018.3.15* **2018**, 1–104.

[34] M. Korb, H. Lang, *Chem. Soc. Rev.* **2019**, *48*, 2829–2882.

[35] V. Snieckus, *Chem. Rev.* **1990**, *90*, 879–933.

[36] V. Balasubramaniyan, *Chem. Rev.* **1966**, *66*, 567–641.

[37] V. Balzani, P. Ceroni, A. Juris, *Photochemistry and Photophysics: Concepts,*

Research, Applications, John Wiley & Sons, **2014**.

[38] G. A. Crosby, J. N. Demas, *J. Phys. Chem.* **1971**, *75*, 991–1024.

[39] C. Würth, M. Grabolle, J. Pauli, M. Spieles, U. Resch-Genger, *Nat. Protoc.* **2013**, *8*, 1535–1550.

[40] J. C. S. Costa, R. J. S. Taveira, C. F. R. A. C. Lima, A. Mendes, L. M. N. B. F. Santos, *Opt. Mater.* **2016**, *58*, 51–60.

[41] N. Elgrishi, K. J. Rountree, B. D. McCarthy, E. S. Rountree, T. T. Eisenhart, J. L. Dempsey, *J. Chem. Educ.* **2018**, *95*, 197–206.

[42] M. Müller, H. Reiss, O. Tverskoy, F. Rominger, J. Freudenberg, U. H. F. Bunz, *Chem. - Eur. J.* **2018**, *24*, 12801–12805.

[43] M. Winkler, K. N. Houk, *J. Am. Chem. Soc.* **2007**, *129*, 1805–1815.

[44] W. E. Jones, M. A. Fox, *J. Phys. Chem.* **1994**, *98*, 5095–5099.

[45] T. Asari, N. Kobayashi, T. Naito, T. Inabe, *Bull. Chem. Soc. Jpn.* **2001**, *74*, 53–58.

[46] G. M. Florio, T. L. Werblowsky, T. Müller, B. J. Berne, G. W. Flynn, *J. Phys. Chem. B* **2005**, *109*, 4520–4532.

[47] G. R. Desiraju, A. Gavezzotti, *Acta Crystallogr., Sect. B: Struct. Sci., Cryst. Eng. Mater.* **1989**, *45*, 473–482.

[48] G. Desiraju, T. Steiner, *The Weak Hydrogen Bond*, **2010**.

[49] G. Dearnaley, *Phys. Bull.* **1980**, *31*, 582.

[50] G. Cavallo, P. Metrangolo, R. Milani, T. Pilati, A. Priimagi, G. Resnati, G. Terraneo, *Chem. Rev.* **2016**, *116*, 2478–2601.

[51] M. Saccone, G. Cavallo, P. Metrangolo, A. Pace, I. Pibiri, T. Pilati, G. Resnati, G. Terraneo, *CrystEngComm* **2013**, *15*, 3102–3105.

[52] P. D. B. Lydia C. Gilday, Sean W. Robinson, Timothy A. Barendt, Mattehew J Langton, Benjamin R. Mullaney, *Chem. Rev.* **2015**, *115*, 7118–7195.

[53] C. Präsang, A. C. Whitwood, D. W. Bruce, *Cryst. Growth Des.* **2009**, *9*, 5319–5326.

[54] R. B. Walsh, C. W. Padgett, P. Metrangolo, G. Resnati, T. W. Hanks, W. T. Pennington, *Cryst. Growth Des.* **2001**, *1*, 165–175.

Chapter 3

Synthesis and Characterisation of N-methyl N-Doped *peri*-Xanthenoxanthene

In this chapter, the design, synthesis and photophysical properties of N-methyl N-doped *peri*-xanthenoxanthene (PXX) are described. The first part addresses the retrosynthetic design and synthesis of the corresponding methylated derivatives of molecules 3,9-diN-PXX **2**, 1,7-diN-PXX **4** and 4,10-NPXX **6**. The second part describes the investigation of the optoelectronic properties by spectroscopic and cyclic voltammetry measurements. The third part focuses on the single crystal XRD analysis of the molecules.

The chapter is divided into six main sections: *i) section 3.1*: general introduction on N-methylated Polycyclic Aromatic Hydrocarbons (PAHs); *ii) section 3.2*: aim of the project; *iii) section 3.3*: retrosynthetic approach and synthesis of the N-methylated NPXX molecules; i*v) section 3.4*: photophysical characterisation of the synthesised molecules; *v) section 2.5*: electrochemical characterisation via cyclic voltammetry; *vi) section 3.6*: solid-state characterisation by single crystal X-ray diffraction (XRD).

The X-ray analysis presented in this chapter were performed by *Deborah Romito* (*Cardiff University, School of Chemistry, Cardiff*).

3.1 Introduction about N-alkyl Polycyclic Aromatic Hydrocarbon

The N-alkylation of N-heteroacenes leads to the formation of quaternary ammonium salts. Their applications have dramatically expanded from their early use as herbicides,[1] to their employment as electron transfer relays, [2,3] as components of charge-transfer complexes, [4,5] of supramolecular assemblies [6–8] and in electronic devices.[9–14] In this context, viologens, di-quaternised-4,4'-bipyridyl salts, possess interesting redox properties. For instance, methyl viologen (MV^{2+}) can be reduced into its radical cation (MV^{+}) at -0.81 V (vs Fc/Fc^{+}) and to the neutral species (MV) at -1.22 V (vs Fc/Fc^{+}), scheme 3.1.[15] MV^{2+} colour is dependent on the oxidations state of the molecule, (MV^{2+} uncoloured, MV^{+} violet-blue and MV brown-yellow).[16]

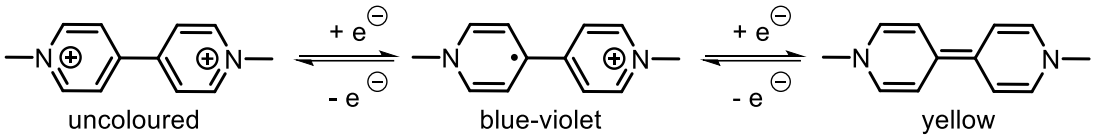

Scheme 3.1. The three reversible redox states of methyl viologen (MV^{2+}).

3.1.1 Optoelectronic properties of N-methyl Polycyclic Aromatic Hydrocarbons.

The π-extension of viologens has been investigated to enhance the photophysical and electronic properties for applications in electronic technologies.[17–21] An interesting example by Schilling e*t al.* describes the synthesis, photophysical and electrochemical investigation of diazadibenzoperylenes **1.A** and N-alkyl diazadibenzoperylenes **1.B** and **C**, figure 3.1a.[22] The UV-Vis absorption spectrum of molecule **1.A** in CH_2Cl_2 shows the lowest S_0-S_1 transition at λ = 497 nm, figure 3.1b. The fluorescence emission spectrum is the mirror image of the absorption spectrum with the highest energy transition centred at λ = 514 nm. The alkylation of the two nitrogen atoms of molecule **1.A** to form molecule **1.B** induces a 33 nm red-shift of the S_0-S_1 transition in the absorption spectrum and a 31 nm red-shift in the fluorescence emission (λ_{max} = 545 nm), figure 3.1b. The nitrogen atoms alkylation affects negatively the fluorescence quantum yield, which decreases from 75% for molecule **1.A** for 50% of molecule **1.B**. The cyclic voltammogram of molecule **1.B** shows one reversible wave in the reductive cycle at -1.75 V (vs Fc/Fc+), where reduction to the radical anion $\mathbf{1.B}^{\bullet-}$ occurs, figure 3.1c. The oxidation of molecule **1.A** is irreversible and accompanied by adsorption of the oxidized species on the platinum electrode surface. For molecule **1.A**, the cyclic voltammetric trace shows two reversible waves at -1.32 V and -0.92 V in the reductive

cycle, which are significantly higher than that observed for molecule **1.B**, figure 3.4c. These suggest that **1.B** is reduced to the neutral antiaromatic π-system **1.C** through a radical cationic intermediate.

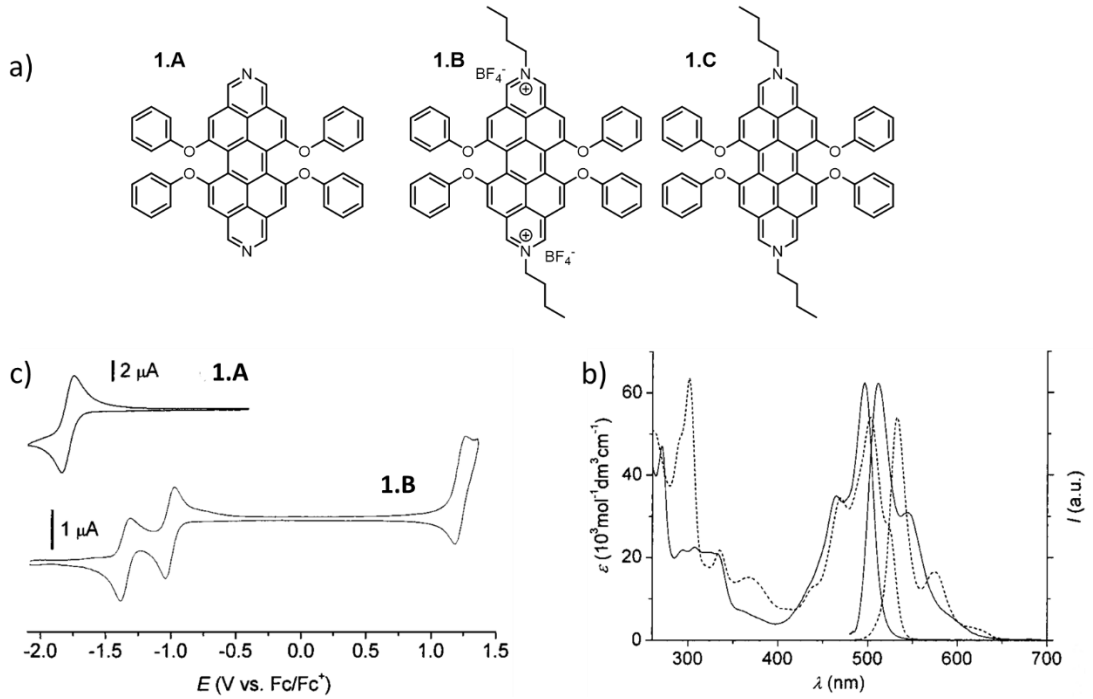

Figure 3.1. a) Chemical structures of **1.A**, **1.B** and 1.**C**; b) UV/vis absorption and fluorescence spectra of **1.A** (solid lines) and **1.B** (dashed lines) in CH_2Cl_2; c) cyclic voltammogram of **1.A** and **1.B** in CH_2Cl_2 (scan rate 100 $mV \cdot s^{-1}$).

Similarly, Weber *et al.* reported the synthesis, structural and photophysical characterization of a novel isomeric pair of π-extended helical viologens, **2.B** and **2.D** in figure 3.2.[23] The UV−Vis absorption and emission spectra of viologens **2.B** and **2.D** exhibit similar outlines despite the different placement of nitrogen atoms in the helicoidal scaffold, figure 3.2. and table 3.1. In addition, the lowest energy absorption bands for **2.B** and **2.D** show nearly identical bathochromic shift, of 68 and 67 nm respectively, from the lowest energy peak from their bipyridine precursors **2.A** and **2.C**. The vibronic transitions in the absorption spectra are more defined in bipyridines **2.A** and **2.C** than in the corresponding viologen **2.B** and **2.D**.

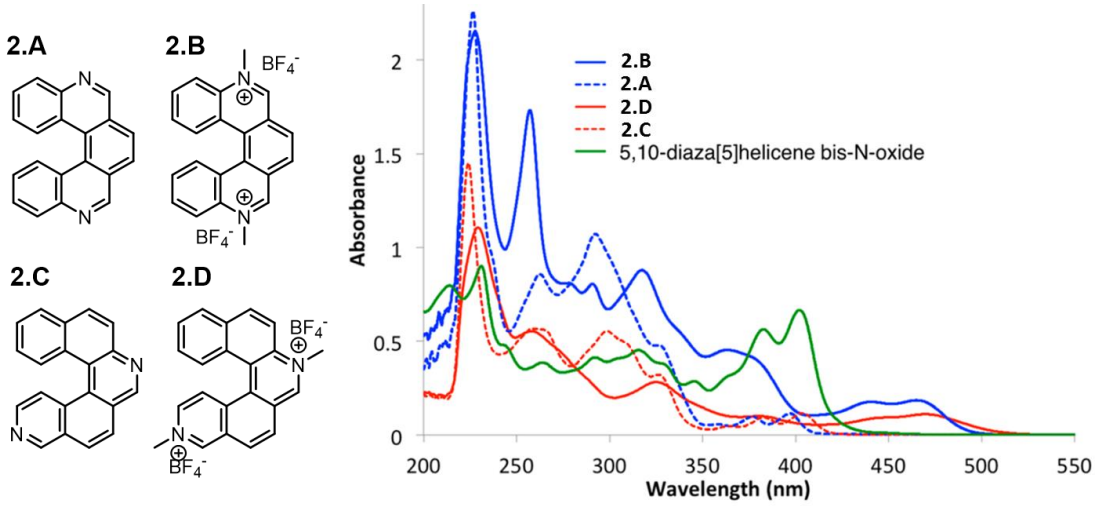

Figure 3.2. UV-Vis absorption spectra of molecules **2.A**, **2.B**, **2.C** and **2.D** in CH_3CN at r.t..

Table 3.1. Photophysical data for molecules **2.A**, **2.B**, **2.C** and **2.D** in acetonitrile at r.t..

	Absorbance		Emission			
	λ_{max} (nm) [eV]	ε ($M^{-1}cm^{-1}$)	λ_{max} (nm) [eV]	τ (ns)	Φ_{em} [a] (%)	E_g^{opt} [b] (eV)
2.A	397 [3.12]	3000	455 [2.72]	6.3	75	2.92
2.B	465 [2.66]	4000	504 [2.46]	5.8	61	2.48
2.C	403 [3.07]	5300	463 [2.68]	4.2	61	2.95
2.D	470 [2.64]	6000	566 [2.19]	10.2	41	2.39

Molecule **2.B** is photochemically inert when exposed to ambient light. Conversely, molecule **2.D** yields the formation of molecule **2.E** under identical conditions and in presence of O_2, scheme 3.2.

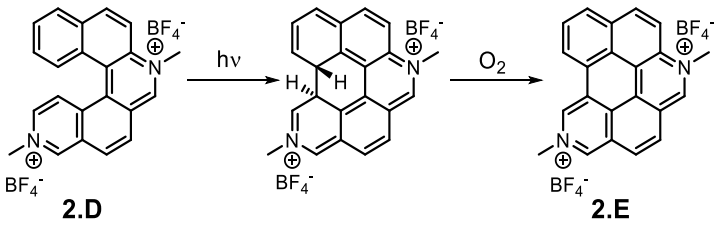

Scheme 3.2. UV-Vis absorption spectra of molecules **2.A**, **2.B**, **2.C** and **2.D** in CH_3CN at r.t..

π-extended viologens have also been investigated in supramolecular chemistry as building block for catenanes and rotaxanes.[7,24]. Stoddart *et al.* studied the intramolecular energy transfer (EnT) in $DAPPBox^{4+}$ which is made by two different viologens, diazadibenzoperylenes ($DAPP^{2+}$) and paraquat-p-phenylene ($ExBIPY^{2+}$), figure 3.3a.[7] After excitation at maximum absorbance of $ExBIPY^{2+}$ (339 nm), the emission spectrum of $DAPPBox^{4+}$ shows only enhanced green emission at 517 nm corresponding to $DAPP^{2+}$ fluorescence while the UV emission of $ExBIPY^{2+}$ is not detected, figure 3.3b. The fluorescence quenching of $ExBIPY^{2+}$ and the enhancement

of the $DAPP^{2+}$ emission in the steady-state emission spectrum of $DAPPBox^{4+}$, suggests efficient singlet EnT from the $ExBIPY^{2+}$ to the $DAPP^{2+}$ unit within the cyclophane. The efficiency of the EnT is also in line with the favourable overlap of the emission spectra of $Me\text{-}ExBIPY^{2+}$ and the absorption spectra of $Me\text{-}DAPP^{2+}$, as required for Förster energy transfer, figure 3.3c.[25,26]

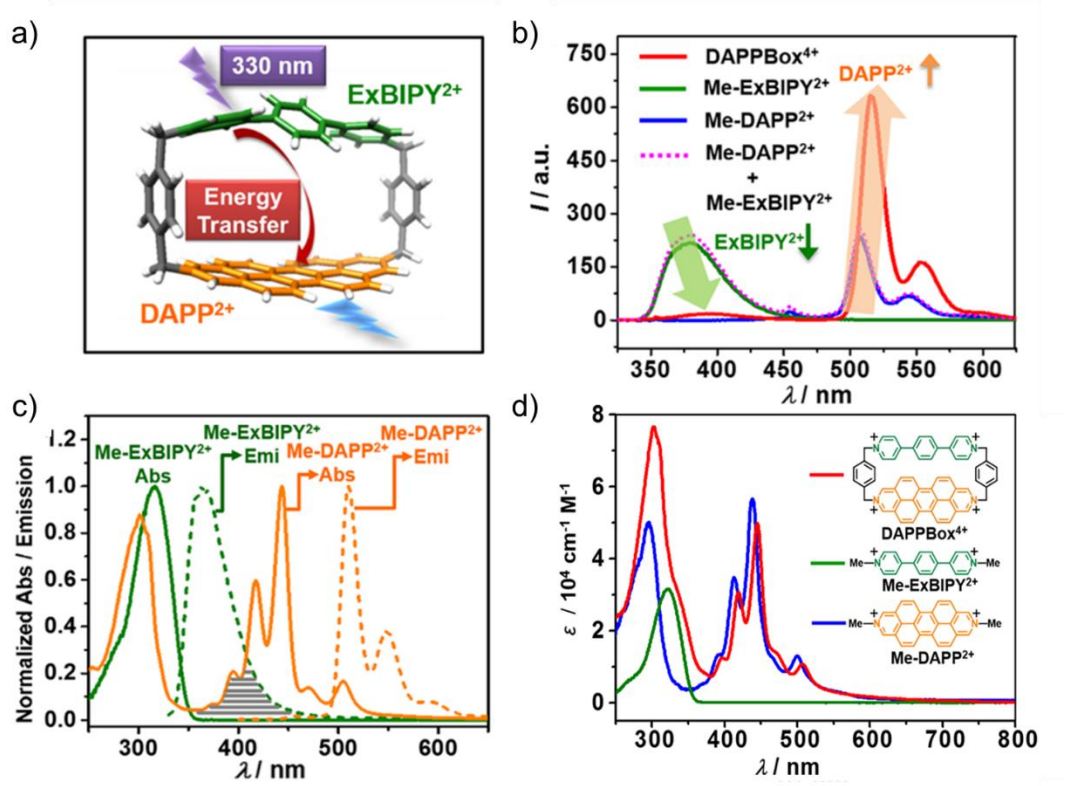

Figure 3.3. a) Energy-transfer process within $DAPPBox^{4+}$; b) emission spectra of $DAPPBox^{4+}$, $Me\text{-}ExBIPY^{2+}$, $Me\text{-}DAPP^{2+}$, and a physical mixture of $Me\text{-}ExBIPY^{2+}$ and $Me\text{-}DAPP^{2+}$ in MeCN upon excitation at 339 nm, 1.6 µM at r.t.; c) normalized spectra showing the overlap between emission of the $Me\text{-}ExBIPY^{2+}$ and the absorption of the $Me\text{-}DAPP^{2+}$; d) absorption spectra of $DAPPBox^{4+}$, $Me\text{-}ExBIPY^{2+}$, and $Me\text{-}DAPP^{2+}$ in MeCN at r.t..

3.1.2 Viologens as electron relay in photo-H_2-evolution.

MV^{2+} has also been exploited as electron relay (R) to achieve the photo induced H_2O splitting for hydrogen evolution..[27–30] The photo induced reaction is performed in the presence of a photosensitiser S, MV^{2+} as R, a H_2-evolving catalyst C and EDTA as sacrificial electron source, figure 3.4. Upon visible light irradiation, the photoexcited S* is oxidised by MV^{2+} yielding $S^{\cdot+}$ and $MV^{\cdot+}$. While $S^{\cdot+}$ is reduced to S by the sacrificial reagent EDTA, the radical cation MV^{+} gives the electron to the catalyst C where the cation H^{+} is reduced to H_2.[31–33] MV^{2+} is a suitable electron acceptor for photoexcited S* because its $E_{1/2}^{red}$ is higher than E_{ox}^{*} of photosensitiser S. Moreover, the electron transfer from $MV^{\cdot+}$ to the catalyst occurs before the back electron transfer.[31,33]

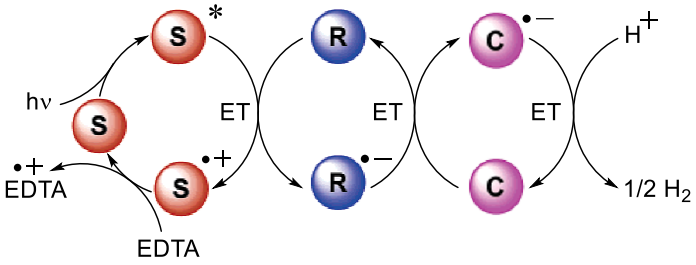

Figure 3.4. Photocatalytic process for H_2-evolution. S denotes a photosensitizer, such as $Ru(bpy)_3^{2+}$. R is an electron relay such as methyl viologen (N,N′-dimethyl-4,4′-bipyridinium, abbreviated as MV^{2+}). C corresponds to a H_2-evolving catalyst, such as colloidal Pt, Pt(II), or Rh(I) complexes.

To enhance the H_2-evolution, Feiters *et al.* used the host-guest interaction between β-cyclodextrin (CD) and MV^{2+} to build a supramolecular photocatalytic system, [31,33] which is composed by an Ir-CD photosensitizer and Pt-particles, both functionalised with CDs, figure 3.5.[33] MV^{2+} works as linker between the Pt-particle and multiple Ir-CD units. The measured H_2-evolution yields were an order of magnitude higher than those reported for Ru-bpy/MV^{2+}/Pt/EDTA systems.[27,28,32,33]

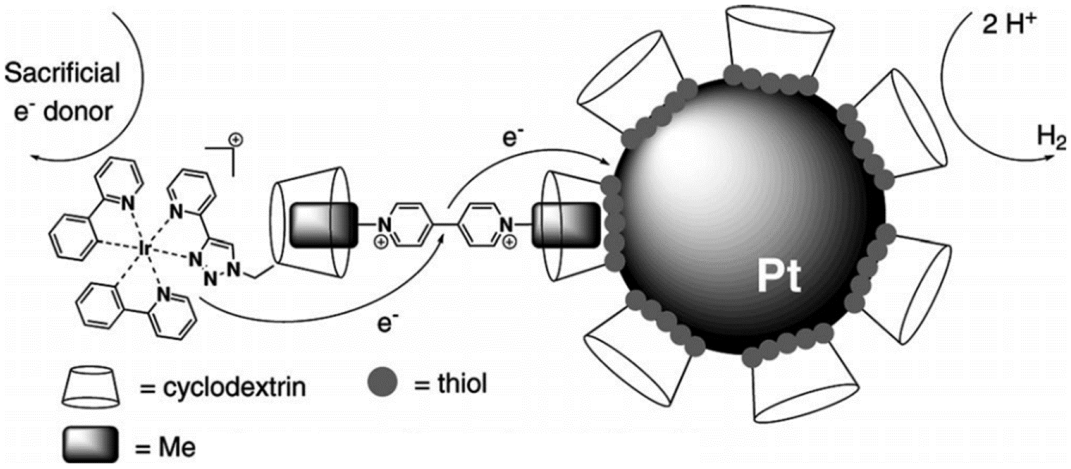

Figure 3.5. Self-assembled three-component system for photoinduced electron transfer involving a platinum nanoparticle, represented as a grey-white sphere

3.2. Aim of the project: synthesis of N-methyl NPXX for application as photosensitiser and electron relay

As showed in the introduction of this chapter, MV^{2+} is used in photocatalytic production of H_2 from H_2O in cooperation with a photosensitiser S and a catalyst C, figure 3.6a. However, Ru or Ir complexes are typically used as photosensitiser and their cost is one of the main drawbacks for large-scale application. The photocatalytic process can be modified by replacing S and R with a new class of molecules (SR) that exploits both R and S roles, figure 3.6b. The SR must be photoactive in the visible range and, upon

irradiation, able to oxidise an electron donor, such as EDTA. Moreover, the radical anion $SR^{\bullet-}$ must have the same $E_{1/2}^{red}$ as MV^{+2} in order to transfer the electron to the catalyst C, figure 3.6b.

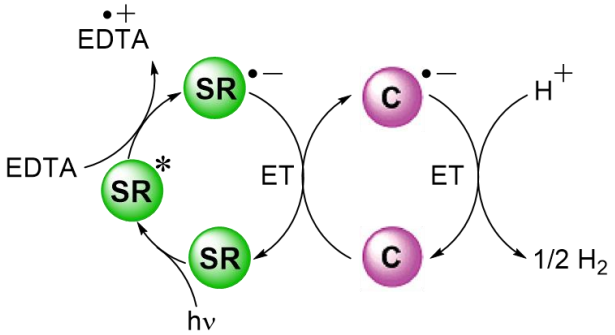

Figure 3.6. Two component photocatalytic process for H_2-evolution; SR denotes the photosensitiser and electron relay; C corresponds to a H_2-evolving catalyst, such as colloidal Pt, Pt(II), or Rh(I) complexes.

Therefore, we envisaged to functionalise the nitrogen moieties in molecules 3,9-diN-PXX **2**, 1,7-diN-PXX **4** and 4,10-NPXX **6** with methyl groups to include the same viologen motif in an O-doped PAH, which, as they possess extended π-conjugation, will be photoactive in the visible region scheme 3.3.[34]

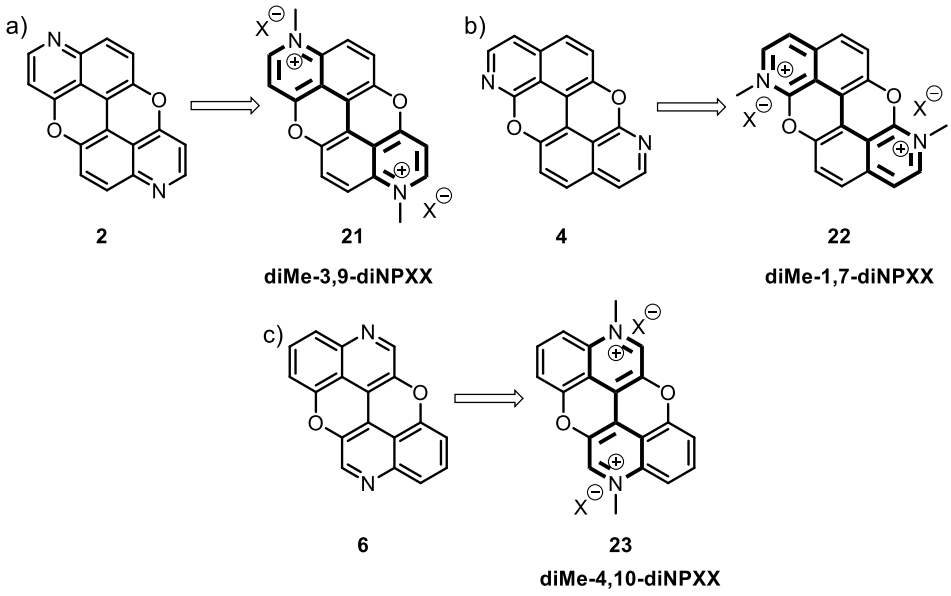

Scheme 3.3. Target molecules **21**, **22** and **23.**

3.3 Synthesis of N-methyl N-doped *peri*-xanthenoxanthene

3.3.1 Retrosynthetic approach for the synthesis of N-methyl N-doped *peri*-Xanthenoxanthene 21, 22 and 23

The synthetic plan towards the preparation of molecules **21**, **22** and **23** is driven by the literature protocols for the synthesis of viologen-like molecules.[34–38] The retrosynthetic pathway, shown in scheme 3.4, starts with the C_{sp}^3-N_{sp}^2 disconnection that leads to CH_3X and the corresponding NPXX as synthetic equivalents, which can react via nucleophilic substitution with S_N2 mechanism. The leaving groups X^- will be the counter anions in the products **21**, **22** and **23**.

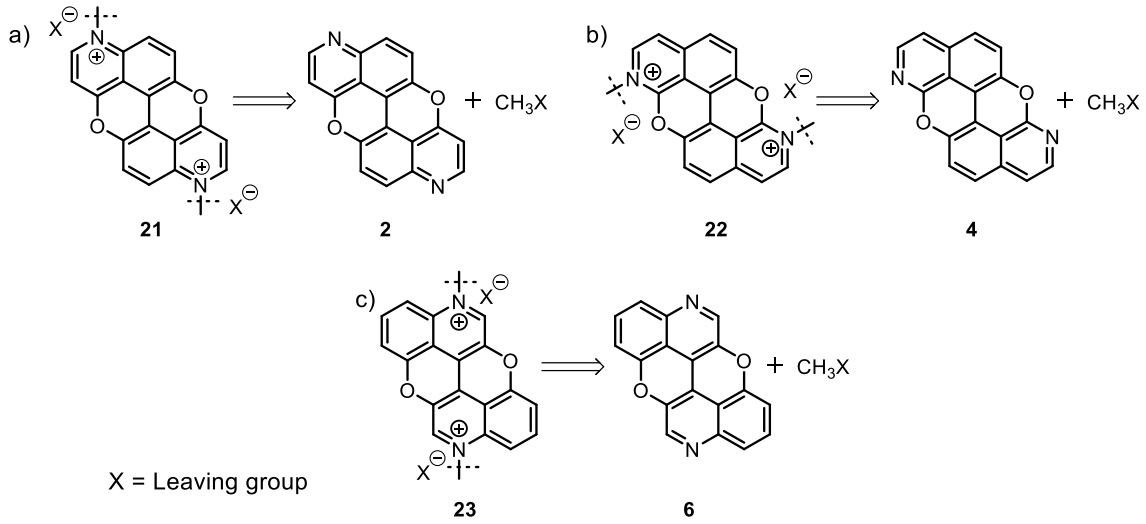

Scheme 3.4. Retrosynthetic pathways for the synthesis of molecules **21**, **22** and **23**.

3.3.2 Synthesis of diMe-1,7-diN-PXX 22

According to the retrosynthetic plan, molecule **4** was dissolved in DMF and treated with CH_3I for 2 days at 55 °C, scheme 3.5. The solvent was removed yielding a yellow solid as reaction crude.

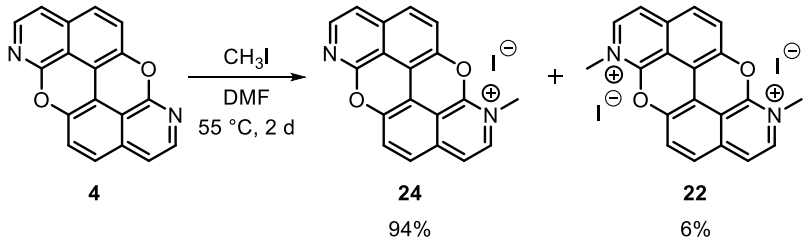

Scheme 3.5. Synthetic protocol for the preparation of molecule **22**. (Yield calculated by ^{1}H-NMR)

The mass spectrum shows the formation of the monomethylated product **24** and the double charged molecule **22**, figure 3.8. Moreover, traces of starting material **4** were detected, figure 3.7.

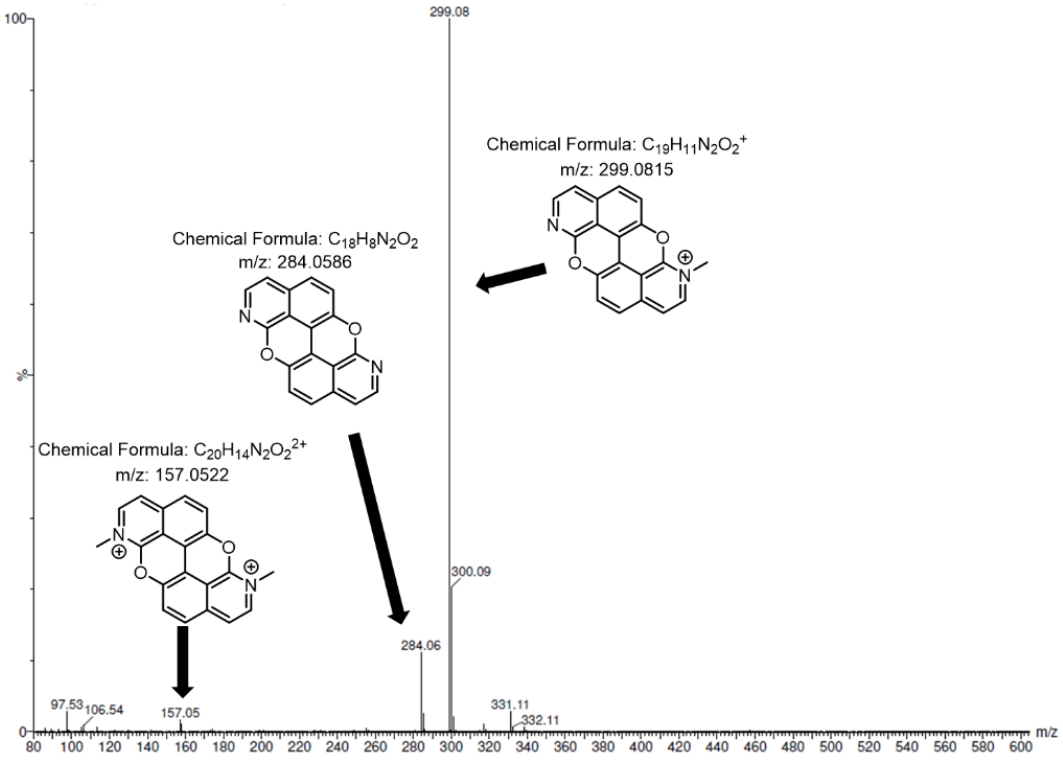

Figure 3.7. TOF-ES$^+$ mass spectrum of molecule **4** methylation reaction crude.

Since the mass analysis cannot be used as a quantitative method, the reaction crude was dissolved in DMSO-d_6 and the solution analysed by ^{1}H-NMR spectroscopy. It is possible to observe the absence of starting material **4** in the reaction crude by comparing the two spectra in figures 3.8a and 3.8b. Moreover, the peaks in the aromatic region do not show the symmetry expected for the protons of molecule **22**, in figure 3.8b. The peaks at 4.03 and 4.12 ppm can be attributed to the methyl groups on molecules **24** and **22**, respectively. The integral ratio of the peaks at 4.03 and 4.12 ppm suggest that the ratio of molecules **22** ad **24** are 6% and 94%, respectively, figure 3.8b.

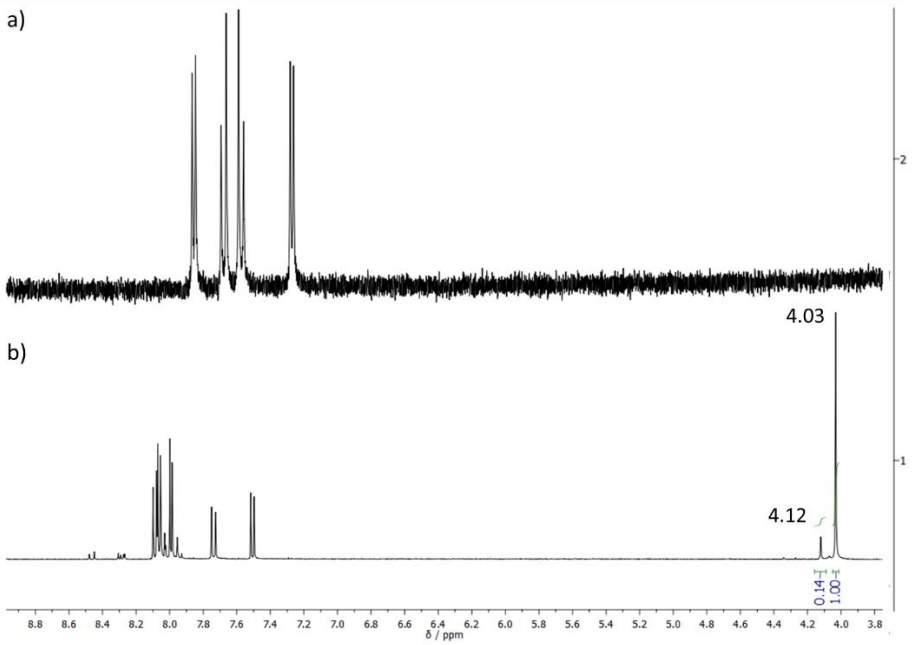

Figure 3.8. a) ^{1}H-NMR spectrum of molecule **4** in DMSO-d_6 at r.t., b) ^{1}H-NMR spectrum of the reaction crude in DMSO-d_6 r.t..

Due to the presence of monomethylated product **24** as main product in the reaction crude, the methylation of NPXX **4** was attempted in CH_3I neat under pressure. Therefore, molecule **4** was suspended in CH_3I and heated at 150 °C for 24 h in a sealed flask, scheme 3.6.

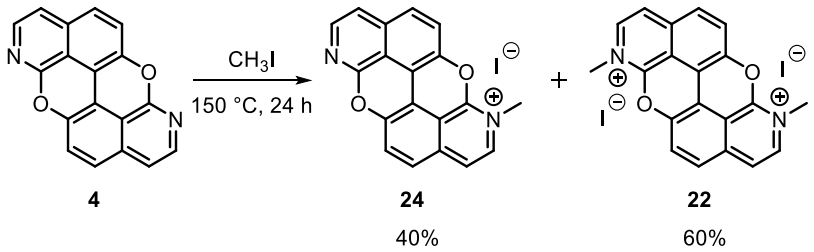

Scheme 3.6. Synthetic protocol for the preparation of molecule **22**. (Yield calculated by ^{1}H-NMR)

The reaction crude was dissolved in DMSO-d_6 and the solution analysed by ^{1}H-NMR spectroscopy. By comparing the two spectra in figure 3.9a and 3.9b, it is possible to observe the absence of starting material **4** in the reaction crude. In figure 3.9b, the integral ratio of the peaks at 4.03 and 4.12 ppm suggests that the yield of molecules **22** and **24** are 60% and 40%, respectively. The purification of the reaction crude was attempted by recrystallisation, but it was unsuccessful.

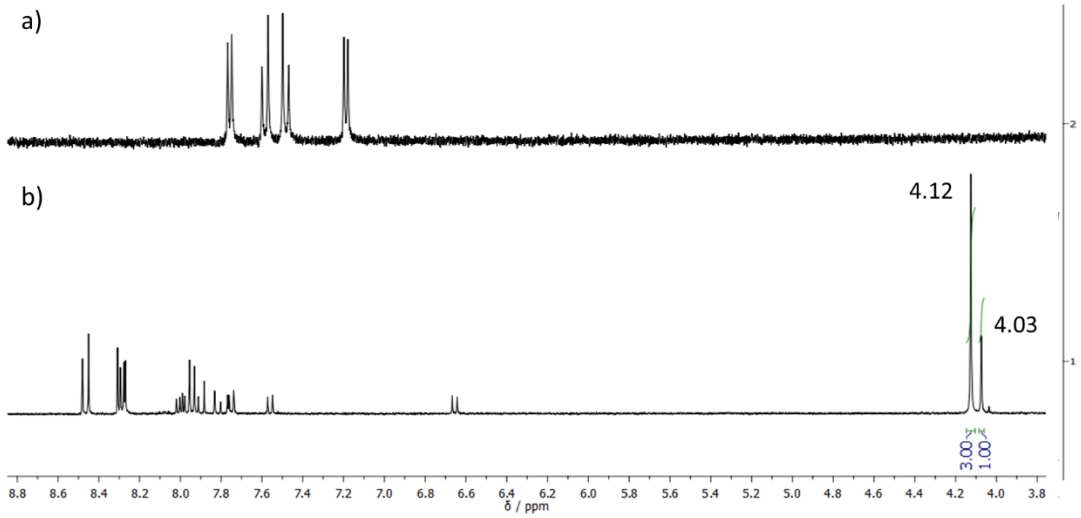

Figure 3.9. a) ^{1}H-NMR spectrum of molecule **4** in DMSO-d_6 at r.t., b) ^{1}H-NMR spectrum of the reaction crude in DMSO-d_6 r.t..

3.3.3 Synthesis of diMe-3,9-diN-PXX 21

Taking into consideration the results obtained during the synthesis of molecule **22**, the same protocol was used for the synthesis of molecule **21**, in order to avoid the formation of the monomethylated product. Molecule **2** was suspended in CH_3I and the mixture stirred for 24 h at 150 °C in a sealed flask, scheme 3.7.

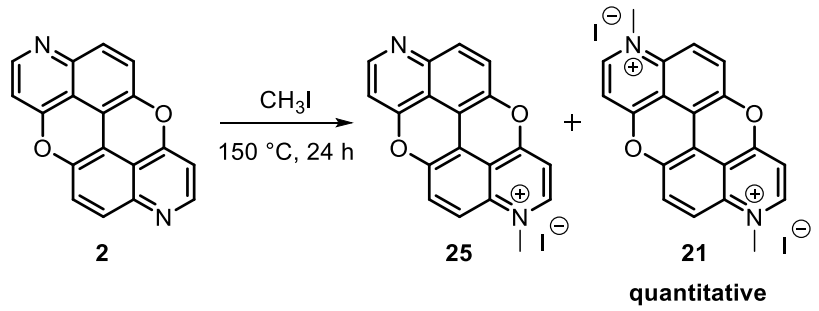

Scheme 3.7. Synthetic protocol for the preparation of diMe-3,9-diN-PXX **21**. (Yield calculated by ^{1}H-NMR)

The crude of reaction was dissolved in DMSO-d_6 and the solution analysed by ^{1}H-NMR spectroscopy. By comparing the two spectra in figure 3.10a and 3.10b, it is possible to observe the absence of starting material **2**. In the aromatic region, the peaks outline in spectrum 3.10b shows the same trend observed in the spectrum of molecule **2** (figure 3.10a) and it is possible to attribute the peak at 4.31 ppm to the methyl groups on the nitrogen atoms. The mass spectrum confirms the formation of product **21** with a peak at 157.0522 m/z, figure 3.10c.

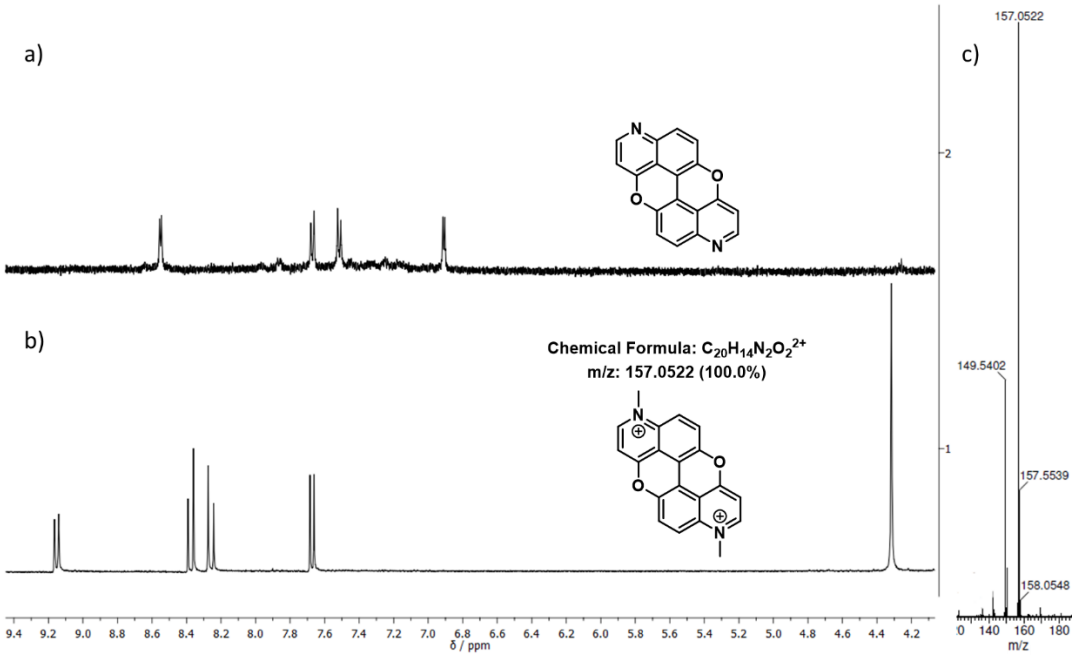

Figure 3.10. a) ^{1}H-NMR spectrum of molecule **2** in DMSO-d_6 at r.t., ^{1}H-NMR spectrum of molecule **21** in DMSO-d_6 r.t.; b) TOF-ES$^+$ mass spectrum of molecule **21**.

3.3.4 Synthesis of diMe-4,10-diN-PXX 23

Molecule **23** was prepared following the same protocol used for the preparation of molecule **22**. Molecule **6** was suspended in CH_3I and the mixture stirred for 24 h at 150 °C in a sealed flask, scheme 3.8.

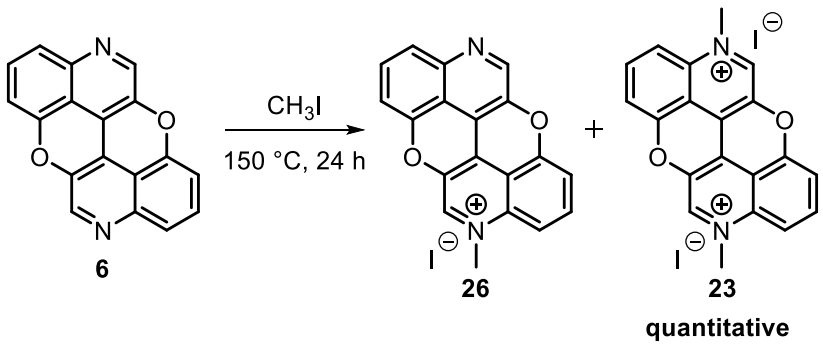

Scheme 3.8. Synthetic protocol for the preparation of diMe-4,10-diN-PXX **23**. (Yield calculated by ^{1}H-NMR)

The crude of reaction was dissolved in DMSO-d_6 and the solution analysed by ^{1}H-NMR spectroscopy. It is possible to observe the absence of starting material **6** by comparing the two spectra in figure 3.11a and 3.11b. In the aromatic region, the peaks outline in spectrum 3.11b shows the same trend observed in the spectrum of molecule **6** (figure 3.11a) and it is possible to attribute the peak at 4.49 ppm to the methyl groups on the

nitrogen atoms. The mass spectrum confirms the formation of product **23** with a peak at 157.0522 m/z, figure 3.11c.

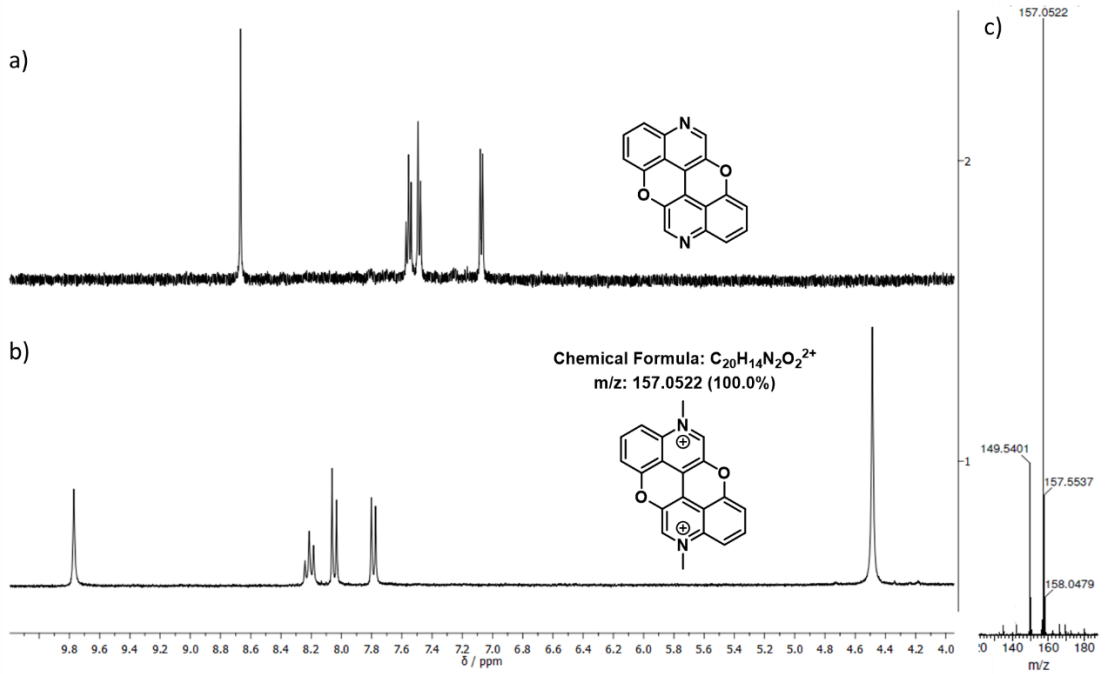

Figure 3.11. a) ^{1}H-NMR spectrum of molecule **6** in DMSO-d_6 at r.t., b) ^{1}H-NMR spectrum of molecule **23** in DMSO-d_6 r.t.; c) TOF-ES$^+$ mass spectrum of molecule **23**.

3.3.5 Conclusion about the synthesis

In this section, the synthesis of N-methyl NPXX has been discussed. The methylation in neat CH_3I of molecule **2** and **6** gave the formation of pure products **21** and **23**. On the other hand, the methylation in neat CH_3I of molecule **4** gave the formation of mono and bis methylated compounds, **24** and **22** respectively. Due to the impossibility of purification the mixture of compounds **24** and **22** by crystallisation, the photophysical characterization was performed only for molecules **21** and **23**.

3.4 Photophysical characterization of molecules 21 and 23.

In this section, the optoelectronic properties of the previously synthesised **21** and **23** are reported and compared with molecule **2** and **6**. The goal was to investigate the effects of the N-methylation on the optoelectronic properties of molecules **2** and **6**. The UV-Vis absorption and emission measurements for molecule **21** and **23** were performed in CH_3CN solution and are depicted in Figures 3.12a and 3.12b. The absorption spectrum of molecule **21** shows $\pi \rightarrow \pi^*$ electronic transitions in the visible range with broader outline. The absorption maximum of **21** is bathochromically shifted by 7 nm in comparison with the absorption spectrum of molecule **2**. The absorption

spectrum of molecule **23** shows a broad outline and the absorption maximum 117 nm red shifted with respect to molecule **6**. The emission spectra of molecules **21** and **23** show a radiative decay of the excited singlet state (S_1) to the ground state S_0 with luminescence lifetimes corresponding with fluorescence phenomena, table 3.2. The fluorescence quantum yield for molecules **21** and **23** are 16% and < 2%, respectively, table 3.2. Molecule **21** shows an emission spectrum that is 63 nm red shifted in comparison with that of molecule **2**, while the emission spectrum of molecule **23** is bathochromic shifted of 146 nm with respect to molecule **6**, figure 3.12a and 3.12b.

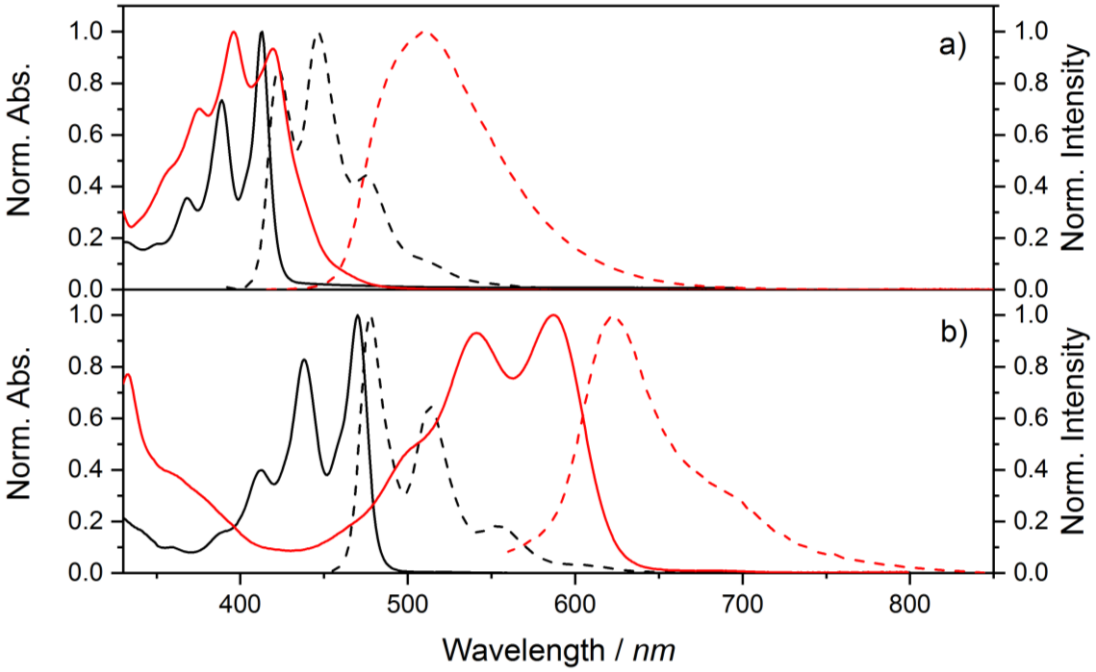

Figure 3.12. a) Normalised absorbance spectra (solid line) and normalised emission spectra (dashed line) for molecule **2** (black lines) and molecule **21** (red lines); b) normalised absorbance spectra (solid line) and normalised emission spectra (dashed line) for molecule **6** (black lines) and molecule **23** (red lines).

Table 3.2. Photophysical data for synthesised NPXXs and PXX in toluene at r.t..

	Absorbance		Emission			
	λ_{max} (nm) [eV]	ε ($M^{-1}cm^{-1}$)	λ_{max} (nm) [eV]	τ (ns)	Φ_{em} [a] (%)	E_g^{opt} [b] (eV)
2	413 [3.00]	11838	423 [2.93]	6.6	75	2.93
21	420 [2.95]	15511	508 [2.44]	5.9	16	2.73
6	470 [2.63]	7448	477 [2.60]	13.5	41	2.57
23	587 [2.11]	6033	624 [1.99]	6.7	< 2	1.98

[a] Standard: Coumarin-153 in EtOH at r.t. (Φ_{em}=0.53). [c] Energy (eV) calculated from normalized absorption spectrum edge λ_{edge}, exploiting the conversion nm to eV: E_g^{opt} = 1240/ λ_{edge}.

The different bathochromic shift observed for molecules **21** and **23** with respect to their precursor **2** and **6** can be explained using the same approach employed in chapter 2. The positions 4 and 10 in PXX are the most electron rich and the positions 3 and 9 are the most electron poor on the charge distribution map of PXX, figure 3.13. Therefore,

the positively charged nitrogen atoms in positions 4 and 10 in molecule **6** stabilise the extra negative charge present in those positions, reducing the lowest absorption transition energy of 0.5 eV, table 3.2. On the contrary, the positively charged nitrogen atoms in position 3 and 9 in molecule **2** do not significatively affect the lowest absorption transition energy, table 3.2.

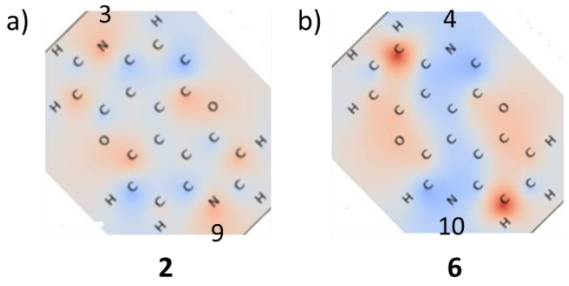

Figure 3.13. Molecules **2** a) and **6** b) excited-state CHELPG charges – ground-state CHELPG charges (radially interpolated over the atomic positions). The colour map ranges from +0.1 (red, donors) to -0.1 (blue, acceptors)

3.5. Electrochemical Investigation

3.5.1 Cyclic voltammetry investigation

The redox properties of molecules **21** and **23** were evaluated by cyclic voltammetry in CH_3CN with $TBAPF_6$ as electrolyte. All the measurements were calibrated against Fc/Fc^+, which was used as reference, table 3.3 and figure 3.14. The cyclic voltammetry trace of molecule **21** displays an irreversible reduction wave at $E_{1/2}^{red}$ = -0.91 V which is 0.9 V higher than $E_{1/2}^{red}$ of molecule **2**. Likewise, the cyclic voltammogram of **23** shows a reversible reduction wave at $E_{1/2}^{red}$ = -1.00 V that is 0.94 V higher than that of molecule **6**. Therefore, the methylation of the nitrogen atoms in molecules **2** and **6** increases the reduction potential by about 0.9 V.

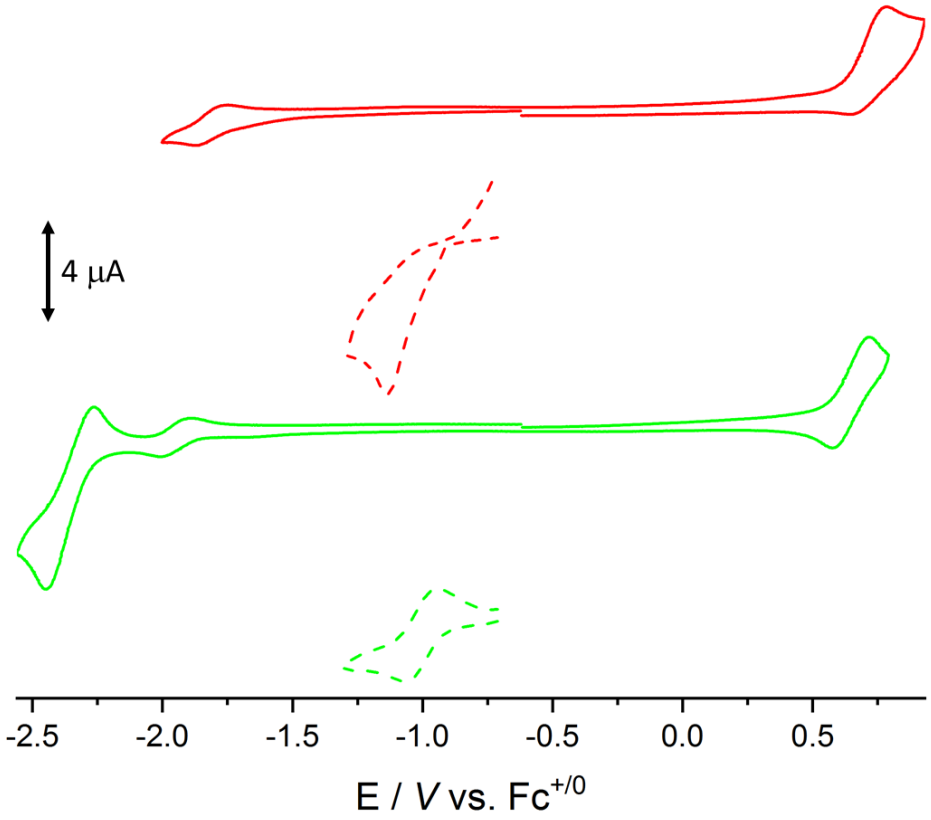

Figure 3.14. Cyclic voltammograms in ODCB at r.t. with electrolyte $TBAPF_6$ 63 mM of **2** (solid red line) and **6** (solid green line). Cyclic voltammograms in acetonitrile at r.t. with electrolyte $TBAPF_6$ 65 mM of **21** (dashed red line) and **23** (dashed green line).

Table 3.3. Cyclic Voltammetry data calculated vs Fc^+/Fc. at r.t. with electrolyte $TBAPF_6$. (in ODCB for **2** and **4**; in acetonitrile for **21** and **23**).

	$E_{1/2}^{ox}$ (V)	ΔE_{pp}^{ox} (mV)	$E_{1/2}^{red}$ (V)	ΔE_{pp}^{red} (mV)	$E_{1/2}^{red}$ [d] (V)	ΔE_{pp}^{red} (mV)	E_g^{CV} (eV)
2	0.71	148	-1.81	116	n.d.		2.52
21	n.d.	-	-0.91[a]	-	-	-	-
6	0.65	229	-1.94	108	-2.35	186	2.59
23	-	-	-1.00	120	-	-	-

[a] Calculated on the onset potential

By knowing the redox potential of S_0 and E_g^{opt}, it is possible to calculate the redox potential of S_1 using equations 2.6a and 2.6b discussed in chapter 2.[39] In table 3.4, E_{red}^* of the S_1 for molecule **21** is 0.7 V higher than E_{red}^* of molecule **2**, meaning that it is a better oxidant than molecule **2** in the excited state. However, the reduction wave of molecule **21** is not reversible, as showed in figure 3.14, hence it cannot be used in photocatalytic reaction as SR for H_2-evolution. Molecule **23** has a E_{red}^* at 0.98 V that is 0.33 V higher than E_{red}^* of molecule **6**. Since viologen **23** has a reversible reduction and absorbs light in the range of 550-625 nm, it is a photooxidant for all the molecules with oxidation potential < 0.98 V. Specifically, upon irradiation in the range of 550-625

nm, it can photooxidise EDTA which has a $E_{1/2}^{ox}$ = -0.21 V.[40,41] Therefore, viologen **23** is a promising candidate as SR in photocatalytic reaction for H_2-evolution.

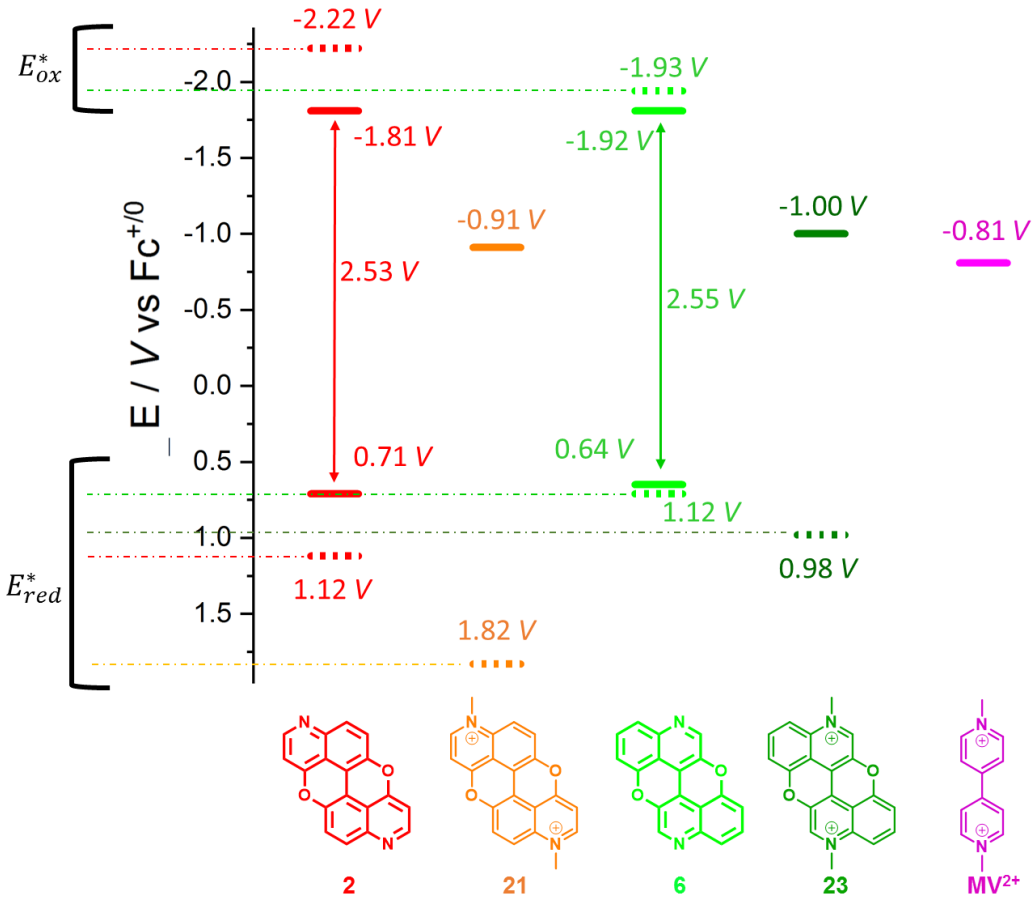

Figure 3.15. Solid line $E_{1/2}^{ox}$ and $E_{1/2}^{red}$ potentials. Dashed lines E_{ox}^{*} and E_{red}^{*} potentials of the S_1.

3.6 Solid-state self-assembly investigation of NPXXs

In this section, the structural and supramolecular properties of molecules **21** and **23** in the solid state, which were determined via single crystal X-ray diffraction (XRD), will be discussed.

3.6.1 diMe-3,9-diN-PXX solid-state self-assembly

Molecule **21** was crystallised by slow evaporation of a CH_3CN solution. The obtained crystals are monoclinic and belong to the $P2_1/n$ space group, R-factor 3.65%. The ORTEP graph in figure 3.16a shows the molecular structure of **21**. The distances between C(8)···N(1) and C(4)···N(1) are 1.333 Å and 1.383 Å respectively and are slightly longer than the homologous bonds in molecule **2**, for which C(9)···N(8) and C(7)···N(8) distances are 1.321 Å and 1.372 Å respectively, figure 3.6b. On the contrary, the distances C(8)···C(9) and C(4)···C(5) in molecule **21**, being 1.380 Å and

1.394 Å respectively, are slightly shorter than the relative bonds in molecule **2**, where the distances between C(9)···C(10) and C(7)···C(2) are both 1.410 Å, figure 3.16a and 3.16b.

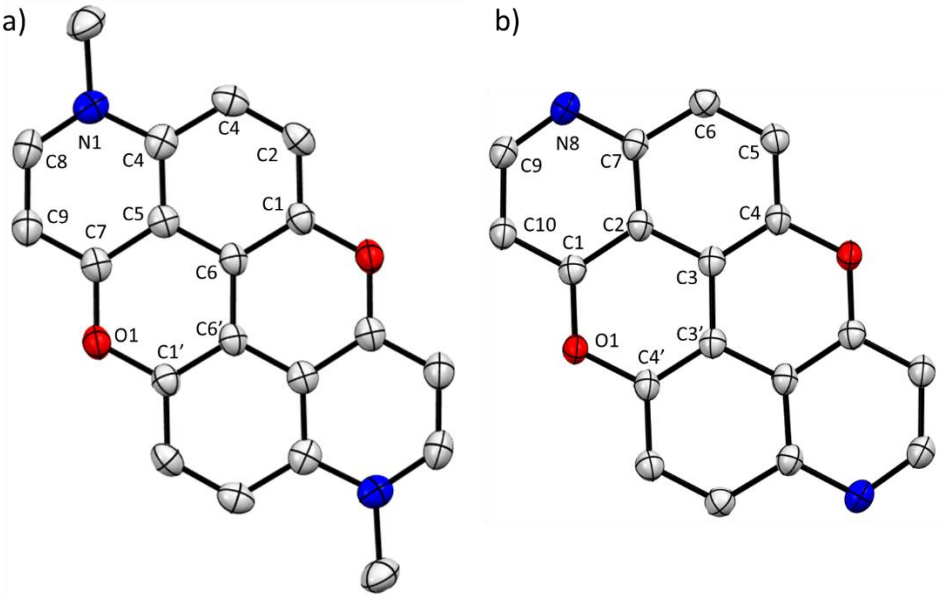

Figure 3.16. a) Molecule **21** ORTEP representation (50% probability ellipsoids) crystallisation solvent CH_3CN; b) molecule **2** ORTEP representation (50% probability ellipsoids) crystallisation solvent $CHCl_3$. Nitrogen (blue), oxygen (red) and carbon (white). (Hydrogen atoms omitted for clarity).

Molecule **21** crystallises in the crystal lattice with two iodide ion and a molecule of H_2O. The distances between the iodide ion and the hydrogen atoms of the water molecule are 2.667 Å and 2.713 Å, respectively, suggesting that they are two different weak hydrogen bond interactions, figure 3.17a.[42] Interestingly, each iodide ion interacts with the hydrogen atoms in position C8 and C9 on two neighbouring molecules **21** with 3.005 Å and 3.091 Å relative distances, producing a square motif, figure 3.17b. Molecule **21** shows a tilted herringbone face-to-edge crystal packing without face-to-face π-π overlap, figures 3.17c and 3.17d.

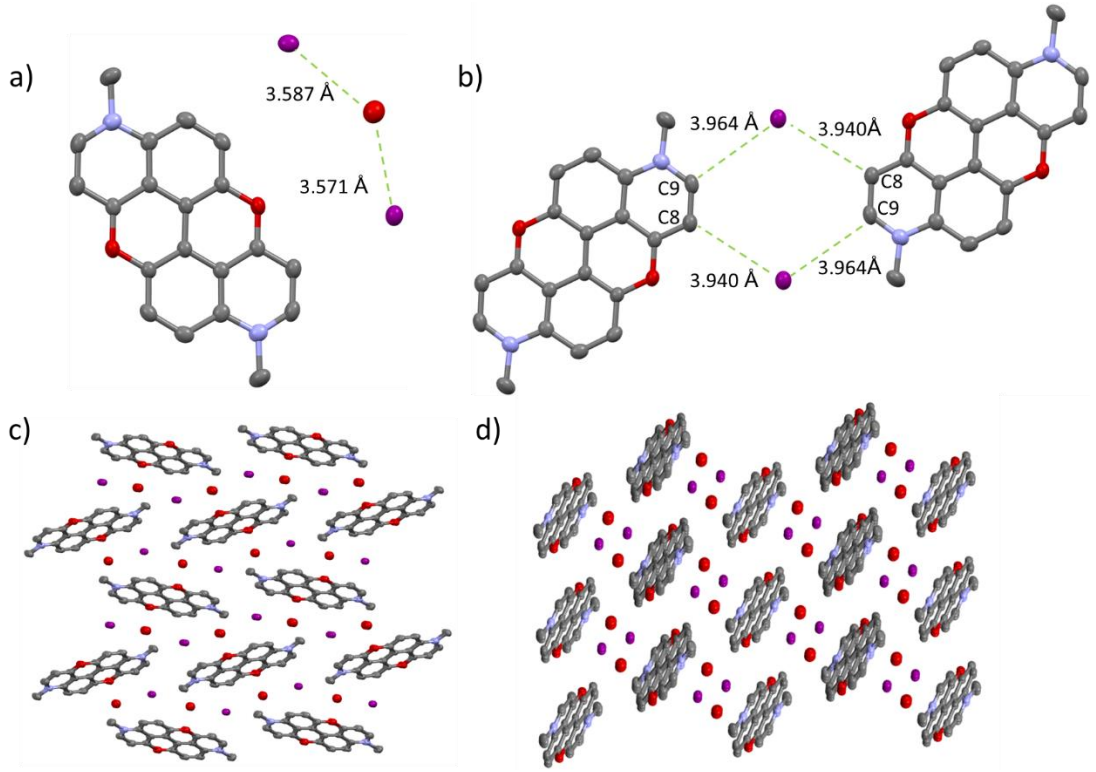

Figure 3.17. Molecule **21** crystal structure. a) $H_2O\cdots I$ interactions, b) C-H···I interactions, c) and d) crystal packing views. Nitrogen (blue), oxygen (red) and carbon (grey), iodine (purple). (Hydrogen atoms omitted for clarity).

3.6.4 diMe-4,10-diN-PXX solid-state self-assembly

Molecule **23** was crystallised by slow evaporation of CH_3CN solution, and formed triclinic crystals with spatial group P-1, R-factor 4.40%. The ORTEP graph in figure 3.18a shows the molecular structure of **23**. The distances C(5)···N(1) and C(6)···N(1) are 1.389 Å and 1.328 Å respectively and are slightly longer than the homologous bonds in molecule **6**, where C(4)···N(1) and C(8)···N(1) are 1.385 Å and 1.323 Å respectively, figure 3.18b. Furthermore, the distance C(7)···O(1) in molecule **23** is 1.368 Å, which is slightly shorter than the homologous bond in molecule **6**, where C(2)···O(1) is 1.390 Å, figures 3.18a and 3.18b.

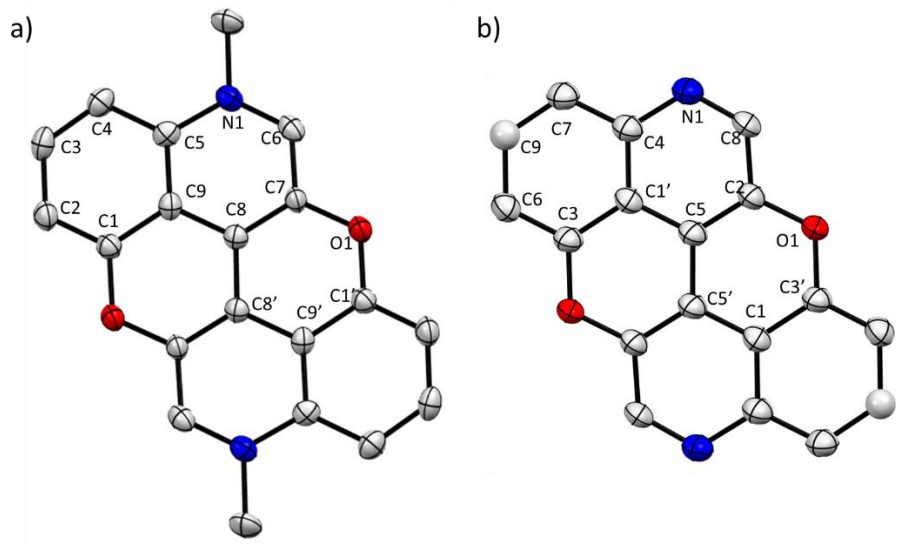

Figure 3.18. a) Molecule **22** ORTEP representation (50% probability ellipsoids) crystallisation solvent CH_3CN; b) molecule **6** ORTEP representation (50% probability ellipsoids) crystallisation solvent $CHCl_3$. Nitrogen (blue), oxygen (red) and carbon (white). (Hydrogen atoms omitted for clarity).

Molecule **23** crystallises in the lattice with two iodide ion and a molecule of H_2O. The H_2O molecules are disordered in the crystal structure and it is not possible to observe any specific interactions with other atoms, figure 3.19a. Similarly to what observed for molecule **21**, each iodide ion interacts with the hydrogen atoms in position C3 and C4 of two adjacent molecules **23**. The relative distances are 3.916 Å and 3.904 Å and therefore a square motif is formed, figure 3.19b. Quite differently from molecule **21**, molecule **23** shows a brick-wall crystal packing with two-dimensional π-π stacking, and layers distance of 3.392 Å, figure 3.19a, 3.19c and 3.19d.

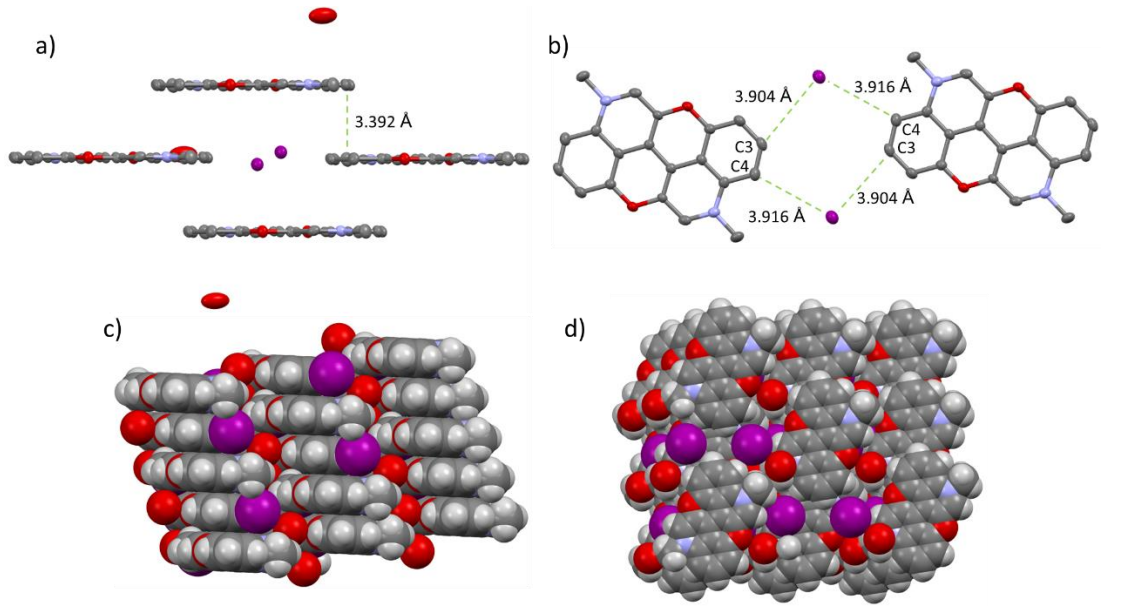

Figure 3.19. 2Me-4,10-diN-PXX **23** crystal structure. a) π-π interaction, b) C-H···I interactions, c) crystal packing side view, d) crystal packing top view. Nitrogen (blue), oxygen (red) and carbon (grey), iodine (purple). (Hydrogen atoms omitted for clarity).

3.9 Conclusion and future works

The work reported in this chapter focused on the synthesis of N-methylated NPXX **21**, **22** and **23**, figure 3.20. The methylation was achieved by treating molecules **2**, **4** and **6** with neat CH_3I. The methylation of molecule **4** gave a mixture of **22** and monomethylated **24**, which were detected by ^{1}H-NMR and cannot be separated by crystallisation. On the contrary, the methylation of molecules **2** and **6** gave right away the pure products **21** and **23** without need for purification.

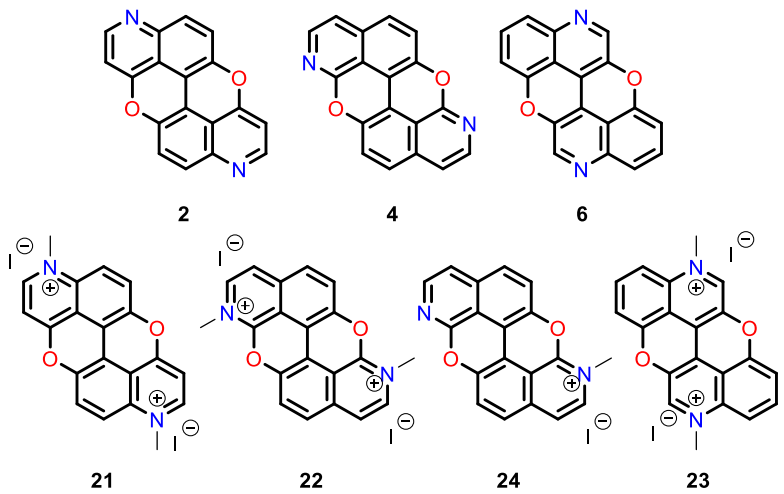

Figure 3.20. Summarising scheme of synthesised molecules **21**, **22** and **23**.

The optoelectronic properties of molecules **21** and **23** were evaluated through steady-state UV-Vis spectroscopy and cyclic voltammetry. Molecule **21** shows an irreversible reduction peak which makes it unsuitable for application as electron relay molecule (RS). On the other hand, molecule **23** has a reversible reduction peak with $E_{1/2}^{red}$ = -1.00 V which is 0.2 V higher than MV^{2+}. The absorption spectrum of molecule **23** shows a maximum at 587 nm in the orange range of the visible light. According to this experimental data, molecule **23** can photooxidise EDTA under visible light irradiation and the corresponding radical anion of molecule **23** could potentially give an electron to C nanoparticles, figure 3.21. In the light of this, molecule **23** is a promising candidate as SR in the photocatalysed H_2-evolution process using visible light, figure 3.21.

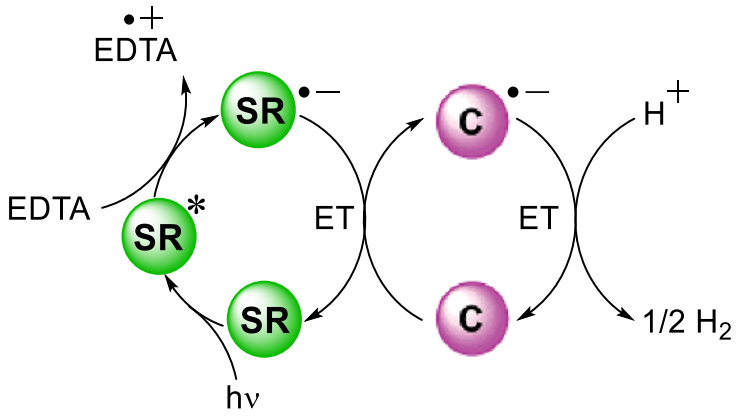

Figure 3.21. Two component photocatalytic process for H_2-evolution; SR denotes the photosensitiser and electron relay; C corresponds to a H_2-evolving catalyst, such as colloidal Pt, Pt(II), or Rh(I) complexes.

3.10 References

[1] A. A. Akhavein, D. L. Linscott, *Residue Rev.* **1968**, *23*, 97–145.

[2] T. Matsuo, T. Sakamoto, K. Takuma, K. Sakura, T. Ohsako, *J. Phys. Chem.* **1981**, *85*, 1277–1279.

[3] M. Z. Hoffman, D. R. Prasad, G. Jones, V. Malba, *J. Am. Chem. Soc.* **1983**, *105*, 6360–6362.

[4] S. J. Woo, E. Kim, H. K. Young, I. Hwang, W. L. Jae, S. Y. Kim, H. J. Kim, K. Kim, *Angew. Chem. Int. Ed.* **2004**, *44*, 87–91.

[5] H. J. Kim, J. Heo, W. S. Jeon, E. Lee, J. Kim, S. Sakamoto, K. Yamaguchi, O. Kim, *Angew. Chem. Int. Ed.* **2001**, *40*, 1526–1529.

[6] X. Gong, J. Zhou, K. J. Hartlieb, C. Miller, P. Li, O. K. Farha, J. T. Hupp, R. M. Young, M. R. Wasielewski, J. F. Stoddart, *J. Am. Chem. Soc.* **2018**, *140*, 6540–6544.

[7] X. Gong, R. M. Young, K. J. Hartlieb, C. Miller, Y. Wu, H. Xiao, P. Li, N. Hafezi, J. Zhou, L. Ma, T. Cheng,W. A. Goddard, O. K. Farha, J. T. Hupp, M. R. Wasielewski and J. F. Stoddart, *J. Am. Chem. Soc.* **2017**, *139*, 4107–4116.

[8] J. C. Barnes, M. Juríček, N. L. Strutt, M. Frasconi, S. Sampath, M. A. Giesener, P. L. McGrier, C. J. Bruns, C. L. Stern, A. A. Sarjeant, J. F. Stoddart et al., *J. Am. Chem. Soc.* **2013**, *135*, 183–192.

[9] T. Nakahira, M. Grätzel, *J. Phys. Chem.* **1984**, *88*, 4006–4010.

[10] R. J. Mortimer, A. L. Dyer, J. R. Reynolds, *Displays* **2006**, *27*, 2–18.

[11] K. W. Willman, R. W. Murray, *J. Electroanal. Chem. Interfacial Electrochem.* **1982**, *133*, 211–231.

[12] P. M. S. Monk, C. Turner, S. P. Akhtar, *Electrochim. Acta* **1999**, *44*, 4817–4826.

[13] M. Stolar, T. Baumgartner, *Phys. Chem. Chem. Phys.* **2013**, *15*, 9007–9024.

[14] R. J. Mortimer, *Annu. Rev. Mater. Res* **2011**, *41*, 241–68.

[15] T. M. Bockman, J. K. Kochi, *J. Org. Chem.* **1990**, *55*, 4127–4135.

[16] P. M. S. Monk, *Wiley: Chichester,* **1998**, *4*, 4562–4569.

[17] F. Lin, X. Zhao, *Tetrahedron* **2015**, *71*, 1124–1131.

[18] X. Zhang, E. L. Clennan, N. Arulsamy, *Org. Lett.* **2014**, *16*, 4610–4613.

[19] L. Adriaenssens, L. Severa, T. Šálová, I. Císařová, R. Pohl, D. Šaman, S. V. Rocha, N. S. Finney, L. Pospíšil, P. Slavíček, F. Tepyl, *Chem. - Eur. J.* **2009**, *15*, 1072–1076.

[20] A. N. Basuray, H. P. Jacquotderouville, K. J. Hartlieb, T. Kikuchi, N. L. Strutt, C. J. Bruns, M. W. Ambrogio, A. J. Avestro, S. T. Schneebeli, A. C. Fahrenbach, J. F. Stoddart, *Angew. Chem. Int. Ed.* **2012**, *51*, 11872–11877.

[21] S. Sampath, A. N. Basuray, K. J. Hartlieb, T. Aytun, S. I. Stupp, J. F. Stoddart, *Adv. Mater.* **2013**, *25*, 2740–2745.

[22] F. Würthner, A. Sautter, J. Schilling, *J. Org. Chem.* **2002**, *67*, 3037–3044.

[23] X. Zhang, E. L. Clennan, N. Arulsamy, R. Weber, J. Weber, *J. Org. Chem.* **2016**, *81*, 5474–5486.

[24] X. Gong, J. Zhou, K. J. Hartlieb, C. Miller, P. Li, O. K. Farha, J. T. Hupp, R. M. Young, M. R. Wasielewski, J. F. Stoddart, *J. Am. Chem. Soc.* **2018**, *140*, 6540–6544.

[25] T. Forster, *Ann. Phys.* **1946**, *437*, 55–75.

[26] G. D. Scholes, *Annu. Rev. Phys. Chem.* **2003**, *54*, 57–87.

[27] K. Kalyanasundaram, M. Grätzel, *Angew. Chem. Int. Ed.* **1979**, *18*, 701–702.

[28] J. Kiwi, E. Borgarello, E. Pelizzetti, M. Visca, M. Grätzel, *Angew. Chem. Int.*

Ed. **1980**, *19*, 646–648.

[29] J. Kiwi, M. Grätzel, *Nature* **1979**, *281*, 657–658.

[30] M. Kirch, J. -M Lehn, J. -P Sauvage, *Helv. Chim. Acta* **1979**, *62*, 1345–1384.

[31] P. Contreras Carballada, N. Mourtzis, M. Felici, S. Bonnet, R. J. M. Nolte, R. M. Williams, L. De Cola, M. C. Feiters, *Eur. J. Org. Chem.* **2012**, 6729–6736.

[32] K. Kalyanasundaram, J. Kiwi, M. Grätzel, *Helv. Chim. Acta* **1978**, *61*, 2720–2730.

[33] N. Mourtzis, P. C. Carballada, M. Felici, R. J. M. Nolte, R. M. Williams, L. De Cola, M. C. Feiters, *Phys. Chem. Chem. Phys.* **2011**, *13*, 7903–7909.

[34] L. Striepe, T. Baumgartner, *Chem. - Eur. J.* **2017**, *23*, 16924–16940.

[35] S. Asaftei, M. Ciobanu, A. M. Lepadatu, E. Song, U. Beginn, *J. Mater. Chem.* **2012**, *22*, 14426–14437.

[36] M. C. Grenier, R. W. Davis, K. L. Wilson-Henjum, J. E. LaDow, J. W. Black, K. L. Caran, K. Seifert, K. P. C. Minbiole, *Bioorg. Med. Chem. Lett.* **2012**, *22*, 4055–4058.

[37] M. R. Geraskina, A. S. Dutton, M. J. Juetten, S. A. Wood, A. H. Winter, *Angew. Chem. Int. Ed.* **2017**, *56*, 9435–9439.

[38] F. Y. Li, J. Zheng, C. H. Huang, L. P. Jin, J. Y. Zhuang, J. Q. Guo, X. S. Zhao, T. T. Liu, *J. Phys. Chem. B* **2000**, *104*, 5090–5095.

[39] W. E. Jones, M. A. Fox, *J. Phys. Chem.* **1994**, *98*, 5095–5099.

[40] S. Bhosale, A. L. Sisson, P. Talukdar, A. Fürstanberg, N. Banetji, E. Vauthey, G. Bollot, J. Mareda, C. Röger, F. Würthner, N. Sakai, S. Matile, *Science* **2006**, *313*, 84–86.

[41] L. Zhu, R. F. Khairutdinov, J. L. Cape, J. K. Hurst, *J. Am. Chem. Soc.* **2006**, *128*, 825–835.

[42] G. Desiraju, T. Steiner, *The Weak Hydrogen Bond*, **2010**.

Chapter 4

Synthesis and Characterisation of S-Doped *peri*-Xanthenoxanthene

In this chapter, the design, synthesis and photophysical properties of a novel family of S-doped peri-xanthenoxanthene are described. The first part addresses the retrosynthetic design and the synthesis of S-doped **PXX** (PTXX) derivatives. The second part describes the investigation of the optoelectronics properties through spectroscopic and cyclic voltammetry measurements. The third part concerns the solid-state characterisation of the target molecules.

The chapter is divided into six main sections: i) section 4.1: general introduction on S-doped Polycyclic Aromatic Hydrocarbons (PAHs); ii) section 4.2:0 diS-doped-**PXX** properties description and aim of the project; iii) section 4.3: retrosynthetic approach and synthesis of the S-doped **PXX** molecules; iv) section 4.4: photophysical characterisation of the synthesised molecules; v) section 4.5: electrochemical characterisation via cyclic voltammetry; vi) section 4.6: solid-state characterisation through single crystal X-ray diffraction (XRD).

The X-ray analysis presented in this chapter were performed by Nicolas Biot and Deborah Romito (Cardiff University, School of Chemistry, Cardiff).

4.1 General introduction about S-doping of Polycyclic Aromatic Hydrocarbons

Heteroarenes containing sulphur embedded in aromatic rings are among the most used semiconducting materials for applications in electronic devices such as OLEDs, OFETs and OPVs.[1–6] The introduction of sulphur atoms in PAHs scaffold: *i*) affects the optoelectronic properties by shrinking the E_g, which can also be tuned by varying the oxidation state of the sulphur atom forming charge transfer (CT) states;[7,8] *ii*) enhances the triplet excited state (T_1) population;[9,10] *iii*) directs solid-state arrangement to improve the charge mobility in organic devices.[11,12]

4.1.1 Tailoring of optoelectronic properties via S-doping and sulphur oxidation.

The E_g of PAHs can be tuned by replacing carbon atoms with heteroatoms, such as nitrogen, oxygen and sulphur. For instance, Müllen *et al*. showed how the doping of the same PAH with different heteroatoms, in this case positively charged, influences its photophysical properties, figure 4.1a.[13] The UV-vis absorption and emission spectra of N-doped DBNT tetrafluoroborate, O-doped **BNAX** bromide and S-doped **BNATX** tetrafluoroborate in CH_2Cl_2 solutions are depicted in figures 4.1b and 4.1c. The three molecules display different absorption spectra in the visible region, with the lowest energy transition for **DBNT**, **BNAX**, and **BNATX** at 512, 573 and 600 nm, respectively. Therefore, **BNATX**, which contains the sulphur atom, is the most red-shifted with respect to **DBNT** and **BNAX**. The emission spectra followed the same red shift order observed in the absorption spectra, with emissions at 531 nm for **DBNT**, 593 nm for **BNAX** and 643 nm for **BNATX**, respectively. This demonstrates the possibility of fine-tuning the optoelectronic properties of PAHs through the incorporation of different heteroatoms without changing the aromatic framework, and, moreover that the sulphur containing molecule has the smallest E_g.

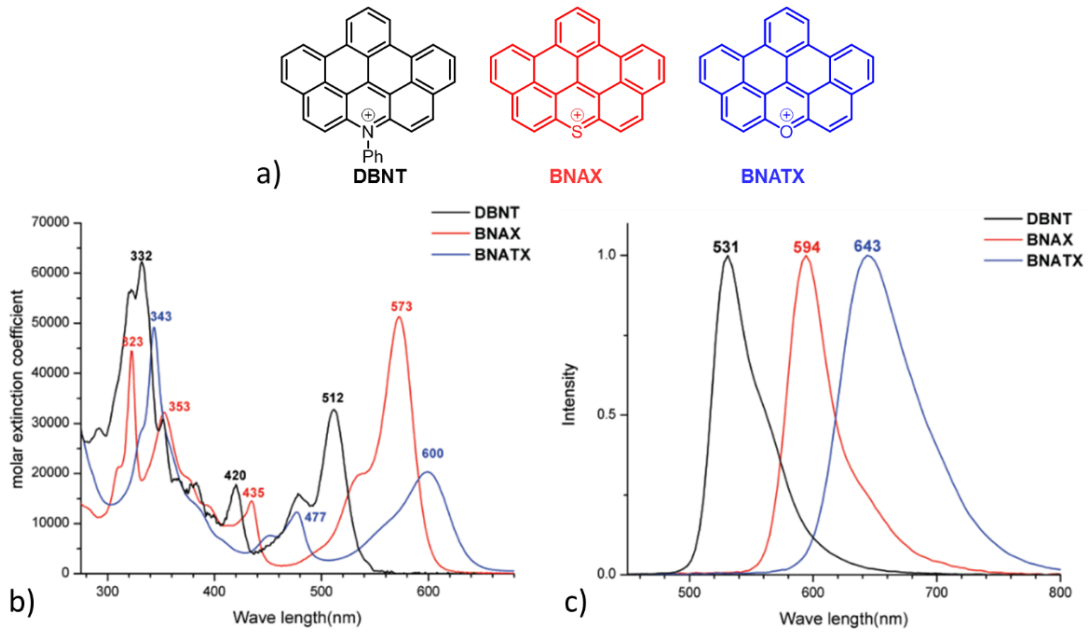

Figure 4.1. a) Molecular structure of **DBNT**, **BNAX** and **BNATX**; b) UV-vis absorption spectra in CH_2Cl_2 measured at 20 °C. c) Fluorescence spectra in CH_2Cl_2 measured at 20 °C (λ_{exc} = 350 nm)

Chi *et al.* investigated the effect introduction of sulphur atoms in pentacene, hexacene and heptacene.[14] The quinoidal dithiaacenes exhibit better chemical stability than analogue acenes, figure 4.2. This class of molecules has 4n π-electrons, two more π-electrons in comparison to their analogue linear acenes. Thus, the 2-electrons oxidation of neutral dithiaacenes leads to the equivalent isoelectronic structures of acenes.[15,16]

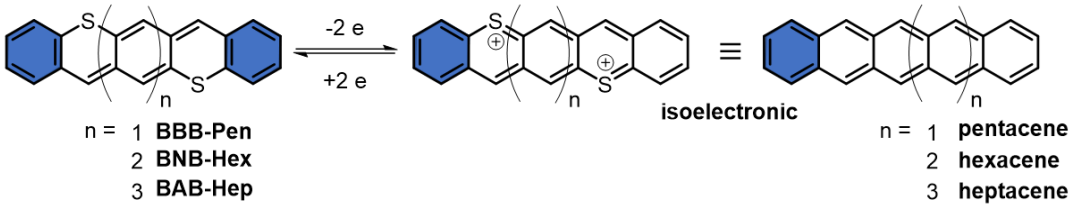

Figure 4.2. Structures of the bis(benzothia)quinodimethanes, their dications, and their acene analogues. The aromatic sextet ring is shaded in blue.

The optical properties of S-doped acenes can be modified through chemical oxidation to the corresponding radical cations and dications. The absorption spectra of **BBB-Pen** and **BNB-Hex** show an absorption band at 555 nm and 620 nm, respectively, figures 4.3a and 4.3b. **BAB-Hep** also displays an intense absorption at 662 nm with a shoulder peak at 716 nm. The radical cations show a lowest energy transition in the NIR region, with a maximum at 1092 nm for **BBB-PenC**$^{\cdot+}$,1381 nm for **BNB-HexC**$^{\cdot+}$ and 1620 nm for **BAB-HepC**$^{\cdot+}$, figures 4.3a, 4.3b and 4.3c. The dications absorption spectra are blue-shifted with respect to the respective radical cations, with an absorption maximum at 780 nm for **BBB-Pen**$^{2+}$, 945 nm for **BNB-Hex**$^{2+}$ and 1246 nm for **BAB-Hep**$^{2+}$, figures 4.3a, 4.3b and 4.3c.

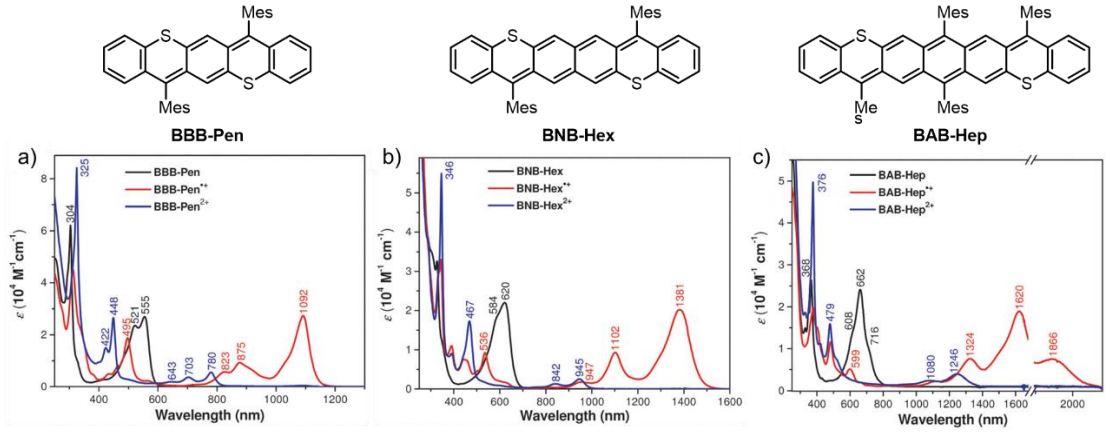

Figure 4.3. UV-Vis-NIR absorption spectra of the neutral (N), cationic radical (R), and dicationic (D) states of a) **BBB-Pen**, b) **BNB-Hex**, and c) **BAB-Hep** in CH_2Cl_2.

In addition, the optoelectronic properties of a S-doped chromophore can also be tuned by varying the oxidation state of the sulphur atom from sulphide to sulphoxide and sulphone. The introduction of an electron withdrawing substituent (A), such as sulphoxide and sulphone, in electron rich molecules (D) allows the formation of charge transfer states (CT). In most D−A systems the HOMO is localized on the electron rich moiety while the LUMO is localized on the electron deficient moiety.[8] The different spatial delocalisation of HOMO and LUMO in D−A molecules leads to the formation of polar excited states, so called CT excited states. Wolf *et al.* demonstrated that it is possible to form CT excited states in molecules containing a sulphur atom, by changing the oxidation state of the sulphur from sulphide to sulphoxide and sulphone.[8] They designed and synthesised a family of molecules containing an anthracene moiety as electron donor connected to a dibenzothiophene, where the sulphur atom can be oxidised to sulphoxide and sulphone, figures 4.4a and 4.4b.

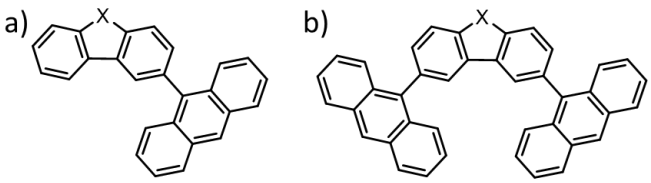

Figure 4.4. a) Mono and b) bis anthracene functionalised dibenzothiophene and sulphoxide and sulphone homologues.

The absorption spectra of $1SO_n$ and $2SO_n$ (n = 0, 1, 2) show the same outline than the anthracene spectrum with a 9 nm bathochromic shift compared to unsubstituted anthracene, figure 4.5a and 4.5b. Interestingly, the differences observed in the absorption spectra for $1SO_n$ and $2SO_n$ is a small broadening of the absorption bands as a function of the oxidation state of the sulphur, figure 4.5a and 4.5b (black arrows).

The emission spectra of $1SO_n$ and $2SO_n$ display substantially different behaviours. The well-defined vibronic transitions present in the absorbance spectra are not observed in the emission spectra, figure 4.5c, 4.5d and 4.5e. By increasing the solvent polarity, from cyclohexane to CH_2Cl_2 and acetonitrile, the sulphoxides (SO) and sulphones (SO_2) show broadening of the emission bands and all the emission spectra are red-shifted.

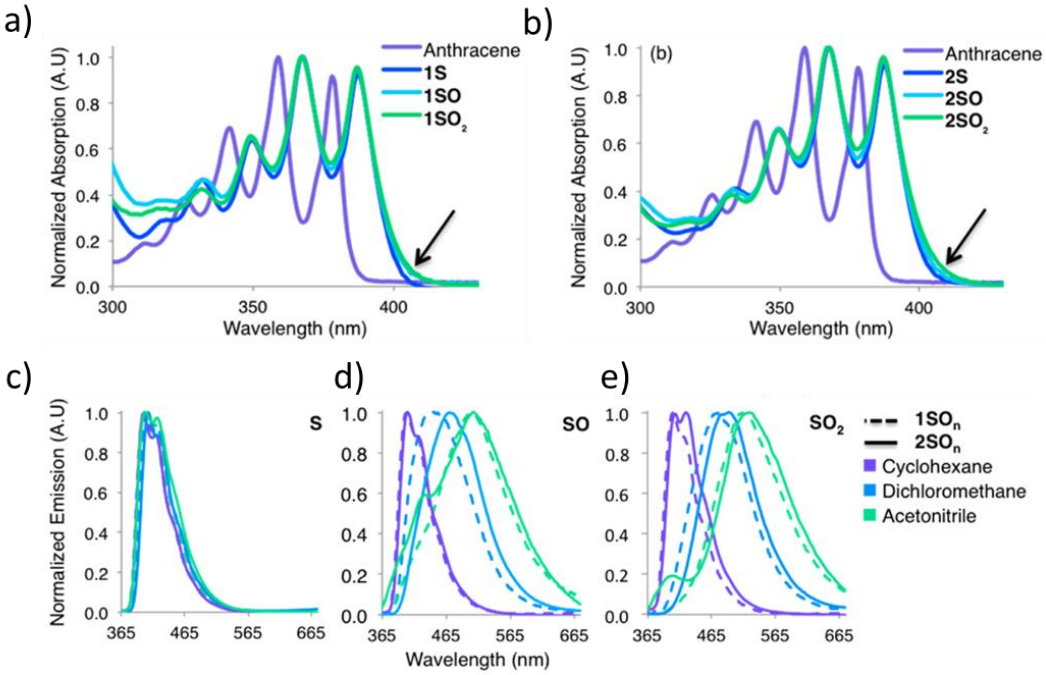

Figure 4.5. Normalized absorption spectra for $1SO_n$ a) and $2SO_n$ b) compared to unsubstituted anthracene; c) normalized photoluminescence spectra for the sulfides c), sulfoxides d), and sulfones e) of $1SO_n$ (dashed line) and $2SO_n$ (solid line) in solvents of increasing polarity (cyclohexane, dichloromethane, and acetonitrile).

The solvatochromism in the emission spectra of **1SO**, **$1SO_2$**, **2SO**, and **$2SO_2$** is the effect of a polar emitting excited state, likely due to the formation of an intramolecular charge transfer (CT) state in the excited state.[17] The authors analysed the solvatochromic effect using the Lippert−Mataga relationship (see section 4.4.1), figure 4.6a and 4.6b.[18,19] This theory relates the Stokes shift ($\Delta\nu$) to the solvent polarizability (Δf). The sulphoxides and sulphones display excellent linear relationships, ($R^2 \geq 0.95$) while the sulphides 1S and 2S do not show dependence on solvent polarity. These experiments suggest that the CT contribution in the excited state can be controlled by changing the oxidation state of the sulphur atom.

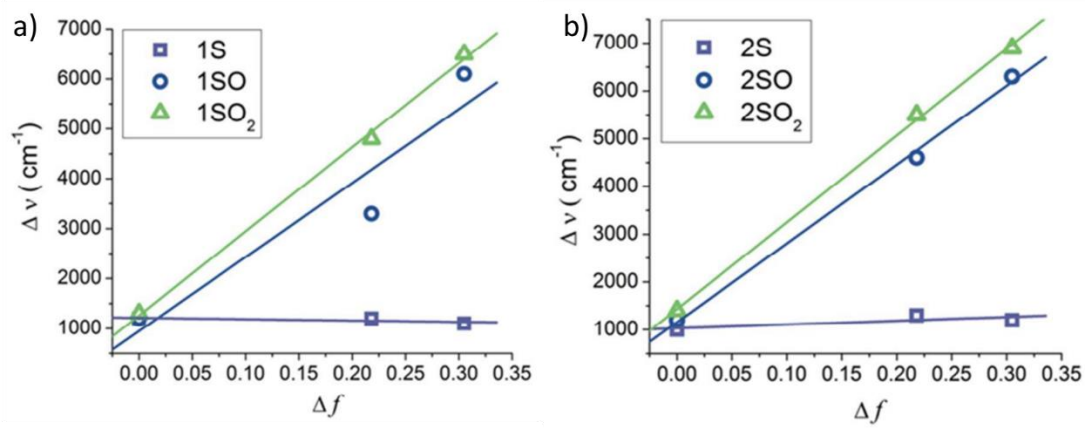

Figure 4.6. Plot of Stokes shift (Δv) vs. solvent polarizability (Δf) for $1SO_n$ (a) and $2SO_n$ (b). Oxidized molecules 1SO (R^2 = 0.95), $1SO_2$ (R^2 = 0.99), 2SO (R^2 = 0.99), and $2SO_2$ (R^2 = 0.99) exhibit excellent linear relationships, however, both 1S ($R^2 \simeq 0$) and 2S (R^2 = 0.82) deviate significantly from linearity.

Moreover, the introduction of heavy chalcogen atoms in chromophores increases the intersystem crossing (*ISC*) yield by promoting triplet exited-state population (T_1).[9,20] The decay from T_1 can follow two different pathways: *non*-radiative and radiative emitting photons as phosphorescence.[21] Intense research is currently directed towards phosphorescent materials because of their application in flat-panel displays as phosphorescent organic light-emitting diodes (PHOLEDs).[22–24] In organic-based LED devices, holes and electrons are injected from electrodes and recombine in the photoactive material to form luminescent excitons, figure 4.7a.[25] The excitons have uncorrelated spin states; thus, they can exist as 25% singlet and 75% triplet statistical distribution, figure 4.7b. [26]

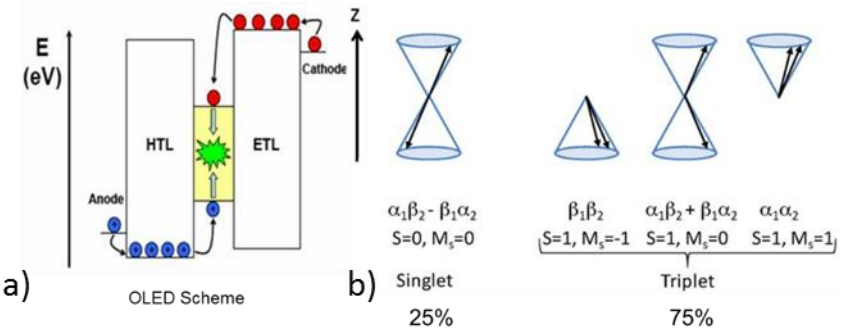

Figure 4.7. a) Energy diagram for OLED diagram; b) Vector diagram illustrating the relative orientations of the two electron spins for the singlet and the triplet state. The two spins, indicated by arrows, precess around a local magnetic field in the z-direction. The anti-parallel and 180° out of phase configuration correspond to the situation in a singlet state, while the other three in phase configurations yield a triplet state.

In fluorescent materials, the only permitted radiative decay is $S_1 \rightarrow S_0$, thus the energy stored in the 75% of the excitons formed in T_1 is lost. Therefore, the synthesis of phosphorescent organic molecules plays an important role for the development of highly efficient OLED devices. In the Bonifazi group, the chalcogen atoms are being thoroughly investigated as doping atoms for PAHs to enhance their triplet population

and programming the solid-state self-assembly.[9,27,28] A representative example is the systematic study of the phosphorescence emission as a function of the chalcogen atom in the benzochalcogenazoles, figure 4.8. The key photophysical data are summarised in table 4.1.

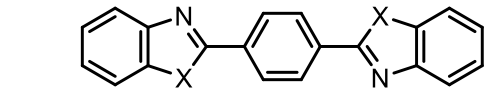

X = O, **1$_O$** X = Se, **1$_{Se}$**

X = S, **1$_S$** X = Te, **1$_{Te}$**

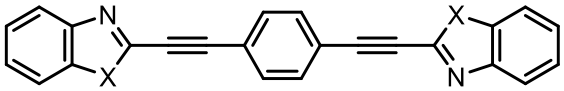

X = O, **2$_O$** X = Se, **2$_{Se}$**

X = S, **2$_S$** X = Te, **2$_{Te}$**

Figure 4.8. Chemical structures of chalcogen-doped luminescent molecules rods **1$_X$** and **2$_X$**.

All compounds demonstrated to be emissive in CH_2Cl_2 solution at room temperature. The molecules containing oxygen, sulphur and selenium show fluorescence emission with λ_{max} in the range of 409-425 nm. As predictable, increasing the size of the chalcogen, the fluorescence quantum yield decreases because of the *ISC* process induced by the presence of the heavy atom.[20] The phosphorescence emission is observed for the sulphur, selenium and tellurium doped molecules and the lifetime decreases drastically from S-doped to Se-doped and Te-doped molecules.

Table 4.1. Emission parameters of **1$_X$** and **2$_X$** at r.t..

	Fluorescence			Phosphorescence	
	λ_{max} (nm)	Φ	τ (ns)	λ_{max} (nm)	τ (μs)
1$_O$	409	0.71	0.99	n.d.	-
1$_S$	425	0.21	0.29	602	336.4
1$_{Se}$	417	< 0.2	< 0.2	620	49.3
1$_{Te}$	n.d.	-	-	640	9.7
2$_O$	397	0.75	0.78	n.d.	-
2$_S$	408	0.42	0.39	n.d.	-
2$_{Se}$	420	< 0.2	< 0.2	617	49.9
2$_{Te}$	n.d.	-	-	639	3.9

n.d. not detected

This study demonstrated that the introduction of heavy chalcogen atoms in chromophore backbones can increase the T_1 population and it is possible to observe the phosphorescence phenomena at room temperature for organic molecules.

4.1.2 S-doped induced PAH solid-state self-assembly

The introduction of a sulphur atom into PAH skeletons induces also a lamellar solid-state packing arrangement. It improves the face-to-face interaction between the π-cloud which is expected to enhance the charge mobility inside the material.[29] Pei *et al*. presented a crystal engineering strategy to direct the solid-state organization of S-doped perylenes, enforcing face-to-face π-stacking with channels for hole transport.[11] The perylene bay regions have been bridged by sulphur atoms achieving dithiophene-like structure, figure 4.9a. As expected, the supramolecular self-assembly is guided by S···S short contacts (3.51 Å) between adjacent columns, figure 4.9b. The solid-state dithioperylene arrangement exhibits typical p-channel FET properties with charge-mobility 2.13 $cm^2V^{-1}s^{-1}$, which is three times higher than perylo[1,12- b,c,d]thiophene (PET), 0.8 $cm^2V^{-1}s^{-1}$.[12]

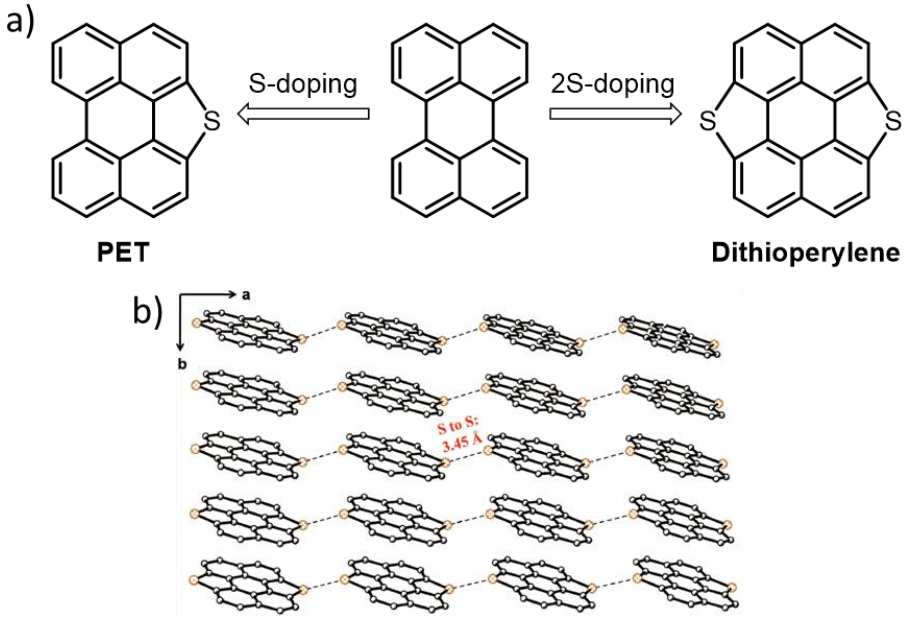

Figure 4.9. Packing arrangement of dithioperylene illustrating the ideal π-π molecular stacking along the b axis, and a compressed highly ordered packing mode induced by marked intercolumnar S···S interactions within the a-b plane (hydrogen atoms were omitted for clarity)

4.2 Aim of the project: S-doped *peri*-Xanthenoxanthene

The di-sulphur-doped **PXX** (**PTXTX**) synthesis was reported the first time by Anthony *et al.* in a Samsung patent.[30] Recently in the Bonifazi Group, **PTXTX** and its derivatives properties have been thoroughly photophysically investigated and a full analysis of the data will be reported in an article. The UV-Vis absorption and emission spectra of **PTXTX** are ca. 60 nm red-shifted with respect to **PXX**, figure 4.10. **PTXTX** has a fluorescence quantum yield of 2%, which is lower than **PXX** (60%).[31] Moreover, **PTXTX** shows phosphorescence emission at 77 K with a maximum at 717 nm.

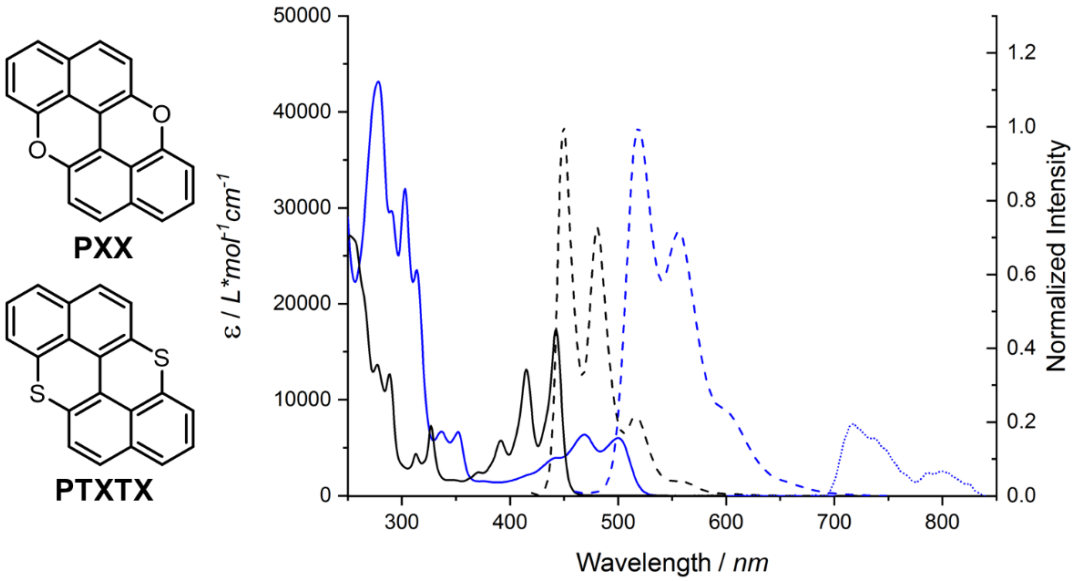

Figure 4.10. UV-Vis spectra of PTXTX

The aim of this work is to modify the molecular structure of **PXX** by replacing one oxygen atom with a sulphur atom in order to tune its optoelectronic properties, increase the T_1 population and control its solid-state organisation. Considering the structure of the already cited **PXX**, the target molecule can be rationalised as mono S-doping of the **PXX**, scheme 4.1.

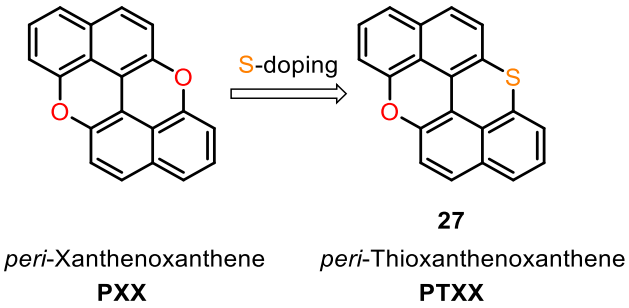

Scheme 4.1. Doping scheme for molecule **27**.

The introduction of a sulphur atom in the **PXX** periphery can enhance the *ISC* rate favouring the population of the T_1 and the presence of one oxygen atom will keep the structural rigidity avoiding *non*-radiative decay pathways. Moreover, target molecule **27** can be oxidised to sulphoxide **28** and sulphone **29** that could induce the formation of

CT excited states, scheme 4.2. We expecte that the presence of CT states will affect the absorption and emission spectra by showing a bathochromic shift.

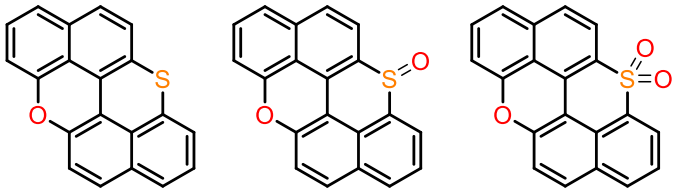

27 PTXX **28** PTXX-SO **29** PTXX-SO_2

Scheme 4.2. Targeted molecules **27**, **28** and **29**.

4.3 Synthesis of mono S-doped *peri*-Xanthenoxanthene

4.3.1 Retrosynthetic approach

The target molecules **27**, **28** and **29** can be ideally converted into one another by using redox processes, scheme 4.3. From the synthetic point of view, the precise controls of the redox reaction is very difficult, however the oxidation of molecule **27** to **28** and **27** to **29** is possible by using well known literature protocols.[32–34] The structural asymmetry of PTXX **27** forces us to think about a retrosynthetic pathway different from that adopted for the syntheses of **PXX** and **PTXTX**. Three different retrosynthetic routes (**a**, **b** and **c** in scheme 4.3), which differ in the disconnection order of the C_{sp}^2-O and C_{sp}^2-S bonds, were contemplated to address the synthesis of molecule **27**. The retrosynthetic path **a** starts with a C_{sp}^2-S disconnection, which would have as synthetic equivalent methyl sulphoxide **30**. It could undergo S-cyclisation in strong acid conditions.[35] The following step is the same homolytic disconnection of C_{sp}^2-O that has already been discussed in *chapter 2,* and the synthetic equivalent is a simple hydroxyl containing moiety **31** that can be cyclised via Cu-mediated oxidation.[36,37] The last retrosynthetic step concerns the sulphoxide moiety which can be obtained through functional group interconversion (FGI) from the corresponding thioether derivative **32**. The retrosynthetic route **b** starts with the C_{sp}^2-O disconnection that leads to synthetic equivalent **33** followed by the FGI of the hydroxyl moiety to the methoxy group which takes us back to **34**, scheme 4.3. The C_{sp}^2-S disconnection leads to the synthetic equivalent **35** that can be cyclised through electrophilic aromatic substitution promoted by strong acids.[35] The protection of the hydroxyl moiety of molecule **33** with a methyl group is a trivial choice in order to protect the oxygen from the electrophilic aromatic substitution and favour the C_{sp}^2-S bond formation. Molecule **35** can be obtained via methylation and oxidation of molecule **32**. The main drawback of the synthetic route b is the C_{sp}^2-O bond formation through oxidative protocols as the sulphide moiety in

molecule **28** can be oxidised non-selectively giving decomposition products. The synthetic pathway **c** allows to overcome the drawback of the route **b**. It envisages molecules **29** as target molecule that can be converted into molecule **27** and **28** through redox processes, as described before. The C_{sp}^2-O bond of molecule **23** can be disconnected leading to synthetic equivalent **31** that can be converted into molecule **32** via FGI of the hydroxyl moiety to methoxyl moiety. The C_{sp}^2-O cyclisation via Cu-mediated oxidation on molecule **37** might avoid degradation products that can be observed in the red route from the oxidation of molecule **33**. Molecule **38** can be achieved by FGI of the sulphide bridge to sulphone of molecule **34**.

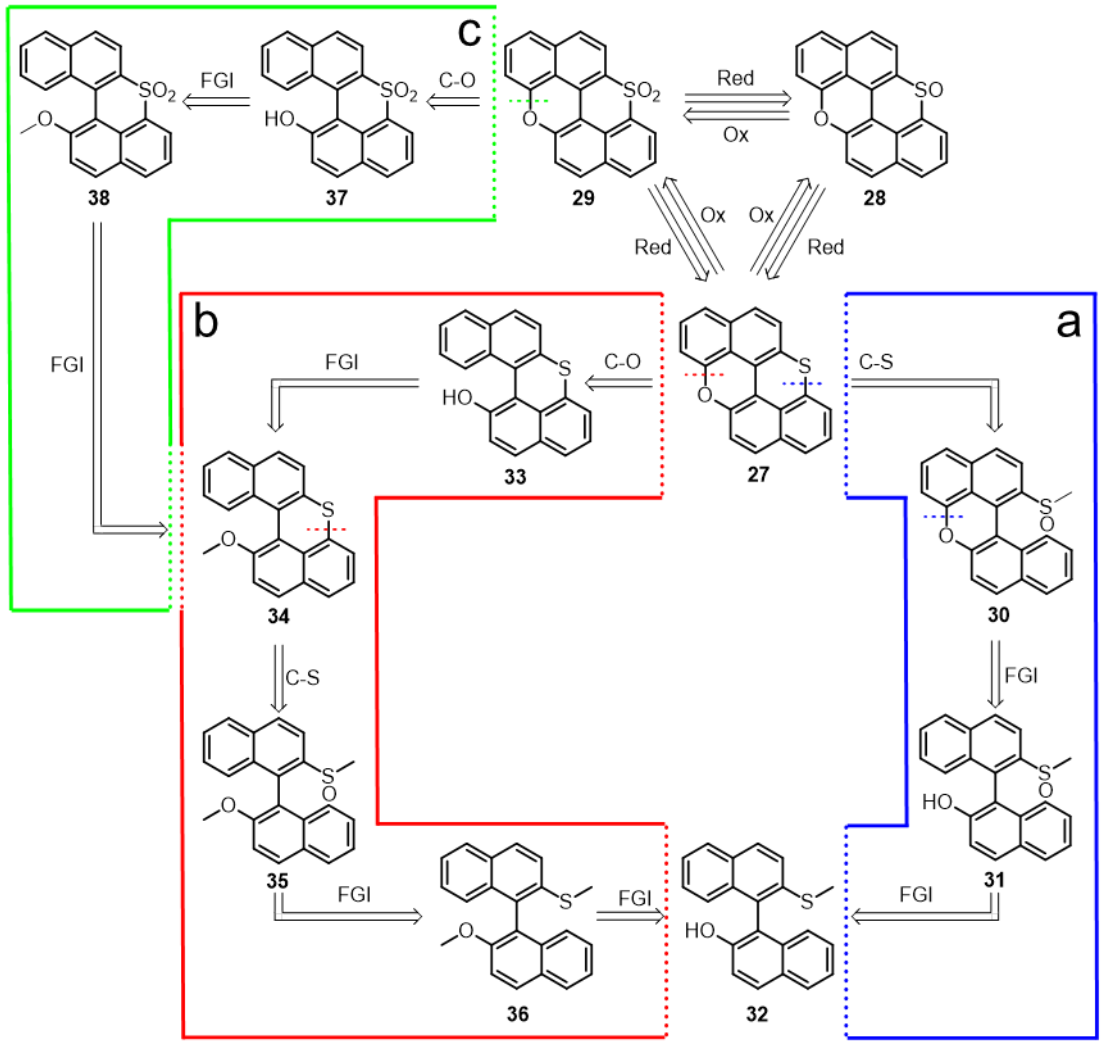

Scheme 4.3. Retrosynthetic schemes for the synthesis of **27**, **28** and **29**.

The three synthetic pathways have in common the same synthetic thiomethyl-hydroxyl binaphthyl intermediate **32** which can be obtained by heterolytic C_{sp}^2-C_{sp}^2 bond formation between the two naphthyl rings, scheme 4.4. Two different retrosynthetic pathways were considered. The first route involves the possibility of using the well-known Pd-mediated cross couplings, scheme 4.4a.[38–40] The second synthetic route

envisages a metal-free approach for C_{sp}^2-H/ C_{sp}^2-H coupling between phenols and aryl sulfoxides through interrupted Pummerer reaction, scheme 4.4b.[41] The latter synthetic approach was chosen for the preparation of molecule **32** because it avoids both the halogenation and metalation of the substrates needed for the Pd-mediated cross-coupling and represents an useful shortcut for the synthesis of the target molecules.

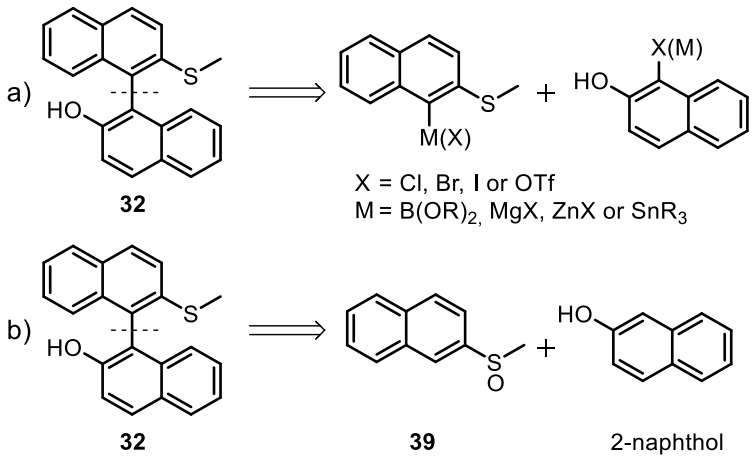

Scheme 4.4. a) Retrosynthetic scheme for the synthesis of molecule **26** through Pd-mediated cross-coupling; b) interrupted Pummerer reaction.

Naphthyl-sulfoxide derivative **33** and 2-naphthol are the two main building blocks for the synthesis of intermediate **26**. While 2-naphthol is commercially available, **33** can be easily prepared from 2-thionaphthol by methylation followed by oxidation, scheme 4.5.

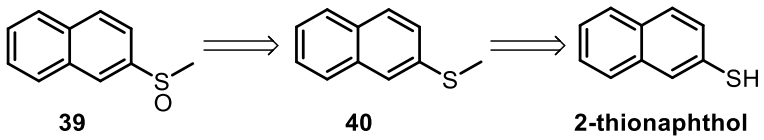

Scheme 4.5. Retrosynthetic scheme for the synthesis of molecule **33** from 2-thionaphthol.

4.3.2 Metal-free C-C formation via interrupted Pummerer reaction

The Pummerer reaction is used for nucleophilic α-functionalisation of alkyl-sulphoxides mediated by a Lewis acid (LA) and a Lewis base (LB), scheme 4.6a.[42] The reaction involves three steps: 1) sulphoxide activation with LA forming the sulphonium ion, 2) α-hydrogen deprotonation by a LB and concerted oxygen-LA elimination to yield the reactive thionium cation species, and 3) α-nucleophilic attack of a generic nucleophile (Nu). The reactivity of the sulphoxide is strictly related to the nature of the side chain. For instance, alkenyl sulphoxides under Pummerer-type activation lead to the formation of different products enabling also the γ-functionalisation and the bis-functionalisation on the α and β carbon, schemes 4.6b and 4.6c respectively.[43–45] In the interrupted Pummerer reaction, the sulphoxides is

functionalised with aryl groups and, due to the lack of electrophilic carbon, the Nu can attack only the positively charged sulphur, scheme 4.6d.

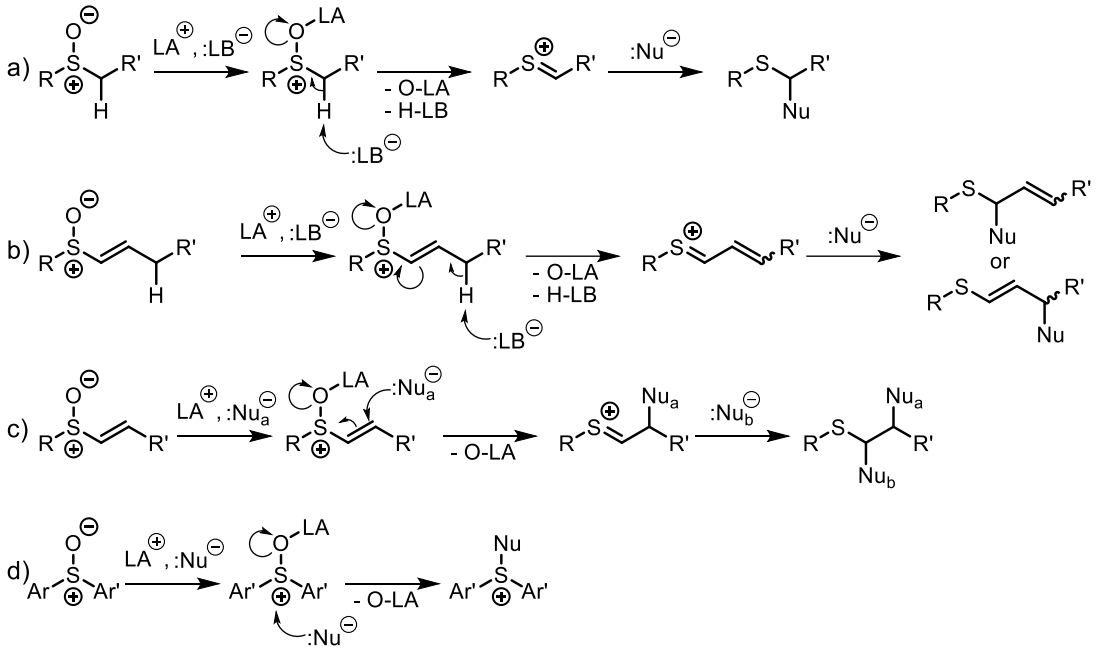

Scheme 4.6. a) Original Pummerer reaction; b) and c) Pummerer reactions with alkenyl-sulphoxides; d) interrupted Pummerer reaction.

Osuka *et al.* developed the metal-free regiocontrolled dehydrogenative C_{sp^2}−H/C_{sp^2}−H cross-coupling of aryl sulfoxides with phenols by exploiting the interrupted Pummerer reaction, scheme 4.7.[41] Dehydrogenative C_{sp^2}−H/C_{sp^2}−H coupling are formally a redox process where two C_{sp^2}−H bonds are oxidised by an oxidant to form a C_{sp^2}-C_{sp^2} bond. In the interrupted Pummerer reaction, the sulphoxide works as oxidant allowing the C_{sp^2}-C_{sp^2} bond formation without external oxidant. A plausible mechanism envisages the sulfoxide activation with trifluoroacetic anhydride (TFAA) and nucleophilic attack of the phenol oxygen on the resulting sulfonium. The C_{sp^2}-C_{sp^2} bond formation is achieved by sulphonium-accelerated [3,3]-sigmatropic rearrangement with concomitant loss of the aromaticity of the aromatic rings, and the last step terminates with rearomatisation of the aryl rings, scheme 4.7. Therefore, the interrupted Pummerer reaction is very interesting for C_{sp^2}-C_{sp^2} bond formation due to its regioselectivity and metal-free conditions.

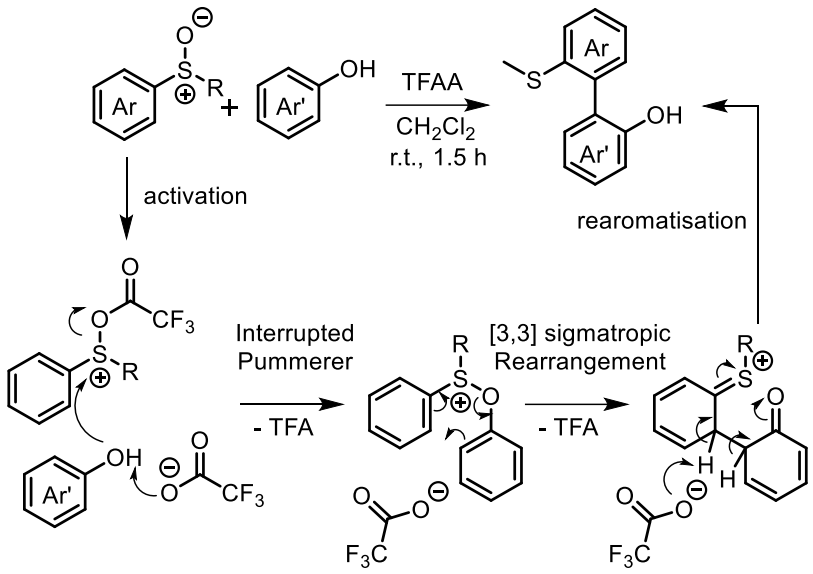

Scheme 4.7. Mechanism of dehydrogenative biaryl synthesis.

4.3.3 *peri*-Thioxanthenoxanthene synthesis: synthetic routes a and b

In agreement with the discussed retrosynthetic pathways, the methylation of 2-thiol naphthalene was achieved with methyl iodide in basic conditions in degassed DMF to give product **40** as white a solid in 97% yield. The use of degassed solvent is needed to avoid the oxidation of the starting material to the relative disulphide, scheme 4.8. Thioether **40** was oxidised with $NaIO_4$ in acetone/H_2O 1:1 mixture at 55 °C for 16 hours to respective sulphoxide **39**. Molecule **32** was prepared via interrupted Pummerer reaction by reacting 2-naphthol and sulphoxide derivative **39** with trifluoroacetic anhydride (TFAA) in dichloromethane at room temperature. Product **32** was obtained as colourless oil in 70% yield.

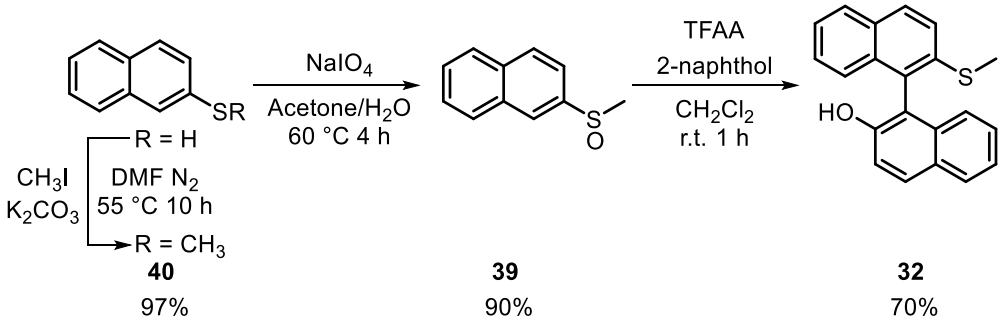

Scheme 4.8. Synthetic protocol for the preparation of molecule **32**.

It has been decided to follow the synthetic route **a** because it requires less steps than the pathway **b** to reach target molecule **27**, scheme 4.9. Thioether **32** was oxidised to sulphoxide derivative **31** with $NaIO_4$ in acetone/water mixture at 60 °C for 4 hours. O-cyclisation of molecule **31** to form the pyranyl-ring was attempted using the protocol developed by Kamei *et al*.[37] Unexpectedly, desired product **40** was not formed and only degradation of the starting material was observed.

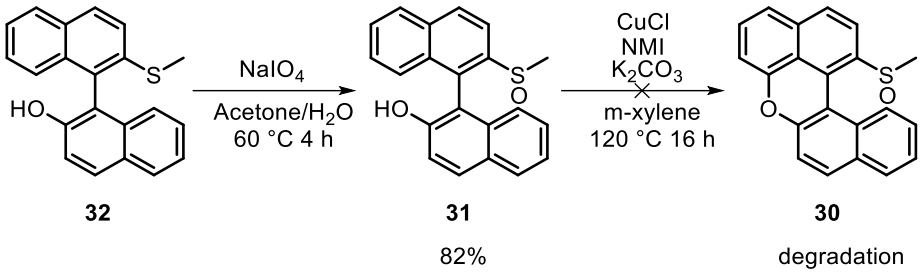

Scheme 4.9. Synthetic protocol for the preparation of molecule **30**.

In the light of these results, it was decided to attempt the synthetic pathway **b**, scheme 4.10. The hydroxyl moiety of molecule **32** was methylated with methyl iodide and K_2CO_3 in dry acetone. Product **36** was oxidised to sulphoxide using the already showed protocol with $NaIO_4$ as oxidant at 60 °C for 4 hours. Sulphoxide derivative **35** was then intramolecularly cyclised forming a thioether bridge using the protocol developed by Müllen *et al*.[35] Compound **35** was stirred for 16 hours in triflic acid at room temperature and then boiled in H_2O/pyridine 8:2 mixture for 1 hour yielding desired compound **34** in 3% yield as a yellow solid. Methoxy helicene **34** was air and light sensitive in chlorinated solvents.

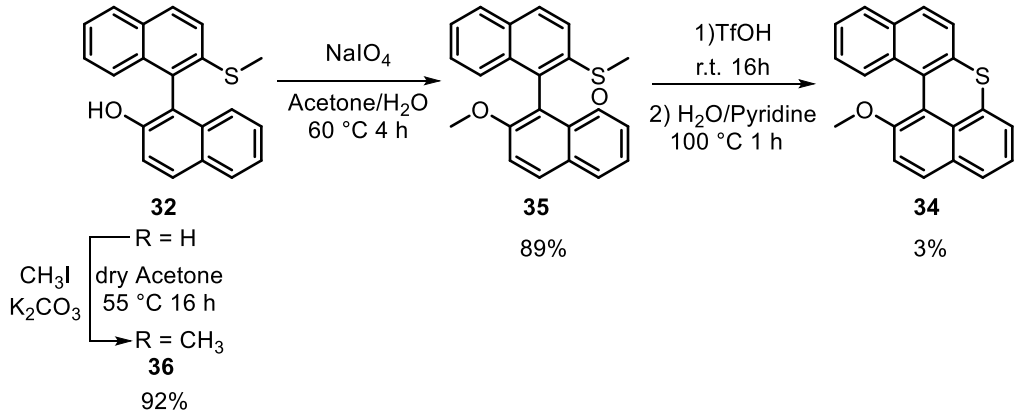

Scheme 4.10. Synthetic protocol for the preparation of molecule **34**.

Compound **34** was crystallised by slow evaporation of a CH_2Cl_2 solution and analysed by XRD to confirm the molecular structure. The ORTEP scheme shows the molecular structure of **34** which has a helicoidal shape due to the steric repulsion between the methoxy group and the naphthalene moiety, figure 4.11a. The two helicoidal enantiomers P and M crystallise together without displaying any stereospecificity, figures 4.11b and 4.11c.

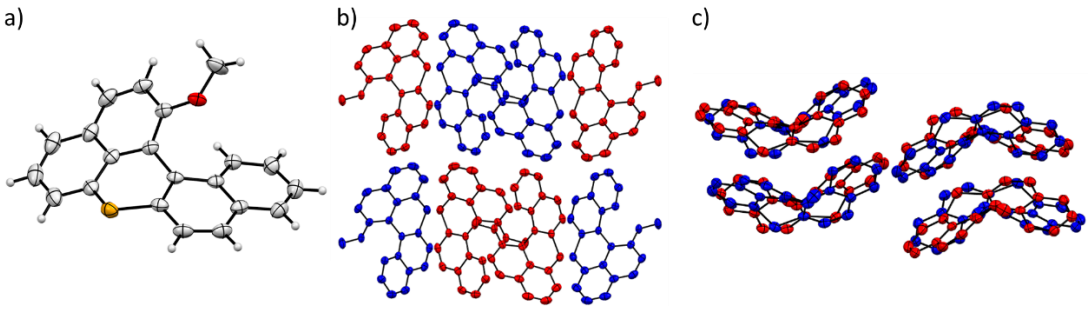

Figure 4.11. Space Group Pbca, Rf = 3.59 %. a) ORTEP representation of molecule **34** (50% probability ellipsoids), solvent for crystallisation: CH_2Cl_2; b) unit cell view along b axis; c) unit cell view along an axis. P enantiomer in red and M enantiomer in blue. Sulphur (orange), oxygen (red) and carbon (grey).

Due to the low yield of the S-cyclisation step, the optimisation of the reaction conditions was attempted. The investigation was carried out by modifying reagents and reaction time, stirring the reaction mixture at room temperature for the first step and at 100 °C for the second step, scheme 4.11. From the table 4.2, it is possible to observe that the best yield was obtained for the entry 7 with reaction times of 1 hour for the first step and 24 hours for the second step. It means that the C_{sp}^2-S bond formation in the first step is faster than the demethylation in the second step. Moreover, the presence of H_2O in the second step reduces the reaction yield. Therefore, the best synthetic protocol envisages the C_{sp}^2-S bond formation treating the sulphoxide **35** with TfOH at room temperature for 1 hour followed by the demethylation with dry pyridine at 100 °C for 24 hours.

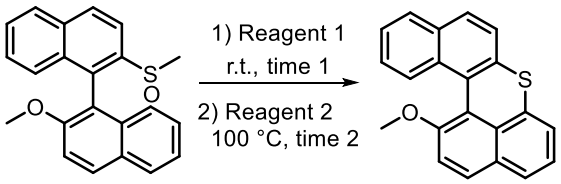

35 **34**

Scheme 4.11. Optimisation scheme for the preparation of molecule **34**.

Table 4.2. Optimisation table for the preparation of molecule **34**.

Entry	1)Reagent 1	2)Reagent 2	Time 1) (h)	Time 2) (h)	**34** Yield (%)
1	TfOH	H_2O/Py	16	1	3
2	TfOH/Tf_2O	H_2O/Py	16	1	6
3	TfOH	Py	16	1	13
4	TfOH/Tf_2O	Py	16	1	0
5	TfOH	Py	1	1	6
6	TfOH	Py	1	5	15
7	TfOH	Py	1	24	35
9	PCl_3	Py	1	24	0

Following the retrosynthetic route **b**, the obtained methoxyl helicene **34** was demethylated with 1-dedecanethiol and NaOH in NMP at 130 °C for 1 hour giving unstable intermediate **33**. The O-cyclisation was performed under mild conditions to selectively form the C_{sp}^2-O bond avoiding undesired over oxidation of the sulphur moiety, scheme 4.12. The first attempt was performed using $NOSbF_6$ in CH_3CN at room temperature under inert atmosphere, nevertheless only degradation was observed.[46] In a second attempt, 2,3-dichloro-5,6-dicyano-1,4-benzoquinone (DDQ) was used as oxidant and, again, only degradation was observed.

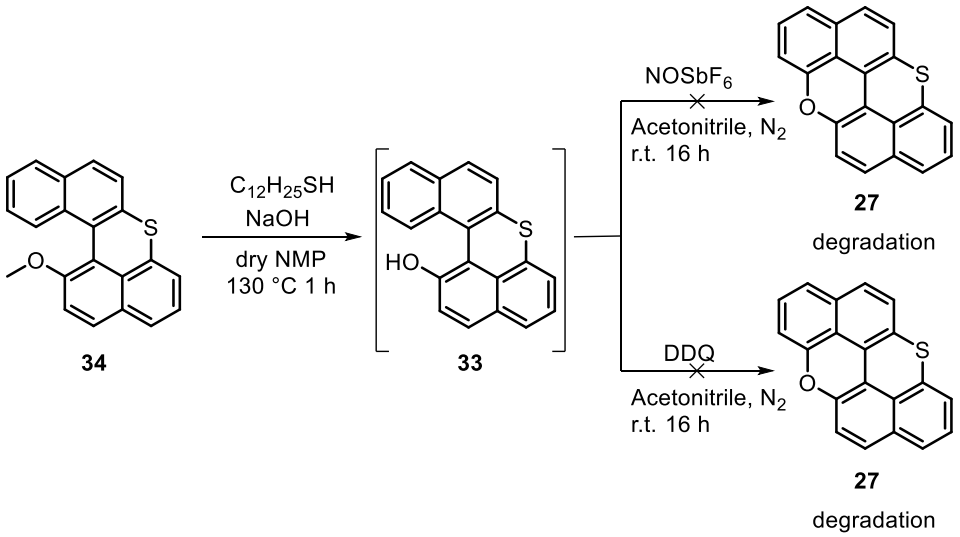

Scheme 4.12. Reaction schemes for the preparation of molecule **27**.

The high reactivity of molecules **33,** can be explained considering the crystal structure of **34**. From the crystallographic characterisation, molecule **34** shows a torsion angle of 35° between the two naphthyl rings, figure 4.12b. Moreover, the thiopyranyl-ring has a half-chair-like conformation with the sulphur atom out of the plane with an angle of 22°, figure 4.12c. The ring strain in the thiopyran cycle makes the sulphur moiety high reactive towards oxidation. Therefore, the formation of the C_{sp}^2-O bond through oxidation is unfavoured with respect to the unspecific oxidation of the sulphur atom, and it makes this synthetic pathway unsuitable for the synthesis of molecule **27**.

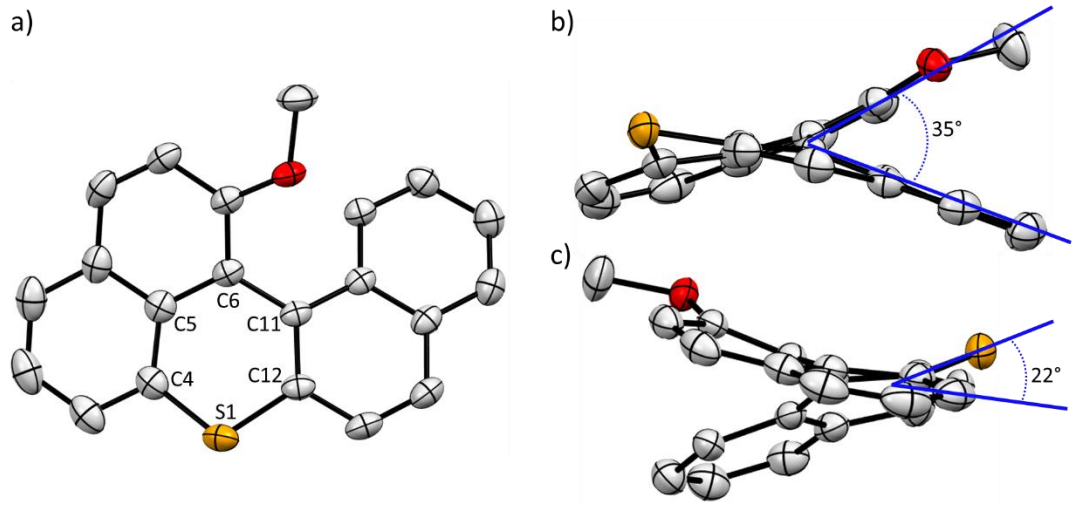

Figure 4.12. ORTEP representation of molecule **34** (50% probability ellipsoids), solvent for crystallisation: CH_2Cl_2, a) Top view; b) side view and side view 2. Sulphur (orange), oxygen (red) and carbon (grey).

4.3.4 *peri*-Thioxanthenoxanthene synthesis: synthetic route c

In the light of the previous consideration, we decided to attempt the **c** synthetic route for the synthesis of molecules **27**, **28** and **29.** Methoxy helicene **34** was oxidised with meta-chloroperbenzoic acid (m-CPBA) in chloroform at 60 °C for 16 hours to the sulphone derivative **38** in 98% yield, scheme 4.13. The obtained product was demethylated with BBr_3 in CH_2Cl_2 giving molecule **37** and then O-cyclised with Cu-catalysed reaction giving PTXX-SO_2 **29** as yellow solid in 50% yield.[37]

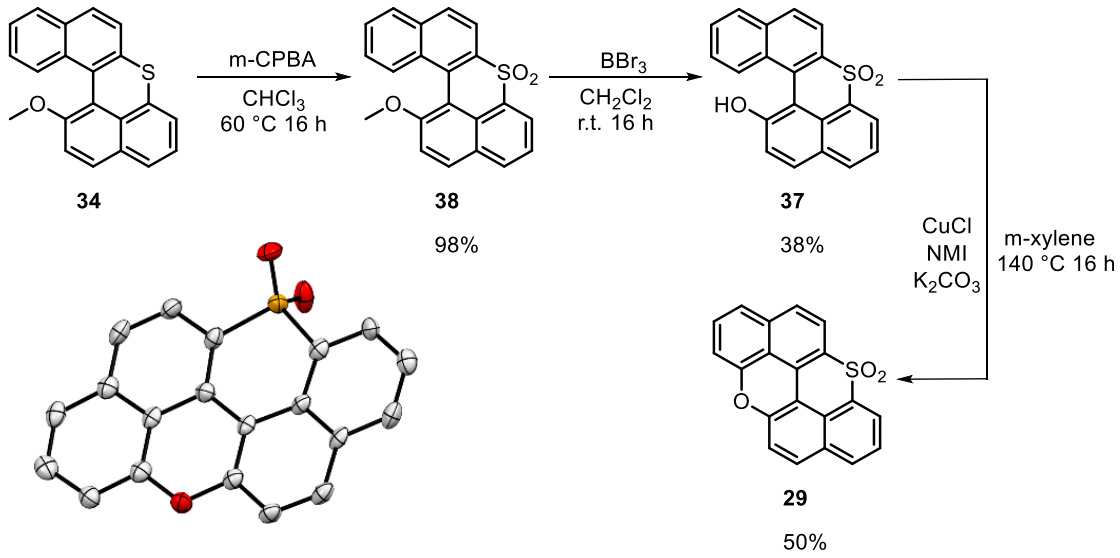

Scheme 4.13. Synthetic protocol for the preparation of molecule **29** and ORTEP representation of molecule **29** (50% probability ellipsoids), solvent for crystallisation: $CHCl_3$.

Compounds **29** and **38** were crystallised from slow evaporation of a $CHCl_3$ solution and analysed by XRD to confirm the molecular structure. Molecule **38** has an helicoidal shape such as molecule **34**, as shown in the ORTEP scheme, figure 4.13a. The two helicoidal enantiomer P and M crystallise together like for molecule **34**, figure 4.13b

and figure 4.13c. Since molecule **29** is one of our target molecules, its molecular packing in the crystal is more thoroughly discussed in section 4.6.

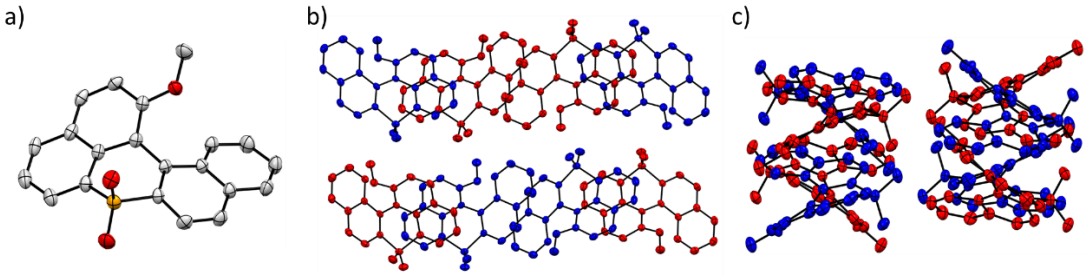

Figure 4.13. Space Group P bca, Rf = 6.02 %. a) ORTEP representation of molecule **38** (50% probability ellipsoids), solvent for crystallisation: CH_2Cl_2; b) unit cell view along b axis; c) unit cell view along a axis. P enantiomer in red and M enantiomer in blue. Sulphur (orange), oxygen (red) and carbon (grey).

4.3.5 Conclusion about the synthesis

In this section, three different synthetic pathways were investigated for the synthesis of **27**, **28** and **29** to address the different reactivity of the synthetic intermediates. The successful pathway envisaged the metal-free $C_{sp}{}^2$-$C_{sp}{}^2$ bond formation via interrupted Pummerer reaction between molecule **39** and 2-naphthol, followed by oxidation of the sulphur to sulphone and S-cyclisation to give helicene **34**. Due to the high sensitivity to oxidizing conditions of the sulphide moiety, molecule **34** was oxidised selectively to sulphone derivative **38** and then demethylated and O-cyclised through Cu-mediated oxidation. This work will proceed with the reduction PTXX-SO_2 **29** to sulphide PTXX **27** using a strong reductant such as lithium aluminium hydride, Zn/HCl, $B(C_6F_5)/Et_3SiH$ or SmI_2, scheme 4.14. [47–50] In agreement with the synthetic scheme 4.14, sulphoxide PTXX-SO **28** will be synthesised by selective oxidation of the sulphide moiety to sulphone. [32,51–53]

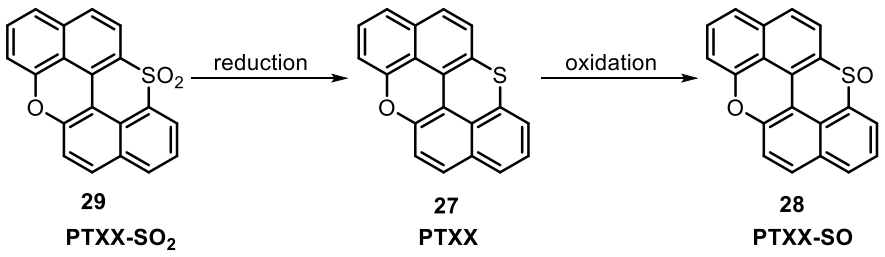

Scheme 4.14. Synthetic scheme for the preparation of molecule **27** and **28** from molecule **29**.

4.4 Photophysical characterization

4.4.1 General remarks about intramolecular charge transfer

Organic π-systems functionalised with an electron donor (D) and an electron acceptor (A) are molecules commonly known as push–pull systems. Due to the D–A cross-conjugation, the molecular orbitals (MO) are shuffled generating charge transfer (CT) excited state.[54] Therefore, new electronic transitions can take place between S_0 and

CT states usually at low energies. The effect of the cross-conjugation on the absorption spectrum of π-conjugated molecules can be appraised looking at the aniline, nitrobenzene, 4-nitroaniline and 3-nitroaniline spectra, figure 4.14. The absorption bands of the aniline and nitrobenzene are located between 250 and 300 nm in the UV region like most of the mono-functionalised benzene rings. On the other hand, the nitroanilines show a clear bathochromic shift of the absorption spectra. In the case of 4-nitroaniline, the intense and red shifted lowest energy absorption maximum is due to the cross-conjugation between the amino (D) and nitro (A) moieties.

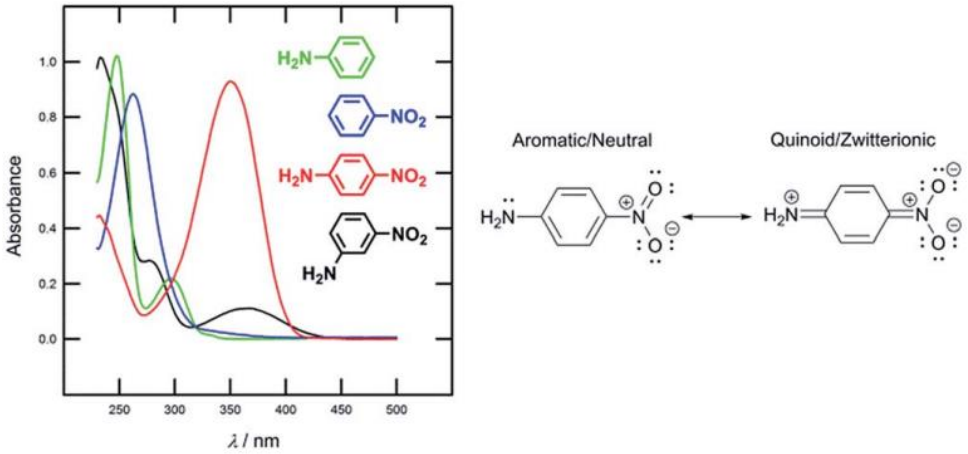

Figure 4.14. Limiting resonance forms and UV/Vis spectra for nitroaniline.

Common electron donors (D) are embodied by functional group with positive mesomeric and inductive effects (+M/+I) such as OH, NH_2, OR and NR_2, electron-rich heteroaromatic like thiophene and proaromatic pyran-4-ylidines as well as some metallocenes.[55–57] Conversely, the most representative electron acceptors (A) involve substituents containing -M/-I effects such as NO_2, CN, CHO and electron deficient heteroaromatic compounds like pyridines, di-azines, and benzo-thiazole.[58,59] The electronic properties of specific electron-withdrawing and donating moieties can be estimated by the modified Hammett constant σ, table 4.3. For molecules with D and A, the classic σ from the Hammett equation tend to underestimate the electronic effect, thus σ^- for an electron withdrawing and σ^+ for an electron donating group have to be considered.[60,61] Taking into account the σ^+/σ^- values for the most common functional groups, those with positive σ value are defined electron acceptors, conversely those with negative σ values are electron donors.

Table 4.3. Hammet-like σ values of selected groups used as acceptors and donors in push–pull chromophores.

R	σ^-	R	σ^+
NO_2	1.27	NH_2	-1.3
CN	1	OH	-0.92
SO_2Me	1.05	OMe	-0.78
F	0.07	CH_3	-0.31
N_2^+	3		

In the case of electronic transitions $S_0 \rightarrow$CT and CT$\rightarrow S_0$, the absorption and emission spectra are sensitive to the solvent polarity because the polar excited state can be energetically stabilised by polar solvents. The effect of solvent polarity on the excited state can be analysed using the Lippert−Mataga relationship which correlates the Stokes shift ($\Delta\nu$) to the polarizability of the solvent (Δf), equation 4.1a.[18,19] Δf is a unitless constant calculated as a function of the refractive index (η) and the dielectric constant (ε) of the medium, $\Delta\mu$ is the changing of molecular dipole moment from ground state to excited state, a is the solvent cavity, h is the Plank's constant, c is the speed of light, ε_0 is the dielectric permittivity of the vacuum, M is the molecular weight, N is the Avogadro's number, d is the molecular density, equations 4.1b and equation 4.1c.

$$\Delta\nu = \frac{2(\Delta\mu)^2}{\varepsilon_0 hca^3}\Delta f + \Delta\nu^0 \quad \text{(a)}$$

$$\Delta f = \frac{\varepsilon - 1}{2\varepsilon + 1} - \frac{\eta^2 - 1}{2\eta^2 + 1} \quad \text{(b)}$$

$$a = \left(\frac{3M}{4N\pi d}\right)^{1/3} \quad \text{(c)}$$

Equation 4.1. a) Lippert-Mataga equation; b) solvent polarizability equation; c) solvent cavity equation.

According to equation 4.1a, $\Delta\nu$ is linearly dependent from Δf and the higher is the slope the bigger is $\Delta\mu$. Therefore, by analysing the influence of the solvent polarity on the absorption and emission spectra of molecules containing electron donor and acceptor groups, it is possible to determine if there is the formation of a CT state.

4.4.2 Photophysical characterization of PTXX-SO_2 and molecule 38

In this section, the optoelectronics properties of PTXX-SO_2 **29** and molecule **38** were investigated through steady-state UV/Vis absorption and emission spectroscopy and, in order to appreciate the effect of the sulphoxide moiety, the measurements were

referred to the properties of **PXX**. The UV-vis absorption and emission spectra were measured in $CHCl_3$ at room temperature, figure 4.15. Conversely to the absorption spectrum of **PXX**, the absorption spectra of molecules **29** and **38** show a different electronic envelop. The $\pi \rightarrow \pi^*$ transitions in the visible region do not show the defined vibronic transitions for molecule **38** and **29**. For this reason, it is not possible to determine the lowest energy absorption maximum with high precision and the effect of the SO_2 group insertion in the **PXX** scaffold was evaluated in terms of E_g^{opt}, table 4.4. Due to the planarization effect from helicene **38** to PTXX-SO_2 **29**, the energy gap for molecule **29** (E_g^{opt} = 2.65 eV) is 0.30 eV lower than that observed for molecule **38**. Moreover, PTXX-SO_2 shows E_g^{opt} bathochromic shifted of 0.1 eV with respect to **PXX**. Compound **29** and **38** does not show phosphorescence emission.

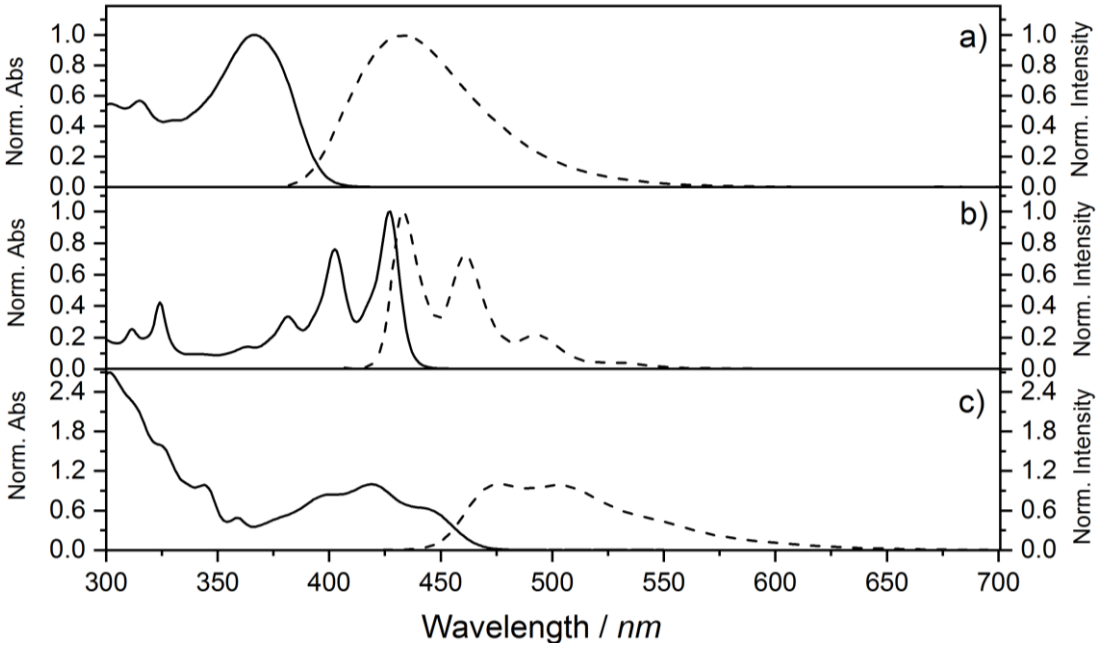

Figure 4.15. Normalised absorbance spectra on λ_{max} (solid line) and normalised emission spectra (dashed line) recorded in toluene at r.t.; a) **38**; b) **PXX** and c) **29**.

Table 4.4. Photophysical data for **29**, **38** and **PXX** in $CHCl_3$ at r.t..

	Absorbance		Fluorescence			
	λ_{max} (nm)	ε ($M^{-1}cm^{-1}$)	λ_{max} (nm)	τ (ns)	Φ_{Fluo} (%)	E_g^{opt} (eV)
PXX	443	17560	450	5.0	61	2.74
38	383	14677	466	1.46	17	2.95
29	445	3619	476	5.4	16	2.65

The bathochromic shift and the peak broadening observed for **29** and **38** with respect to **PXX** could be due to the cross-conjugation between the oxygen and the sulphone

moiety. This can be visualised considering the limiting resonance structure for molecules **38** and **29**, figures 4.16a and 4.16b.

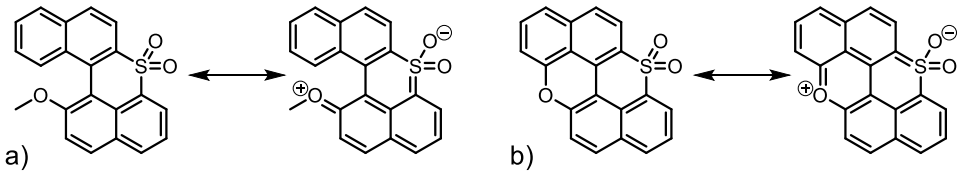

Figure 4.16. Limiting resonance forms for molecule **38** a) and **29** b).

To verify whether CT states in molecule **29** and **38** are forming, absorption and emission spectra were measured in different solvents with different polarity and compared to **PXX** absorption and emission spectra, figure 4.17a, 4.17b and 4.17c. The **PXX** spectra show a well-defined vibrational fine structure in all solvents. On the contrary, the spectra of molecule **38** display only broad continuous bands. The spectra of molecule **29** have a more defined vibrational structure in nonpolar solvents and the width of peaks increase as a function of the solvent polarity (see chapter 5 Figure 5.17). The Lippert-Mataga plots for **PXX** and molecule **38** highlight the independence of the Stoke shift on the solvent polarity, meaning that the molecular dipole moment does not change from ground state to excited state, figures 4.17a and 4.17b. Conversely, the Lippert-Mataga plot for molecule **29** shows the linear dependence of the Stoke shift on solvent polarity (R^2=0.92), figure 4.17c, confirming that the band at 445 nm can be considered an intramolecular CT of the lowest energy electronic transition.

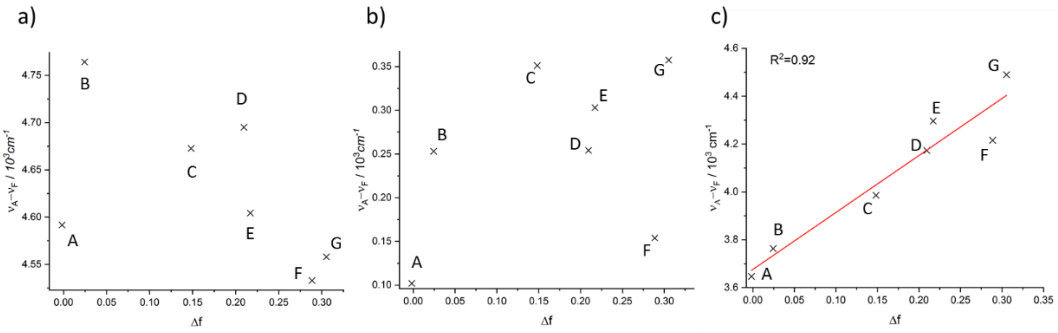

Figure 4.17. Lippert-Mataga plot for a) **38** b) **PXX** and c) **29** (A: cyclohexane; B: 1,4-dioxane; C: chloroform; D: tetrahydrofuran; E: dichloromethane; F: ethanol; G: acetonitrile). Linear fitting (red line) is also shown.

4.5. Electrochemical investigation

4.5.1 Cyclic voltammetry investigation.

The redox properties of the new molecules synthesised were studied by CV in CH_2Cl_2 with $TBAPF_6$ as electrolyte. All the measurements were calibrated against Fc/Fc^+, used as internal standard. The cyclic voltammograms of PTXX-SO_2 **29** and molecule **38** are reported in figure 4.18 and the experimental parameters in table 4.5.

The cyclic voltammetry trace of **PXX** in CH_2Cl_2 displays the same behaviour showed in the section 2.52 in ODCB with a reversible oxidation wave at $E_{1/2}^{ox}$ = 0.3 V and no reduction waves in the potential window scanned. It is known from the literature that the reduction wave of **PXX** can be detected in CH_3CN at $E_{1/2}^{red}$ = -2.59 V.[62] The cyclic voltammogram of molecule **38** shows a reversible reduction wave peak at $E_{1/2}^{red}$ = -1.95 V and the oxidation process is not observed. On the contrary, PTXX-SO_2 **29** displays an irreversible oxidation wave peak that is 0.7 V higher than that of **PXX**. It also shows a reversible reduction wave at $E_{1/2}^{red}$ = -1.98 V, which is approximately equal to the reduction potential of helicene **38**.

Table 4.5. Cyclic Voltammetry data calculated vs Fc^+/Fc. in CH_2Cl_2 at r.t. with electrolyte $TBAPF_6$ 63 mM

	$E_{1/2}^{ox}$ (V)	ΔE_{pp}^{ox} (mV)	$E_{1/2}^{red}$ (V)	ΔE_{pp}^{red} (mV)	E_g^{CV} (eV)
PXX	0.30	132	-2.59[a]	-	2.89
29	1.01[b]	119	-1.98	124	-2.98
38	-	-	-1.95	110	

[a]detected in acetonitrile; [b]irreversible peak

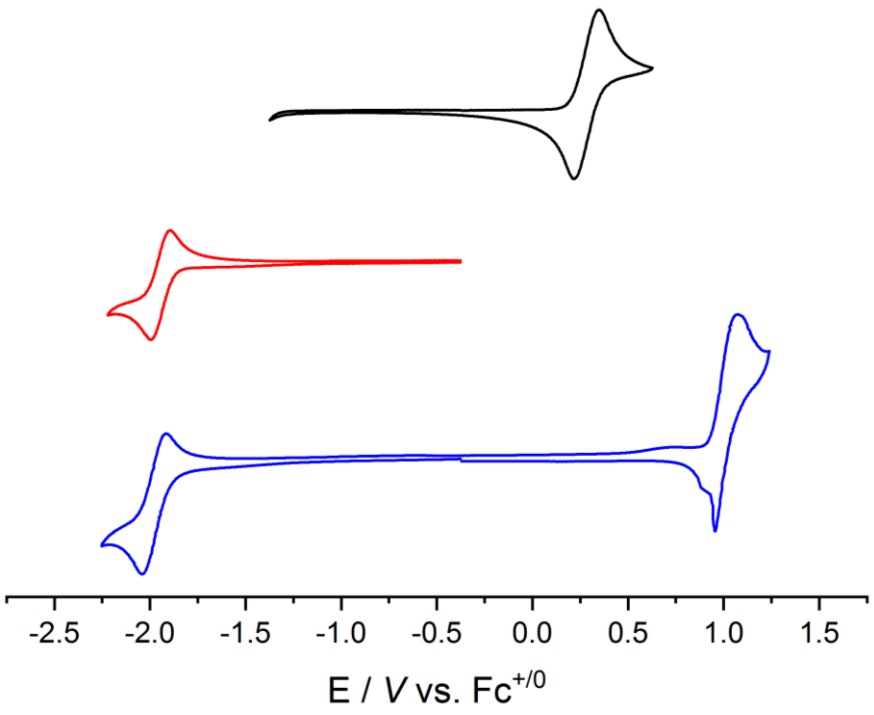

Figure 4.18. Cyclic voltammograms in CH_2Cl_2 at r.t. with electrolyte $TBAPF_6$ 61 mM. Black line **PXX**; red line molecule **38** 0.63 mM; blue line molecule **29** 0.68 mM.

The presence of the reduction waves in the CVs of molecules **29** and **38** could be attributed to the presence of the sulphone moiety which, being an electron withdrawing group, lowers the reduction potential. Moreover, the reduction potentials of PTXX-SO_2 **29** and helicene **38** are approximately the same, showing their dependence on the functional group present on the molecule and not on its π-conjugated system. The

oxidation potential of PTXX-SO_2 **29** is higher than that of **PXX**, demonstrating that it is also affected by the presence of the sulphone group. Moreover, the oxidation process observed for PTXX-SO_2 is irreversible due to side reactions which involve the radical cations generated during the oxidative process.[63] Increasing the voltammetry scan rate from 0.05 V/s to 1 V/s, it is possible to observe the change in shape of the anodic peak in the oxidation wave for PTXX-SO_2, figure 4.19. The oxidative process seems to become more reversible at high scan rate. This observation indicates that the reduction process of the oxidised species to the neutral species is faster than side reaction rate.[63]

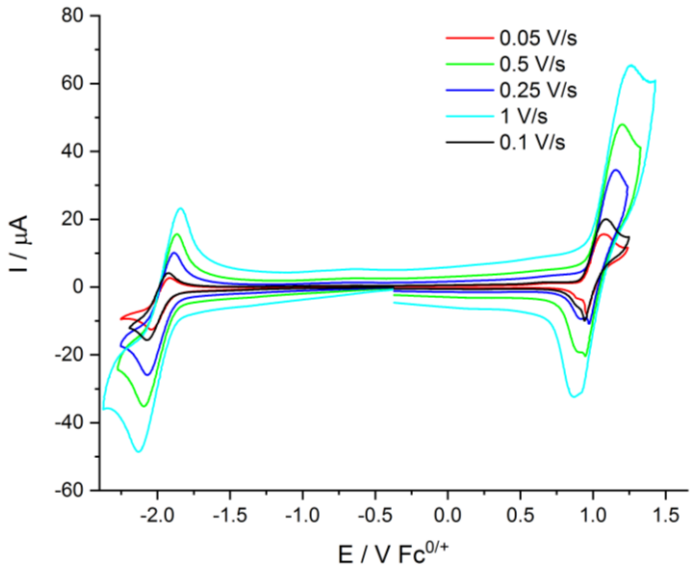

Figure 4.19. Cyclic voltammograms of PTXX-SO_2 **29** in CH_2Cl_2 at r.t. with electrolyte $TBAPF_6$ 61 mM at different scan rate

4.5.2 Frontier orbital energies determination of molecules 29 and 38

The frontier orbitals energies of PTXX-SO_2 **29** and molecule **38** have been determined using the previously cited equation 2.5. and reported in table 4.6. The introduction of the SO_2 group decreases both the HOMO and the LUMO energy levels for PTXX-SO_2, by 0.70 eV and 0.61 eV respectively, with respect to **PXX**. As depicted in the cyclic voltammogram in figure 4.19, molecule **38** shows only one reduction wave, thus it is possible to calculate only the LUMO energy level. As expected, helicene **38** and PTXX-SO_2 LUMO energy have approximately the same value since they have the same reduction potential.

Table 4.6. Cyclic Voltammetry data in CH_2Cl_2 at r.t. with electrolyte $TBAPF_6$ 63 mM, HOMO and LUMO energies calculated considering the formal potential of the Fc^+/Fc redox couple approximately -5.1 eV vs. *vacuum*.

	$E_{1/2}^{ox}$ (V)	$E_{1/2}^{red}$ (V)	HOMO (eV)	LUMO (eV)	E_g^{CV} (eV)	E_g^{opt} (eV)
PXX	0.30	-2.59[a]	-5.41	-2.51[a]	2.89*	2.74
38	-	-1.95		-3.15	-	2.95
29	1.01	-1.98	-6.11	-3.12	2.98	2.65

[a] detected in acetonitrile

To shed further light on the optoelectronic properties of molecules **29** and **38**, we calculated the HOMO and LUMO orbitals via Density Functional Theory (DFT) using the functional B3LYP with basis set 6-31+G**. Even though, the calculated energy values do not match the experimental values, they show the same trend, figure 4.20. It is also possible to observe the CT from the HOMO and LUMO. It emerges that the HOMO and LUMO of **PXX** are homogenously distributed over the molecule framework, whereas the HOMO and LUMO of molecule **29** are asymmetrically distributed in different parts of the molecule. This spatial separation of HOMO and LUMO is typical in molecule which present CT excited states.[8]

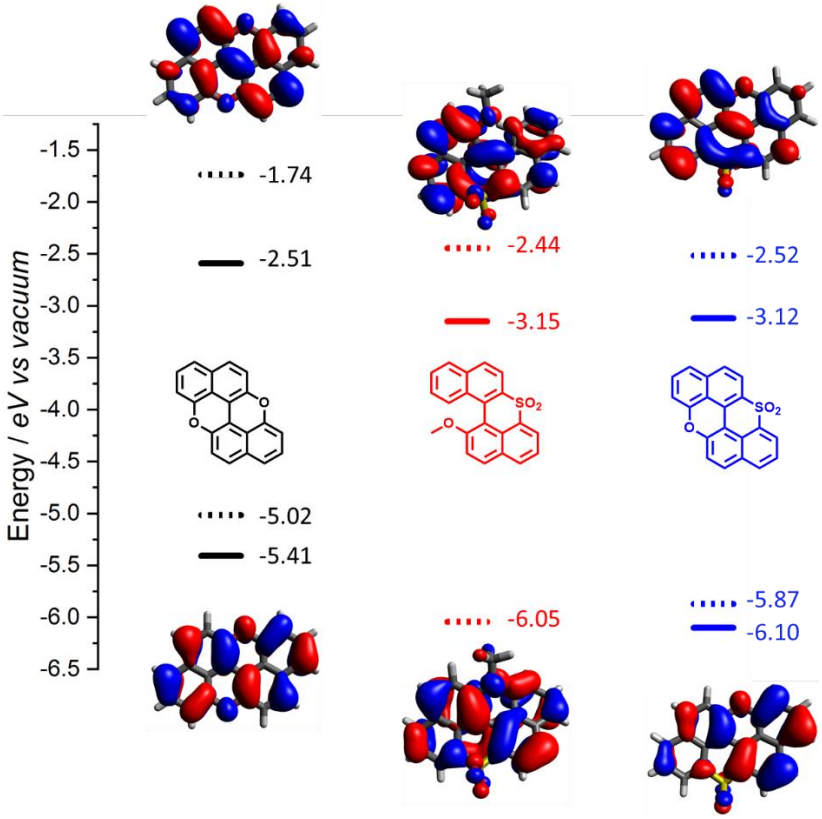

Figure 4.20. Frontier orbital energies estimated from the CV and photo- physical data for molecules **29**, **38** and **PXX** together with their HOMO and LUMO profiles at B3LYP/6-31G(d,p) level of theory (Gaussian09)

By knowing the $E_{1/2}^{ox}$ and $E_{1/2}^{red}$ energy and E_g^{opt}, it is possible to calculate the redox potential of the excited state S_1 using the equations 2.6a and 2.6b discussed in section 2.53, figure 4.21.[64] It results that the calculated redox potentials of S_1 for molecules **29** and **38** are lowered with respect to **PXX**. The E_{red}^* of the S_1 for PTXX-SO_2 is higher than the E_{red}^* for **PXX**, meaning that S_1 of PTXX-SO_2 **29** is a stronger oxidant than the excited **PXX**. Moreover, the E_{red}^* for helicene **38** is even higher than the one observed for PTXX-SO_2 as this molecule has a wider E_g^{opt}.

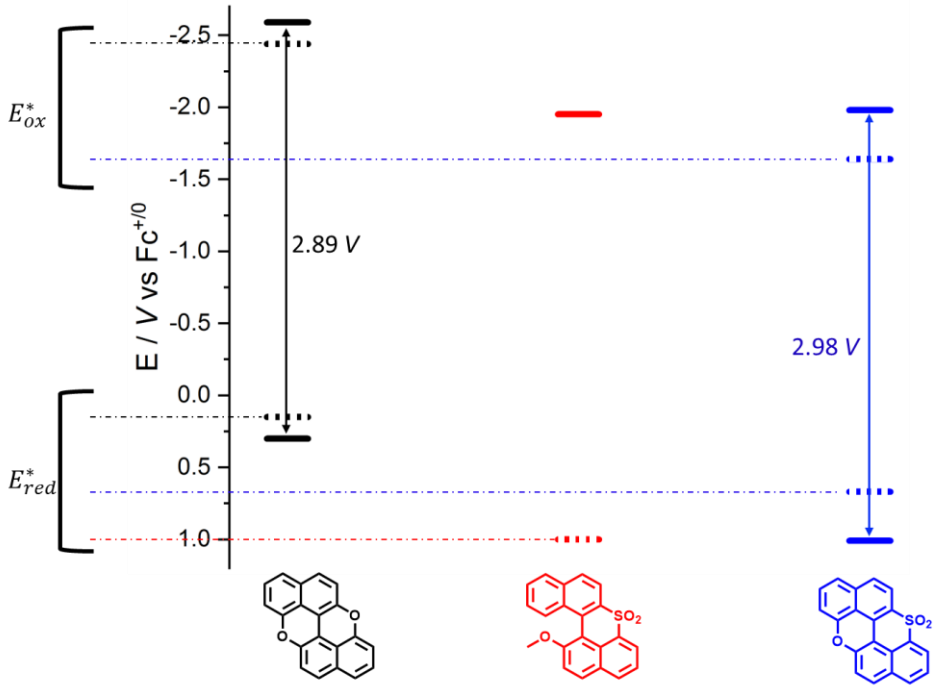

Figure 4.21. Solid line $E^{ox}_{1/2}$ and $E^{red}_{1/2}$ for the ground states measured in ODCB. Dashed lines E^*_{ox} and E^*_{red} potentials of excited states S_1.

4.6 Solid-state self-assembly investigation of PTXX-SO_2

In this section, we describe the solid-state organisation of molecule **29** (PTXX-SO_2) as determined by single crystal X-ray diffraction (XRD) analysis and rationalise the supramolecular interactions with the support of computational chemistry.

4.6.1 Crystal structure and packing of PTXX-SO_2

PTXX-SO_2 was crystallised by slow $CHCl_3$ evaporation and triclinic crystals with P -1 spatial group were obtained (R-factor 5.5%). From the molecular structure it could be seen that the hexagonal ring that includes the sulphone group is slightly bigger than the pyran ring and this induces a light distortion on the molecule, figure 4.22. The distances C(4)···S(1) and C(12)···S(1) are 1.759 Å and 1.747 Å, which are larger than the homologous bonds in **PXX**, C(19)···O(1) 1.392 Å and C(1)···O(1) 1.380 Å. The distortion also affects the bond angle C(4)···S(1)···C(12) 104° which is 18° smaller than the homologue in **PXX**, C(1)···O(1)···C(19) 122°. The bond lengths C(5)···O(3) and C(19)···O(3) in the pyranyl ring of PTXX-SO_2 are 1.363 Å and 1.378 Å comparable with those observed in **PXX** pyran rings for the analogous bonds.

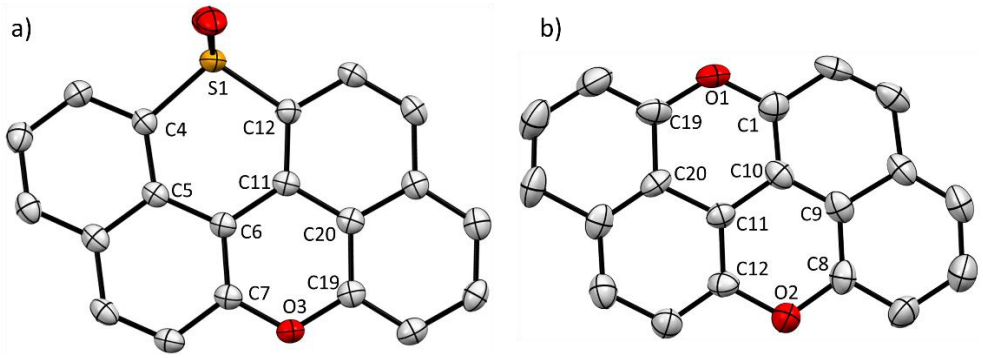

Figure 4.22. a) Molecule **29** ORTEP representation (50% probability ellipsoids) crystallisation solvent $CHCl_3$; b) **PXX** ORTEP representation (50% probability ellipsoids) crystallisation method vacuum sublimation.

In the crystal lattice, the molecules are spatially organised into one-dimensional columnar stackings, figures 4.23a, 4.23c and 4.23d. The interplanar distance between two molecules of PTXX-SO_2 is 3.33 Å which is shorter than the interplanar distance in graphite layers, 3.41 Å.[65] The presence of the SO_2 group and the O atom at the PTXX-SO_2 periphery induces a molecular dipole moment which is oriented from the sulphoxide moiety to the oxygen bridge. The solid-state organisation is driven by the dipole-dipole interaction in cooperation with π-π face-to-face interaction, figure 4.23a and 4.23b.[66,67]. From the figure 4.23b, it is possible to observe the offset of 3.22 Å among the stacked molecules, which we think it is due to the steric and electronic repulsion between the sulphoxide oxygens and peripheral molecular framework.

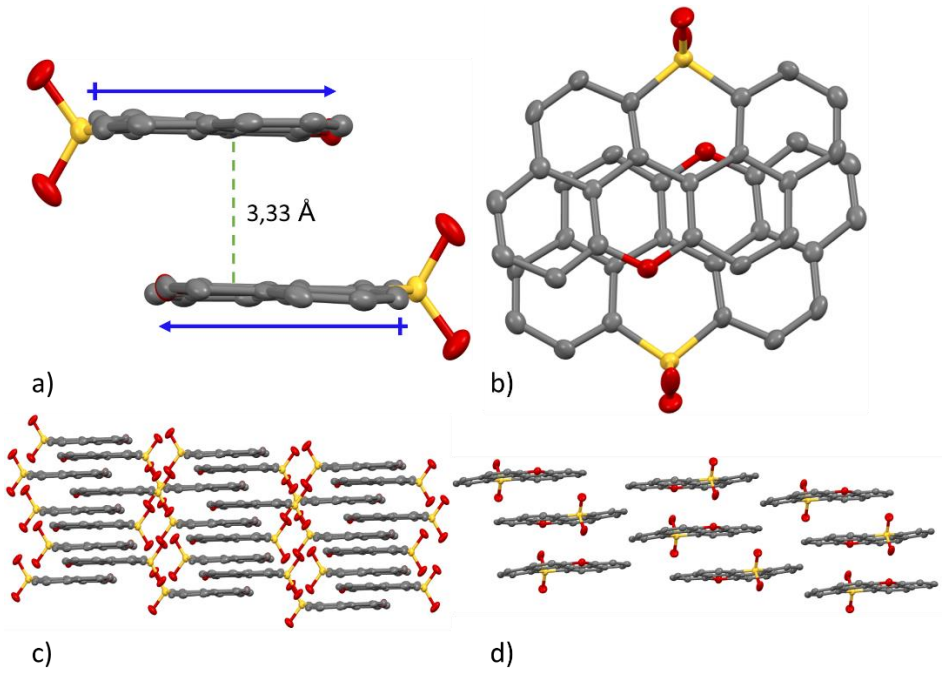

Figure 4.23. Molecule **29** a) dipole-dipole interaction and face-to-face interaction side view, b) dipole-dipole interaction and face-to-face interaction top view; c) crystal packing side view; d) crystal packing side view 2.

From figures 4.24a and 4.24b, it could be seen that the intermolecular distances between C(14)···O(1) and C(8)···O(1) are 3.451 Å and 3.372 Å, respectively. Those distances, can be associated to weak hydrogen bonding interactions and are very similar to those observed in others heteroatoms doped PAHs.[68]

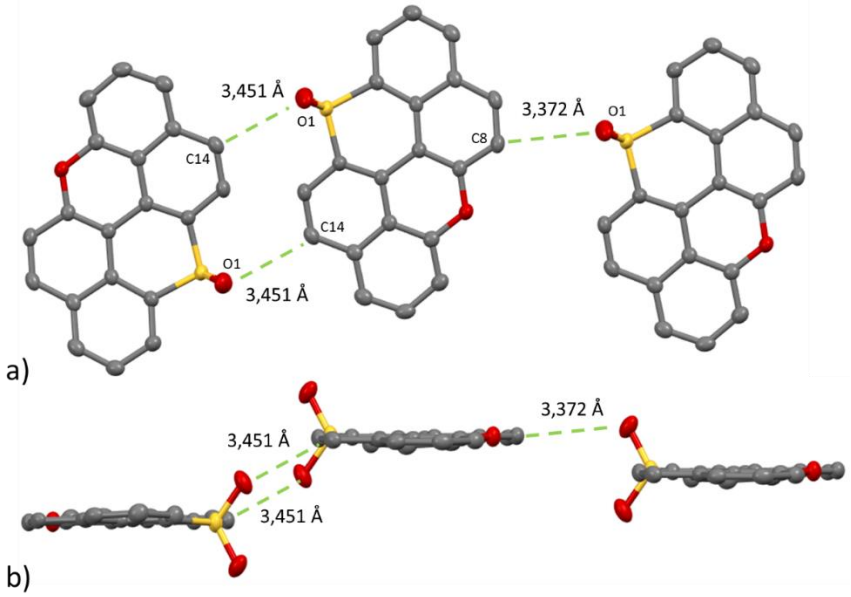

Figure 4.24. Molecule **29** a) weak hydrogen bonding interaction top view, b) weak hydrogen bonding interaction top view.

These interactions are also supported by DFT and ESP surface calculations, figure 4.25. The calculated molecular dipole has magnitude of 5.82 Debye and, as expected, is oriented from the SO_2 group to the O atom of molecule **29**, figure 4.25a and 4.25b. The calculated ESP maps show the negative polarised parts on the oxygen atoms of the sulfone group, which, as we can be see from the crystal structure, constitute the hydrogen bond acceptors, figures 4.25a, 4.25d and 4.25d. The positive blue regions in

the ESP surface highlight the hydrogen bond donors which are the hydrogen atoms positively charged on the C14 and C8 atoms, figures 4.26a, 4.26d and 4.26d.

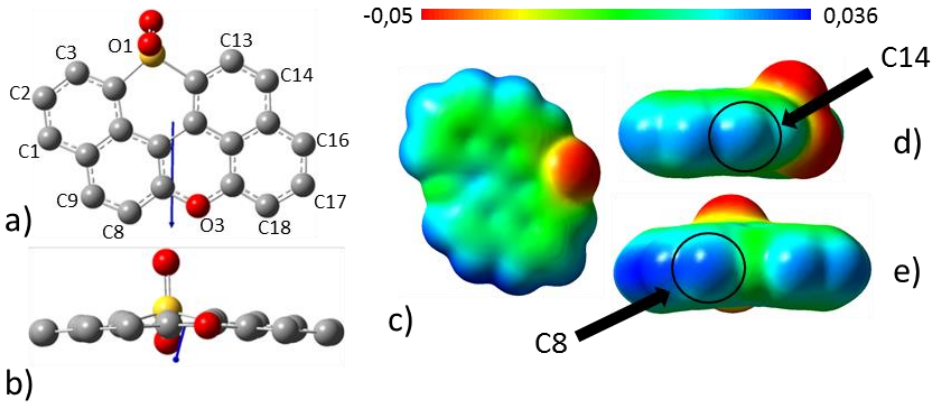

Figure 4.25. Molecule **29** DFT optimised geometry and calculate dipole moment a) top view and b) side view. ESP for molecule **29** mapped on the vdW surface up to an electron density of 0.001 electron bohr-,. c) top view, d) side view1, e) side view 2.

4.7 Conclusion and future work

The work reported in this chapter concerned the synthesis of novel chromophores obtained from S-doping of PXX **27** and oxidised homologues sulphoxide **28** and sulphone **29**, figure 4.26. The chosen strategy towards the synthesis of these molecules involved an intermolecular $C_{sp}{}^2$-$C_{sp}{}^2$ bond formation between 2-naphthol and naphthyl sulphoxide through interrupted Pummerer reaction followed by S-cyclisation and O-cyclisation. It was not possible to synthesise molecules **27** by this method since S-cyclised molecule **33** was highly unstable and preferentially decomposed instead of undergoing O-cyclisation. To overcome this issue, we selectively oxidised the sulphide bridge to sulphone yielding molecule **38**, which was then O-cyclised into molecule **29**. In accordance with the contemplated retrosynthetic pathway, PTXX-SO_2 will be the starting point for the preparation of molecule **27** and **28**. Molecule **29** has been photophysically characterised and the properties compared to helicene **38** and **PXX**. Absorption and emission spectra in different solvents showed the formation of CT excited state, which was proved by Lippert-Mataga theory. None of the investigated molecule showed phosphorescence radiative emission, thus we will investigate the population of the T_1 through singlet oxygen sensitisation.[20] The introduction of sulphone moiety in the **PXX** scaffold changed also the interaction at solid-state of PTXX-SO_2 as showed from XRD analysis. The molecular dipole guided the solid-state organisation of the molecules into a lamellar crystal packing. In the next future, we aim to synthesise molecules **27** and **28** in order to completely investigate and rationalise

the variation of the optoelectronic properties as a function of sulphur atom and its oxidation state.

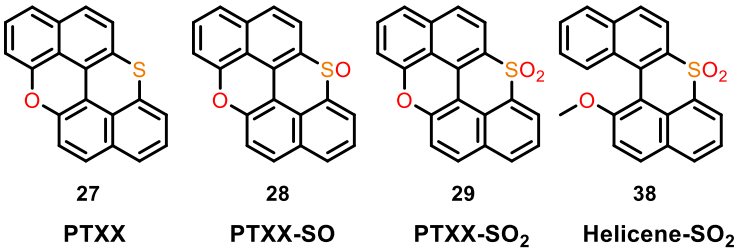

Figure 4.26. Summarising scheme of synthesised molecules **29** and **38** with to be synthesised target molecules **27** and **28**.

3.8 References

[1] J. Roncali, *Macromol. Rapid Commun.* **2007**, *28*, 1761–1775.

[2] J. Roncali, *Chem. Rev.* **1992**, *92*, 711–738.

[3] J. Roncali, P. Leriche, P. Blanchard, *Adv. Mater.* **2014**, *26*, 3821–3838.

[4] A. Operamolla, G. M. Farinola, *Eur. J. Org. Chem.* **2011**, 423–450.

[5] Y. J. Cheng, S. H. Yang, C. S. Hsu, *Chem. Rev.* **2009**, *109*, 5868–5923.

[6] G. R. Hutchison, M. A. Ratner, T. J. Marks, *J. Am. Chem. Soc.* **2005**, *127*, 16866–16881.

[7] P. R. Christensen, J. K. Nagle, A. Bhatti, M. O. Wolf, *J. Am. Chem. Soc.* **2013**, *135*, 8109–8112.

[8] P. Pahlavanlu, P. R. Christensen, J. A. Therrien, M. O. Wolf, *J. Phys. Chem. C* **2016**, *120*, 70–77.

[9] A. Kremer, C. Aurisicchio, F. Deleo, B. Ventura, J. Wouters, N. Armaroli, A. Barbieri, D. Bonifazi, *Chem. - Eur. J.* **2015**, *21*, 15377–15387.

[10] J. T. E. Quinn, J. Zhu, X. Li, J. Wang, Y. Li, *J. Mater. Chem. C* **2017**, *5*, 8654–8681.

[11] W. Jiang, H. Geng, W. Hu, Z. Wang, Z. Shuai, Y. Zhou, J. Pei, S. Jiang, S. Yan, *J. Am. Chem. Soc.* **2011**, *133*, 1–3.

[12] Y. Sun, L. Tan, S. Jiang, H. Qian, Z. Wang, D. Yan, C. Di, Y. Wang, W. Wu, G. Yu, et al., *J. Am. Chem. Soc.* **2007**, *129*, 1882–1883.

[13] D. Wu, W. Pisula, M. C. Haberecht, X. Feng, K. Müllen, *Org. Lett.* **2009**, *11*, 5686–5689.

[14] S. Dong, T. S. Herng, T. Y. Gopalakrishna, H. Phan, Z. L. Lim, P. Hu, R. D. Webster, J. Ding, C. Chi, *Angew. Chem. Int. Ed.* **2016**, *55*, 9316–9320.

[15] C. Rovira, J. Veciana, N. Santaló, J. Tarrés, J. Cirujeda, E. Molins, J. Llorca, E. Espinosa, *J. Org. Chem.* **1994**, *59*, 3316–3313.

[16] C. E. Smith, S. O. Odoh, S. Ghosh, L. Gagliardi, C. J. Cramer, C. D. Frisbie, *J. Am. Chem. Soc.* **2015**, *137*, 15735–15741.

[17] N. J. Turro, V. Ramamurthy, J. C. Scaiano, *Modern Molecular Photochemistry of Organic Molecules*, **2012**.

[18] E. Lippert, *Z. Naturforsch., A: Phys. Sci.* **1955**, *10*, 541–545.

[19] N. Mataga, Y. Kaifu, M. Koizumi, *Bull. Chem. Soc. Jpn.* **1956**, *26*, 465–470.

[20] T. Y. Ohulchanskyy, D. J. Donnelly, M. R. Detty, P. N. Prasad, *J. Phys. Chem. B* **2004**, *108*, 8668–8672.

[21] V. Balzani, P. Ceroni, A. Juris, *Photochemistry and Photophysics: Concepts, Research, Applications*, John Wiley & Sons, **2014**.

[22] X. Yang, D. Neher, D. Hertel, T. K. Däubler, *Adv. Mater.* **2004**, *16*, 161–166.

[23] M. Bian, D. Zhang, Y. Wang, Y. H. Chung, Y. Liu, H. Ting, L. Duan, Z. Chen, Z. Bian, Z. Liu, L. Xiao, *Adv. Funct. Mater.* **2018**, *28*, 1–9.

[24] K. S. Yook, J. Y. Lee, *Adv. Mater.* **2012**, *24*, 3169–3190.

[25] A. P. Monkman, *ISRN Mater. Sci.* **2013**, *2013*, 1–19.

[26] A. Köhler, H. Bässler, *Mater. Sci. Eng., R* **2009**, *66*, 71–109.

[27] A. Kremer, A. Fermi, N. Biot, J. Wouters, D. Bonifazi, *Chem. - Eur. J.* **2016**, *22*, 5665–5675.

[28] N. Biot, D. Bonifazi, *Chem. - Eur. J.* **2018**, *24*, 5439–5443.

[29] V. C. Sundar, J. Zaumseil, V. Podzorov, E. Menard, R. L. Willett, T. Someya, M. E. Gershenson, J. Rogers, *Science* **2004**, *303*, 1644–1646.

[30] P. L. Anthony James Wigglesworth, Yillang Wu, *US 2012/0205630 A1, 2012,8,16.* **2012**, 1–10.

[31] A. Sciutto, A. Fermi, A. Folli, T. Battisti, J. Beames, D. Murphy, D. Bonifazi, *Chem. - Eur. J.* **2018**, *24*, 4382–4389.

[32] S. F. Nelsen, Y. Luo, M. N. Weaver, J. V. Lockard, J. I. Zink, *J. Org. Chem.* **2006**, *71*, 4286–4295.

[33] B. Waldecker, F. Kraft, C. Golz, M. Alcarazo, *Angew. Chem. Int. Ed.* **2018**, *57*, 12538–12542.

[34] W. Li, J. Li, Y. Wu, F. Rancati, S. Vallese, L. Raveglia, J. Wu, R. Hotchandani, N. Fuller, K. Cunningham, P. Morgan, S. Fish, R. Krykbaev, X. Xu, S. Tam, S. J. Goldman, W.Abraham, C. Williams, J. Sypek, T. S. Mansouret, *J. Med. Chem.* **2009**, *52*, 5408–5419.

[35] H. Sirringhaus, R. H. Friend, C. Wang, K. Mullen, *J. Mater. Chem.* **1999**, 2095–2101.

[36] N. Kobayashi, M. Sasaki, K. Nomoto, *Chem. Mater.* **2009**, *21*, 552–556.

[37] T. Kamei, M. Uryu, T. Shimada, *Org. Lett.* **2017**, *19*, 2714–2717.

[38] N. Miyaura, K. Yamada, A. Suzuki, *Tetrahedron Lett.* **1979**, *20*, 3437–3440.

[39] N. A. S. Miyaura, S. Chem, *J. Chem. Soc., Chem. Commun.* **1979**, 866–867.

[40] J. K. Stille, *Angew. Chem. Int. Ed.* **1986**, *25*, 508–524.

[41] T. Yanagi, S. Otsuka, Y. Kasuga, K. Fujimoto, K. Murakami, K. Nogi, H. Yorimitsu, A. Osuka, *J. Am. Chem. Soc.* **2016**, *138*, 14582–14585.

[42] H. Yorimitsu, *Chem. Rec.* **2017**, *17*, 1156–1167.

[43] S. K. Bur, A. Padwa, *Chem. Rev.* **2004**, *104*, 2401–2432.

[44] L. H. S. Smith, S. C. Coote, H. E. Sneddon, D. J. Procter, *Angew. Chem. Int. Ed.* **2010**, *49*, 5832–5844.

[45] A. P. Pulis, D. J. Procter, *Angew. Chem. Int. Ed.* **2016**, *55*, 9842–9860.

[46] C. Song, T. M. Swager, *Macromolecules* **2009**, 1472–1475.

[47] E. Akgün, K. Mahmood, C. A. Mathis, *J. Chem. Soc., Chem. Commun.* **1994**, 761–762.

[48] F. G. Bordwell, W. H. McKelln, *J. Am. Chem. Soc.* **1951**, *73*, 2251–2253.

[49] D. Porwal, M. Oestreich, *Synth.* **2017**, *49*, 4698–4702.

[50] J. N. Gardner, S. Kaiser, A. Krubiner, H. Lucas, *Can. J. Chem.* **2006**, *51*, 1419–1421.

[51] Z. He, A. P. Pulis, D. J. Procter, *Angew. Chem. Int. Ed.* **2019**, *58*, 7813–7817.

[52] K. Bahrami, *Tetrahedron Lett.* **2006**, *47*, 2009–2012.

[53] L. L. Baldassari, A. C. Mantovani, S. Senoner, B. Maryasin, N. Maulide, D. S. Lüdtke, *Org. Lett.* **2018**, *20*, 5881–5885.

[54] F. Bureš, *RSC Adv.* **2014**, *4*, 58826–58851.

[55] N. J. Long, *Angew. Chem. Int. Ed.* **1995**, *34*, 21–28.

[56] H. S. Nalwa, *Appl. Organomet. Chem.* **1991**, *5*, 349–377.

[57] Y. L. Wu, F. Bureš, P. D. Jarowski, W. B. Schweizer, C. Boudon, J. P. Gisselbrecht, F. Diederich, *Chem. - Eur. J.* **2010**, *16*, 9592–9605.

[58] S. Achelle, N. Plé, A. Turck, *RSC Adv.* **2011**, 364–388.

[59] V. Hrobáriková, P. Hrobárik, P. Gajdoš, I. Fitilis, M. Fakis, P. Persephonis, P. Zahradník, *J. Org. Chem.* **2010**, *75*, 3053–3068.

[60] H. C. Brown, Y. Okamoto, *J. Am. Chem. Soc.* **1958**, *80*, 4979–4987.

[61] G. A. Dilabio, K. U. Ingold, *J. Org. Chem.* **2004**, *69*, 1620–1624.

[62] A. Sciutto, A. Fermi, A. Folli, T. Battisti, J. M. Beames, D. M. Murphy, D. Bonifazi, *Chem. - Eur. J.* **2018**, *24*, 4382–4389.

[63] N. Elgrishi, K. J. Rountree, B. D. McCarthy, E. S. Rountree, T. T. Eisenhart, J. L. Dempsey, *J. Chem. Educ.* **2018**, *95*, 197–206.

[64] W. E. Jones, M. A. Fox, *J. Phys. Chem.* **1994**, *98*, 5095–5099.

[65] G. Dearnaley, *Phys. Bull.* **1980**, *31*, 582.

[66] A. D. McNaught, A. Wilkinson, M. Nic, J. Jirat, B. Kosata, in *IUPAC. Compendium of Chemical Terminology, 2nd Ed. (the "Gold Book"). Compiled by A. D. McNaught and A. Wilkinson. Blackwell Scientific Publications, Oxford (1997).*, **2014**.

[67] M. Dong, K. Miao, Y. Hu, J. Wu, J. Li, P. Pang, X. Miao, W. Deng, *Phys. Chem. Chem. Phys.* **2017**, *19*, 31113–31120.

[68] G. Desiraju, T. Steiner, *The Weak Hydrogen Bond*, **2010**.

Chapter 5

Experimental Part

5.1 Instrumentation

Thin layer chromatography (TLC) was conducted on pre-coated aluminium sheets with 0.20 mm Merk Millipore Silica gel 60 with fluorescent indicator F254.

Column chromatography was carried out using Merck Gerduran silica gel 60 (particle size 40-63 µm).

Melting points (mp) were measured on a Gallenkamp apparatus in open capillary tubes and have not been corrected.

Nuclear magnetic resonance: (NMR) spectra were recorded on a Bruker Fourier 300 MHz spectrometer equipped with a dual (^{13}C, ^{1}H) probe, a Bruker AVANCE III HD 400MHz NMR spectrometer equipped with a Broadband multinuclear (BBFO) SmartProbeTM or a Bruker AVANCE III HD 500MHz Spectrometer equipped with Broadband multinuclear (BBO) Prodigy CryoProbe. ^{1}H spectra were obtained at 300, 400 or 500 MHz, ^{13}C spectra were obtained at 75, 100 or 125 MHz NMR. All spectra were measured at r.t. if not otherwise stated. Chemical shifts were reported in ppm relative to tetramethylsilane using the solvent residual signal as an internal reference (CDCl3: δ_H = 7.26 ppm, δ_C = 77.16 ppm; THF: δ_H = 1.73 ppm, δ_C = 25.30 ppm; DMSO-d_6: δ_H = 2.50 ppm, δ_C = 39.52 ppm, CD_2Cl_2: δ_H = 54.00 ppm, δ_C = 40.45 ppm). Coupling constants (*J*) were given in Hz. Resonance multiplicity was described as s (singlet), d (doublet), t (triplet), q (quartet) and broad (broad signal). Carbon spectra were acquired with a complete decoupling for the proton. The Attached Proton Test (APT) experiments were used to determine C-H multiplicities in carbon spectra and the peaks assigned as singlet (s) for quaternary and doublet (d) for tertiary carbon atoms.

Infrared spectra (IR) were recorded on a Shimadzu IR Affinity 1S FTIR spectrometer in ATR mode with a diamond mono-crystal. Selected absorption bands are reported by wavenumber (cm^{-1}).

Mass spectrometry: (i) High-resolution ESI mass spectra (HRMS) were performed on a Waters LCT HR TOF mass spectrometer in the positive or negative ion mode. (ii)

High-resolution MALDI mass spectra (HRMS) were performed on a Waters Synapt G2-Si QTOF mass spectrometer, all these analyses were carried out at Cardiff University.

Photophysical analysis: Absorption spectra of compounds were recorded on air equilibrated solvents at room temperature with Agilent Cary 5000 UV-Vis spectrophotometer, using quartz HELLMA cells with path length of 1.0 cm. Emission spectra were recorded on Agilent Cary Eclipse fluorescence spectrofluorometer. Emission lifetime measurements were performed on a JobinYvon-Horiba FluoroHub single photon counting module, using Nano-LED pulsed source at 405 nm or 280 nm. Quantum yield values were calculated using Coumarin 153 in air equilibrated ethanol (Φ = 0.53) or rhodamine 6G in Ethanol (Φ = 0.94), following the method of Demas and Crosby.[1] Electrochemical characterization: Cyclic voltammetry experiments were performed at room temperature in dry nitrogen-purged ortho-dichlorobenzene (ODCB), CH_2Cl_2 or CH_3CN (previously filtered on alumina, 50 - 200 µm), with a Model 800 potentiostat (CH Instruments). The working electrode used is a glassy carbon S3 electrode (3 mm diameter), the counter electrode was a Pt spiral and a Ag wire was used as quasi-reference electrode (AgQRE). Working electrode and quasi-reference electrodes were polished on a felt pad with 0.05 or 0.3 µm alumina suspension and sonicated in deionized water for 1 minute before each experiment; the Pt wire was flame-cleaned. Tetrabutylammonium hexafluorophosphate ($TBAPF_6$) were added to the solution as supporting electrolytes at concentrations typically 2 orders of magnitude higher than the electroactive analyte. The couple ferrocene/ferrocenium was used as internal reference ($E_{1/2}^{ox}$=0.45 V in ODCB, $E_{1/2}^{ox}$=0.37 V in CH_2Cl_2). HOMO and LUMO energies were calculated from the first formal redox potentials (halfwave potentials) using equations: $E_{HOMO} = -(E_{1/2}^{ox} + 5.1\ eV)$; $E_{LUMO} = -(E_{1/2}^{red} + 5.1\ eV)$. In the cases where oxidation or reduction waves were not detected by means of cyclic voltammetry, HOMO or LUMO levels are calculated using the optical gap E_{opt}, considering the crossing point between normalized absorption and emissione spectra, recorded with the same experimental conditions, in the same solvent. The corresponding eV were calculated following equation: $E_{opt} = 1240 / \lambda_{cross}$ (nm).

X-ray measurements: Crystallographic studies were undertaken on single crystal mounted onto a MiTiGen Microloop TM using paratone oil and studied on an Agilent SuperNova Dual three-circle diffractometer using Cu-Kα (λ = 1.540598 E) or Mo-Kα (λ = 0.7093187 E) radiation and a CCD detector. Measurements were typically made at 150(1) K with temperatures maintained using an Oxford Cryostream unless otherwise stated. Data were collected, integrated and corrected for absorption using a numerical

absorption correction based on gaussian integration over a multifaceted crystal model within CrysAlisPro. The structures were solved by direct methods and refined against F2 within SHELXL-2013.

Electrostatic surface potential (ESP) were created at B3LYP/6-31G(d,p) level of theory and mapped on the van Der Waals surface of molecules up to an electron density of 0.001 electron/bohr3. ESP images were obtained with Gaussview 4. [2,3]

5.2 Material and General Methods

Chemicals were purchased from *Sigma Aldrich*, *Acros Organics*, *TCI, Apollo Scientific*, *Alfa Aesar* and *Fluorochem* and were used as received unless specified otherwise. Solvents were purchased from *Fluorochem*, *Sigma Aldrich* and *Acros Organics*. Deuterated solvents were purchased from *Eurisotop* and *Sigma Aldrich*. THF, Et_2O and CH_2Cl_2 were dried on a *Braun* MB SPS-800 solvent purification system. Et_3N was distilled on CaH_2 and then stored over KOH. DMF and pyridine were dried on molecular sieves 4 Å and then stored over molecular sieves 4 Å. Sulfuric acid (H_2SO_4 >95%) was purchased from *Fluorochem*. Low temperature baths were prepared using different solvent mixtures depending on the desired temperature: -84 °C with ethyl acetate/liq. N_2, -78 °C with acetone/dry ice and 0 °C with ice/H_2O. Anhydrous conditions were achieved by flaming two necked flasks with a heat gun under vacuum and purging with N_2. The inert atmosphere was maintained using N_2-filled balloons equipped with a syringe and needle that was used to penetrate the rubber stoppers used to close the flask's necks. Additions of liquid reagents were performed using dried plastic or glass syringes. All reactions were performed in dry conditions and under inert atmosphere unless otherwise stated.

5.3 Experimental Procedures

Synthesis of [8,8'-biisoquinoline]-7,7'-diol 3

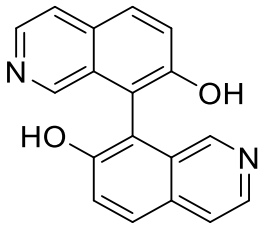

3

To a stirred solution of $CuCl_2 \cdot 2H_2O$ (2.82 g, 16.53 mmol) in MeOH (130 mL) was added a solution of benzylamine (5.91 mg, 55.11 mmol) in MeOH (30 mL) and the reaction mixture was stirred for 5 min. A solution of 7-hydroxylisoquinoline (1 g, 6.89 mmol) in MeOH (30 mL) was added and the reaction mixture stirred at rt for 16 h. During this period the colour of the mixture turned from green to brown. The reaction solvent was halved. The brown precipitate filtered and washed with MeOH. The crude was dissolved in a 5 mL of HCl 37 % aqueous solution and reprecipitate upon addition of 10 mL of NH_3 35% aqueous solution. The brown precipitate was filtered and washed with 30 mL of H_2O and 5 mL of MeOH yielding **3** as pure brown solid (614 mg, 62 %).

mp 170–175°C. IR (neat): cm^{-1} 3062.9, 3001.2, 2632.1, 2600.0, 2553.7, 2005.9, 1959.6, 1867.1, 1705.7, 1597.6, 1504.4, 1435.0, 1404.1, 1365.0, 1319.3, 1288.4, 1273.2, 1234.4, 1165.0, 1095.7, 1049.8, 972.2, 933.5, 825.5, 779.4, 740.6, 702.9, 655.0, 578.4, 540.7, 493.7, 439.7, 416.2. ^{1}H-NMR (300 MHz, DMSO-d_6) δ: 9.86 (s, 2H), 8.33 (broad d, *J* = 18.0 Hz, 4H), 7.98 (d, *J* = 9.0 Hz, 2H), 7.80 (s, 2H), 7.60 (d, *J* = 9.0 Hz, 2H). ^{13}C-NMR (125 MHz, DMSO-d_6) δ 154.6, 149.2, 140.3, 130.6, 128.6, 123.5, 114.15. HRMS (ES+): m/z $[M+H]^+$ calcd for ($C_{18}H_{13}N_2O_2$): 289.0977; found: 289.0977.

Synthesis of 1,7-diaza peri-xanthenoxantene 4

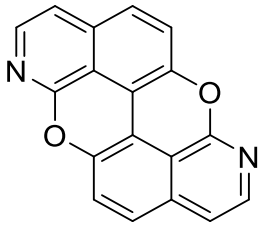

4

In a round bottomed flask, **3** (200 mg, 0.69 mmol) and CuO (496.6 mg, 6.24 mmol) were suspended in 3 mL of $PhNO_2$. The reaction mixture was stirred at 200 °C for 10 h. The solvent was evaporated under reduced pressure and the reaction mixture dissolved in hot THF (50 mL), then filtered on celite. The organic phase was concentrated under reduced pressure. The crude was purified through column chromatography on silica gel with eluent (toluene/THF 9:1) to give product **4** as a yellow solid (118 mg, 60%)

m.p. 182-185 °C. IR (neat): cm^{-1} 3039.8, 2954.9, 2916.3, 2854.6, 1905.6, 1805.3, 1743.6, 1697.3, 1620.2, 1581.6, 1473.6, 1427.3, 1319.3, 1226.7, 1064.7, 941.2, 833.2, 771.5, 725.2, 678.9, 586.3, 524.6, 493.7. ^{1}H-NMR (500 MHz, $CDCl_3$): δ 7.91 (d, *J* = 6.0 Hz, 2H), 7.50 (d, *J* = 9.0 Hz, 2H), 7.42 (d, *J* = 9.0, 1H), 7.09 (d, *J* = 6.0 Hz, 2H). ^{13}C-NMR (125 MHz, $CDCl_3$): δ 142.7, 125.5, 121.7, 115.9, 113.4, four carbon peaks are missing. HRMS (ES+): m/z $[M+H]^+$ calcd for ($C_{18}H_9N_2O_2$): 285.0664; found: 285.0670

Synthesis of [5,5'-biquinoline]-6,6'-diol 1

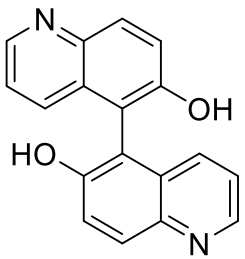

1

To a stirred solution of $CuCl_2 \cdot 2H_2O$ (2.82g, 16.53 mmol) in MeOH (130 mL) was added a solution of benzylamine (5.91 mg, 55.11 mmol) in MeOH (30 mL) and the solution was stirred for 5 min. A solution of quinolin-6-ol (1 g, 6.89 mmol) in methanol (30 mL) was added and the reaction mixture was stirred at r.t. for 16 h. During this period the colour of the mixture turned from green to brown. The reaction solvent was halved, and the brown precipitate filtered and washed with MeOH. The crude was dissolved in 5 mL of HCl 37 % solution and reprecipitated by adding 10 mL of NH_3 35%. The brown precipitate was filtered and washed with 30 mL of water and 5 mL of MeOH yielding product **1** as a brown solid (550 mg, 55 %).

mp 174–176°C. ^{1}H-NMR (500 MHz, DMSO-d) δ: 9.63 (s, 2H), 8.66 (s, 2H), 7.99 (d, *J* = 8.6 Hz, 2H), 7.56 (d, *J* = 8.6 Hz, 2H), 7.33 (m, 4H). ^{13}C-NMR (125 MHz, DMSO-d) δ 153.7, 147.2, 143.2, 132.7, 130.6, 129.3, 122.2, 121.8, 114.5. HRMS (EI+): m/z $[M]^+$

calcd for ($C_{18}H_{12}N_2O_2$): 288.0899; found: 288.0897 Characterization in accordance with literature.[4]

Synthesis of 3,9-diaza peri-xanthenoxantene 2

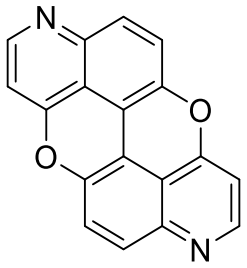

2

In a round bottomed flask, **1** (50 mg, 0.174 mmol) and CuO (137.9 mg, 1.73 mmol) were suspended in 1 mL of $PhNO_2$. The reaction mixture was stirred at 200 °C for 16 h. The solvent was distilled off under reduced pressure, the reaction mixture dissolved in hot THF (50 mL) and filtered on celite. The organic phase was concentrated under reduced pressure. The crude was purified through silica gel column chromatography (toluene/THF 7:3) to give product **2** as orange solid (14 mg, 28%).

m.p. 176-181 °C. IR (neat): cm^{-1} 3086.1, 3055.2, 2916.3, 2854.6, 1975.1, 1905.6, 177.5, 1720.5, 1620.1, 1573.9, 1465.9, 1404.1, 1342.6, 1257.5, 1211.3, 1134.1, 1080.1, 941.2, 894.9, 825.5, 779.2, 756.1, 735.95 663.5, 594.0, 563.2, 516.9, 486.0, 447.4, 408.9. ^{1}H-NMR (500 MHz, $CDCl_3$): δ 8.46 (d, *J* = 5.3 Hz, 2H), 7.64 (d, *J* = 9.3 Hz, 2H), 7.24 (d, *J* = 9.3 Hz, 2H), 6.61 (d, *J* = 5.3 Hz, 2H). ^{13}C-NMR (125 MHz, $CDCl_3$): δ 153.3, 143.2, 127.9, 120.6, 116.6, 111.9, 105.2, two carbon peaks missing. HRMS (ES+): m/z $[M+H]^+$ calcd for ($C_{18}H_9N_2O_2$): 285.0664; found: 285.0668

Synthesis of molecule 7

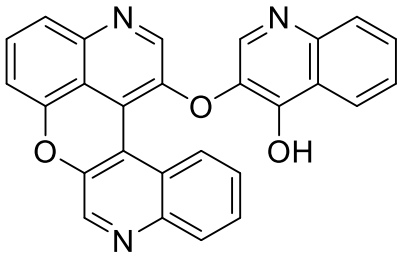

7

In a round bottomed flask, quinolin-3-ol (100 mg, 0.69 mmol) and CuCl (68 mg, 0.69 mmol) were dissolved in 1 mL of DMSO. The reaction mixture was stirred at 120 °C for 16 h. The reaction mixture was quenched with 3 mL of NH_4Cl aq. sat. solution, the organic phase extracted with AcOEt (10 mL x 3) and washed with brine (20 mL x 5). The organic phase was dried over $NaSO_4$ and evaporated under reduce pressure. The crude material was purified through column chromatography on silica gel with eluent (CH_2Cl_2/AcOEt 7:3) to give product 7 as a yellow solid (18 mg, 30%).

m.p. 186-189 °C. IR (neat): cm^{-1} 418.5, 432.0, 459.0, 484.1, 538.1, 563.2, 592.1, 611.4, 628.79, 688.9, 715.5, 759.9, 788.8, 817.8, 864.1, 883.4, 910.4, 945.1, 987.5, 1001.0, 1029.9, 1047.3, 1068.5, 1114.8, 1147.6, 1220.9, 1232.5, 1257.5, 1269.1, 1303.8, 1338.6, 1363.6, 1413.8, 1465.9, 1473.6, 1496.7, 1556.5, 1598.9, 1624.0, 2924.0, 2981.9, 3064.8, 3396.6. ^{1}H-NMR (500 MHz, $CDCl_3$): δ 8.97 (s, 1H), 8.79 (dd, *J* = 8.6, 0.8 Hz, 1H), 8.53 (s, 1H), 8.34 (s, 1H), 8.22 (dd, *J* = 8.2, 1.1 Hz, 1H), 8.02 (dd, *J* = 8.3, 0.9 Hz, 1H), 7.76 – 7.70 (m, 1H), 7.69 – 7.60 (m, 4H), 7.48 (ddd, *J* = 8.4, 6.9, 1.3 Hz, 1H), 7.41 (ddd, *J* = 8.1, 6.9, 1.1 Hz, 1H), 7.28 (dd, *J* = 6.9, 1.8 Hz, 1H).^{13}C-NMR (125 MHz, $CDCl_3$): δ 148.8, 148.4, 145.91, 144.7, 144.6, 144.5, 142.7, 135.0, 133.5, 132.1, 129.2, 128.1, 128.4, 128.3, 126.6, 126.4, 125.5, 123.7, 123.6, 121.8, 119.6, 119.5, 118.5, 115.7, 109.3, 107.0 (1 carbon peak is missing). LRMS (ASAP+): m/z $[M+H]^+$ calcd for ($C_{27}H_{15}N_3O_3$): 428.11; found: 428.12.

Synthesis of quinolin-3-yl diethylcarbamate 8

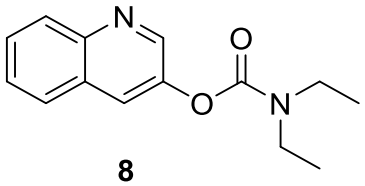

8

To a stirred solution of quinolin-3-ol (0.69 mmol, 100 mg) in 1 mL of dry pyridine at r.t. under N_2 was added dethylaminocarbonyl chloride (0.69 mmol, 0.16 mL). The resulting brown solution was heated to 100 °C and stirred for 16 h. After this time the mixture was allowed to cool to r.t. and partitioned between EtOAc (15 mL) and H_2O (10 mL). The pH of the aqueous layer was adjusted to 9 by the addition of aq. $NaHCO_3$ sat. solution and the layers were shaken and separated. The aqueous phase was extracted with EtOAc (15 mL x 3) and the combined organic dried on Na_2SO_4 and concentrated in vacuo. The crude residue was further purified in a silica gel column chromatography (EtOAc) yielding **8** as a colourless oil (113.00 mg, 67%).

IR (neat): cm^{-1} 428.2, 482.2, 555.5, 615.2, 748.3,759.9, 827.4, 908.4, 920.0, 956.6, 1001.0, 1045.4, 1076.2, 1093.6, 1147.6, 1207.4, 1255.6, 1307.7, 1352.1, 1409.9, 1425.4, 1463.9, 1498.6, 1568.1, 1604.7, 1641.4, 1714.7, 2873.9, 2931.0, 2974.2, 3059.1. ^{1}H-NMR (300 MHz, $CDCl_3$): δ 8.67 (broad s, 1H), 8.02 (broad d, *J* = 8.5 Hz, 1H), 7.88 (d, *J* = 2.5 Hz, 1H), 7.70 (dd, *J* = 8.2, 1.5 Hz, 1H), 7.57 (ddd, *J* = 8.5, 6.9, 1.5 Hz, 1H), 7.44 (ddd, *J* = 8.2, 6.9, 1.1 Hz, 1H), 3.37 (m, 4H), 1.16 (m, 6H).^{13}C-NMR (75 MHz, $CDCl_3$): δ 153.6, 146.2, 145.7, 144.9, 129.2, 128.6, 128.3, 127.5, 127.1, 125.9, 42.5, 42.0, 14.3, 13.3. HRMS (ES+): m/z $[M+H]^+$ calcd for ($C_{14}H_{17}N_2O_2$): 245.1290; found: 245.1296

Synthesis of [4,4'-biquinoline]-3,3'-diyl bis(diethylcarbamate) 9

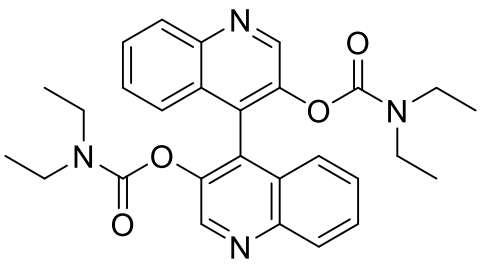

9

To a stirred solution of **8** (2.70 mmol, 660 mg) in 5 mL of dry THF was cooled down at -78 °C and LDA (3.51 mmol, 3.51 mL) added dropwise. The dark brown solution was stirred for 30 min, at –78 °C. In parallel, anhydrous $FeCl_3$ (2.70 mmol, 440 mg) was suspended in dry THF (5 mL) and cooled at -78 °C (dry powdered $FeCl_3$ had been previously dried at 120 °C at 0.5 mmHg for 16 h). The suspension of $FeCl_3$ was

carefully added to the dark brown solution. The resulting dark brown mixture was allowed to warm to 0 °C and stirred for 11 h. The mixture was quenched with NH_4Cl aq. sat. and diluted EtOAc with H_2O (2 mL) and extracted with EtOAc (20 mL x 3) and the combined organic phase dried on Na_2SO_4 and concentrated in *vacuo*. The crude residue was purified a silica gel column chromatography (petroleum ether/EtOAc 7:3) yielding **9** as a colourless oil (252 mg, 38%).

IR (neat): cm^{-1} 425.2, 486.3, 549.6, 617.3, 750.4, 757.5, 828.6, 908.5, 923.0, 957.5, 1008.4, 1043.4, 1077.2, 1095.6, 1145.7, 1202.9, 1254.9, 1308.2, 1355.1, 1411.2, 1425.9, 1468.0, 1405.8, 1571.1, 1601.4, 1649.4, 1718.8, 2877.0, 2932.8, 2976.1, 3060.1. ^{1}H-NMR (500 MHz, $CDCl_3$): δ 9.04 (s, 2H), 8.21 (broad dd, *J* = 8.1 Hz, 2H), 7.69 (broad m, 2H), 7.43 (broad m, 2H), 7.32 (broad dd, 2H), 3.09 (m, 4H), 2.75 (m, 4H), 0.88 (t, *J* = 7 Hz, 6H) 0.43 (t, *J* = 7 Hz, 6H). ^{13}C-NMR (75 MHz, $CDCl_3$): δ 152.6, 147.2, 145.5, 142.8, 129.7, 129.6, 128.9, 127.6, 127.1, 125.5, 42.3, 4.7, 13.2, 13.0. HRMS (ES+): m/z $[M+H]^+$ calcd for ($C_{28}H_{31}N_4O_4$): 487.2345; found: 487.2341

Synthesis of [4,4'-biquinoline]-3,3'-diol 5

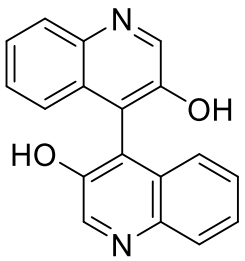

5

A solution of diaryl-dicarbamate in 10 wt.% methanolic KOH (7 mL) was stirred at reflux for 18 h. The resulting solution was cooled to r.t. and concentrated in *vacuo*. The residue was dissolved in H_2O (5 mL) and the pH adjusted to 7 by the careful addition of 2 M aq. HCl. The aqueous phase was saturated with NaCl and the formed precipitate filtered and washed with H_2O and cold EtOH. The precipitate was dried under *vacuo* yielding **9** as a white solid (80 mg, 54%).

m.p. 176-179 °C. IR (neat): cm^{-1} 403.1, 418.5, 457.1, 466.7, 480.2, 514.9, 563.2, 655.8, 669.3, 719.4, 746.4, 808.1, 844.8, 883.4, 920.5, 954.7, 1062.7, 1103.2, 1136.0, 1151.5, 1195.8, 1220.9, 1296.1, 1330.8, 1388.7, 1446.6, 1490.9, 1506.4, 1573.9, 1600.9, 1627.9, 1716.5, 1749.4, 2358.9, 2926.0, 2980.0, 3080.3. ^{1}H-NMR (300 MHz, DMSO-d_6): δ 10.1 (s, 2H), 8.8 (s, 2H), 8.03 (dd, *J* = 8.4 Hz, *J* = 0.9 Hz, 2H), 7.53 (ddd, *J* = 8.3 Hz, *J* = 6.8 Hz, *J* = 1.4 Hz, 2H), 7.35 (ddd, *J* = 8.2 Hz, *J* = 6.9 Hz, *J* = 1.2 Hz, 2H), 7.03 (dd, *J* = 8.3 Hz, *J* = 1.0 Hz, 2H). ^{13}C-NMR (75 MHz, DMSO-d_6): δ 148.6, 143.6, 142.5,

129.1, 127.9, 127.0, 125.8, 124.2, 120.2. HRMS (ES+): m/z $[M+H]^+$ calcd for ($C_{18}H_{13}N_2O_2$): 289.0977; found: 289.0982

Synthesis of 4,10-diaza peri-xanthenoxanten 6

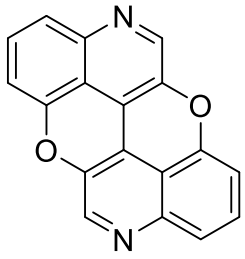

6

In a round bottomed flask, **5** (50 mg, 0.174 mmol) and CuO (137.9 mg, 1.73 mmol) were suspended in 1 mL of $PhNO_2$. The reaction mixture was stirred at 200 °C for 16 h. The solvent was evaporated under reduced pressure and the reaction mixture dissolved in hot THF (50 mL) and filtered on celite. The organic phase was concentrated under reduced pressure. The crude was purified through column chromatography on silica gel with eluent (toluene/THF 9:1) to give product **6** as orange solid (10 mg, 20%).

m.p. 180-184 °C. IR (neat): cm^{-1} 403.1, 418.5, 457.3, 466.7, 480.2, 514.9, 563.2, 655.8, 669.3, 719.4, 746.5, 808.1, 844.8, 883.4, 920.0, 954.7, 1062.7, 1103.2, 1136.0, 1151.5, 1195.7, 1220.9, 1296.1, 1330.8, 1388.7, 1446.6, 1465.9, 1490.9, 1506.4, 1573.9, 1600.9, 1627.9, 1683.8, 1716.6, 1749.4, 2358.9, 2926.0, 2980.0, 3080.3.^{1}H-NMR (500 MHz, $CDCl_3$): δ 8.53 (s, 2H), 7.48 (m, 4H), 6.91 (dd, *J* = 7.2, J = 1.2 Hz, 2H) ^{13}C-NMR (125 MHz, $CDCl_3$): δ 151.2, 145.5, 141.8, 141.3, 130.5, 122.2, 116.6, 115.8, 110.1. HRMS (ES+): m/z $[M+H]^+$ calcd for ($C_{18}H_9N_2O_2$): 285.0664; found: 285.0667

Synthesis of isoquinolin-3-yl diethylcarbamate 12

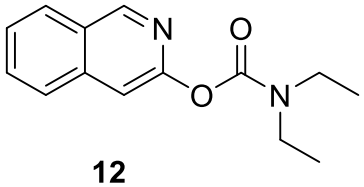

12

To a stirred solution of isoquinolin-3-ol (0.69 mmol, 100 mg) in 1 mL of dry pyridine at r.t. under N_2 was added dethylaminocarbonyl chloride (1.38 mmol, 0.16 mL). The resulting brown solution was heated to 100 °C and stirred for 16 h. After this time the mixture was allowed to cool to r.t. and partitioned between EtOAc (15 mL) and H_2O (10 mL). The pH of the aqueous layer was adjusted to 9 by the addition of $NaHCO_3$ aq. sat. solution and the layers were shaken and separated. The aqueous phase was extracted with EtOAc (15 mL x 3) and the combined organic dried on Na_2SO_4 and concentrated in vacuo. The crude residue was further purified in a silica gel column chromatography (EtOAc) yielding **12** as a yellow oil (59.00 mg, 35%).

IR (neat): cm^{-1} 426.2, 481.2, 557.5, 617.2, 756.3,759.9, 827.5, 901.4, 923.0, 956.7, 1006.5, 1051.4, 1074.8, 1096.6, 1149.9, 1207.4, 1265.2, 1301.0, 1363.1, 1409.5, 1433.2, 1455.2, 1520.6, 1578.1, 1609.1, 1646.9, 1730.0, 2886.0, 2935.1, 2965.3, 3063.1. ^{1}H-NMR (300 MHz, $CDCl_3$): δ 9.08 (s, 1H), 7.96 (dd, *J* = 8.1, 0.9, 1H), 7.79 (dd, *J* = 8.3, 0.9, 1H), 7.66 (ddd, *J* = 8.3, 6.8, 0.9 Hz, 1H), 7.52 (ddd, *J* = 8.1, 6.8, 0.9 Hz, 1H), 7.47 (s, 1H), 3.46 (q, *J* = 7.1 Hz, 2H), 3.36 (q, *J* = 7.1, Hz, 2H), 1.24 (t, *J* = 7.0 Hz, 3H), 1.23 (t, *J* = 7.1, 3H).^{13}C-NMR (75 MHz, $CDCl_3$): δ 154.7, 154.0, 151.6, 138.6, 130.7, 127.6, 127.3, 126.6, 126.4, 110.7, 42.3, 42.1, 14.4, 13.4.HRMS (ES+): m/z $[M+H]^+$ calcd for ($C_{14}H_{17}N_2O_2$): 245.1290; found: 245.1299

Synthesis of [4,4'-biisoquinoline]-3,3'-diyl bis(diethylcarbamate) 13

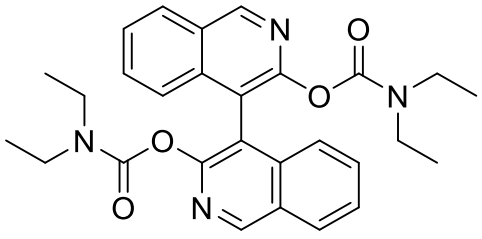

13

To a stirred solution of **12** (2.70 mmol, 660 mg) in 5 mL of dry THF was cooled down at -78 °C and LDA (3.51 mmol, 3.51 mL) added dropwise. The dark brown solution was stirred for 30 min, at –78 °C. In parallel, anhydrous $FeCl_3$ (2.70 mmol, 440 mg) was suspended in dry THF (5 mL) and cooled at -78 °C (powdered $FeCl_3$ had been previously dried at 120 °C at 0.5 mmHg for 16 h). The suspension of $FeCl_3$ was

carefully added to the dark brown solution. The resulting dark brown mixture was allowed to warm to 0 °C and stirred for 11 h. The mixture was quenched with sat. aq. NH_4Cl and diluted EtOAc with H_2O (2 mL) and extracted with EtOAc (20 mL x 3) and the combined organic phase dried on Na_2SO_4 and concentrated in *vacuo*. The crude residue was purified by silica gel column chromatography (petroleum ether/EtOAc 7:3) yielding **13** as a colourless oil (252 mg, 38%).

IR (neat): cm^{-1} 430.2, 487.3, 551.6, 616.5, 753.9, 753.6, 825.6, 905.1, 925.5, 960.5, 1010.23, 1048.3, 1072.8, 1097.7, 1165.5, 1208.0, 1254.1, 1310.2, 1357.1, 1419.2, 1465.2, 1451.2, 1408.8, 1575.1, 1606.4, 1653.5, 1721.5, 2875.5, 2933.1, 2977.3, 3062.1. ^{1}H-NMR (300 MHz, $CDCl_3$): δ 9.22 (s, 2H), 8.09 – 8.00 (m, 2H), 7.61 – 7.48 (m, 4H), 7.40 – 7.33 (m, 2H), 3.27 – 2.77 (m, 8H), 0.79 (t, *J* = 7.1 Hz, 6H), 0.64 (t, *J* = 7.0 Hz, 6H).^{13}C-NMR (75 MHz, $CDCl_3$): δ 153.1, 152.9, 152.1, 138.1, 131.1, 127.7, 127.3, 126.8, 125.3, 115.4, 42.0, 41.8, 13.5, 13.0. HRMS (ES+): m/z $[M+H]^+$ calcd for ($C_{28}H_{31}N_4O_4$): 487.2345; found: 487.2347.

Synthesis of [4,4'-biisoquinoline]-3,3'-diol 10

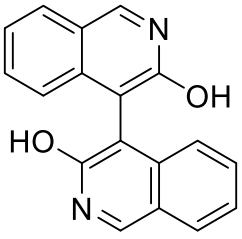

10

A solution of **13** (47 mg, 0.97 mmol) in 10 wt.% methanolic KOH (10 mL) was stirred at reflux for 18 h. The resulting solution was cooled to r.t. and concentrated in *vacuo*. The residue was dissolved in H_2O (7 mL) and the pH adjusted to 7 by a careful addition of 2 M aq. HCl. The aqueous phase was saturated with NaCl and the formed precipitate filtered and washed with H_2O and cold EtOH. The precipitate was dried under *vacuo* yielding **10** as a yellow solid (26 mg, 92%).

m.p. 177-180 °C. IR (neat): cm^{-1} 405.1, 421.0, 455.2, 468.7, 482.0, 511.9, 563.5, 659.8, 667.8, 721.6, 743.3, 805.0, 845.2, 888.0, 921.1, 953.2, 1068.0, 1105.4, 1136.9, 1151.5, 1197.6, 1233.0, 1293.1, 1338.0, 1386.8, 1448.5, 1493.2, 1502.9, 1571.8, 1605.4, 1625.2, 1717.8, 1754.8, 2352.2, 2930.1, 2983.6, 3082.4. ^{1}H-NMR (500 MHz, DMSO-d_6): δ 10.81 (s, 2H), 9.01 (s, 2H), 8.03 (d, *J* = 8.2 Hz, 2H), 7.41 (m, 2H), 7.31 (m, 2H), 6.96 (d, *J* = 8.6 Hz, 2H).^{13}C-NMR (125 MHz, DMSO-d_6): δ 158.4, 138.5, 130.5, 128.2,

123.2, 123.1, (3 carbon peaks are missing). HRMS (ES+): m/z $[M+H]^+$ calcd for ($C_{18}H_{13}N_2O_2$): 289.0977; found: 289.0981.

Synthesis of quinolin-3-yl diethylcarbamate 16

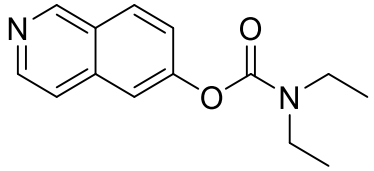

16

To a stirred solution of isoquinolin-6-ol (0.69 mmol, 100 mg) in 1 mL of dry pyridine at r.t. under N_2 was added with dethylaminocarbonyl chloride (1.38 mmol, 0.16 mL). The resulting brown solution was heated to 100 °C and stirred for 16 h. After this time the mixture was allowed to cool to r.t. and partitioned between EtOAc (15 mL) and H_2O (10 mL). The pH of the aqueous layer was adjusted to 9 by the addition of sat. aq. solution $NaHCO_3$ and the layers were shaken and separated. The aqueous phase was extracted with EtOAc (15 mL x 3) and the combined organic dried on Na_2SO_4 and concentrated in vacuo. The crude residue was further purified by silica gel column chromatography (EtOAc) yielding **16** as a yellow oil (161.00 mg, 95%).

IR (neat): cm^{-1} 423.2, 478.3, 566.8, 623.5, 751.7,755.4, 828.7, 905.17, 922.3, 959.0, 1022.1, 1015.9, 1075.5, 1089.0, 1150.2, 1208.4, 1252.3, 1312.5, 1358.1, 14011.0, 1423.9, 1458.4, 1496.7, 1552.8, 1603.5, 1648.3, 1716.5, 2879.0, 2933.5, 2974.5, 3072.1. ^{1}H-NMR (300 MHz, $CDCl_3$): δ 9.29 (s, 1H), 8.54 (d, *J* = 4.7 Hz, 1H), 7.97 (d, *J* = 8.9 Hz, 1H), 7.62 (d, *J* = 4.7 Hz, 1H), 7.58 (d, *J* = 2.2 Hz, 1H), 7.40 (dd, *J* = 8.9, 2.2 Hz, 1H), 3.66 – 3.17 (m, 4H), 1.35 –1.17 (m, 6H). ^{13}C-NMR (75 MHz, $CDCl_3$): δ 153.6, 152.7, 152.0, 143.3, 136.7, 129.1, 126.4, 123.2, 120.3, 117.0, 42.4, 42.1, 14.3, 13.4. HRMS (ES+): m/z $[M+H]^+$ calcd for ($C_{14}H_{17}N_2O_2$): 245.1290; found: 245.1292

Synthesis of 5-hydroxyisoquinolin-6-yl diethylcarbamate 18

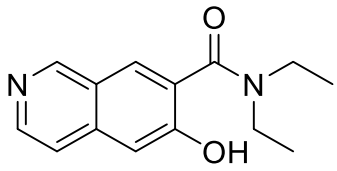

18

To a stirred solution of **16** (0.49 mmol, 120 mg) in 5 mL of dry THF was cooled down at -78 °C and LDA (0.64 mmol, 0.64 mL) added dropwise. The dark brown solution was stirred for 30 min at –78 °C. In parallel, anhydrous $FeCl_3$ (0.49 mmol, 79.7 mg) was suspended in dry THF (5 mL) and cooled at -78 °C (powdered $FeCl_3$ had been previously dried at 120 °C at 0.5 mmHg for 16 h). The suspension of $FeCl_3$ was carefully added to the dark brown solution. The resulting dark brown mixture was allowed to warm to 0 °C and stirred for 11 h. The mixture was quenched with sat. aq. NH_4Cl and diluted EtOAc with H_2O (2 mL) and extracted with EtOAc (20 mL x 3) and the combined organic phase dried on Na_2SO_4 and concentrated in *vacuo*. The crude residue was purified a silica gel column chromatography (petroleum ether/EtOAc 7:3) yielding **18** as a colourless oil (252 mg, 38%).

m.p. = 86-93 °C. IR (neat): cm^{-1} 405.0, 410.8, 416.6, 443.3, 472.5, 530.4, 545.8, 578.6, 640.3, 665.4, 721.3, 736.8, 750.3, 771.5, 815.8, 864.1, 896.9, 941.2, 972.1, 1033.8, 1068.5, 1095.5, 1155.3, 1166.9, 1186.2, 1217.8, 1234.4, 1274.9, 1290.3, 1311.5, 1336.6, 1359.8, 1379.1, 1409.9, 1427.3, 1475.5, 1616.3, 2933.7, 2978.0.^{1}H-NMR (300 MHz, CD_3OD): δ 10.63 (s, 1H), 9.85 (d, *J* = 6.0 Hz, 1H), 9.50 (s, 1H), 9.18 (d, *J* = 6.0 Hz, 1H), 8.75 (s, 1H), 5.17 (m, 2H), 4.82 (m, 2H), 2.85 (t, *J* = 6.7 Hz, 3H), 2.67 (t, *J* = 6.8 Hz, 3H), one proton peak is missing. ^{13}C-NMR (75 MHz, CD_3OD): δ 172.8, 154.9, 145.6, 142.2, 133.6, 131.3, 127.1, 123.3, 111.4, 47.2, 43.2, 16.6, 15.6, (1 carbon is missing). HRMS (ES+): m/z $[M+H]^+$ calcd for ($C_{14}H_{17}N_2O_2$): 245.1290; found: 245.1292

Synthesis of 1,9-diaza peri-xanthenoxantene

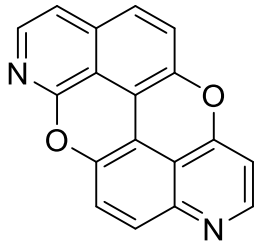

20

To a stirred solution of $CuCl_2 \cdot 2H_2O$ (564 mg, 3.31 mmol) in MeOH (20 mL) was added a solution of benzylamine (1.18 g, 11.02 mmol) in MeOH (20 mL) and the solution was stirred for 5 min. A solution of quinolin-6-ol (100 mg, 0.69 mmol) and isoquinolin-7-ol (100 mg, 0.69 mmol) in MeOH (40 mL) was added and the reaction mixture was stirred at r.t. for 16 h. During this period the colour of the mixture turned from green to brown. The reaction solvent was halved, and the brown precipitate filtered and washed with MeOH. The crude was dissolved in 5 mL of HCl 37 % solution and reprecipitate by adding 10 mL of NH_3 35%. The brown precipitate was filtered and washed with 30 mL of water and 5 mL of MeOH. The brown solid and CuO (1.08 g, 13.60 mmol) were suspended in 1 mL of $PhNO_2$. The reaction mixture was stirred at 200 °C for 16 h. The solvent was evaporated under reduce pressure, the reaction mixture dissolved in hot THF (50 mL) and filtered on celite. The organic phase was concentrated under reduced pressure. The crude was purified by silica gel column chromatography (toluene/THF 7:3) to give product **20** as orange solid (12 mg, 3%).

m.p. 178-185 °C. IR (neat): cm^{-1} 422.2, 458.2, 467.2, 483.0, 515.0, 559.6, 657.2, 673.0, 717.5, 747.7, 801.8, 834.3, 886.1, 921.5, 961.0, 1059.7, 1107.8, 1134.9, 1155.5, 1196.2, 1215.6, 1298.1, 1333.7, 1395.3, 1453.3, 1488.0, 1495.3, 1505.0, 1577.5, 1603.2, 1628.6, 1678.5, 2361.0, 2933.5, 2978.5, 3083.0. ^{1}H-NMR (500 MHz, $CDCl_3$): δ 8.52 (d, *J* = 5.2 Hz, 1H), 7.87 (d, *J* = 6.0 Hz, 1H), 7.71 (d, *J* = 9.3 Hz, 1H), 7.38 (d, *J* = 9.0 Hz, 1H), 7.38 (d, *J* = 9.3 Hz, 2H), 7.25 (d, *J* = 9.0 Hz, 1H), 7.02 (d, *J* = 6.0 Hz, 1H), 6.65 (d, *J* = 5.2 Hz, 1H).^{13}C-NMR (125 MHz, $CDCl_3$): δ 160.5, 159.7, 153.6, 146.7, 144.6, 144.6, 143.0, 135.3, 128.7, 125.0, 121.2, 121.0, 116.7, 115.8, 115.8, 115.1, 110.2, 105.2. HRMS (AP+): m/z $[M+H]^+$ calcd for ($C_{18}H_9N_2O_2$): 285.0664; found: 285.0666.

Synthesis of methyl(naphthalen-2-yl)sulfane 40

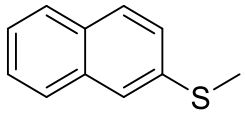

40

In a round bottomed flask, 2-thionaphthol (500 mg, 3.12 mmol), K_2CO_3 (863 mg, 6.24 mmol) were dissolved in dry DMF (10 mL). The solution was degassed bubbling N_2 and CH_3I (2.21 g, 15.6 mmol) was added. The reaction mixture was stirred at 60 °C for 16 h. The reaction was diluted with H_2O (10 mL) was added and the resulting biphasic solution extracted with EtOAc (70 mL x 3). The combined organic layer was washed with brine, dried over Na_2SO_4, and concentrated under reduced pressure. The residue was purified by silica gel chromatography with eluent (Petroleum ether/CH_2Cl_2 = 7/3) to provide product **33** (525 mg, 3.01 mmol, 97%) as a white solid.

m.p. 57-59 °C. ^{1}H-NMR (300 MHz, $CDCl_3$): δ 7.80 – 7.76 (m, *J* = 0.8 Hz, 1H), 7.76 – 7.71 (m, 2H), 7.61 (dd, *J* = 1.9, 0.6 Hz, 1H), 7.50 – 7.35 (m, 3H), 2.59 (s, 3H).^{13}C-NMR (75 MHz, $CDCl_3$): δ 136.2, 134.0, 131.4, 128.3, 127.8, 126.9, 126.6, 125.8, 125.3, 123.5, 15.9. HRMS (EI+): m/z $[M]^+$ calcd for ($C_{11}H_{10}S$): 174.0503; found: 174.0500. Characterization in accordance with literature.[5]

Synthesis of 2-(methylsulfinyl)naphthalene 39

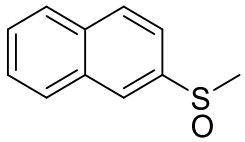

39

In a round bottomed flask molecule **40** (408 mg, 2.34 mmol) and $NaIO_4$ (551 mg, 2.58 mmol)were dissolved in H_2O (20 mL) and acetone (40 mL). The reaction mixture was stirred for 16 h at 50 °C. 25 mL of H_2O was added to the reaction mixture, the organic phase extracted with AcOEt (50 mL x 3), dried on Na_2SO_4 and concentrated under reduced pressure. The residue was purified by silica gel chromatography using EtOAc as eluent to provide product **34** as a white solid (403 mg, 90%).

m.p. 105-107 °C.^{1}H-NMR (300 MHz, $CDCl_3$): δ 8.22 (dd, *J* = 1.0, 0.6 Hz, 1H), 7.99 (d, *J* = 9.0 Hz, 1H), 7.96 – 7.87 (m, 2H), 7.63 – 7.56 (m, 3H), 2.79 (s, 3H).^{13}C-NMR (125 MHz, $CDCl_3$): δ 142.8, 134.5, 133.0, 129.7, 128.6, 128.1, 127.9, 127.5, 124.1, 119.5, 43.9. HRMS (AP+): m/z $[M+H]^+$ calcd for ($C_{11}H_{11}OS$): 191.0531; found: 191.0531. Characterization in accordance with literature.[6]

Synthesis of 2'-(methylthio)-[1,1'-binaphthalen]-2-ol 32

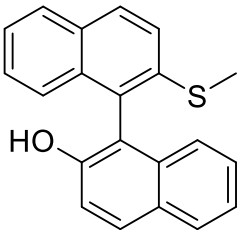

32

To a solution of nathalylmethyl sulfoxide **39** (200 mg, 1.06 mmol) and 2-naphthol (305 mg, 2.11 mmol) in CH_2Cl_2 (3 mL) at r.t. was added trifluoroacetic anhydride (333 mg, 1.59 mmol) in one portion and stirred at r.t. for 1 h. The reaction mixture was quenched with saturated aqueous solution of $NaHCO_3$. The resulting biphasic solution was extracted with EtOAc (15 mL × 3). The combined organic layer was washed with brine, dried over Na_2SO_4, and concentrated under reduced pressure. The residue was purified by silica gel chromatography with an eluent (Petroleum Eather/CH_2Cl_2 = 1:1) to provide product **32** (232 mg, 69 %) as a white solid.

(300 MHz, $CDCl_3$): 8.03 (dd, *J* = 8.8, 0.4 Hz, 1H), 7.98 – 7.86 (m, 3H), 7.60 (d, *J* = 8.8 Hz, 1H), 7.44 (ddd, *J* = 8.1, 6.8, 1.2 Hz, 1H), 7.39 – 7.29 (m, 3H), 7.28 – 7.23 (m, 1H), 7.16 (ddd, *J* = 8.5, 1.2, 0.7 Hz, 1H), 6.97 (ddd, *J* = 8.3, 1.3, 0.6 Hz, 1H), 4.82 (s, 1H), 2.44 (s, 3H). ^{13}C-NMR (125 MHz, $CDCl_3$): δ 151.1, 139.0, 133.4, 133.3, 131.5, 130.6, 129.9, 129.3, 128.4, 128.3, 127.7, 126.9, 125.7, 124.9, 124.4, 123.7, 122.8, 119.6, 117.7, 116.6, 15.5. HRMS (ES+): m/z $[M+H]^+$ calcd for ($C_{21}H_{17}OS$): 317.1000; found: 317.1004. Characterization in accordance with literature.[7]

Synthesis of 2'-(methylsulfinyl)-[1,1'-binaphthalen]-2-ol 31

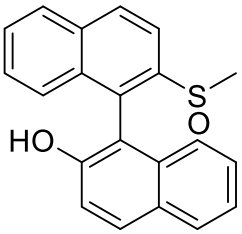

31

To a solution of **32** (58 mg, 0.18 mmol) in acetone (6 mL) was added a solution of $NaIO_4$ (43 mg, 0.2 mmol) in H_2O (3 mL) and stirred at 55 °C for 6 h. The reaction mixture was diluted in 10 mL of H_2O and the organic phase extracted with EtOAc (10 mL x 3) and concentrated under reduced pressure. The reaction crude was purified by

silica gel chromatography eluting with EtOAc to provide product **31** (51 mg, 84 %) as a white solid.

m.p. 132-135 °C. IR (neat): cm^{-1} 418.5, 435.9, 470.6, 495.7, 532.3, 559.3, 576.7, 615.2, 630.2, 667.3, 684,7, 744.5, 773.4, 860.5, 935.4, 968.2, 1120.6, 1174.6, 1203.58, 1062.7, 1267.2, 1313.5, 1346.3, 1379.1, 1431.1, 1465.90 1500.6, 1581.6, 1595.1, 1618.2, 2918.3, 2980.0, 3053.3, 3390.8, 3485.3. ^{1}H-NMR (500 MHz, $CDCl_3$): δ 10.02 (s, 1H), 8.33 (d, *J* = 8.6 Hz, 1H), 8.14 (d, *J* = 8.6, 1H), 8.13 (d, *J* = 7.9, 1H) , 7.99 (d, *J* = 8.9, 1H), 7.93 (d, *J* = 7.9, 1H), 7.63 (ddd, *J* = 8.1, 6.8, 1.2 Hz, 1H), 7.42 (ddd, *J* = 8.2, 6.8, 1.2 Hz, 1H), 7.35 (d, *J* = 8.9, 1H), 7.33 – 7.32 (m, 2H), 7.15 (d, *J* = 8.2 Hz, 1H), 6.79 (d, *J* = 8.1 Hz, 1H), 2.62 (s, 3H). ^{13}C-NMR (125 MHz, $CDCl_3$): δ 153.3, 143.1, 134.3, 133.1, 132.1, 131.8, 130.5, 129.6, 128.5, 128.1, 127.8, 127.5, 127.3, 127.1, 125.8, 123.2, 123.0, 119.1, 118.0, 113.3, 42.3. HRMS (ES+): m/z $[M+H]^+$ calcd for ($C_{21}H_{17}O_2S$): 333.0949; found: 333.0952.

Synthesis of (2'-methoxy-[1,1'-binaphthalen]-2-yl)(methyl)sulfane 36

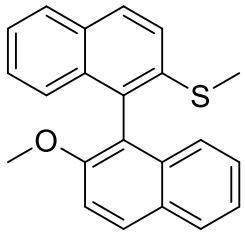

36

To a solution of **32** (3.5 g, 11.06 mmol) in dry acetone (25 mL) K_2CO_3 (3.06 g, 22.12 mmol) was added under N_2 atmosphere and the solution stirred at r.t. for 15 min. CH_3I (7.85 g, 55.31 mmol) was added and the solution stirreded at 60 °C for 16 h. H_2O (25 mL) was added and the resulting biphasic solution was extracted with EtOAc (100 mL × 3). The combined organic layer was washed with brine, dried over Na_2SO_4, and concentrated under reduced pressure. The residue was purified by silica gel chromatography with eluent (Petroleum ether/CH_2Cl_2 = 7:3) to provide product **36** (3.25 g, 0.183 mmol, 89 %) as a white solid.

m.p. 110-122 °C. IR (neat): cm^{-1} 405.0, 420.4, 435.9, 476.4, 565.1, 594.0, 615.2, 628.8, 669.3, 707.8, 771.5, 781.1, 802.3, 858.3, 873.7, 904.6, 948.9, 1018.4, 1049.2, 1049.2, 1080.1, 1126.4, 1145.7, 1178.5, 1246.0, 1328.9, 1346.3, 1463.9, 1500.6, 1577.7, 1591.2, 11618.2, 2835.3, 2916.3, 299.4, 3047.5.^{1}H-NMR (300 MHz, CD_2Cl_2): δ 7.96 (d, J = 9.0 Hz, 1H), 7.89 (d, *J* = 8.6 Hz, 1H), 7.84 – 7.78 (m, 2H), 7.51 (d, *J* = 8.6 Hz, 1H), 7.41 (d, *J* = 9.0 Hz, 1H), 7.31 (ddd, *J* = 8.1, 6.8, 1.2 Hz, 1H), 7.24 (ddd, *J* = 8.1,

6.8, 1.2 Hz, 1H), 7.18 – 7.08 (m, 2H), 6.95 (ddd, *J* = 8.5, 2.0, 0.8 Hz, 1H), 6.85 (ddd, *J* = 8.5, 2.0, 0.8 Hz, 1H), 3.71 (s, 3H), 2.32 (s, 3H). ^{13}C-NMR (125 MHz, $CDCl_3$): δ 155.0, 136.4, 133.5, 133.2, 131.4, 130.2, 129.3, 128.5, 128.1, 128.1, 126.8, 126.7, 125.4, 125.0, 124.8, 123.8, 123.3, 120.9, 114.1, 57.0, 16.0, 1 carbon peak is missing. HRMS (AP+): m/z $[M+H]^+$ calcd for ($C_{22}H_{19}O_1S$): 331.1157; found: 331.1156.

Synthesis of 2-methoxy-2'-(methylsulfinyl)-1,1'-binaphthalene 35

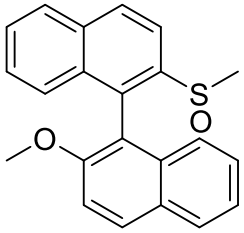

35

To a solution of **36** (3.5 g, 11.06 mmol) in dry acetone (25 mL) K_2CO_3 (3.06 g, 22.12 mmol) was added under N_2 atmosphere and the solution stirred at r.t. for 15 min. CH_3I (7.85 g, 55.31 mmol) was added and the solution stirred at 60 °C for 16 h. H_2O (25 mL) was added and the resulting biphasic solution was extracted with EtOAc (100 mL × 3). The combined organic layer was washed with brine, dried over Na_2SO_4, and concentrated under reduced pressure. The residue was purified by silica gel chromatography with eluent (Petroleum Eather/CH_2Cl_2 = 7:3) to provide product **35** (3.25 g, 89 %) as a white solid.

m.p. 119-123 °C. IR (neat): cm^{-1} 408.9, 418.5, 437.8, 497.3, 628.7, 678.9, 709.8, 746.4, 775.3, 867.9, 904.6, 945.1, 1018.4, 1043.4, 1076.2, 1122.5, 1147.6, 1247.9, 1259.5, 1332.8, 1355.9, 1431.1, 1462.0, 1506.4, 1593.2, 1620.2, 1732.0, 2839.2, 2935.6, 2991.9, 3055.2. ^{13}C-NMR (125 MHz, $CDCl_3$): δ 154.3, 142.7, 134.7, 133.6, 133.2, 132.3, 131.1, 131.0, 130.0, 129.9, 128.9, 128.7, 128.5, 128.5, 128.4, 127.9, 127.6, 127.5, 127.4, 127.3, 127.1, 126.3, 126.2, 124.6, 124.2, 124.2, 123.7, 119.0, 119.0, 116.6, 113.3, 112.4, 56.4, 56.0, 42.6, 42.3. (diasteroisomer mixture) HRMS (EI+): m/z $[M]^+$ calcd for ($C_{22}H_{18}O_2S$): 346.1028; found: 346.1027.

Synthesis of 1-methoxydibenzo[a,kl]thioxanthene 34

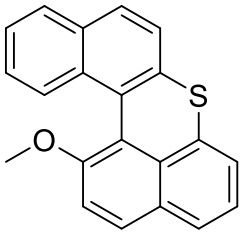

34

In a dry round bottomed flask **35** (300 mg, 0.67 mmol) was dissolved in 2 mL of TfOH under N2 atmosphere and stirred at r.t. for 16 h. To the reaction mixture, 16 mL of H_2O and 4 of pyridine were added and heated at 100 °C for 1 h. The reaction mixture was diluted with EtOAc (25 mL) and the organic phase extracted with EtOAc (20 mL x 3). The combined organic phases were dried over Na_2SO_4 and concentrated under reduced pressure. The reaction crude was purified by silica gel chromatography with an eluent (Petroleum Ether/EtOAc = 95:5) to provide product **34** as a yellow solid (7 mg, 3% yield).

m.p. 123-129 °C. IR (neat): cm^{-1} 420.4, 462.9, 497.6, 520.7, 547.7, 621.0, 678.9, 746.4, 777.9, 858.3, 918.1, 977.9, 1039.6, 1070.4, 1082.0, 1124.5, 1149.5, 1166.9, 1203.8, 1219.0, 1298.0, 1323.1, 1419.6, 1448.5, 1458.1, 1546.9, 1577.7, 1604.7, 2833.4, 2927.9, 3049.4. ^{1}H-NMR (300 MHz, CD_2Cl_2): δ 7.85 – 7.77 (m, 2H), 7.72 (d, J = 8.5 Hz, 1H), 7.56 (dd, J = 7.9, 1.2 Hz, 1H), 7.52 – 7.34 (m, 5H), 7.26 (qd, J = 7.5, 4.3 Hz, 2H), 3.75 (s, 3H).^{13}C-NMR (125 MHz, $CDCl_3$): δ 155.3, 135.8, 134.9, 133.4, 130.8, 130.0, 129.5, 128.9, 128.6, 128.3, 126.7, 126.5, 125.7, 125.6, 124.7, 124.7, 124.5, 121.2, 117.6, 116.0, 56.1. HRMS (ASAP+): m/z $[M+H]^+$ calcd for ($C_{21}H_{15}OS$): 315.0844; found: 315.0842.

Synthesis of 1-methoxydibenzo[a,kl]thioxanthene 7,7-dioxide 38

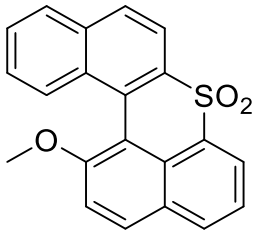

38

To a solution of **34** (50 mg, 0.16 mmol) in $CHCl_3$ (2 mL) mCPBA (82.3 mg, 0.48 mmol) was added and the reaction mixture stirred for 60 °C for 16 h. The reaction mixture was quenched with H_2O (5 mL) and the organic phase extracted with EtOAc (25 mL x 3). The combined organic phase was dried over Na_2SO_4 and concentrated under reduced

pressure. The reaction crude was purified by silica gel chromatography with eluent (Petroleum ether/CH_2Cl_2/EtOAc = 5/2/3) to provide product **38** as a yellow solid (54 mg, 98% yield.

m.p. 152-157 °C. IR (neat): cm^{-1} 465.0, 496.6, 523.9, 551.8, 623.2, 673.5, 741.4, 777.9, 863.5, 912.3, 986.6, 1043.1, 1068.6, 1119.5, 1156.7, 1168.2, 1212.2, 1211.6, 1306.8, 1335.6, 1411.5, 1439.3, 1461.1, 1550.1, 1570.5, 1608,3, 2835.7, 2928.0, 3055.9. ^{1}H-NMR (500 MHz, CD_2Cl_2): δ 8.37 (d, *J* = 7.2 Hz, 1H), 8.28 (d, *J* = 8.6 Hz, 1H), 8.16 – 8.03 (m, 3H), 7.94 (d, *J* = 8.2 Hz, 1H), 7.79 (d, *J* = 8.7 Hz, 1H), 7.65 – 7.56 (m, 3H), 7.53 – 7.47 (m, 1H), 3.84 (s, 3H).^{13}C-NMR (125 MHz, $CDCl_3$): δ 158.0, 135.2, 134.4, 133.0, 131.6, 131.5, 131.3, 129.4, 129.0, 128.8, 128.6, 128.4, 127.9, 127.7, 126.2, 124.3, 123.8, 118.9, 116.4, 110.4, 56.4. HRMS (ESI+): m/z $[M+H]^+$ calcd for ($C_{21}H_{15}O_3S$): 347.0742; found: 347.0736.

Synthesis of 1-hydroxydibenzo[a,kl]thioxanthene 7,7-dioxide

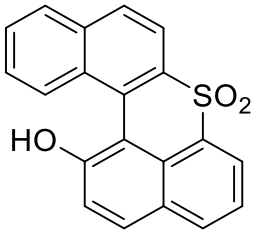

37

To a solution of **38** (90 mg, 0.26 mmol) in dry CH_2Cl_2 (2 mL) was added BBr_3 1 M (1.3 mL, 1.3 mmol) in CH_2Cl_2 under N_2 atmosphere and stirred at r.t. for 20 h. The reaction mixture was quenched with H_2O (3 mL) and the organic phase extracted with CH_2Cl_2 (20 mL x 3). The combined organic phases were dried over Na_2SO_4 and concentrated under reduced pressure. The reaction crude was purified by silica gel chromatography eluting with (Petroleum ether/CH_2Cl_2/EtOAc = 5/2/3) to provide product **37** as a yellow solid (20 mg, 38% yield).

^{1}H-NMR (300 MHz, CD_2Cl_2): δ 8.39 – 8.32 (m, 2H), 8.15 – 8.08 (m, 2H), 8.04 – 7.93 (m, 3H), 7.71 – 7.60 (m, 3H), 7.41 (d, *J* = 8.9 Hz, 1H), 5.88 (s, 1H). HRMS (ES+): m/z $[M+H]^+$ calcd for ($C_{20}H_{13}O_3S$): 333.0585; found: 333.0577.

Synthesis of thioxantheno[2,1,9,8-klmna]xanthene 12,12-dioxide

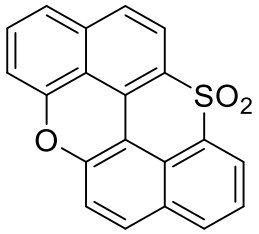

29

To a stirred solution of **37** (30 mg, 0.09 mmol) in m-xylene (3 mL) were added K_2CO_3 (25 mg, 0.18 mmol), NMI (4.4 mg, 0.054 mmol) and CuCl (2.7 mg, 0.027 mmol), and stirred at 140 °C for 16 h. The reaction mixture was quenched with H_2O (5 mL) and the organic phase extracted with $CHCl_3$ (20 mL x 3). The combined organic phases were dried over Na_2SO_4 and concentrated under reduced pressure. The reaction crude was purified by silica gel chromatography with eluent (Petroleum ether/$CHCl_3$/EtOAc = 7/2/1) to afford product **29** as a yellow solid (15 mg, 50% yield).

m.p. 176-182 °C. IR (neat): cm^{-1} 468.3, 492.1, 525.5, 551.8, 633.9, 677.1, 744.2, 767.2, 863.1, 914.4, 989.7, 1051.0, 1071.6, 1115.2, 1149.5, 1176.5, 1227.3, 1218.2, 1307.0, 1337.9, 1415.1, 1464.2, 1555.3, 1577.0, 1613.2, 3026.9, 3055.9. ^{1}H-NMR (300 MHz, CD_2Cl_2): 8.54 (dd, *J* = 7.5, 1.1 Hz, 1H), 8.24 (dd, *J* = 8.1, 1.1 Hz, 1H), 8.10 (d, *J* = 9.1 Hz, 1H), 7.99 (d, *J* = 9.0 Hz, 1H), 7.86 (dd, *J* = 8.0, 7.5 Hz, 1H), 7.84 (d, *J* = 9.0 Hz, 1H), 7.66 (dd, *J* = 8.1, *J* = 7.7 Hz, 1H), 7.57 (dd, *J* = 8.1, 1.0 Hz, 1H), 7.55 (d, *J* = 9.0 Hz, 1H), 7.28 (dd, *J* = 7.7, 1.0 Hz, 1H). ^{13}C-NMR (125 MHz, CD_2Cl_2): δ 133.8, 133.7, 132.6, 130.6, 129.7, 128.8, 127.5, 126.3, 126.0, 121.5, 120.6, 119.7, 110.9, (7 carbon peaks are missing). HRMS (ASAP+): m/z $[M+H]^+$ calcd for ($C_{20}H_{11}O_2S$): 331.0429; found: 331.0428.

Synthesis of N,N-dimethyl-1,7-diaza peri-xanthenoxantene 24 and 22

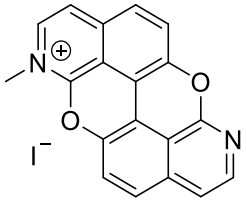

24

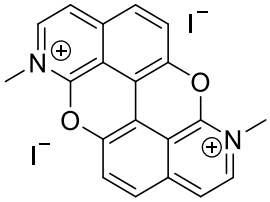

22

In a gas tight flask, **4** (10 mg, 0.035 mmol) was suspended in CH_3I (5 mL) and stirred at 150 °C for 24 h under pressure. CH_3I was evaporated and the mixture of product **22** and **24** collected without further purification as a yellow solid (19 mg, **22** yield 66.7%, **24** yield 33.3% calculated by ^{1}H-NMR)

Synthesis of N,N-dimethyl-3,9-diaza peri-xanthenoxantene 21

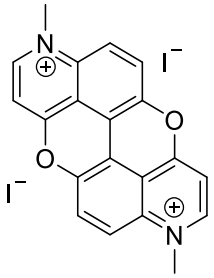

21

In a gas tight flask, **6** (1.6 mg, 0.006 mmol) was suspended in CH_3I (2 mL) and stirred at 150 °C for 24 h under pressure. CH_3I was evaporated and product **21** collected without further purification as a yellow solid (1.77 mg, 100% calculated by ^{1}H-NMR)

m.p. 178-183 °C. IR (neat): cm^{-1} 416.5, 435.1, 455.2, 481.1, 499.0, 529.5, 559.3, 588.2, 612.6, 643.3, 661.6, 725.8, 752.6, 803.9, 885.9, 1019.2, 1036.8, 1057.0, 1098.2, 1144.4, 1182.4, 1255.3, 1262.8, 1323.1, 1365.3, 1382.3, 1412.0, 1437.1, 1468.7, 1486.2, 1517.0, 1593.3, 1643.7, 2934.2, 3018.6, 3043.5. ^{1}H-NMR (300 MHz, DMSO-d_6): δ 9.15 (d, *J* = 7.2 Hz, 2H), 8.38 (d, *J* = 9.6 Hz, 2H), 8.26 (d, *J* = 9.6 Hz, 2H), 7.67 (d, *J* = 7.2 Hz, 2H), 4.32 (s, 6H). ^{13}C-NMR (125 MHz, DMSO-d_6): δ 164.6, 153.9, 144.0, 137.1, 124.9, 120.4, 117.3, 113.0, 107.3, 43.4. HRMS (ES+): m/z $[M]^+$ calcd for ($C_{20}H_{14}N_2O_2^{2+}$): 157.0522; found: 157.0522.

Synthesis of N,N-dimethyl-4,10-diaza peri-xanthenoxantene 26

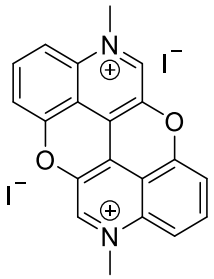

26

In a gas tight flask, **6** (1.7 mg, 0.006 mmol) was suspended in CH_3I (2 mL) and stirred at 150 °C for 24 h under pressure. CH_3I was evaporated and product **21** collected without further purification as a purple solid (1.75 mg, 100% calculated by ^{1}H-NMR)

m.p. 176-181 °C. IR (neat): cm^{-1} 418.5, 433.9, 460.9, 478.3, 495.7, 522.7, 561.9, 586.3, 605.6, 636.5, 661.5, 723.3, 756.1, 802.3, 891.1, 1016.4, 1037.7, 1056.9, 1095.5, 1143.7, 1172.7, 1249.8, 1259.5, 1328.9, 1359.8, 1386.8, 1411.8, 1438.9, 1463.9, 1483.6, 1517.9, 1589.3, 1645.3, 2924.1, 3012.8, 3041.7. ^{1}H-NMR (300 MHz, DMSO-

d_6): δ 9.77 (s, 2H), 8.21 (t, *J* = 8.5, 8.2 Hz, 2H), 8.05 (d, *J* = 8.5 Hz, 2H), 7.79 (d, *J* = 8.2 Hz, 2H), 4.49 (s, 6H). ^{13}C-NMR (125 MHz, DMSO-d_6): δ 150.5, 143.6, 141.3, 136.7, 136.5, 123.1, 116.6, 114.3, 114.0, 46.0. HRMS (ES+): m/z $[M]^+$ calcd for ($C_{20}H_{14}N_2O_2^{2+}$): 157.0522; found: 157.0522.

5.4 Lifetime measurements

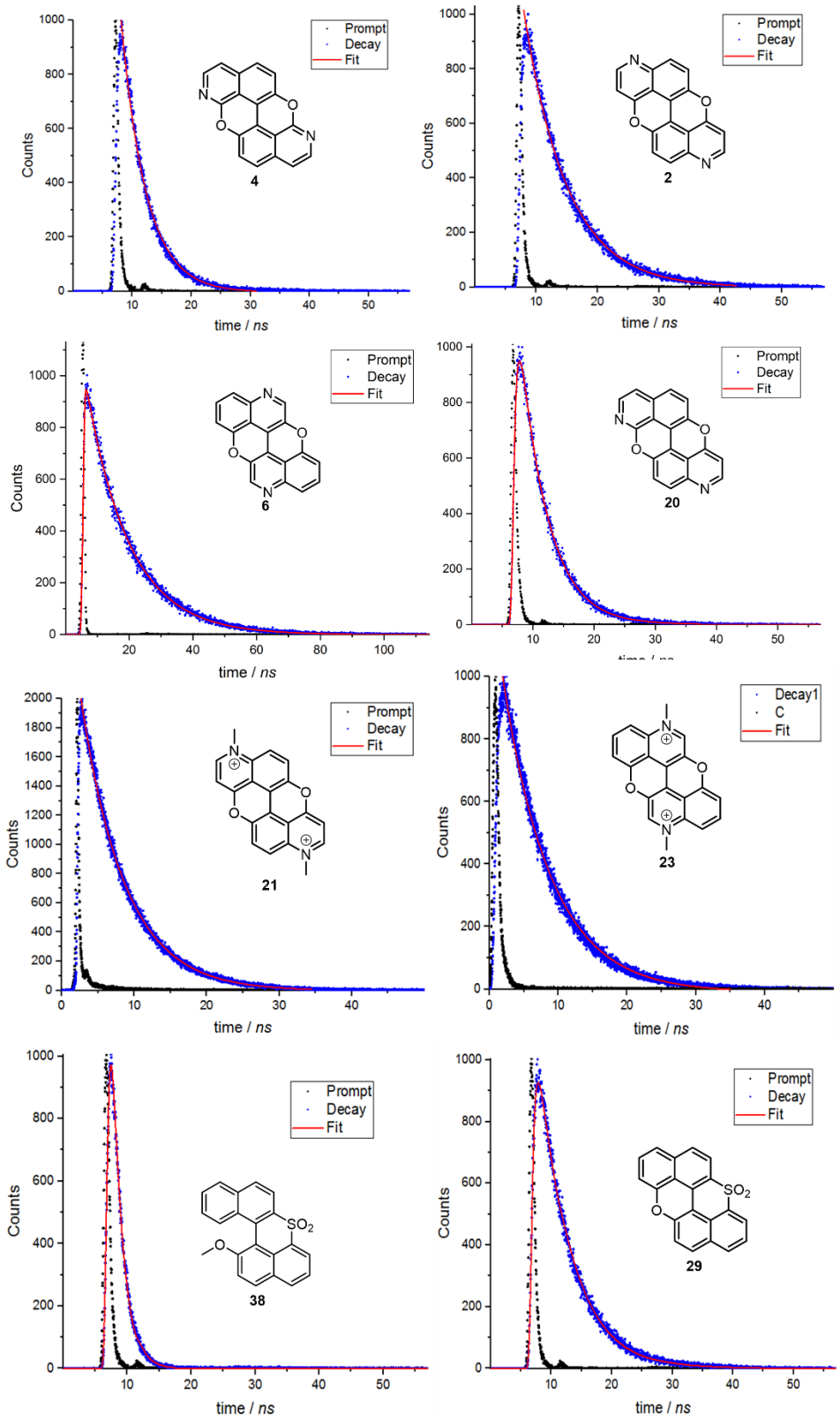

Figure 5.1. Fluorescence emission lifetime decays (blue dots), relative fittings (red lines) and decay of excitation source (black line).

5.5 Cyclic Voltammetry

Cyclic Voltammetry of 1,7-diaza peri-xanthenoxantene 4

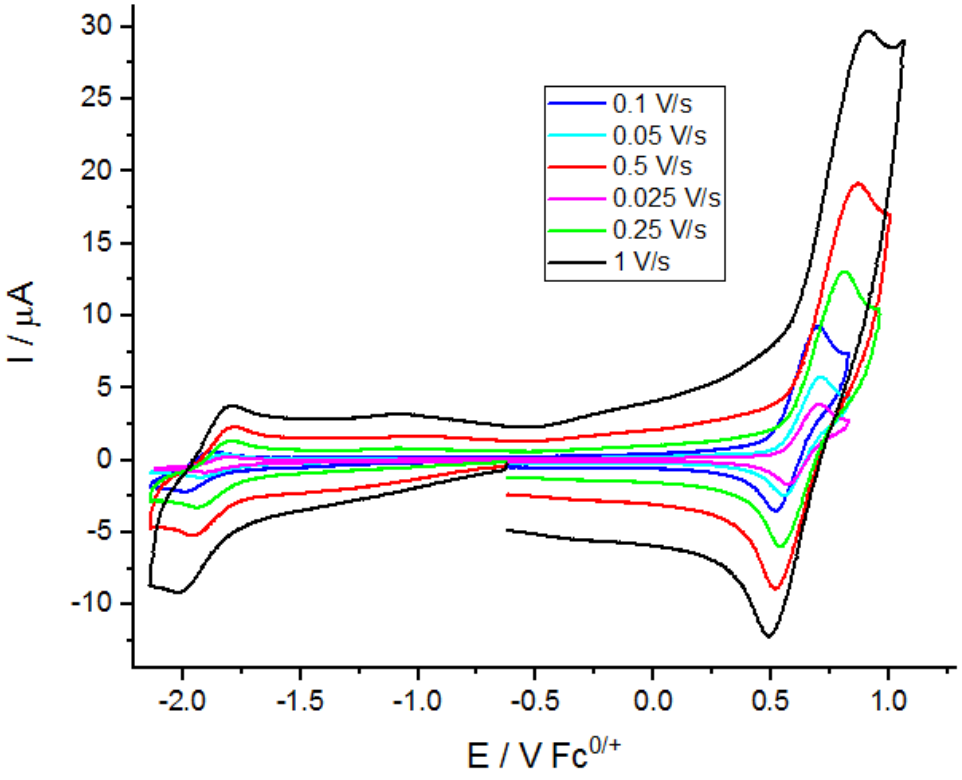

Figure 5.2. Cyclic voltammograms of **1** in ODCB (ca. 0.70 mM) at different scan rates. $TBAPF_6$ (0.08 M) is used as a supporting electrolyte; ferrocene/ferrocenium redox couple (Fc/Fc^+) is used as reference.

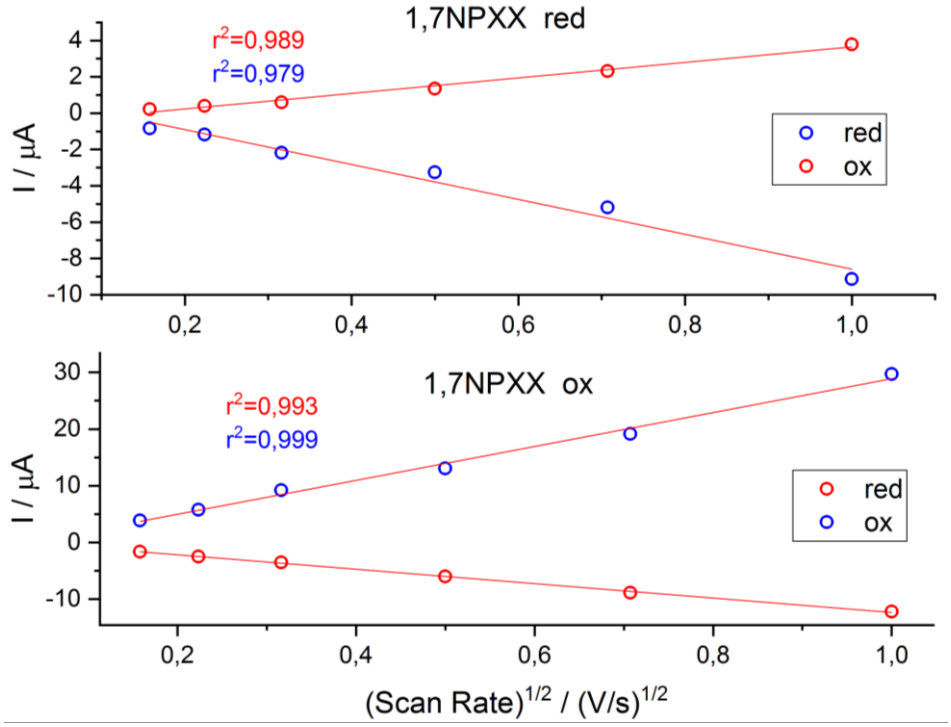

Figure 5.3. Linear dependence between anodic or cathodic peak currents and scan $rate^{1/2}$.

Cyclic Voltammetry of 3,9-diaza peri-xanthenoxantene 2

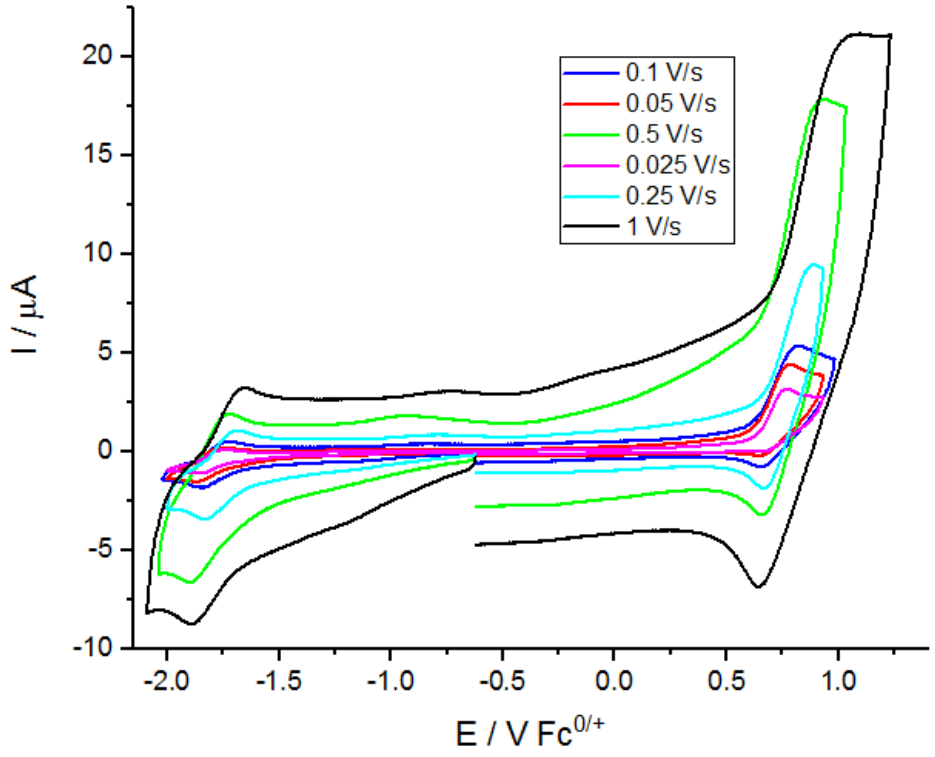

Figure 5.4. Cyclic voltammograms of **2** in ODCB (ca. 0.70 mM) at different scan rates. $TBAPF_6$ (0.08 M) is used as a supporting electrolyte; ferrocene/ferrocenium redox couple (Fc/Fc^+) is used as reference.

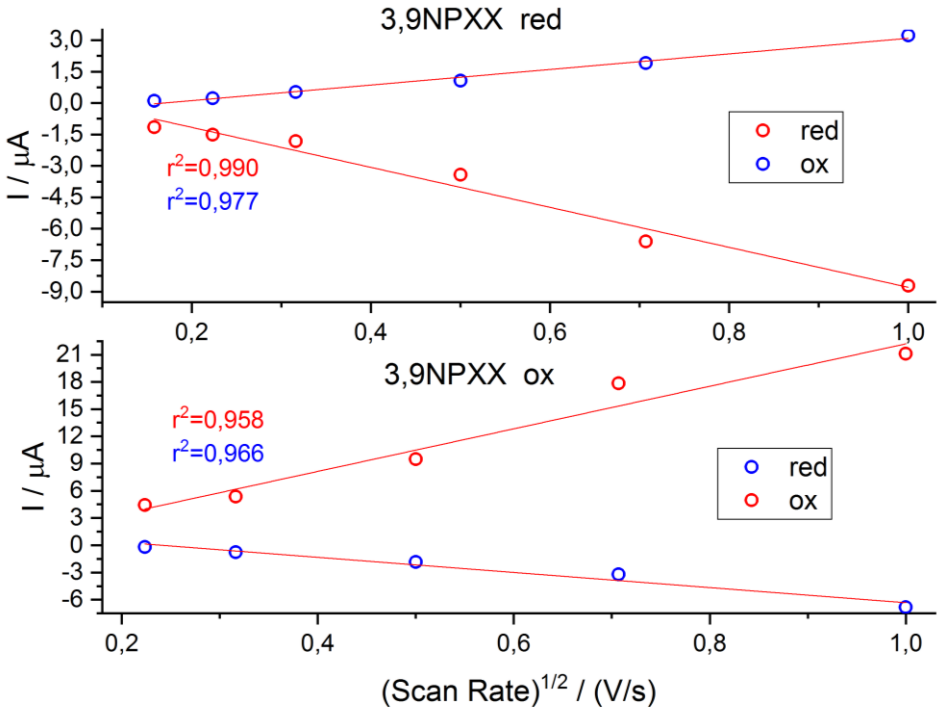

Figure 5.5. Linear dependence between anodic or cathodic peak currents and scan $rate^{1/2}$.

Cyclic Voltammetry of 4,10-diaza peri-xanthenoxantene 6

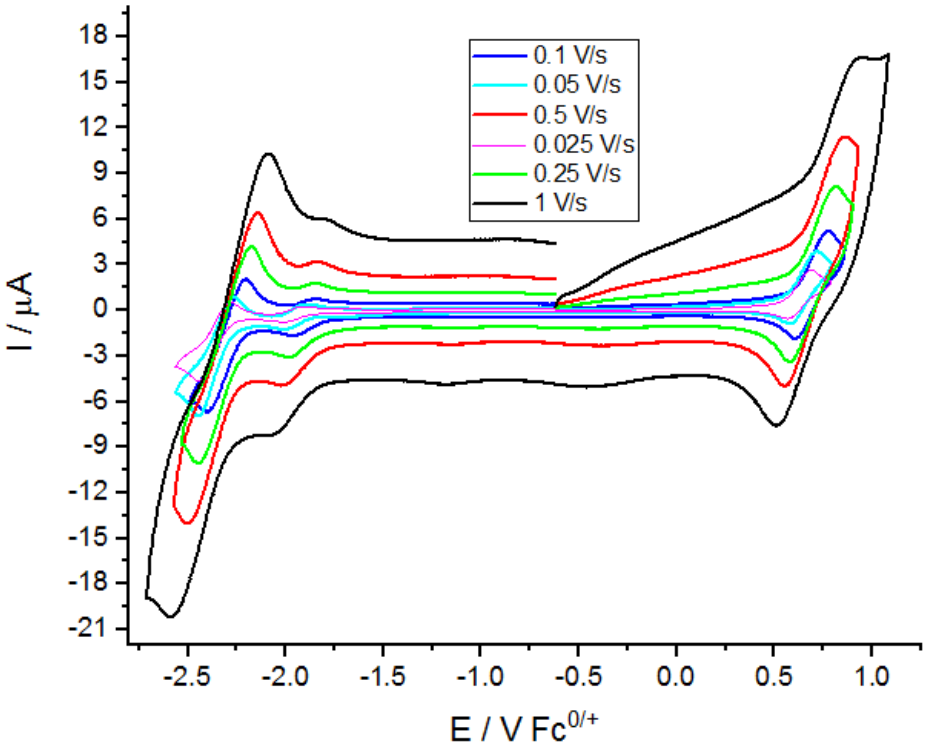

Figure 5.6. Cyclic voltammograms of **6** in ODCB (ca. 0.70 mM) at different scan rates. $TBAPF_6$ (0.08 M) is used as a supporting electrolyte; ferrocene/ferrocenium redox couple (Fc/Fc^+) is used as reference.

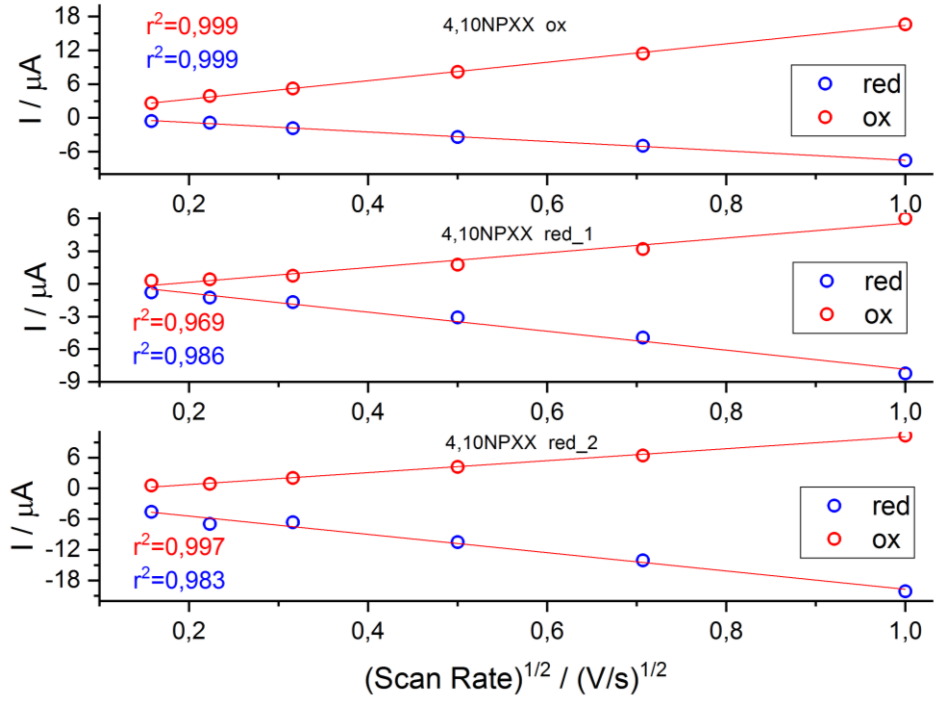

Figure 5.7. Linear dependence between anodic or cathodic peak currents and scan rate$^{1/2}$.

Cyclic Voltammetry of 1,9-diaza peri-xanthenoxantene 20

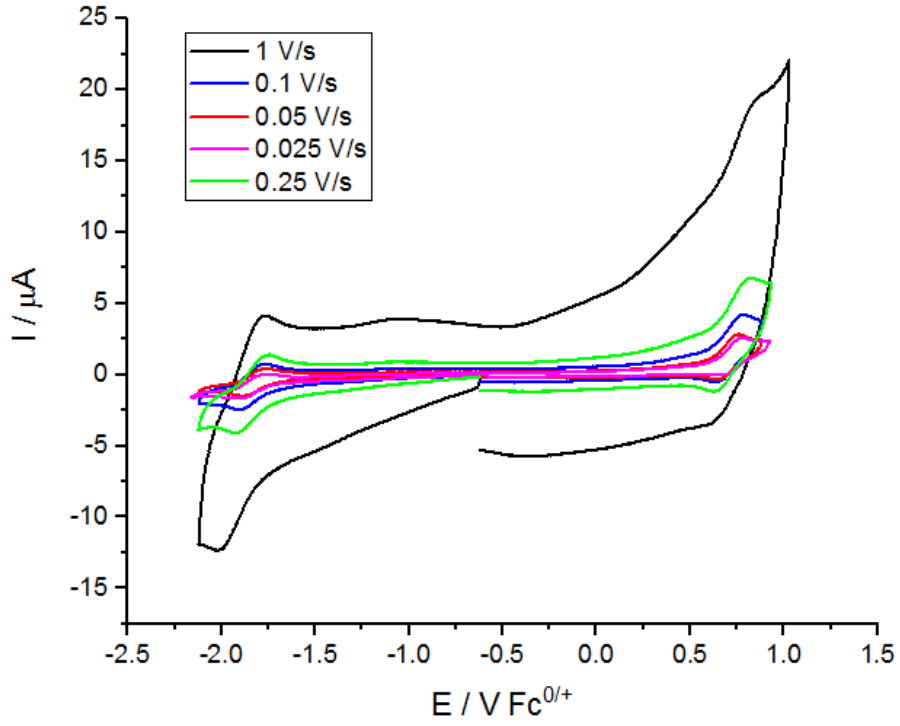

Figure 5.8. Cyclic voltammograms of **20** in ODCB (ca. 0.72 mM) at different scan rates. $TBAPF_6$ (0.08 M) is used as a supporting electrolyte; ferrocene/ferrocenium redox couple (Fc/Fc^+) is used as reference.

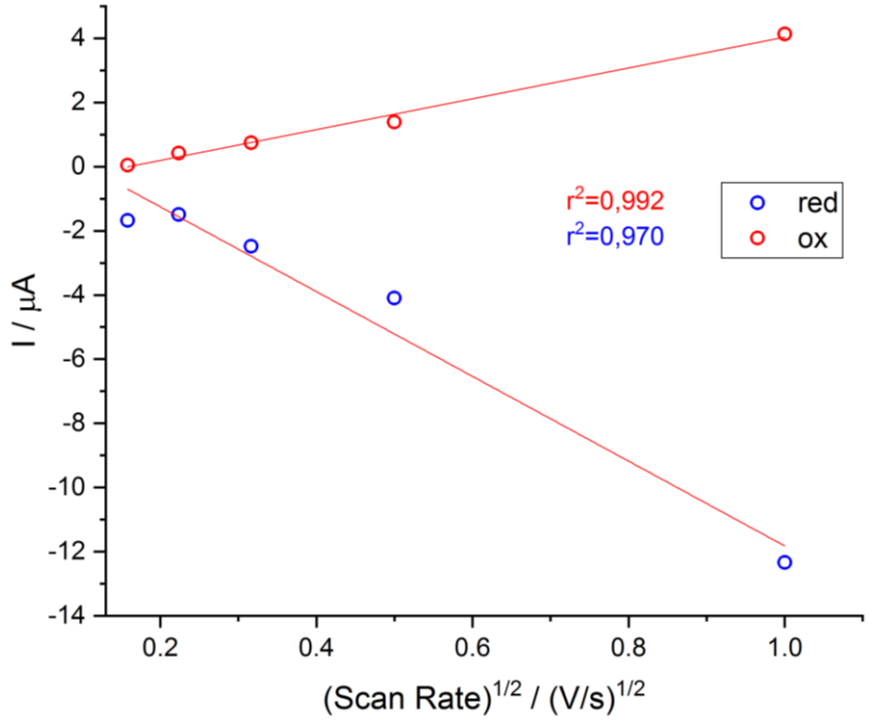

Figure 5.9. Linear dependence between anodic or cathodic peak currents and scan $rate^{1/2}$.

Cyclic Voltammetry of PTXX-SO_2 29

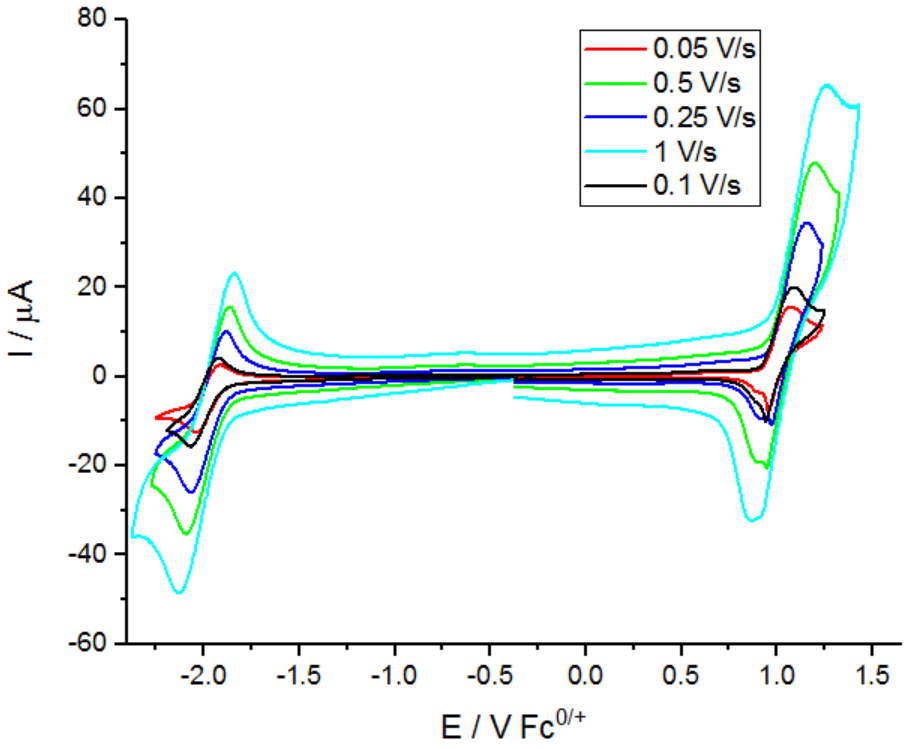

Figure 5.10. Cyclic voltammograms of **29** in CH_2Cl_2 (ca. 0.82 mM) at different scan rates. $TBAPF_6$ (0.07 M) is used as a supporting electrolyte; ferrocene/ferrocenium redox couple (Fc/Fc^+) is used as reference.

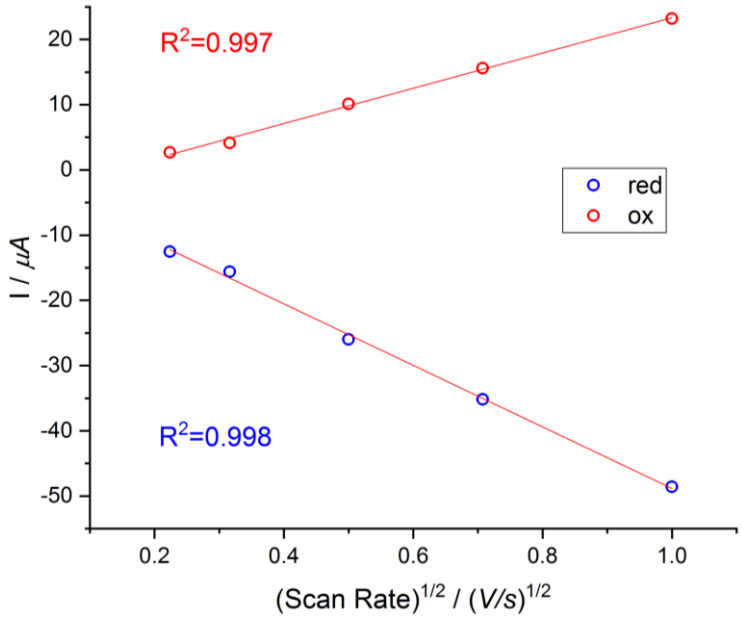

Figure 5.11. Linear dependence between anodic or cathodic peak currents and scan rate$^{1/2}$.

Cyclic Voltammetry of 2'-(methylthio)-[1,1'-binaphthalen]-2-ol 38

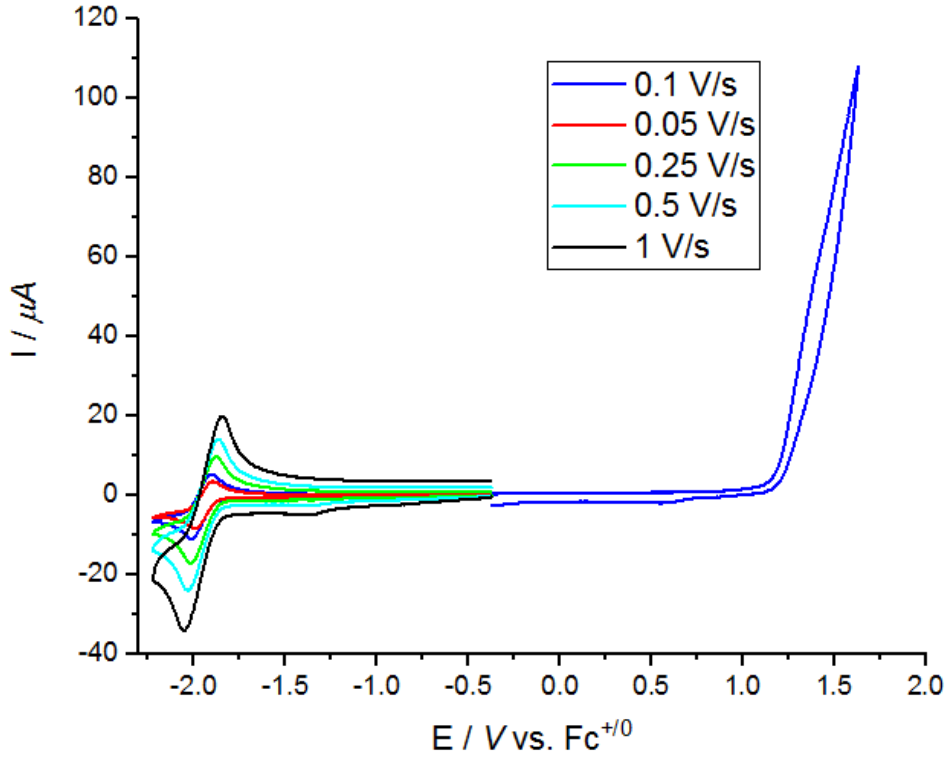

Figure 5.12. Cyclic voltammograms of **32** in CH_2Cl_2 (ca. 0.86 mM) at different scan rates. $TBAPF_6$(0.09 M) is used as a supporting electrolyte; ferrocene/ferrocenium redox couple (Fc/Fc^+) is used as reference.

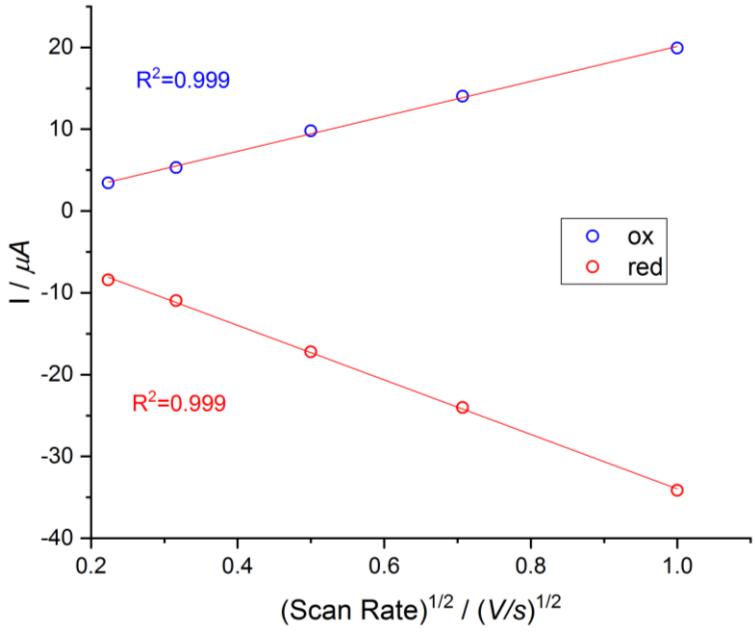

Figure 5.13. Linear dependence between anodic or cathodic peak currents and scan rate$^{1/2}$.

Cyclic Voltammetry of diMe-3,9-diaza peri-xanthenoxantene 21

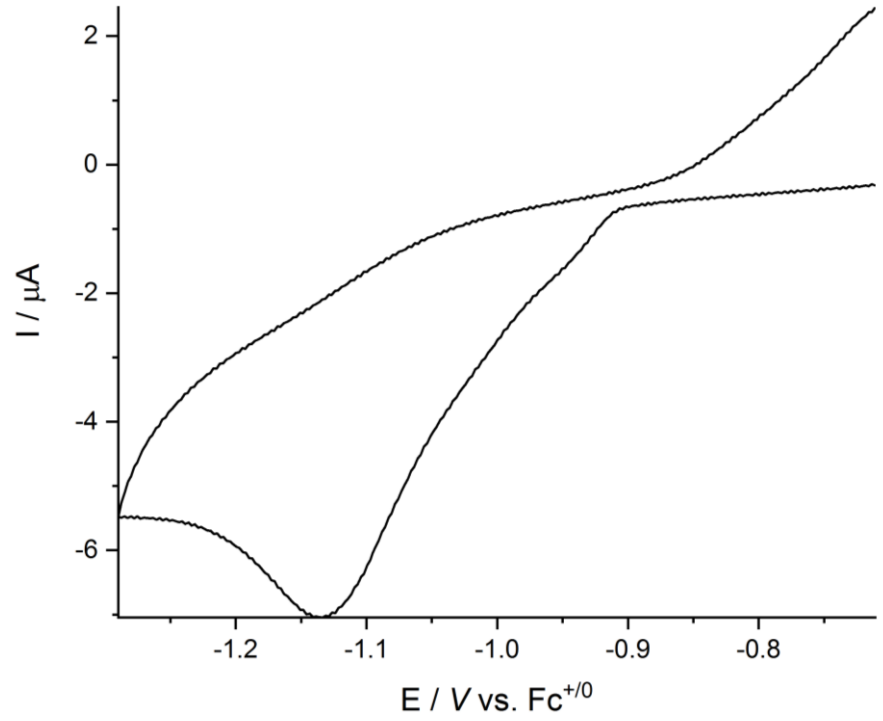

Figure 5.14. Cyclic voltammograms of **21** in CH_2Cl_2 (ca. 0.73 mM) at 0.1 V/s. $TBAPF_6$(0.09 M) is used as a supporting electrolyte; ferrocene/ferrocenium redox couple (Fc/Fc^+) is used as reference.

Cyclic Voltammetry of diMe-4,10-diaza peri-xanthenoxantene 26

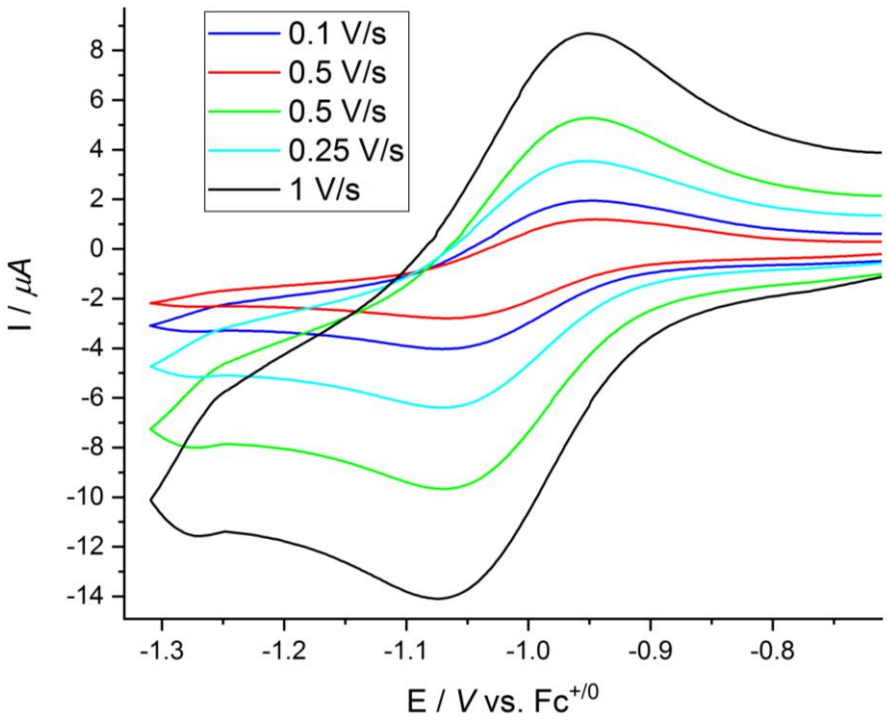

Figure 5.15. Cyclic voltammograms of in **26** CH_2Cl_2 (ca. 0.76 mM) at different scan rates. $TBAPF_6$(0.09 M) is used as a supporting electrolyte; ferrocene/ferrocenium redox couple (Fc/Fc^+) is used as reference.

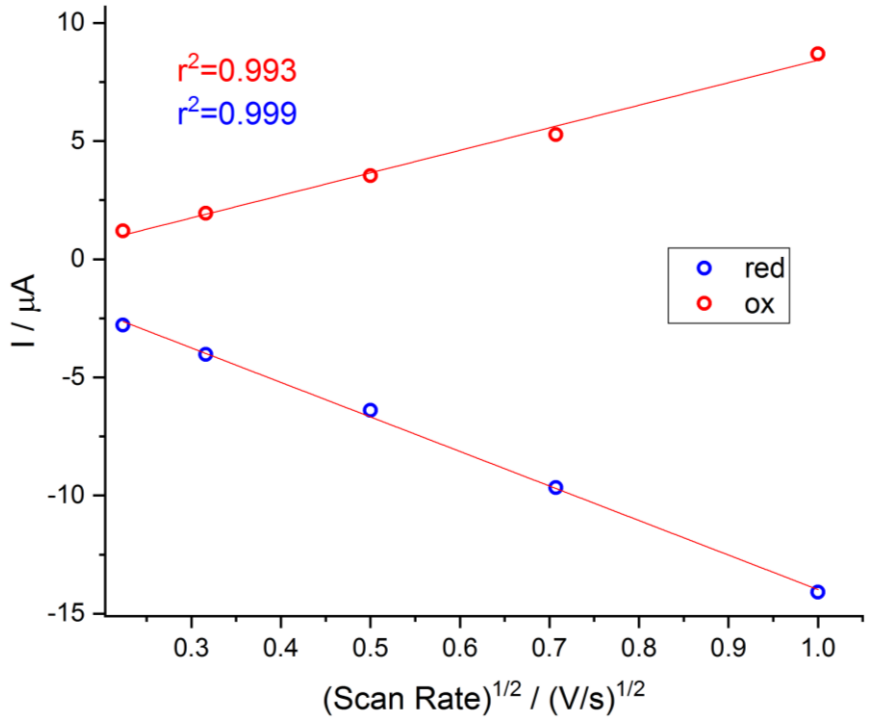

Figure 5.16. Linear dependence between anodic or cathodic peak currents and scan rate$^{1/2}$.

5.6 Lippert Matanga plot for molecules 38, 29 and PXX.

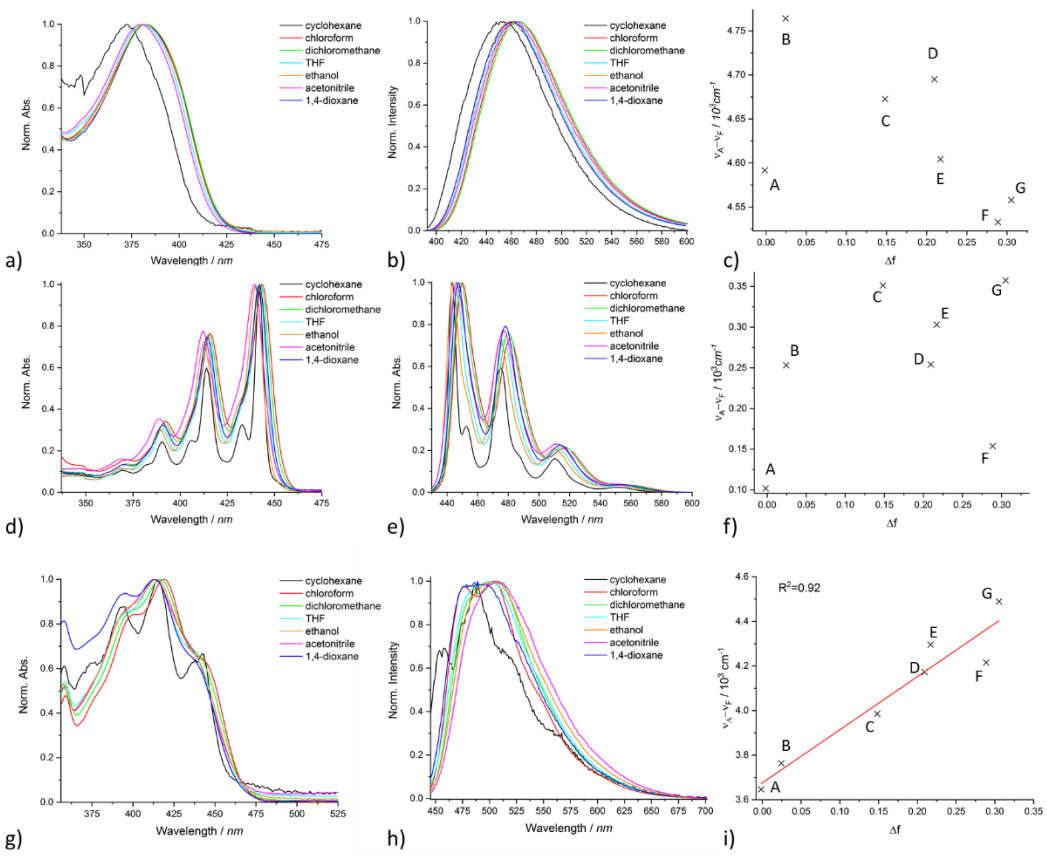

Figure 5.17. Normalised absorption in various solvents at r.t of a) **32** d) PXX and g) **23**. Emission spectra collected in various solvents at r.t. of b) **38** e) PXX and d) **29.** Lippert-Mataga plot for c) **38** f) PXX and i) **29** (A: cyclohexane; B: 1,4-dioxane; C: chloroform; D: tetrahydrofuran; E: dichloromethane; F: ethanol; G: acetonitrile; THF: tetrahydrofuran). Linear fitting (green line) is also shown

5.7 X-ray Data

Crystal data and structure refinement of 1,7-diaza peri-xanthenoxanthene 1

1,7-diaza peri-xanthenoxantene	1985339	
Empirical formula	C18 H8 N2 O2	
Formula weight	284.26	
Temperature	150(2) K	
Wavelength	0.71073 Å	
Crystal system	Monoclinic	
Space group	P 21/c	
Unit cell dimensions	a = 4.3819(9) Å	α= 90°.
	b = 13.469(3) Å	β= 97.073(19)°.
	c = 10.1801(18) Å	γ = 90°.

Volume	596.3(2) $Å^3$
Z	2
Density (calculated)	1.583 Mg/m^3
Absorption coefficient	0.106 mm^{-1}
F(000)	292
Crystal size	0.221 x 0.080 x 0.072 mm^3
Theta range for data collection	3.025 to 29.488°.
Index ranges	-6<=h<=4, -15<=k<=18, -13<=l<=13
Reflections collected	2815
Independent reflections	1409 [R(int) = 0.0352]
Completeness to theta = 25.242°	99.9 %
Refinement method	Full-matrix least-squares on F^2
Data / restraints / parameters	1409 / 0 / 100
Goodness-of-fit on F^2	1.010
Final R indices [I>2sigma(I)]	R1 = 0.0684, wR2 = 0.1879
R indices (all data)	R1 = 0.1359, wR2 = 0.2422
Extinction coefficient	n/a
Largest diff. peak and hole	0.394 and -0.358 $e.Å^{-3}$

Crystal data and structure refinement of 3,9-diaza peri-xanthenoxanthene 2

3,9-diaza peri-xanthenoxantene	1985342
Chemical Formula	$C_{18}H_{12}N_2O_4$
Formula weight (g/mol)	320.30
Temperature (K)	100(2)
Wavelength (Å)	0.700
Crystal system	Monoclinic
Space Group	*P* $2_1/c$
Unit cell dimensions	*a* = 7.557(2) Å
	b = 3.668(1) Å
	c = 23.856(3) Å
	α = 90°
	β = 95.85(3)°
	γ = 90°
Volume ($Å^3$)	657.8(2)
Z	2
Density (calculated) ($g \cdot cm^{-3}$)	1.617
Absorption coefficient (mm^{-1})	0.111

F(000)	332
Theta range for data collection	1.69° to 29.53°
Index ranges	-10 ≤ *h* ≤ 10
	-5 ≤ *k* ≤ 5
	-33 ≤ *l* ≤ 33
Resolution (Å)	0.71
Reflections collected	6108
Independent reflections (data with I>2σ(I))	1887 (1252)
Data multiplicity (max resltn)	3.01 (2.86)
I/σ(I) (max resltn)	9.52 (4.06)
R_{merge} (max resltn)	0.0464 (0.1860)
Data completeness (max resltn)	98.1% (96.0%)
Refinement method	Full-matrix least-squares on F^2
Data / restraints / parameters	1887 / 3 / 115
Goodness-of-fit on F^2	1.068
□/□$_{max}$	0.000
Final R indices [I>2σ(I)]	R_1 = 0.0706,
	wR_2 = 0.2095
R indices (all data)	R_1 = 0. 0950,
	wR_2 = 0.2346
Largest diff. peak and hole (eÅ^{-3})	0.377 and -0.556
R.M.S. deviation from mean (eÅ^{-3})	0.080

Crystal data and structure refinement of molecule 7

Chemical Formula	$C_{27}H_{37}N_3O_{8.5}$
Formula weight (g/mol)	539.59
Temperature (K)	100(2)
Wavelength (Å)	0.700
Crystal system	Monoclinic
Space Group	*C 2/c*
Unit cell dimensions	*a* = 12.962(3) Å
	b = 28.903(6) Å

	c = 28.142(6) Å
	α = 90°
	β = 102.73(3)°
	γ = 90°
Volume (Å^3)	10284(4)
Z	16
Density (calculated) (g·cm^{-3})	1.326
Absorption coefficient (mm^{-1})	0.096
F(000)	4224
Theta range for data collection	1.39° to 14.48°
Index ranges	-9 ≤ h ≤ 9
	-20 ≤ k ≤ 20
	-20 ≤ l ≤ 20
Resolution (Å)	1.40
Reflections collected	6872
Independent reflections (data with I>2σ(I))	1938 (992)
Data multiplicity (max resltn)	3.44 (3.58)
I/σ(I) (max resltn)	4.18 (0.84)
R_{merge} (max resltn)	0.1546 (0.6881)
Data completeness (max resltn)	98.7% (99.4%)
Refinement method	Full-matrix least-squares on F^2
Data / restraints / parameters	1938 / 0 / 290
Goodness-of-fit on F^2	1.345
□/□$_{max}$	0.003
Final R indices [I>2σ(I)]	R_1 = 0.1404,
	wR_2 = 0.3649
R indices (all data)	R_1 = 0.2103,
	wR_2 = 0.4218
Largest diff. peak and hole (eÅ^{-3})	0.461 and -0.249
R.M.S. deviation from mean (eÅ^{-3})	0.078

Crystal data and structure refinement 4,10-diaza peri-xanthenoxanthene 6

4,10-diaza peri-xanthenoxanthene	1985344	
Empirical formula	C18 H8 N2 O2	
Formula weight	284.26	
Temperature	150(2) K	
Wavelength	1.54184 Å	
Crystal system	Monoclinic	
Space group	P 21/n	
Unit cell dimensions	a = 11.589(3) Å	α= 90°.
	b = 3.7599(12) Å	β= 112.54(3)°.
	c = 14.384(3) Å	γ = 90°.
Volume	578.9(3) $Å^3$	
Z	2	
Density (calculated)	1.631 Mg/m^3	
Absorption coefficient	0.891 mm^{-1}	
F(000)	292	
Crystal size	0.469 x 0.044 x 0.031 mm^3	
Theta range for data collection	4.195 to 76.679°.	
Index ranges	-14<=h<=14, -4<=k<=4, -17<=l<=17	
Reflections collected	4883	
Independent reflections	1171 [R(int) = 0.0748]	
Completeness to theta = 67.684°	99.9 %	
Refinement method	Full-matrix least-squares on F^2	
Data / restraints / parameters	1171 / 0 / 100	
Goodness-of-fit on F^2	1.011	
Final R indices [I>2sigma(I)]	R1 = 0.0899, wR2 = 0.2405	
R indices (all data)	R1 = 0.1251, wR2 = 0.2993	
Extinction coefficient	n/a	
Largest diff. peak and hole	0.579 and -0.347 $e.Å^{-3}$	

Crystal data and structure refinement of cocrystal 3,9-diN-PXX 2 and 1,4-diiodotetrafluorobenzene

Crystals obtained by slow evaporation of $CHCl_3$ equimolar solution of 3,9-diN-NPXX and 1,4-diiodotetrafluorobenzene

Identification code	
Empirical formula	C20 H18 I2 N2 O4
Formula weight	604.16

Temperature	200(2) K	
Wavelength	0.71073 Å	
Crystal system	Monoclinic	
Space group	P 21/n	
Unit cell dimensions	a = 6.7875(5) Å	α= 90°.
	b = 12.6005(9) Å	β= 91.641(7)°.
	c = 12.2743(8) Å	γ = 90°.
Volume	1049.34(13) $Å^3$	
Z	2	
Density (calculated)	1.912 Mg/m^3	
Absorption coefficient	3.025 mm^{-1}	
F(000)	580	
Crystal size	0.223 x 0.077 x 0.072 mm^3	
Theta range for data collection	3.321 to 29.846°.	
Index ranges	-7<=h<=9, -13<=k<=17, -14<=l<=16	
Reflections collected	5438	
Independent reflections	2526 [R(int) = 0.0283]	
Completeness to theta = 25.242°	99.9 %	
Absorption correction	Gaussian	
Max. and min. transmission	0.946 and 0.626	
Refinement method	Full-matrix least-squares on F^2	
Data / restraints / parameters	2526 / 0 / 135	
Goodness-of-fit on F^2	1.066	
Final R indices [I>2sigma(I)]	R1 = 0.0395, wR2 = 0.0776	
R indices (all data)	R1 = 0.0595, wR2 = 0.0876	
Extinction coefficient	n/a	
Largest diff. peak and hole	0.809 and -0.593 e.$Å^{-3}$	

Crystal data and structure refinement of cocrystal 4,10-NPXX diiodotetrafluorobenzene

Crystals obtained by slow evaporation of $CHCl_3$ equimolar solution of 4,10-diN-NPXX and 1,4-diiodotetrafluorobenzene

Empirical formula	C24 H8 F4 I2 N2 O2
Formula weight	686.12
Temperature	200(2) K

Wavelength	0.71073 Å	
Crystal system	Triclinic	
Space group	P -1	
Unit cell dimensions	a = 4.1848(3) Å	α= 92.097(5)°.
	b = 7.7399(5) Å	β= 90.002(5)°.
	c = 16.2513(11) Å	γ= 99.199(5)°.
Volume	519.25(6) Å^3	
Z	1	
Density (calculated)	2.194 Mg/m^3	
Absorption coefficient	3.091 mm^{-1}	
F(000)	324	
Crystal size	0.390 x 0.122 x 0.080 mm^3	
Theta range for data collection	3.730 to 29.760°.	
Index ranges	-5<=h<=5, -9<=k<=8, -20<=l<=17	
Reflections collected	4071	
Independent reflections	2460 [R(int) = 0.0338]	
Completeness to theta = 25.242°	99.7 %	
Refinement method	Full-matrix least-squares on F^2	
Data / restraints / parameters	2460 / 0 / 154	
Goodness-of-fit on F^2	1.035	
Final R indices [I>2sigma(I)]	R1 = 0.0407, wR2 = 0.0630	
R indices (all data)	R1 = 0.0546, wR2 = 0.0703	
Extinction coefficient	n/a	
Largest diff. peak and hole	0.934 and -0.685 e.Å^{-3}	

Crystal data and structure refinement of PTXX-SO_2 29

Identification code	1985340	
Empirical formula	C20 H10 O3 S	
Formula weight	330.34	
Temperature	150(2) K	
Wavelength	1.54184 Å	
Crystal system	Triclinic	
Space group	P -1	
Unit cell dimensions	a = 7.3962(6) Å	α= 113.515(12)°.
	b = 9.3870(13) Å	β= 99.828(7)°.
	c = 10.8215(11) Å	γ= 90.058(9)°.
Volume	676.82(14) Å^3	

Z	2
Density (calculated)	1.621 Mg/m^3
Absorption coefficient	2.271 mm^{-1}
F(000)	340
Crystal size	0.140 x 0.086 x 0.047 mm^3
Theta range for data collection	4.536 to 72.445°.
Index ranges	-6<=h<=8, -10<=k<=11, -13<=l<=13
Reflections collected	4084
Independent reflections	2546 [R(int) = 0.0428]
Completeness to theta = 67.684°	97.5 %
Absorption correction	Gaussian
Max. and min. transmission	0.950 and 0.708
Refinement method	Full-matrix least-squares on F^2
Data / restraints / parameters	2546 / 0 / 217
Goodness-of-fit on F^2	1.163
Final R indices [I>2sigma(I)]	R1 = 0.1294, wR2 = 0.4308
R indices (all data)	R1 = 0.1468, wR2 = 0.4396
Extinction coefficient	n/a
Largest diff. peak and hole	1.640 and -0.631 $e.Å^{-3}$

Crystal data and structure refinement of 1-methoxydibenzo[a,kl]thioxanthene 7,7-dioxide 38

Identification code	1985343	
Empirical formula	C21 H14 O3 S	
Formula weight	346.38	
Temperature	200(2) K	
Wavelength	0.71073 Å	
Crystal system	Orthorhombic	
Space group	P b c a	
Unit cell dimensions	a = 7.9293(6) Å	α= 90°.
	b = 16.5287(7) Å	β= 90°.
	c = 23.4660(12) Å	γ = 90°.
Volume	3075.5(3) $Å^3$	
Z	8	
Density (calculated)	1.496 Mg/m^3	
Absorption coefficient	0.229 mm^{-1}	
F(000)	1440	

Crystal size	0.344 x 0.271 x 0.103 mm^3
Theta range for data collection	3.337 to 29.794°.
Index ranges	-10<=h<=7, -22<=k<=16, -32<=l<=31
Reflections collected	9842
Independent reflections	3731 [R(int) = 0.0696]
Completeness to theta = 25.242°	99.8 %
Refinement method	Full-matrix least-squares on F^2
Data / restraints / parameters	3731 / 0 / 222
Goodness-of-fit on F^2	1.068
Final R indices [I>2sigma(I)]	R1 = 0.0611, wR2 = 0.1470
R indices (all data)	R1 = 0.0966, wR2 = 0.1729
Extinction coefficient	n/a
Largest diff. peak and hole	0.444 and -0.507 e.$Å^{-3}$

Crystal data and structure refinement of molecule 34

Identification code	1985341	
Empirical formula	C_{21} H_{14} O S	
Formula weight	314.38	
Temperature	150(2) K	
Wavelength	1.54184 Å	
Crystal system	Orthorhombic	
Space group	P b c a	
Unit cell dimensions	a = 18.5276(7) Å	α= 90°.
	b = 8.1632(4) Å	β= 90°.
	c = 19.9145(7) Å	γ= 90°.
Volume	3012.0(2) $Å^3$	
Z	8	
Density (calculated)	1.387 Mg/m^3	
Absorption coefficient	1.905 mm^{-1}	
F(000)	1312	
Crystal size	0.279 x 0.108 x 0.077 mm^3	
Theta range for data collection	4.774 to 74.402°.	
Index ranges	-22<=h<=19, -9<=k<=9, -24<=l<=23	
Reflections collected	9980	
Independent reflections	2859 [R(int) = 0.0212]	
Completeness to theta = 25.000°	86.6 %	
Refinement method	Full-matrix least-squares on F^2	
Data / restraints / parameters	2859 / 0 / 208	

Goodness-of-fit on F^2	1.056
Final R indices [I>2sigma(I)]	R1 = 0.0359, wR2 = 0.0985
R indices (all data)	R1 = 0.0410, wR2 = 0.1033
Extinction coefficient	n/a
Largest diff. peak and hole	0.319 and -0.232 e.Å^{-3}

Crystal data and structure refinement of molecule 2Me-4,10-NPXX (26)

Empirical formula	C20 H14 I2 N2 O4	
Formula weight	600.13	
Temperature	200(2) K	
Wavelength	0.71073 Å	
Crystal system	Triclinic	
Space group	P -1	
Unit cell dimensions	a = 7.2770(6) Å	α= 82.805(6)°.
	b = 7.6243(5) Å	β= 78.986(7)°.
	c = 9.9180(7) Å	γ= 71.023(7)°.
Volume	509.60(7) Å^3	
Z	1	
Density (calculated)	1.956 Mg/m^3	
Absorption coefficient	3.114 mm^{-1}	
F(000)	286	
Crystal size	0.271 x 0.114 x 0.042 mm^3	
Theta range for data collection	3.373 to 29.586°.	
Index ranges	-10<=h<=9, -10<=k<=9, -10<=l<=12	
Reflections collected	4224	
Independent reflections	2391 [R(int) = 0.0428]	
Completeness to theta = 25.242°	99.7 %	
Refinement method	Full-matrix least-squares on F^2	
Data / restraints / parameters	2391 / 0 / 128	
Goodness-of-fit on F^2	1.039	
Final R indices [I>2sigma(I)]	R1 = 0.0440, wR2 = 0.0854	
R indices (all data)	R1 = 0.0561, wR2 = 0.0925	
Extinction coefficient	n/a	
Largest diff. peak and hole	0.869 and -0.733 e.Å^{-3}	

Crystal data and structure refinement of molecule 2Me-3,9-NPXX 21

Empirical formula	C20 H18 I2 N2 O4	
Formula weight	604.16	
Temperature	200(2) K	
Wavelength	0.71073 Å	
Crystal system	Monoclinic	
Space group	P 21/n	
Unit cell dimensions	a = 6.7875(5) Å	α= 90°.
	b = 12.6005(9) Å	β= 91.641(7)°.
	c = 12.2743(8) Å	γ= 90°.
Volume	1049.34(13) Å^3	
Z	2	
Density (calculated)	1.912 Mg/m^3	
Absorption coefficient	3.025 mm^{-1}	
F(000)	580	
Crystal size	0.223 x 0.077 x 0.072 mm^3	
Theta range for data collection	3.321 to 29.846°.	
Index ranges	-7<=h<=9, -13<=k<=17, -14<=l<=16	
Reflections collected	5438	
Independent reflections	2526 [R(int) = 0.0283]	
Completeness to theta = 25.242°	99.9 %	
Absorption correction	Gaussian	
Max. and min. transmission	0.946 and 0.626	
Refinement method	Full-matrix least-squares on F^2	
Data / restraints / parameters	2526 / 0 / 135	
Goodness-of-fit on F^2	1.066	
Final R indices [I>2sigma(I)]	R1 = 0.0395, wR2 = 0.0776	
R indices (all data)	R1 = 0.0595, wR2 = 0.0876	
Extinction coefficient	n/a	
Largest diff. peak and hole	0.809 and -0.593 e.Å^{-3}	

5.7 References

[1] G. A. Crosby, J. N. Demas, *J. Phys. Chem.* **1971**, *75*, 991–1024.

[2] R. G. P. Chengteh Lee, Weitao Yang, *Phys. Rev. B* **1988**, *37*, 785–789.

[3] A. D. Becke, *J. Chem. Phys.* **1993**, *98*, 5648–5652.

[4] Y. X. Chen, L. W. Yang, Y. M. Li, Z. Y. Zhou, K. H. Lam, S. Chan, H. L. Kwong, *Chirality* **2000**, *12*, 510–513.

[5] Y. Uetake, T. Niwa, T. Hosoya, *Org. Lett.* **2016**, *18*, 2758–2761.

[6] C. M. M. Hendriks, P. Lamers, J. Engel, C. Bolm, *Adv. Synth. Catal.* **2013**, *355*, 3363–3368.

[7] T. Yanagi, S. Otsuka, Y. Kasuga, K. Fujimoto, K. Murakami, K. Nogi, H. Yorimitsu, A. Osuka, *J. Am. Chem. Soc.* **2016**, *138*, 14582–14585.

Appendix A

Characterization of [8,8'-biisoquinoline]-7,7'-diol 3

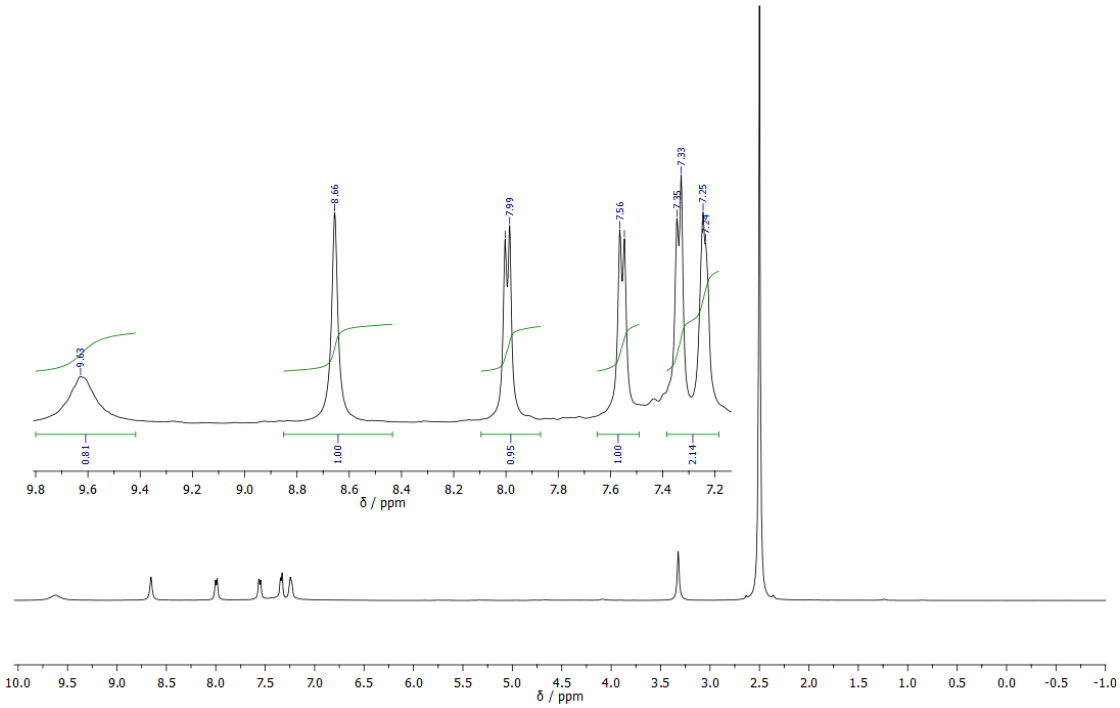

Figure A.1: ^{1}H-NMR, 500 MHz, DMSO-d_6

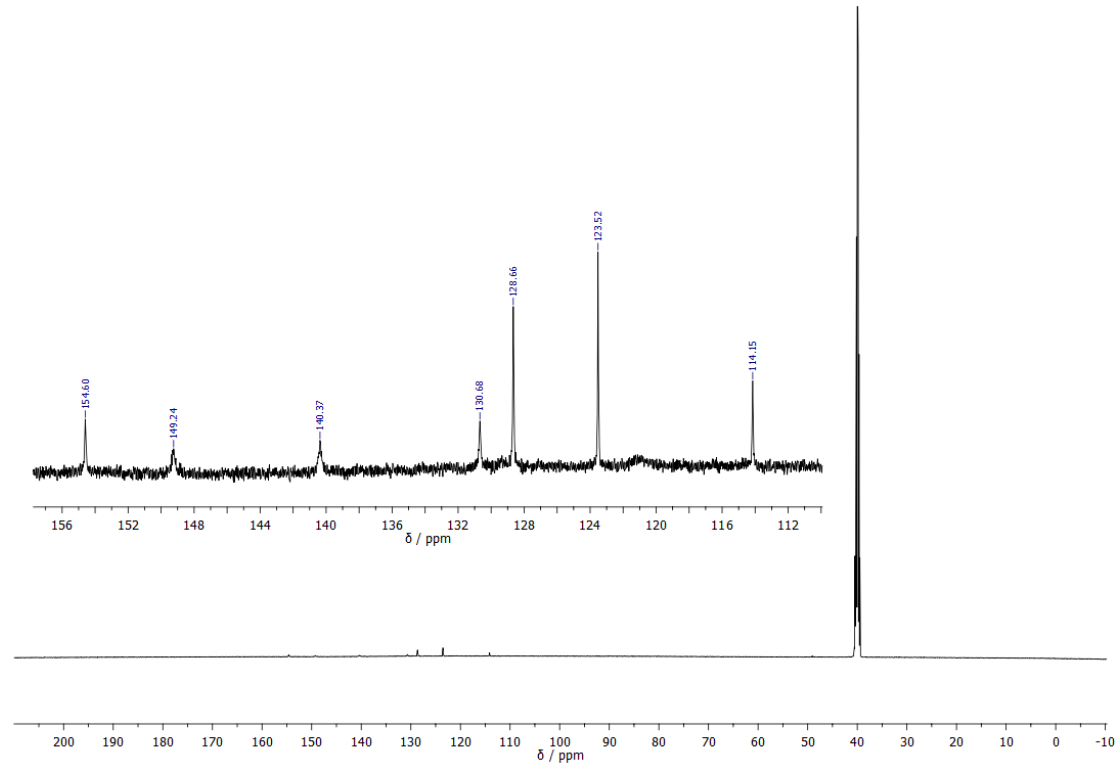

Figure A.2: ^{13}C-NMR, 125 MHz, DMSO-d_6

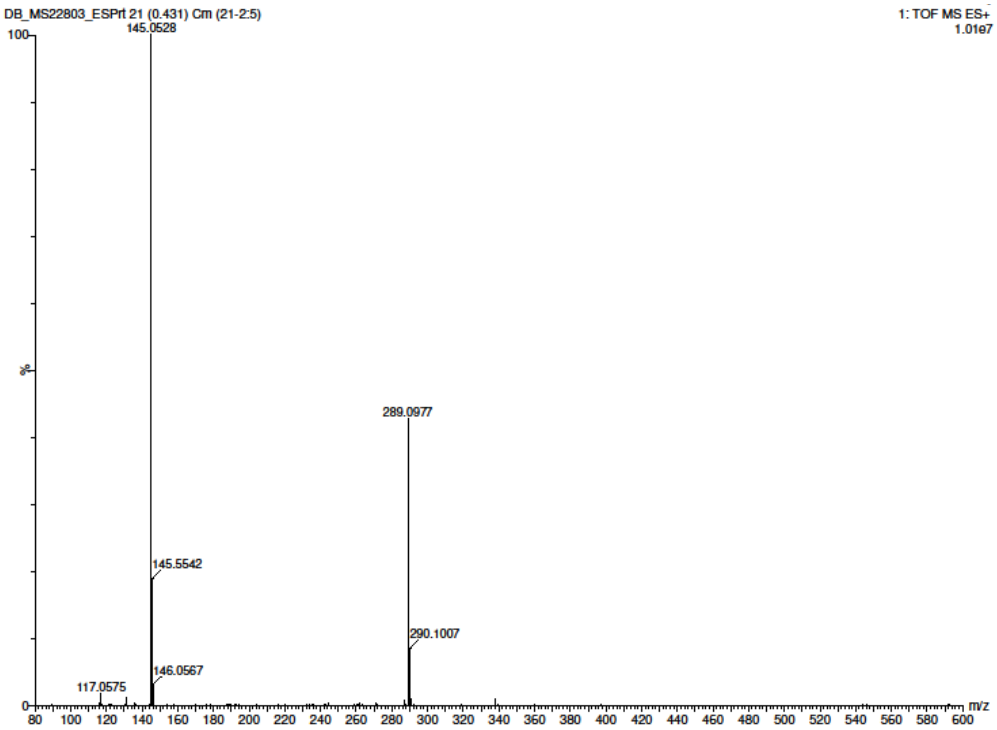

Figure A.3: HR-MS, ESI-TOF.

Elemental Composition Report **Page 1**

Single Mass Analysis
Tolerance = 10.0 PPM / DBE: min = -1.5, max = 100.0
Element prediction: Off
Number of isotope peaks used for i-FIT = 3

Monoisotopic Mass, Odd and Even Electron Ions
4 formula(e) evaluated with 1 results within limits (up to 50 closest results for each mass)
Elements Used:
C: 0-18 H: 0-13 N: 0-2 O: 0-2

Minimum:				-1.5				
Maximum:		5.0	10.0	100.0				
Mass	Calc. Mass	mDa	PPM	DBE	i-FIT	Norm	Conf(%)	Formula
289.0977	289.0977	0.0	0.0	13.5	159.1	n/a	n/a	C18 H13 N2 O2

Figure A.4: Elemental Composition Report.

Characterization 1,7-diaza peri-xanthenoxanten 4

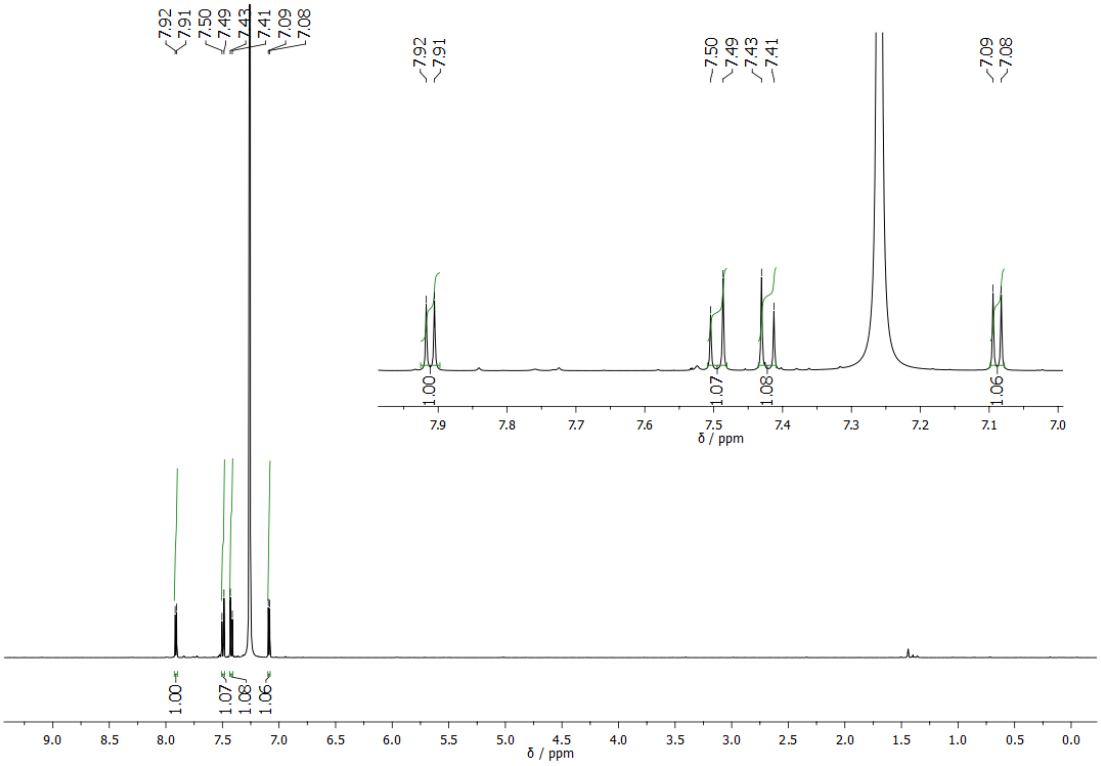

Figure A.5: ^{1}H-NMR, 500 MHz, $CDCl_3$

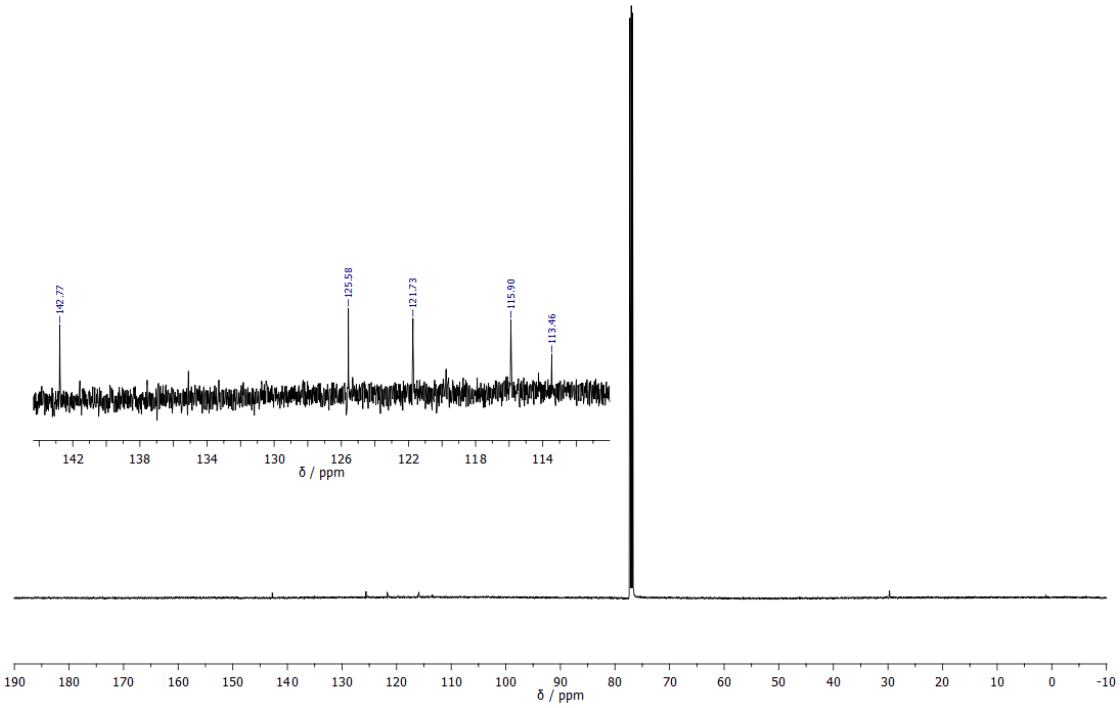

Figure A.6: ^{13}C-NMR, 125 MHz, $CDCl_3$

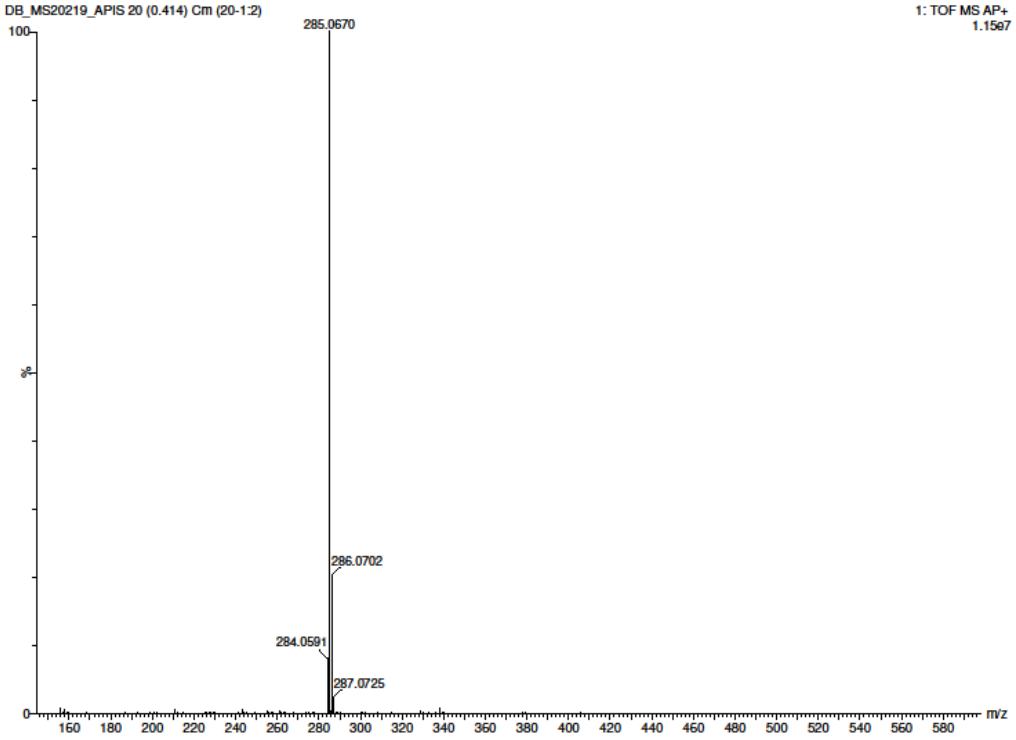

Figure A.7: HR-MS, AP-TOF.

Elemental Composition Report **Page 1**

Single Mass Analysis
Tolerance = 5.0 PPM / DBE: min = -1.5, max = 100.0
Element prediction: Off
Number of isotope peaks used for i-FIT = 3

Monoisotopic Mass, Odd and Even Electron Ions
4 formula(e) evaluated with 1 results within limits (up to 50 best isotopic matches for each mass)
Elements Used:
C: 0-18 H: 0-9 N: 0-2 O: 0-2

Minimum:				-1.5				
Maximum:		5.0	5.0	100.0				
Mass	Calc. Mass	mDa	PPM	DBE	i-FIT	Norm	Conf(%)	Formula
285.0670	285.0664	0.6	2.1	15.5	831.9	n/a	n/a	C18 H9 N2 O2

Figure A.8: Elemental Composition Report.

Characterization [5,5'-biquinoline]-6,6'-diol 1

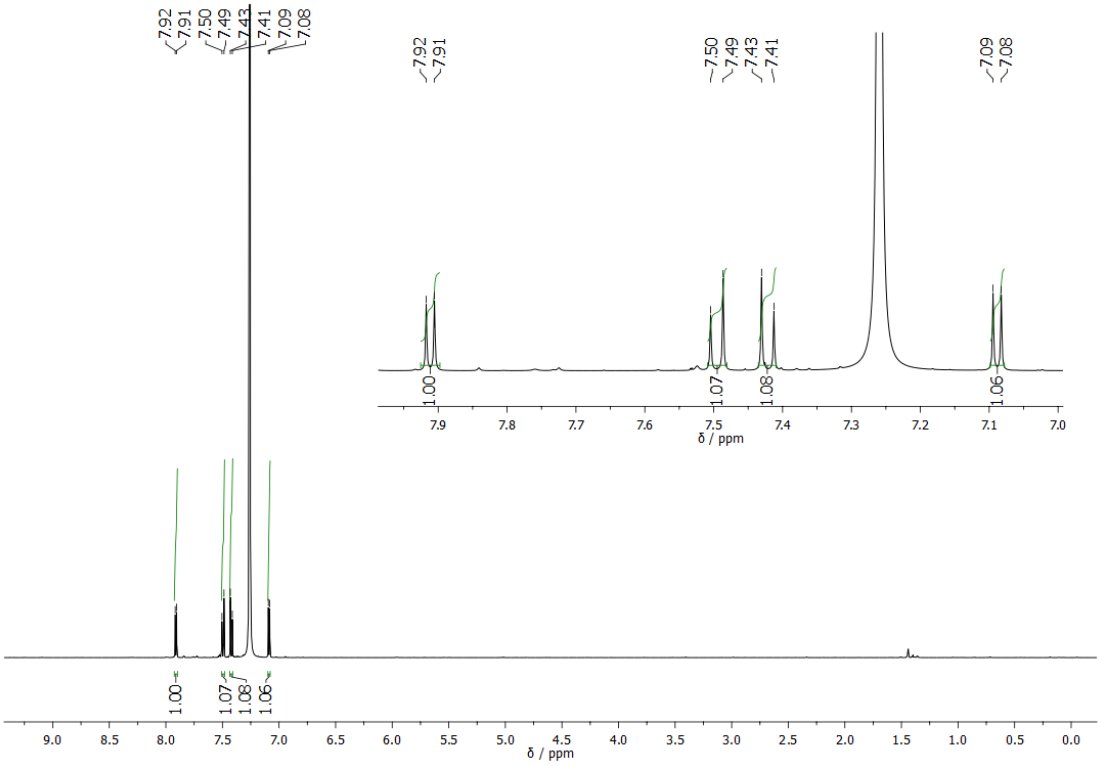

Figure A.9: ^{1}H-NMR, 500 MHz, DMSO-d_6

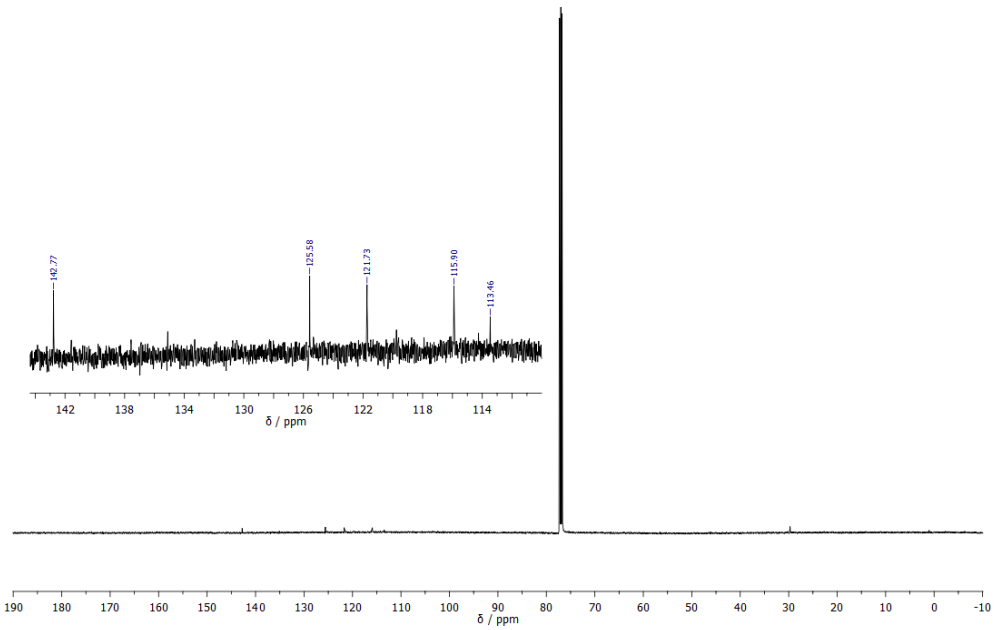

Figure A.10: ^{13}C-NMR, 125 MHz, DMSO-d_6

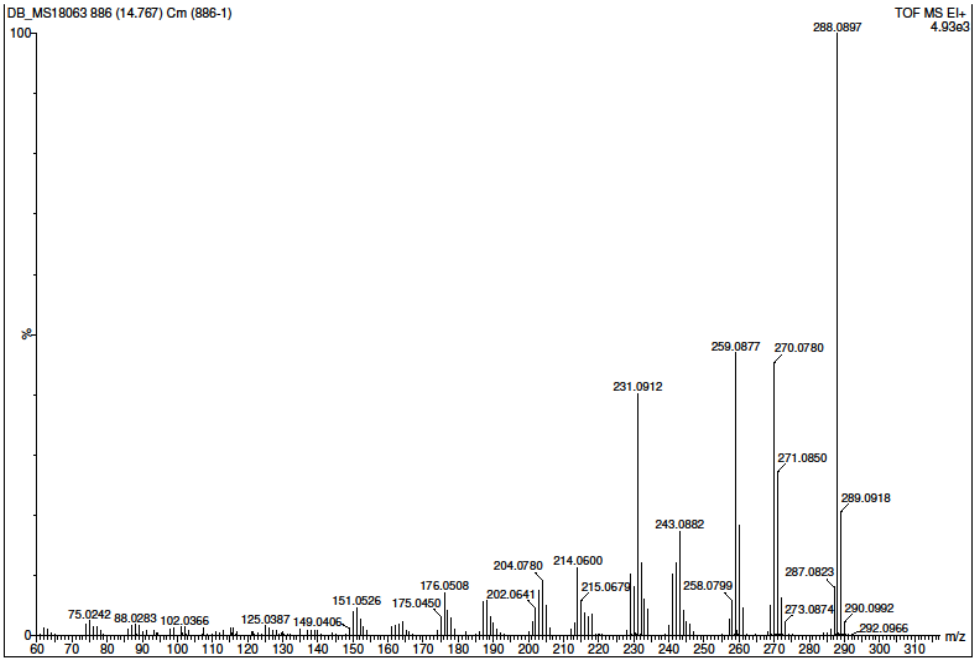

Figure A.11: HR-MS, EI-TOF.

Elemental Composition Report **Page 1**

Single Mass Analysis
Tolerance = 5.0 PPM / DBE: min = -1.5, max = 50.0
Element prediction: Off

Monoisotopic Mass, Odd and Even Electron Ions
4 formula(e) evaluated with 1 results within limits (all results (up to 1000) for each mass)
Elements Used:
C: 0-18 H: 0-12 N: 0-2 O: 0-2

24-Nov-2017 BCV319 School of Chemistry Cardiff University
DB_MS18063 886 (14.767) Cm (886-178) TOF MS EI+
4.93e+003

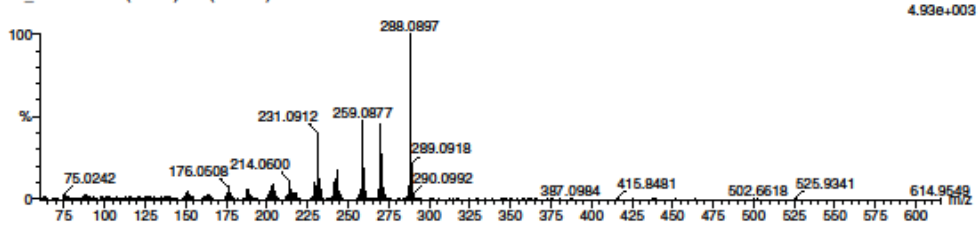

Minimum:				-1.5		
Maximum:		5.0	5.0	50.0		
Mass	Calc. Mass	mDa	PPM	DBE	i-FIT	Formula
288.0897	288.0899	-0.2	-0.7	14.0	0.8	C18 H12 N2 O2

Figure A.12: Elemental Composition Report.

Characterization 3,9-diaza peri-xanthenoxanten 2

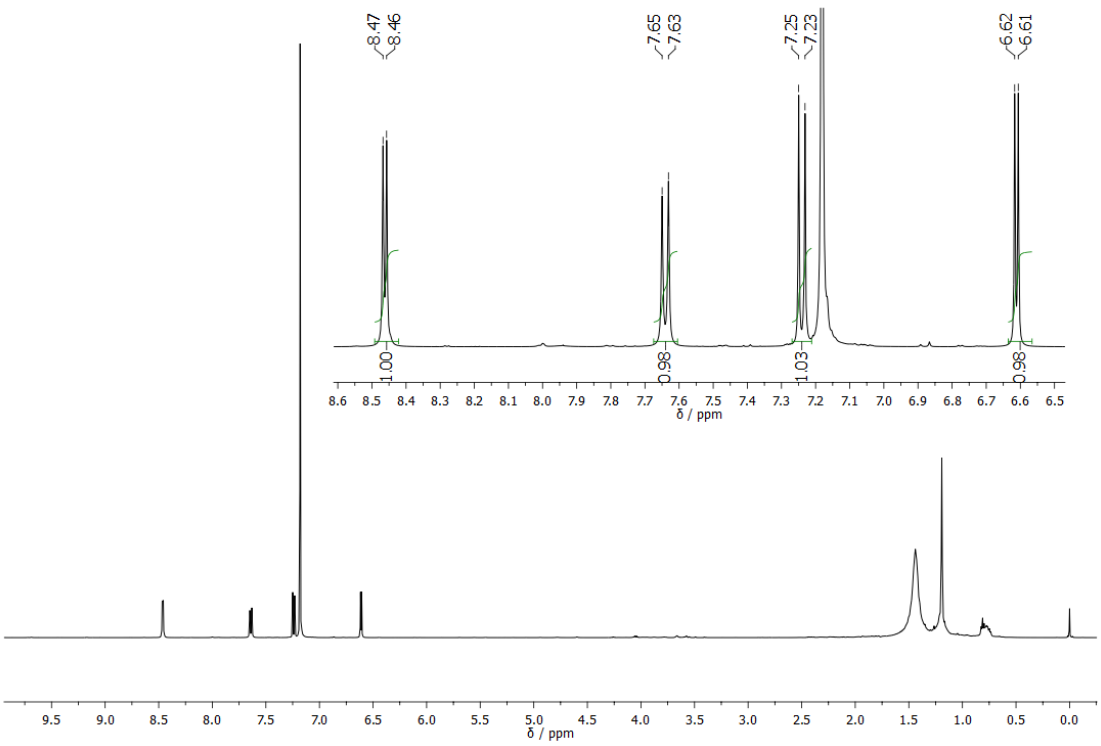

Figure A.13: ^{1}H-NMR, 500 MHz, $CDCl_3$

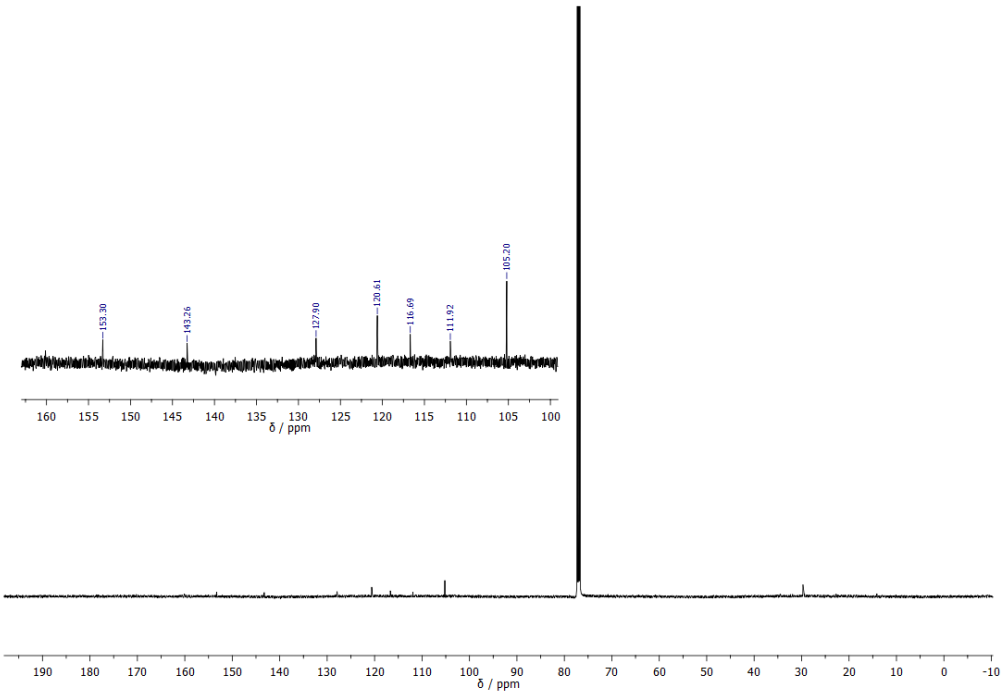

Figure A.14: ^{13}C-NMR, 125 MHz, $CDCl_3$

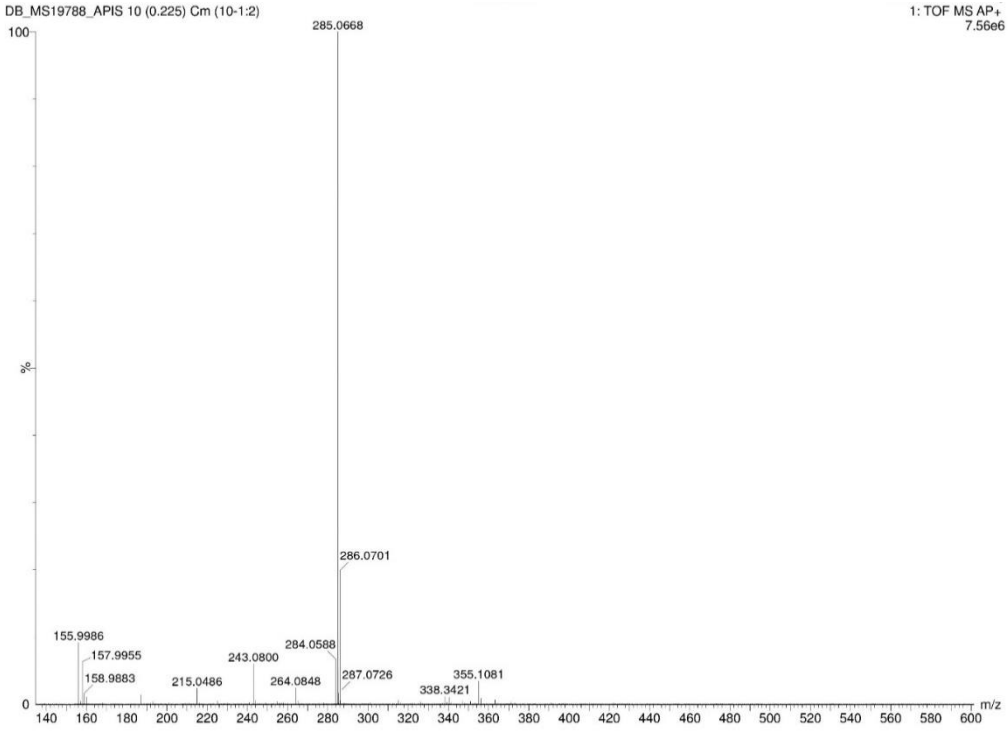

Figure A.15: HR-MS, AP-TOF.

Elemental Composition Report **Page 1**

Single Mass Analysis
Tolerance = 5.0 PPM / DBE: min = -1.5, max = 50.0
Element prediction: Off
Number of isotope peaks used for i-FIT = 3

Monoisotopic Mass, Odd and Even Electron Ions
4 formula(e) evaluated with 1 results within limits (up to 50 best isotopic matches for each mass)
Elements Used:
C: 0-18 H: 0-9 N: 0-2 O: 0-2

Minimum:				-1.5				
Maximum:		5.0	5.0	50.0				
Mass	Calc. Mass	mDa	PPM	DBE	i-FIT	Norm	Conf(%)	Formula
285.0668	285.0664	0.4	1.4	15.5	795.7	n/a	n/a	C18 H9 N2 O2

Figure A.16: Elemental Composition Report.

Characterization Quinolin-3-yl diethylcarbamate 8

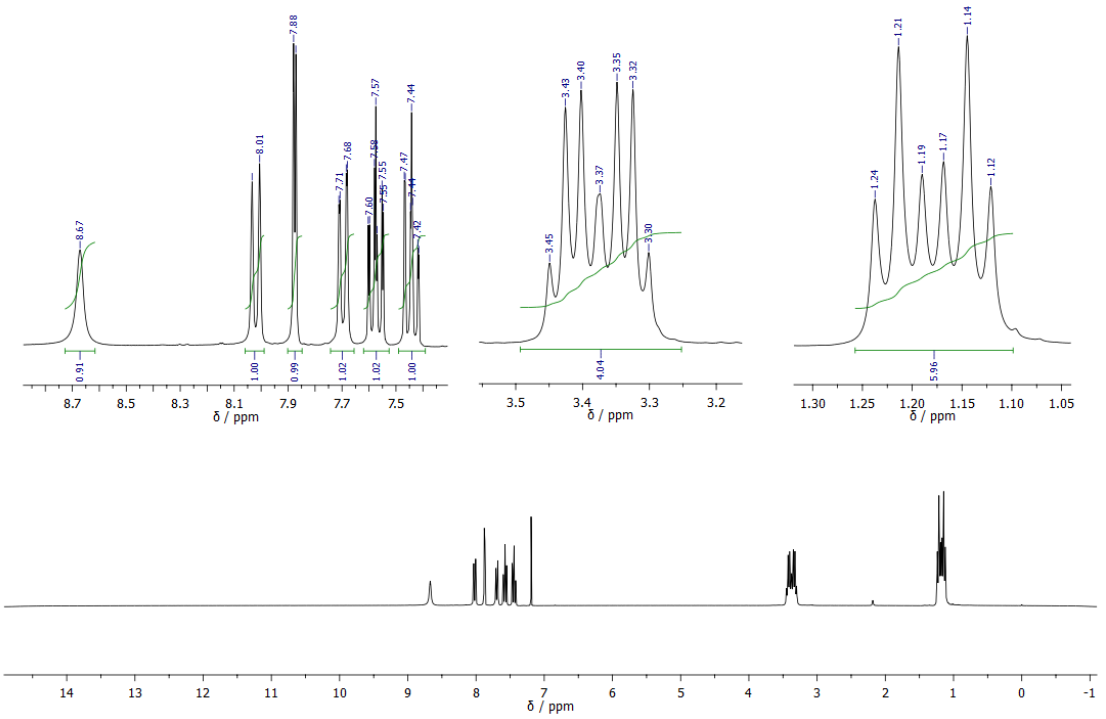

Figure A.17: ^{1}H-NMR, 300 MHz, $CDCl_3$

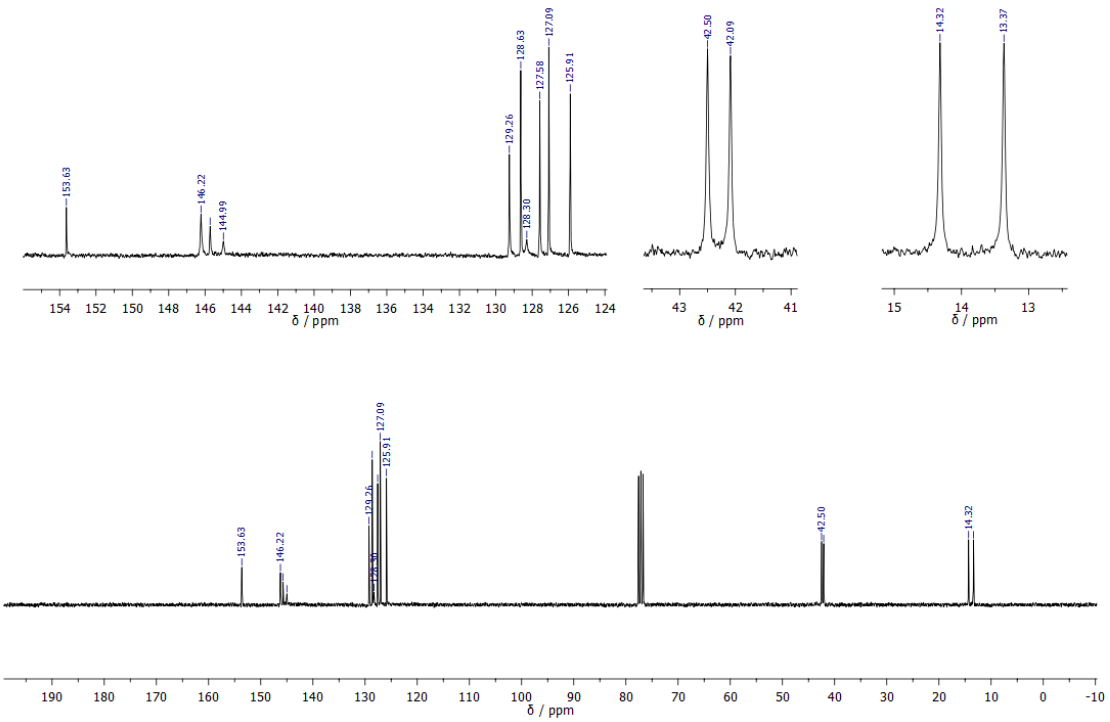

Figure A.18: ^{13}C-NMR, 75 MHz, $CDCl_3$

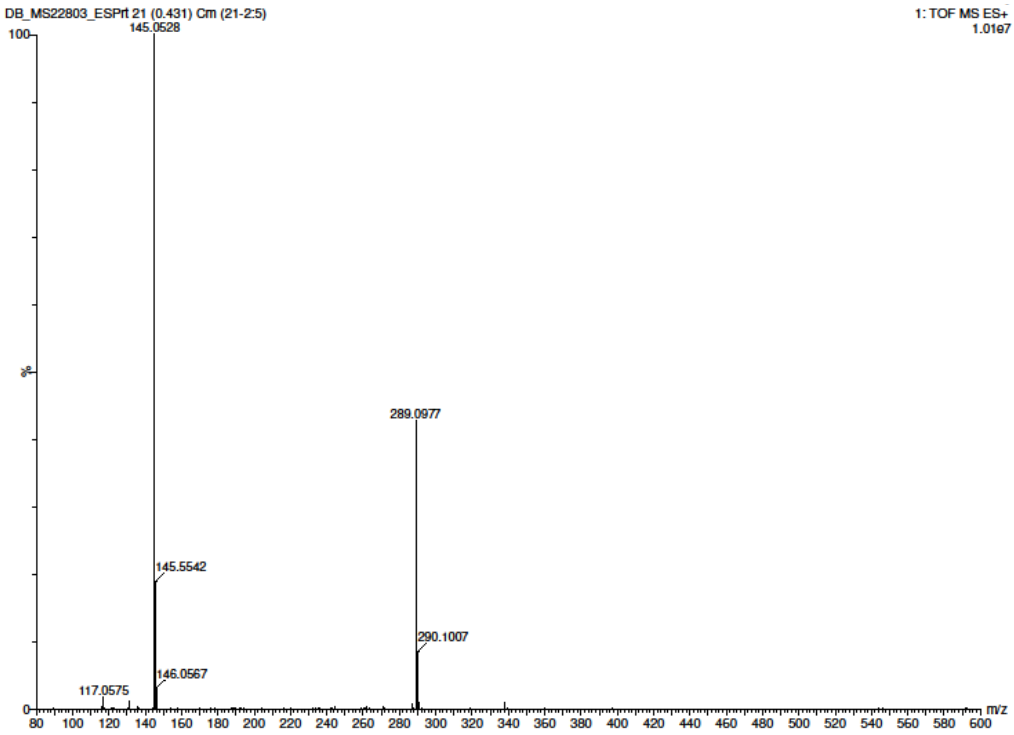

Figure A.19: HR-MS, ES-TOF.

Elemental Composition Report **Page 1**

Single Mass Analysis
Tolerance = 10.0 PPM / DBE: min = -1.5, max = 100.0
Element prediction: Off
Number of isotope peaks used for i-FIT = 3

Monoisotopic Mass, Odd and Even Electron Ions
4 formula(e) evaluated with 1 results within limits (up to 50 closest results for each mass)
Elements Used:
C: 0-18 H: 0-13 N: 0-2 O: 0-2

Minimum:				-1.5				
Maximum:		5.0	10.0	100.0				
Mass	Calc. Mass	mDa	PPM	DBE	i-FIT	Norm	Conf(%)	Formula
289.0977	289.0977	0.0	0.0	13.5	159.1	n/a	n/a	C18 H13 N2 O2

Figure A.20: Elemental Composition Report.

Characterization [4,4'-biquinoline]-3,3'-diyl bis(diethylcarbamate) 9

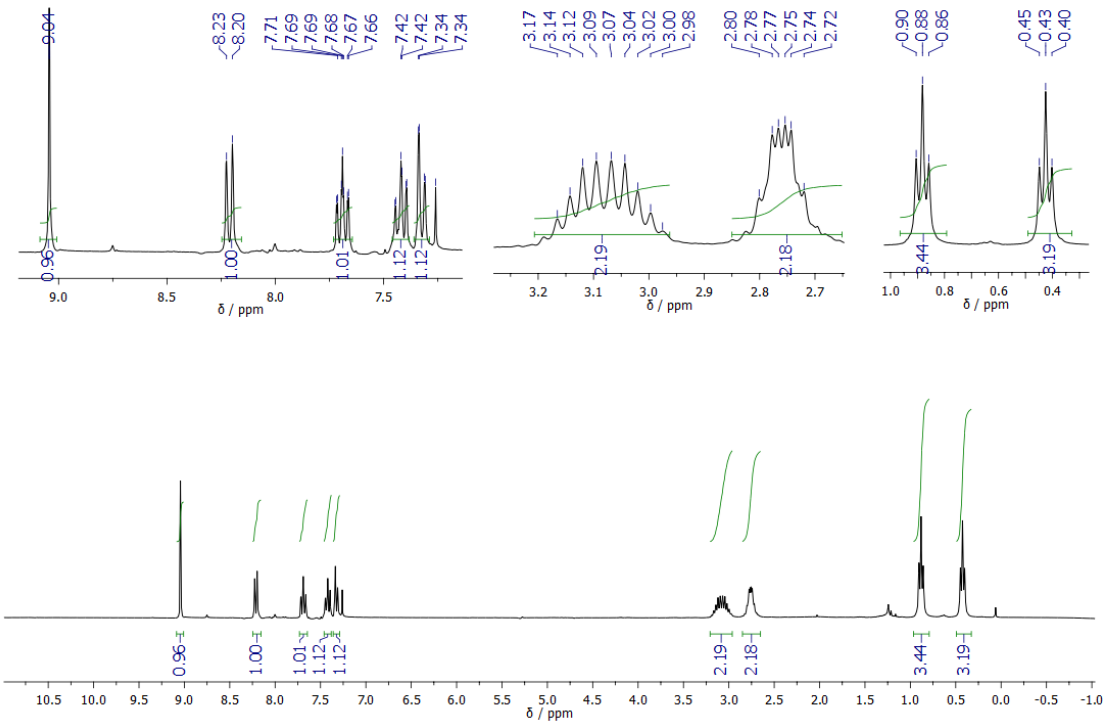

Figure A.21: ^{1}H-NMR, 300 MHz, $CDCl_3$

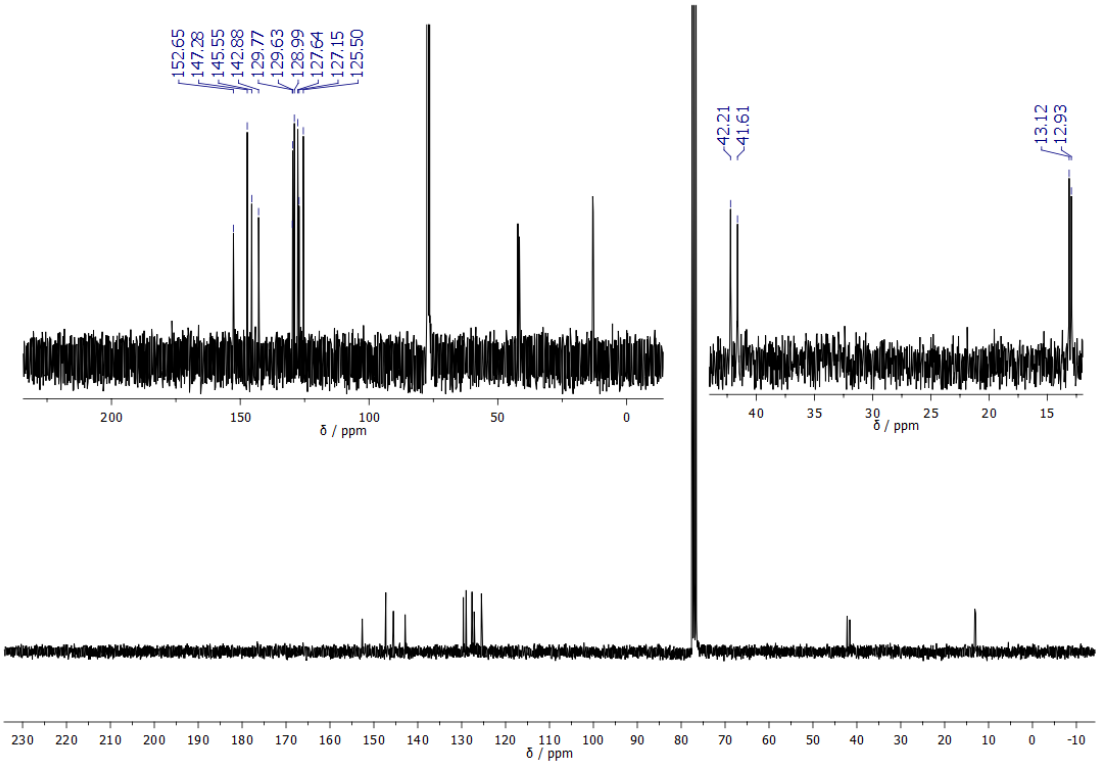

Figure A.22: ^{13}C-NMR, 75 MHz, $CDCl_3$

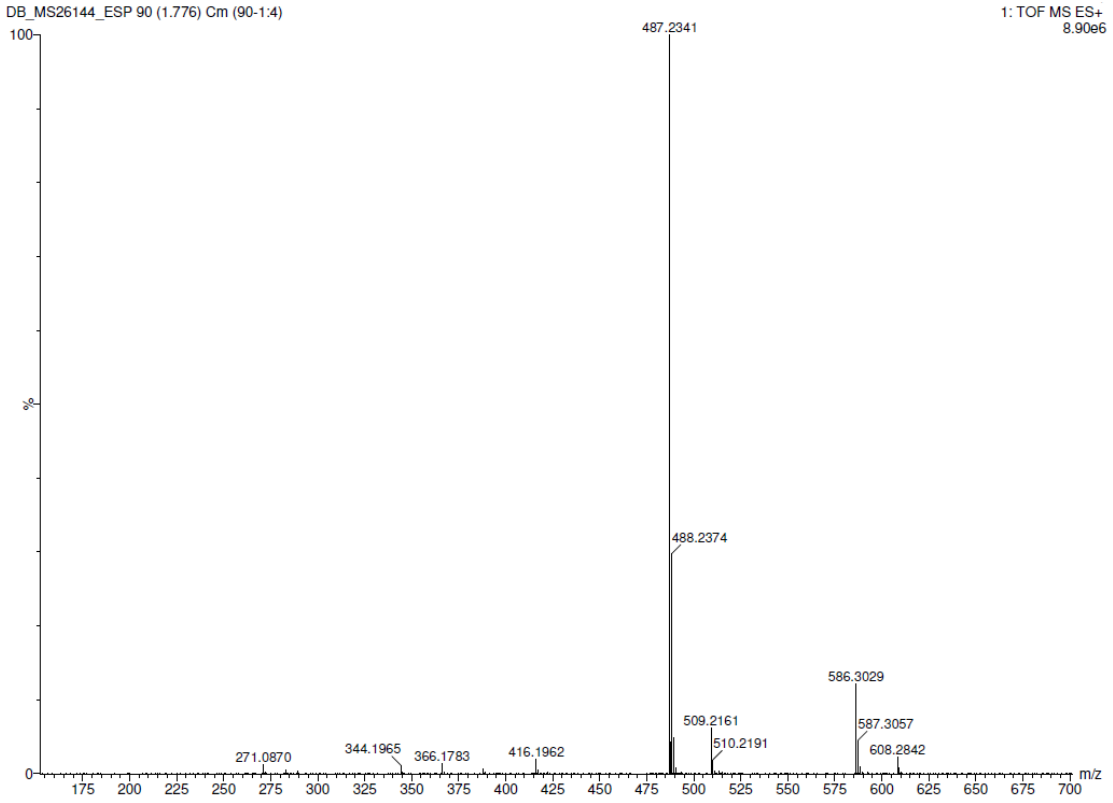

Figure A.23: HR-MS, ES-TOF.

Elemental Composition Report **Page 1**

Single Mass Analysis
Tolerance = 5.0 PPM / DBE: min = -1.5, max = 200.0
Element prediction: Off
Number of isotope peaks used for i-FIT = 3

Monoisotopic Mass, Odd and Even Electron Ions
20 formula(e) evaluated with 1 results within limits (up to 50 closest results for each mass)
Elements Used:
C: 0-28 H: 0-31 N: 0-4 O: 0-4

Minimum:				-1.5				
Maximum:		5.0	5.0	200.0				
Mass	Calc. Mass	mDa	PPM	DBE	i-FIT	Norm	Conf(%)	Formula
487.2341	487.2345	-0.4	-0.8	15.5	304.5	n/a	n/a	C28 H31 N4 O4

Figure A.24: Elemental Composition Report.

Characterization [4,4'-biquinoline]-3,3'-diol 7

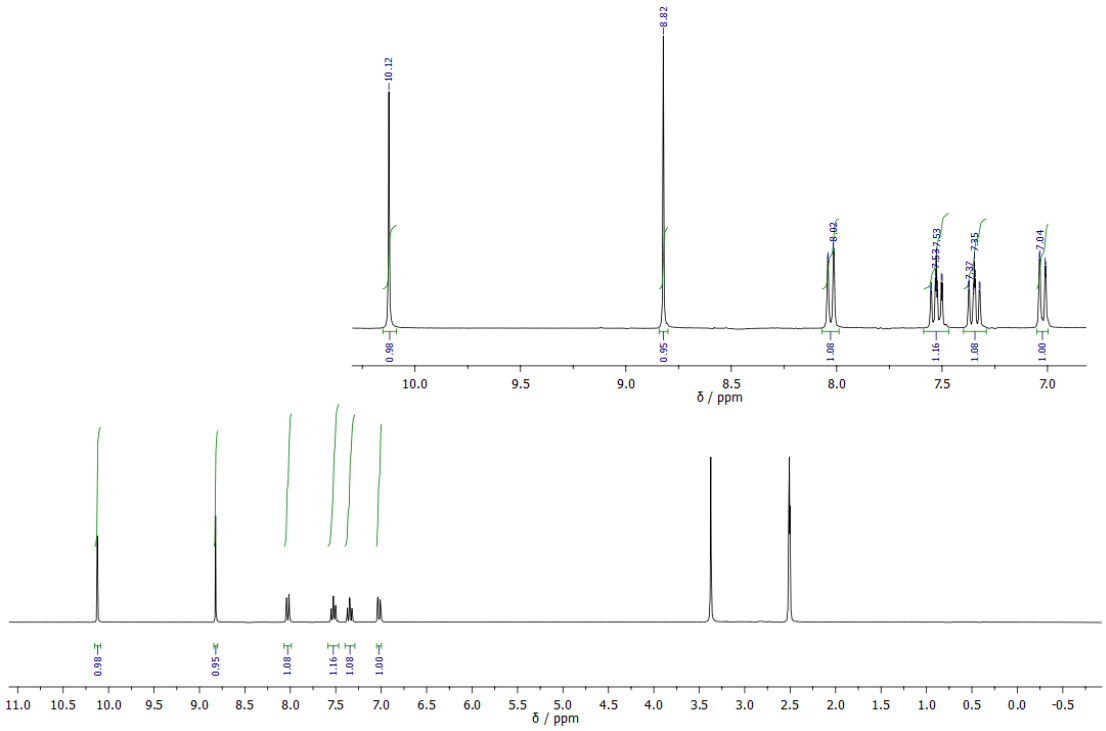

Figure A.25: ^{1}H-NMR, 500 MHz, DMSO-d_6

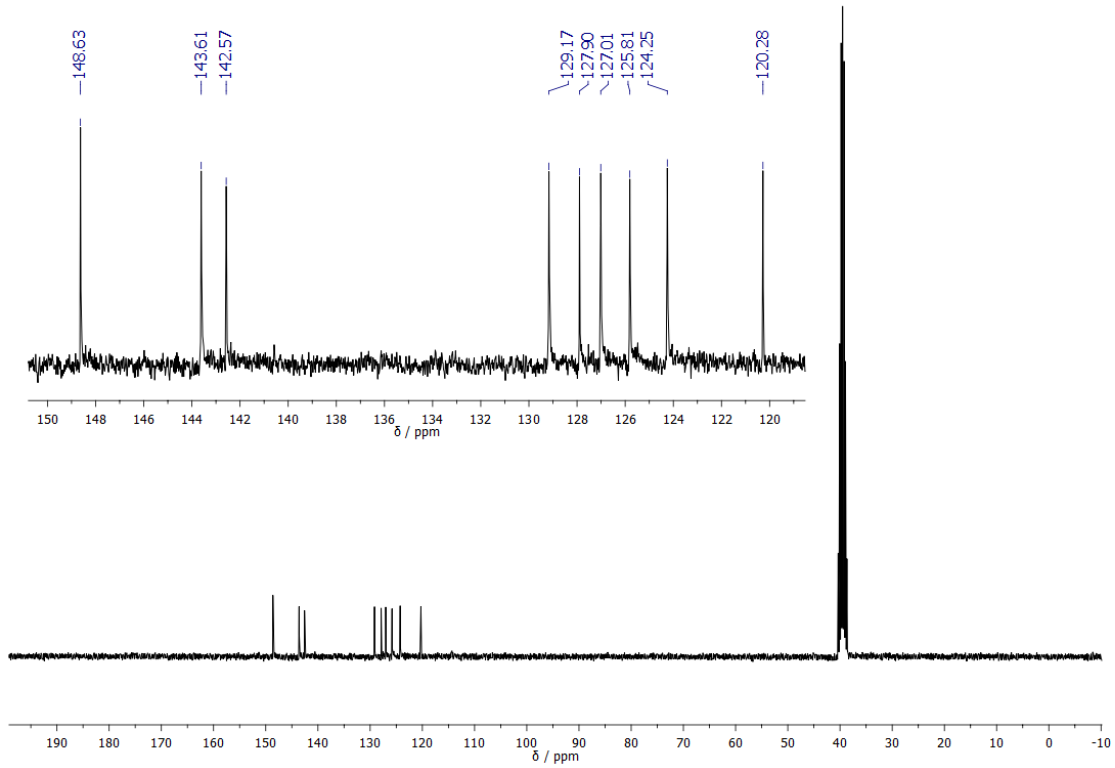

Figure A.26: ^{13}C-NMR, 125 MHz, DMSO-d_6

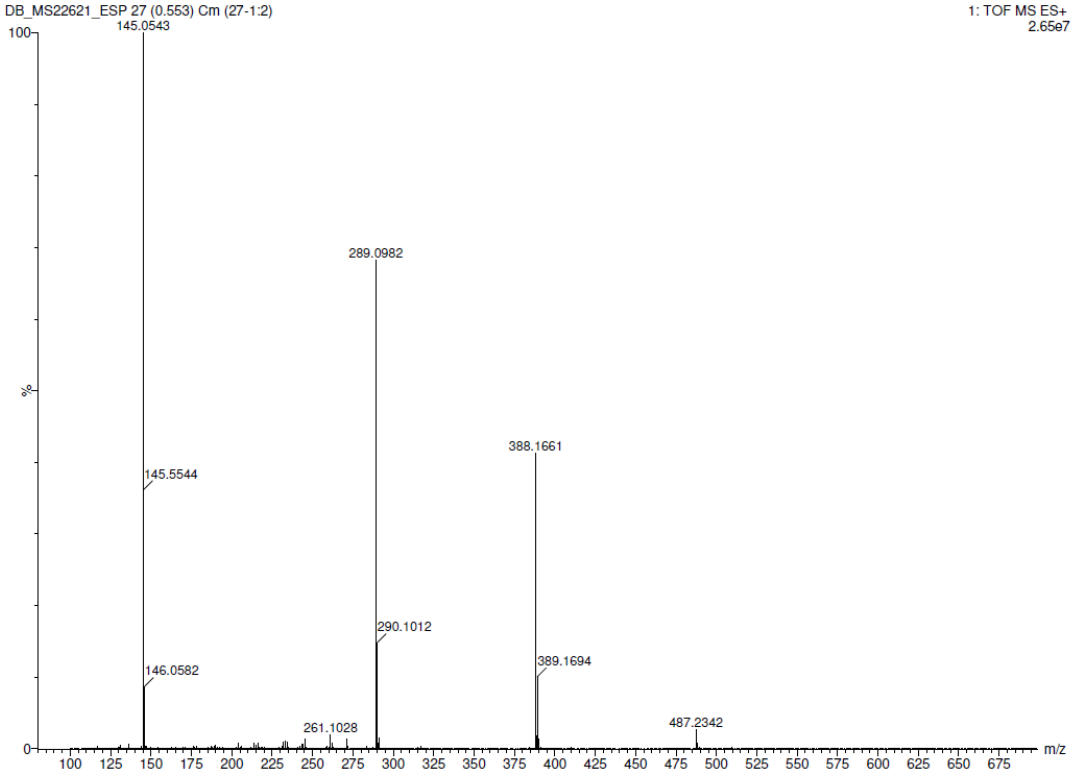

Figure A.27: HR-MS, ES-TOF.

Elemental Composition Report **Page 1**

Single Mass Analysis
Tolerance = 5.0 PPM / DBE: min = -1.5, max = 100.0
Element prediction: Off
Number of isotope peaks used for i-FIT = 3

Monoisotopic Mass, Odd and Even Electron Ions
4 formula(e) evaluated with 1 results within limits (up to 50 best isotopic matches for each mass)
Elements Used:
C: 0-18 H: 0-13 N: 0-2 O: 0-2

Minimum:				-1.5				
Maximum:		5.0	5.0	100.0				
Mass	Calc. Mass	mDa	PPM	DBE	i-FIT	Norm	Conf(%)	Formula
289.0982	289.0977	0.5	1.7	13.5	680.5	n/a	n/a	C18 H13 N2 O2

Figure A.28: Elemental Composition Report.

Characterization 4,10-diaza peri-xanthenoxantene 6

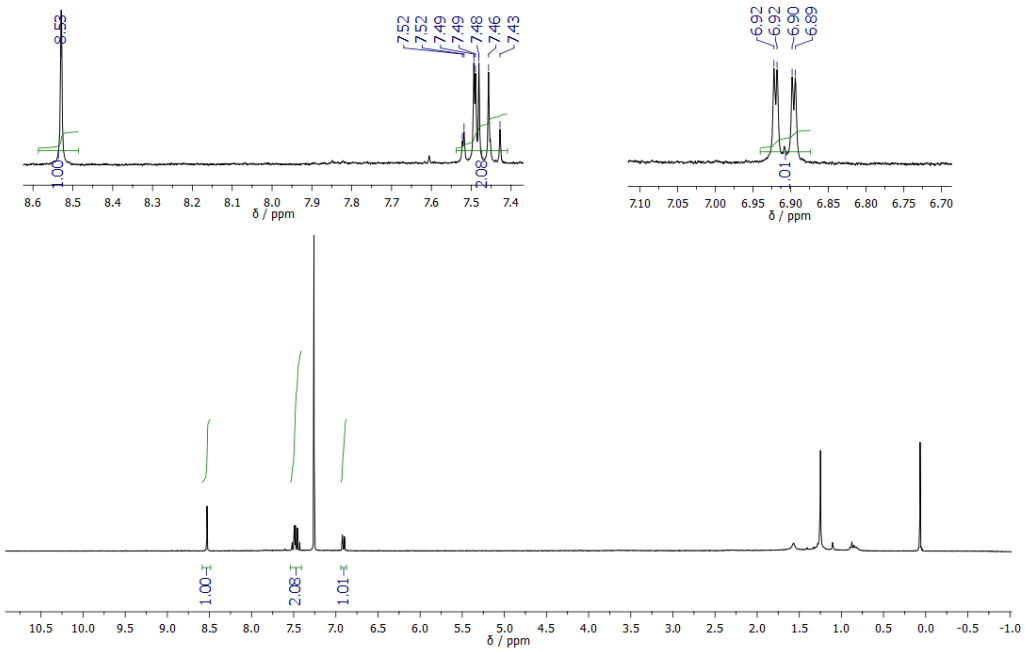

Figure A.29: ^{1}H-NMR, 500 MHz, $CDCl_3$

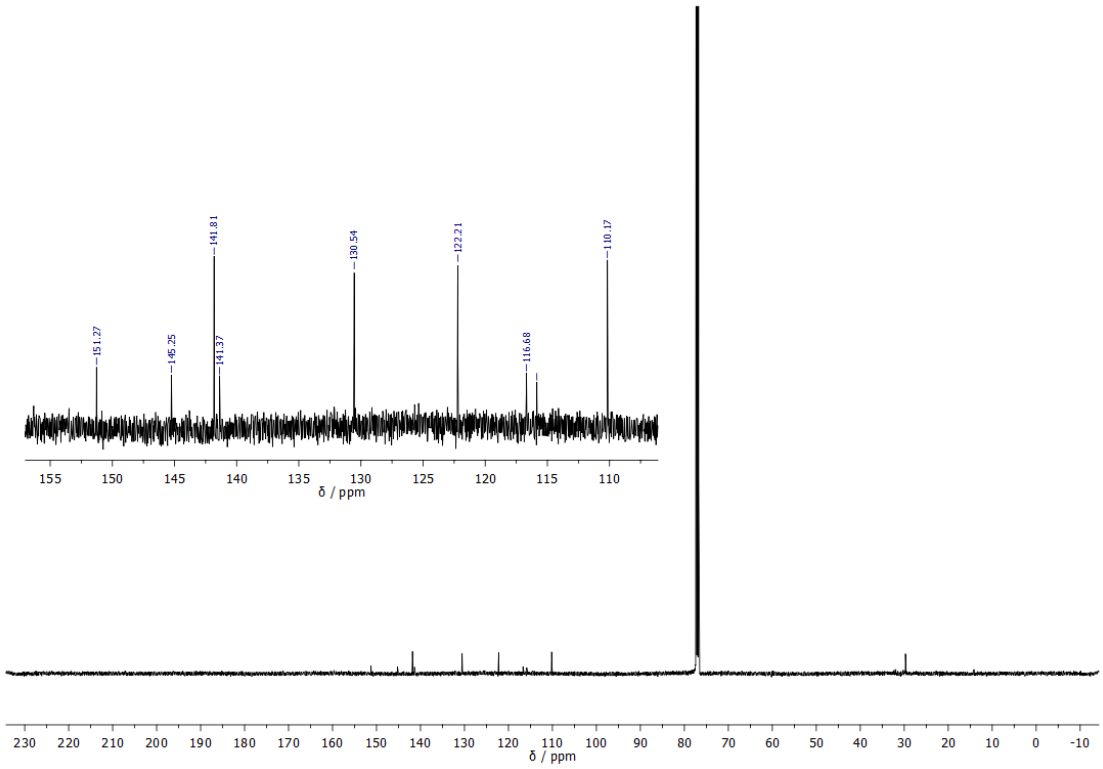

Figure A.30: ^{13}C-NMR, 125 MHz, $CDCl_3$

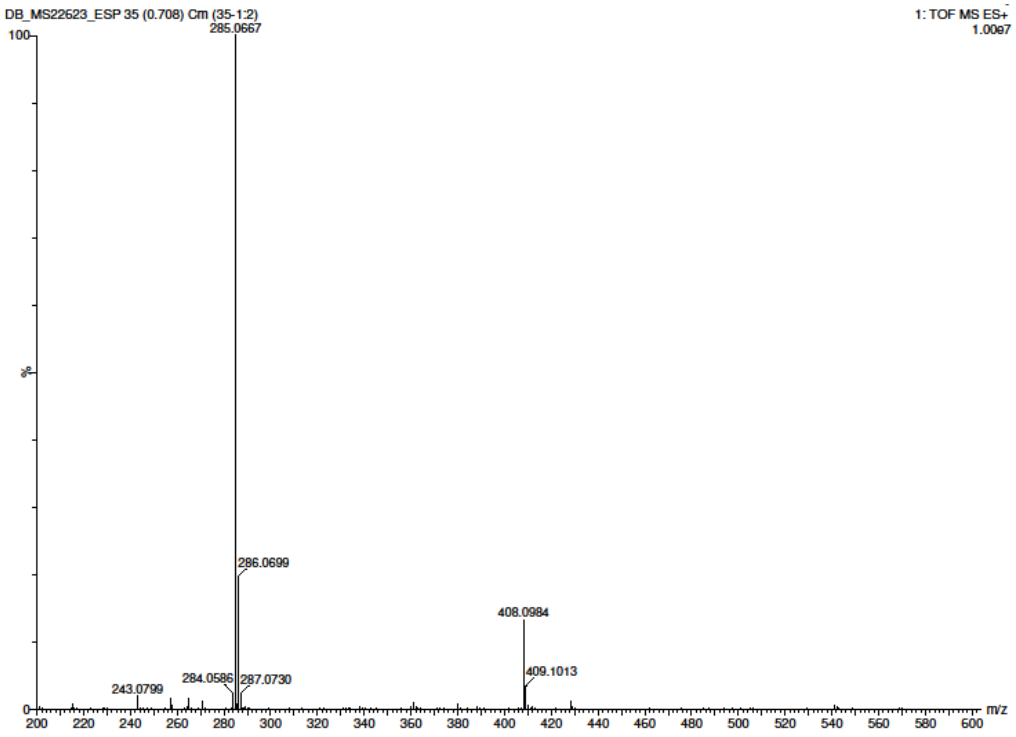

Figure A.31: HR-MS, ES-TOF.

Elemental Composition Report Page 1

Single Mass Analysis
Tolerance = 5.0 PPM / DBE: min = -1.5, max = 100.0
Element prediction: Off
Number of isotope peaks used for i-FIT = 3

Monoisotopic Mass, Odd and Even Electron Ions
4 formula(e) evaluated with 1 results within limits (up to 50 best isotopic matches for each mass)
Elements Used:
C: 0-18 H: 0-9 N: 0-2 O: 0-2

Minimum:				-1.5				
Maximum:		5.0	5.0	100.0				
Mass	Calc. Mass	mDa	PPM	DBE	i-FIT	Norm	Conf(%)	Formula
285.0667	285.0664	0.3	1.1	15.5	556.3	n/a	n/a	C18 H9 N2 O2

Figure A.32: Elemental Composition Report.

Characterization of isoquinolin-3-yl diethylcarbamate

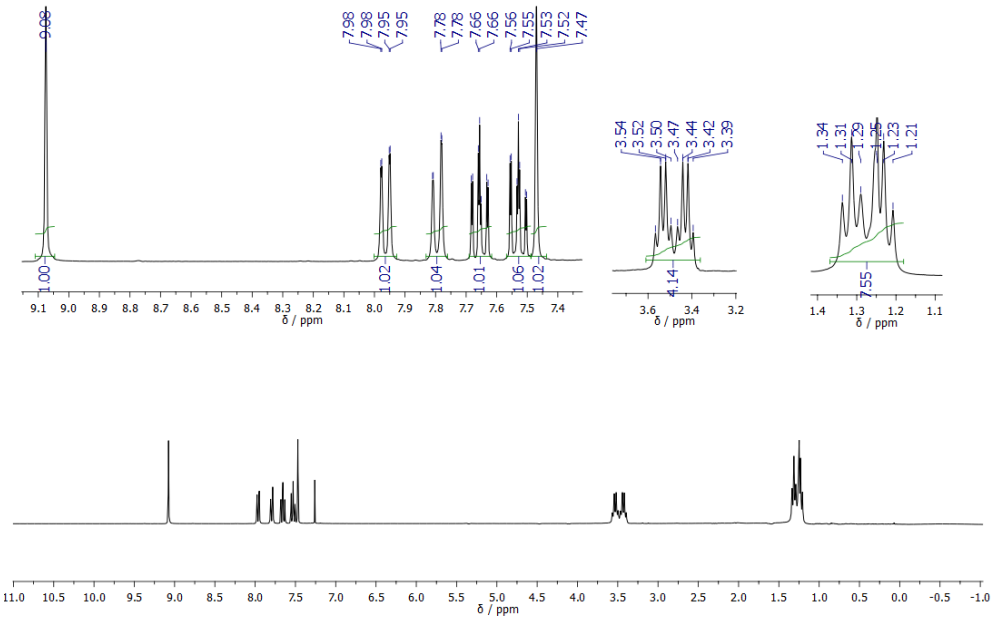

Figure A.33: ^{1}H-NMR, 300 MHz, $CDCl_3$

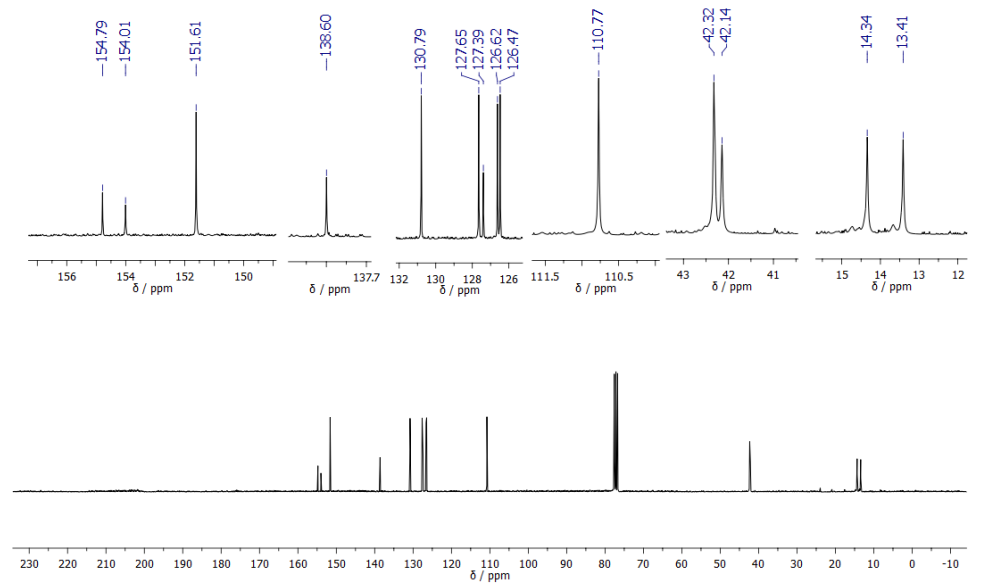

Figure A.34: ^{13}C-NMR, 75 MHz, $CDCl_3$

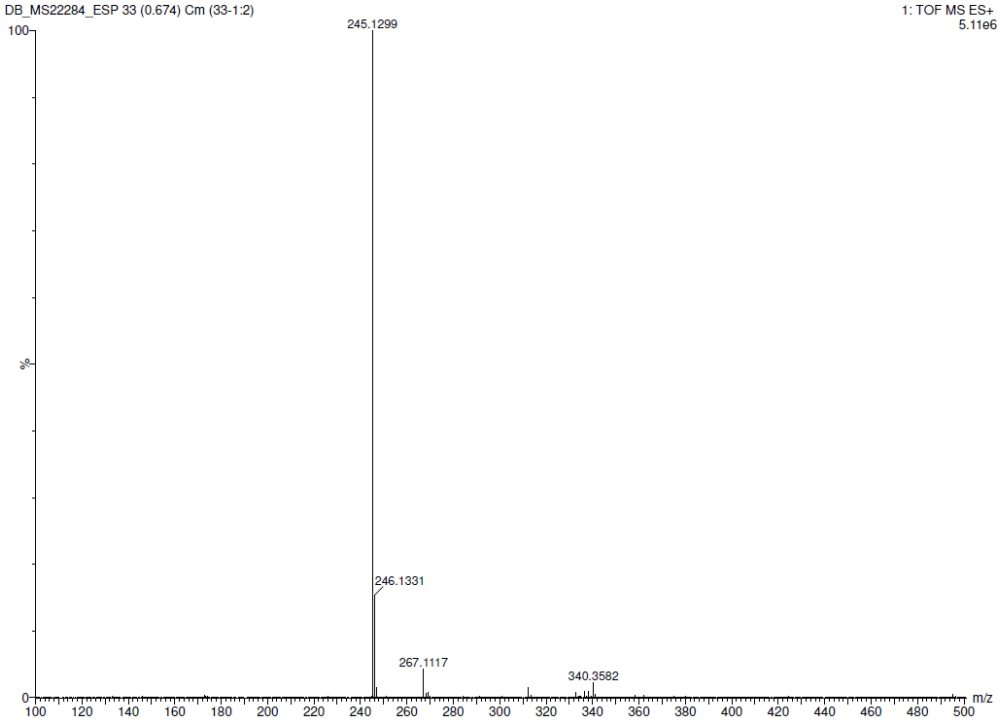

Figure A.35: HR-MS, ES-TOF.

Elemental Composition Report **Page 1**

Single Mass Analysis
Tolerance = 5.0 PPM / DBE: min = -1.5, max = 100.0
Element prediction: Off
Number of isotope peaks used for i-FIT = 3

Monoisotopic Mass, Odd and Even Electron Ions
7 formula(e) evaluated with 1 results within limits (up to 50 best isotopic matches for each mass)
Elements Used:
C: 0-14 H: 0-17 N: 0-2 O: 0-2

Minimum:				-1.5				
Maximum:		5.0	5.0	100.0				
Mass	Calc. Mass	mDa	PPM	DBE	i-FIT	Norm	Conf(%)	Formula
245.1299	245.1290	0.9	3.7	7.5	534.9	n/a	n/a	C14 H17 N2 O2

Figure A.36: Elemental Composition Report.

Characterization of [4,4'-biisoquinoline]-3,3'-diyl bis(diethylcarbamate)

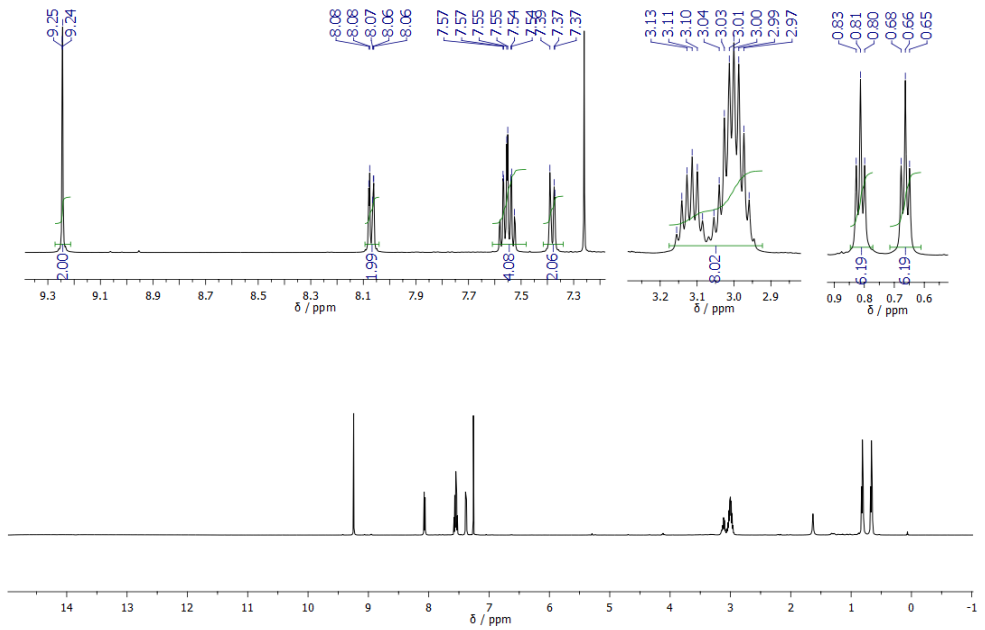

Figure A.37: ^{1}H-NMR, 300 MHz, $CDCl_3$

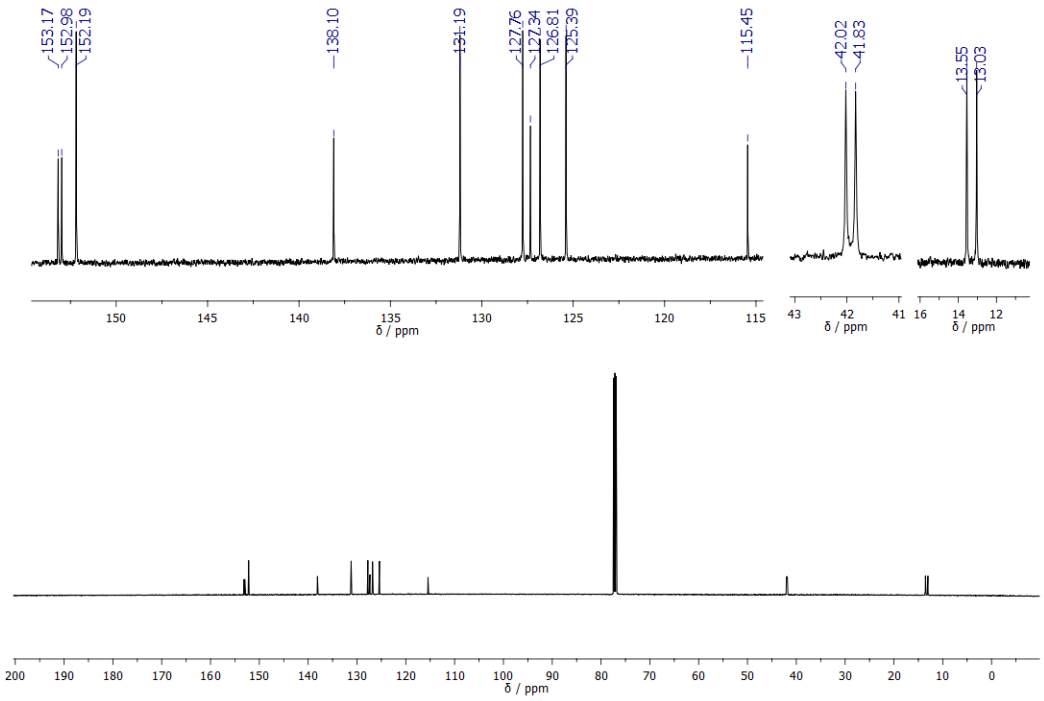

Figure A.38: ^{13}C-NMR, 75 MHz, $CDCl_3$

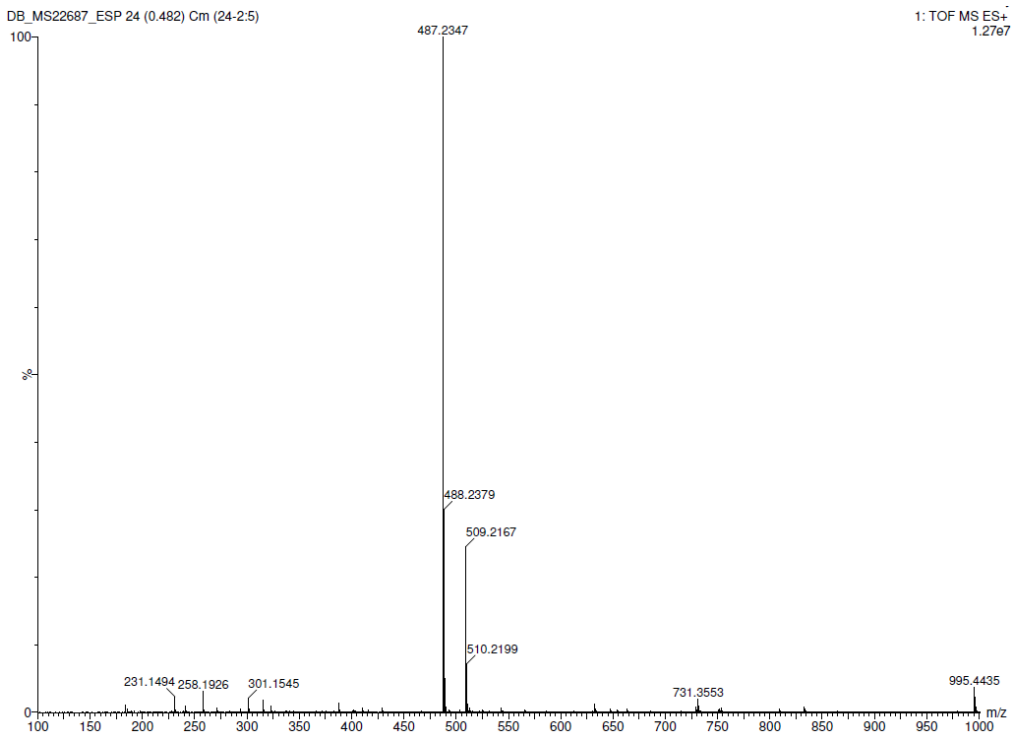

Figure A.39: HR-MS, ES-TOF.

Elemental Composition Report **Page 1**

Single Mass Analysis
Tolerance = 5.0 PPM / DBE: min = -1.5, max = 100.0
Element prediction: Off
Number of isotope peaks used for i-FIT = 3

Monoisotopic Mass, Odd and Even Electron Ions
20 formula(e) evaluated with 1 results within limits (up to 50 best isotopic matches for each mass)
Elements Used:
C: 0-28 H: 0-31 N: 0-4 O: 0-4

Minimum:				-1.5				
Maximum:		5.0	5.0	100.0				
Mass	Calc. Mass	mDa	PPM	DBE	i-FIT	Norm	Conf(%)	Formula
487.2347	487.2345	0.2	0.4	15.5	608.9	n/a	n/a	C28 H31 N4 O4

Figure A.40: Elemental Composition Report.

Characterization of [4,4'-biisoquinoline]-3,3'-diol

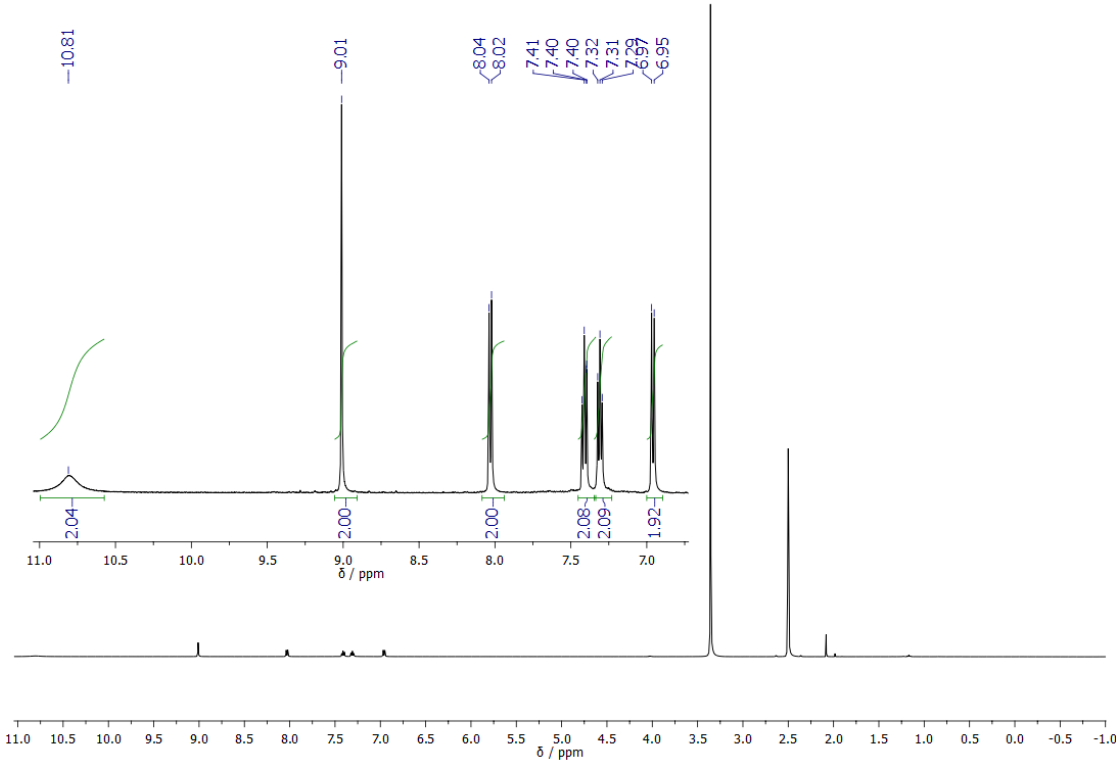

Figure A.41: ^{1}H-NMR, 500 MHz, DMSO-d_6

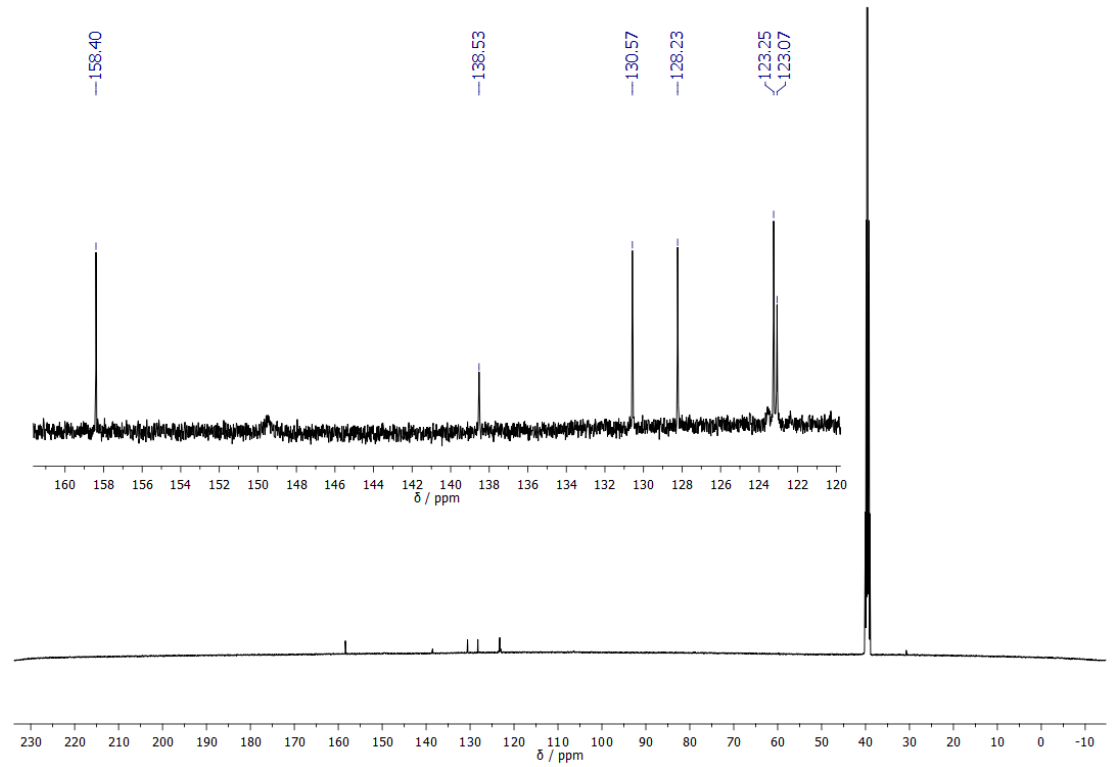

Figure A.42: ^{13}C-NMR, 125 MHz, DMSO-d_6

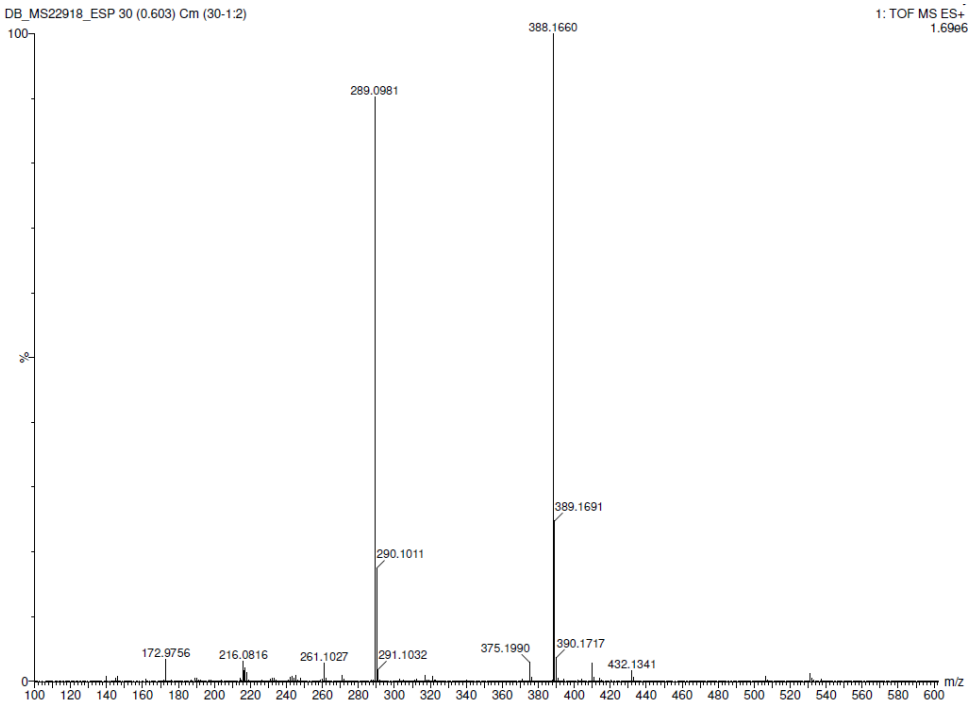

Figure A.43: HR-MS, ES-TOF.

Elemental Composition Report **Page 1**

Single Mass Analysis
Tolerance = 5.0 PPM / DBE: min = -1.5, max = 100.0
Element prediction: Off
Number of isotope peaks used for i-FIT = 3

Monoisotopic Mass, Odd and Even Electron Ions
4 formula(e) evaluated with 1 results within limits (up to 50 closest results for each mass)
Elements Used:
C: 0-18 H: 0-13 N: 0-2 O: 0-2

Minimum:				-1.5				
Maximum:		5.0	5.0	100.0				
Mass	Calc. Mass	mDa	PPM	DBE	i-FIT	Norm	Conf(%)	Formula
289.0981	289.0977	0.4	1.4	13.5	200.5	n/a	n/a	C18 H13 N2 O2

Figure A.44: Elemental Composition Report.

Characterization of quinolin-3-yl diethylcarbamate

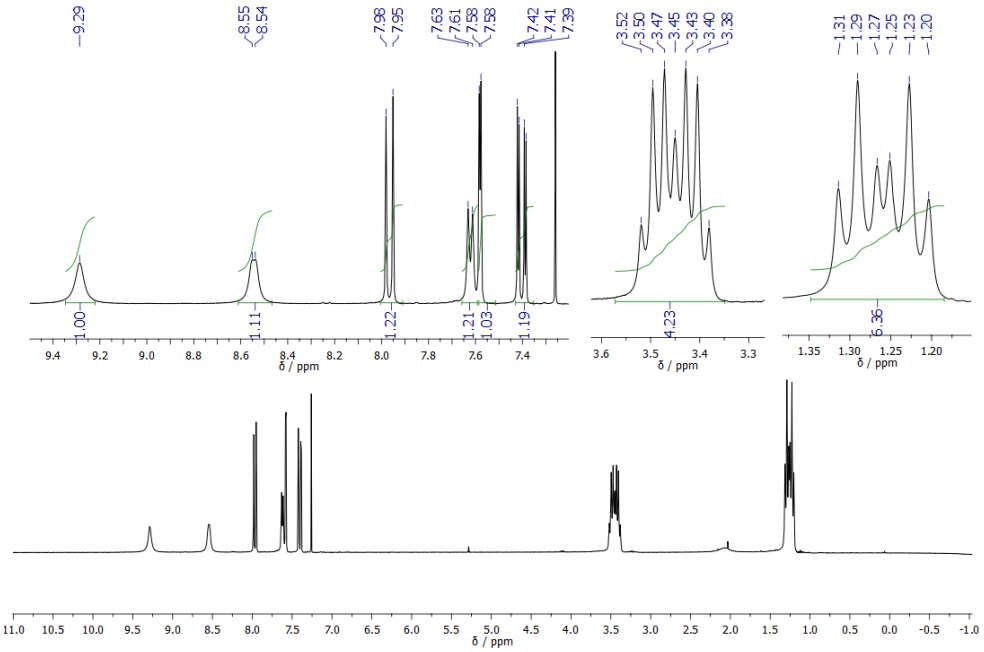

Figure A.45: ^{1}H-NMR, 300 MHz, $CDCl_3$

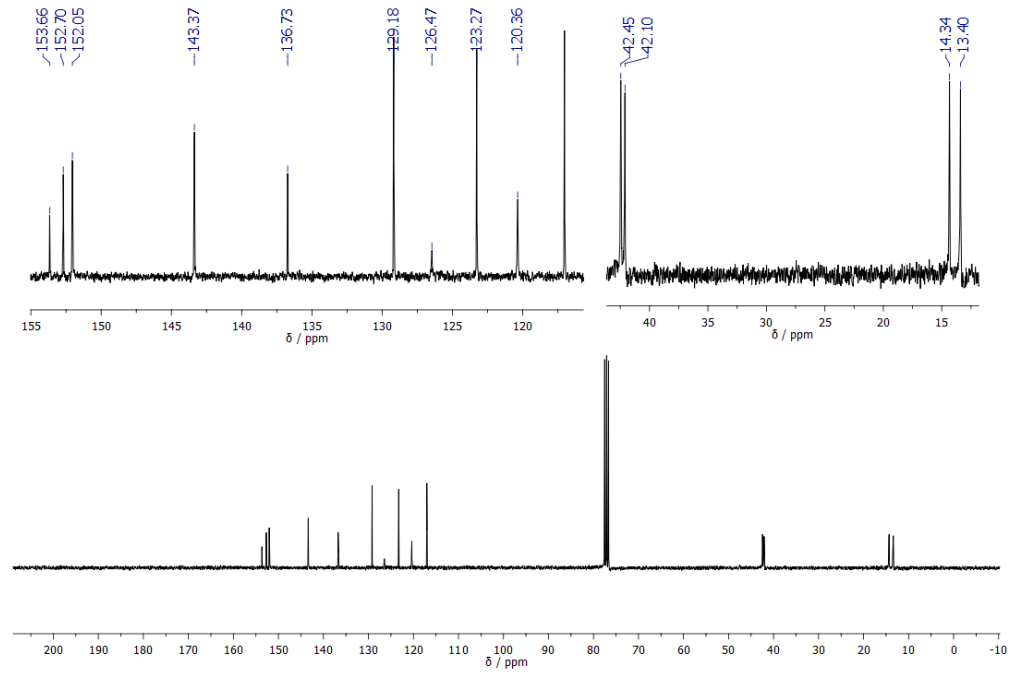

Figure A.46: ^{13}C-NMR, 75 MHz, $CDCl_3$

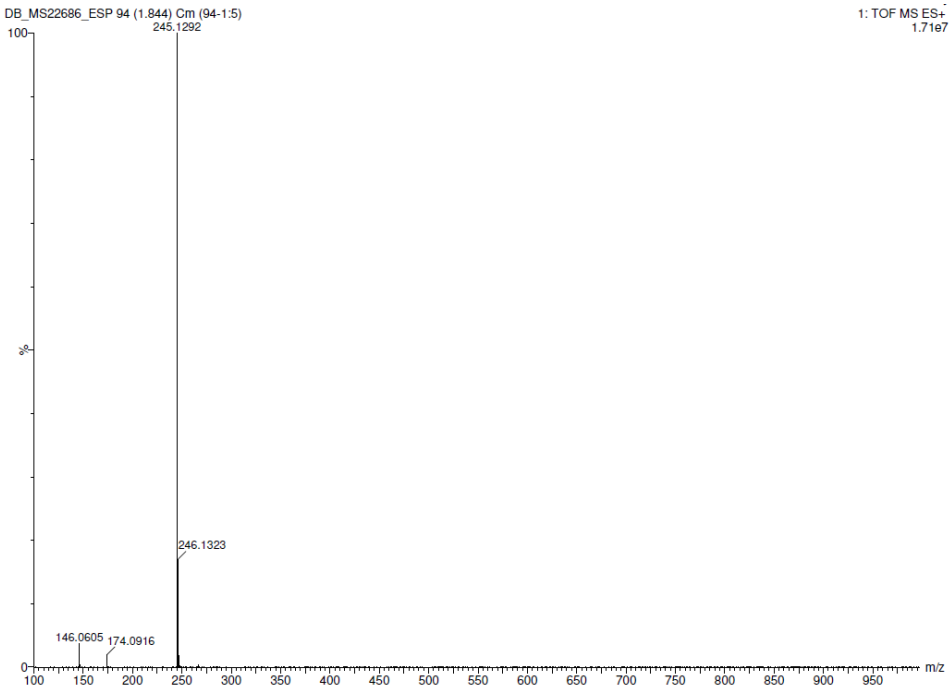

Figure A.47: HR-MS, ES-TOF.

Elemental Composition Report **Page 1**

Single Mass Analysis
Tolerance = 5.0 PPM / DBE: min = -1.5, max = 100.0
Element prediction: Off
Number of isotope peaks used for i-FIT = 3

Monoisotopic Mass, Odd and Even Electron Ions
7 formula(e) evaluated with 1 results within limits (up to 50 best isotopic matches for each mass)
Elements Used:
C: 0-14 H: 0-17 N: 0-2 O: 0-2

Minimum:				-1.5				
Maximum:		5.0	5.0	100.0				
Mass	Calc. Mass	mDa	PPM	DBE	i-FIT	Norm	Conf(%)	Formula
245.1292	245.1290	0.2	0.8	7.5	519.8	n/a	n/a	C14 H17 N2 O2

Figure A.48: Elemental Composition Report.

Characterization of 5-hydroxyisoquinolin-6-yl diethylcarbamate

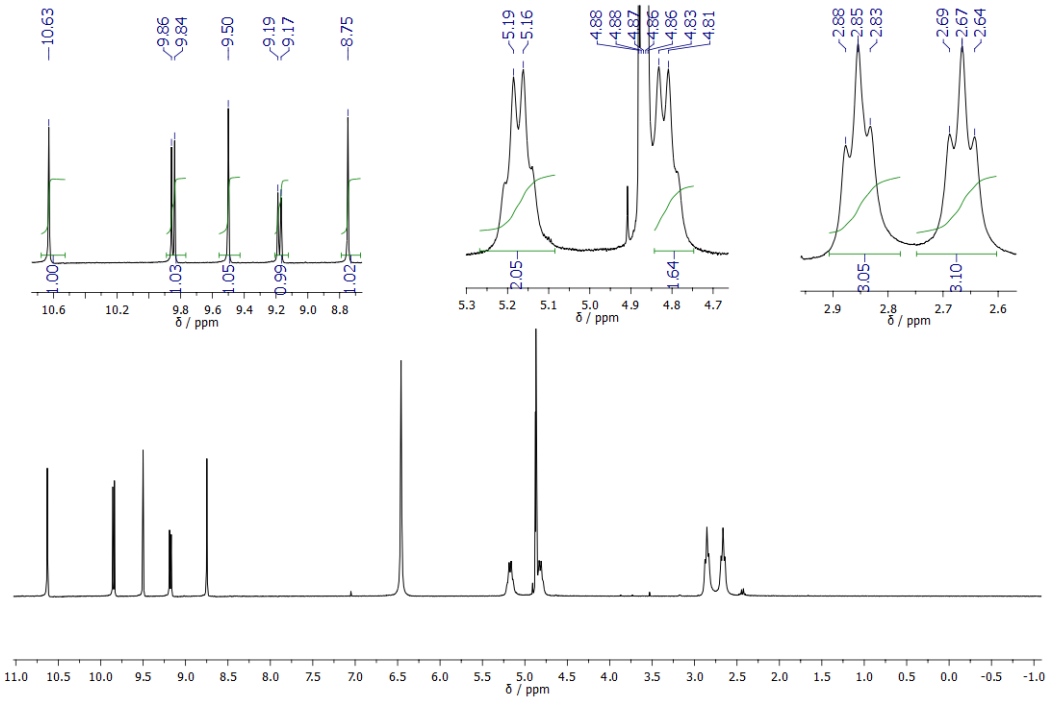

Figure A.49: ^{1}H-NMR, 300 MHz, CD_3OD

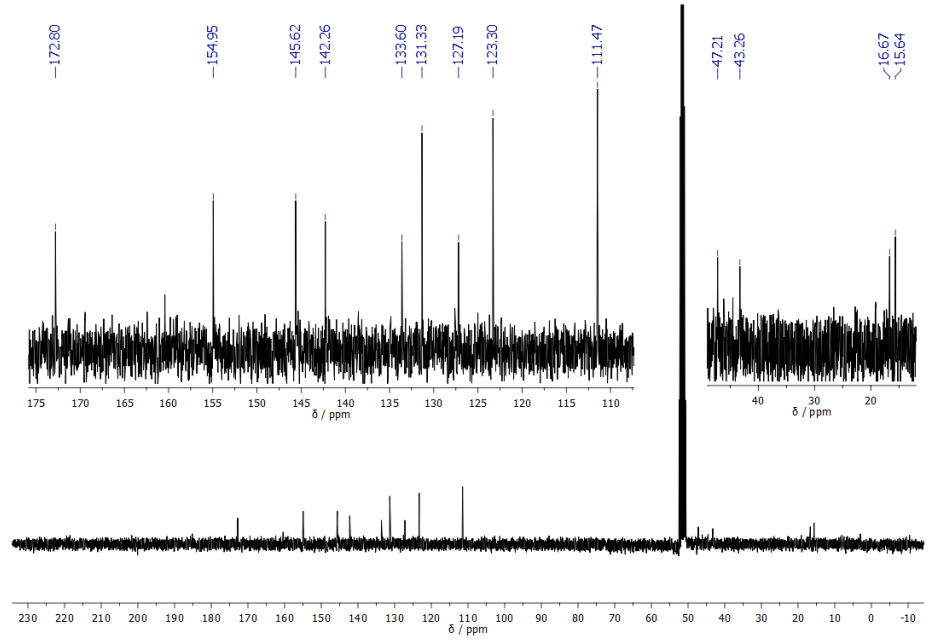

Figure A.50: ^{13}C-NMR, 75 MHz, CD_3OD

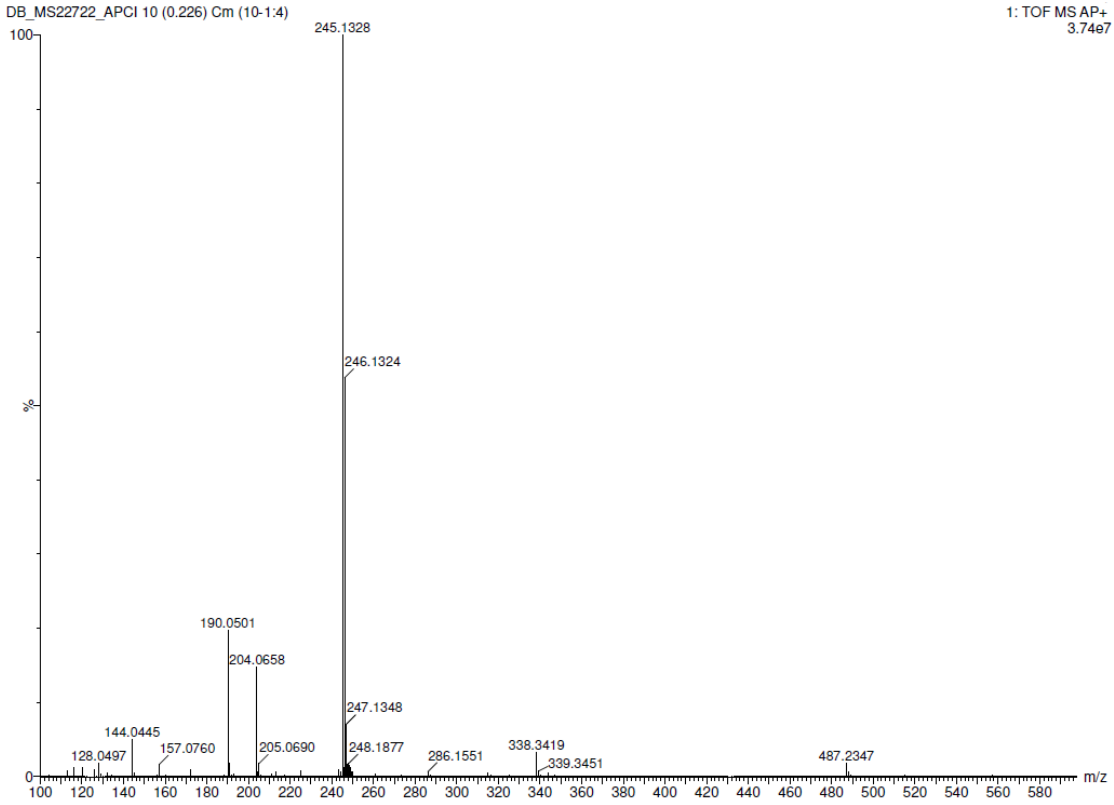

Figure A.51: HR-MS, AP-TOF.

Elemental Composition Report **Page 1**

Single Mass Analysis
Tolerance = 5.0 PPM / DBE: min = -1.5, max = 100.0
Element prediction: Off
Number of isotope peaks used for i-FIT = 3

Monoisotopic Mass, Odd and Even Electron Ions
40 formula(e) evaluated with 1 results within limits (up to 50 best isotopic matches for each mass)
Elements Used:
C: 0-28 H: 0-31 N: 0-4 O: 0-4 S: 0-1

Minimum:				-1.5				
Maximum:		5.0	5.0	100.0				
Mass	Calc. Mass	mDa	PPM	DBE	i-FIT	Norm	Conf(%)	Formula
487.2347	487.2345	0.2	0.4	15.5	335.7	n/a	n/a	C28 H31 N4 O4

Figure A.52: Elemental Composition Report.

Characterization of 1,9-diaza peri-xanthenoxanten

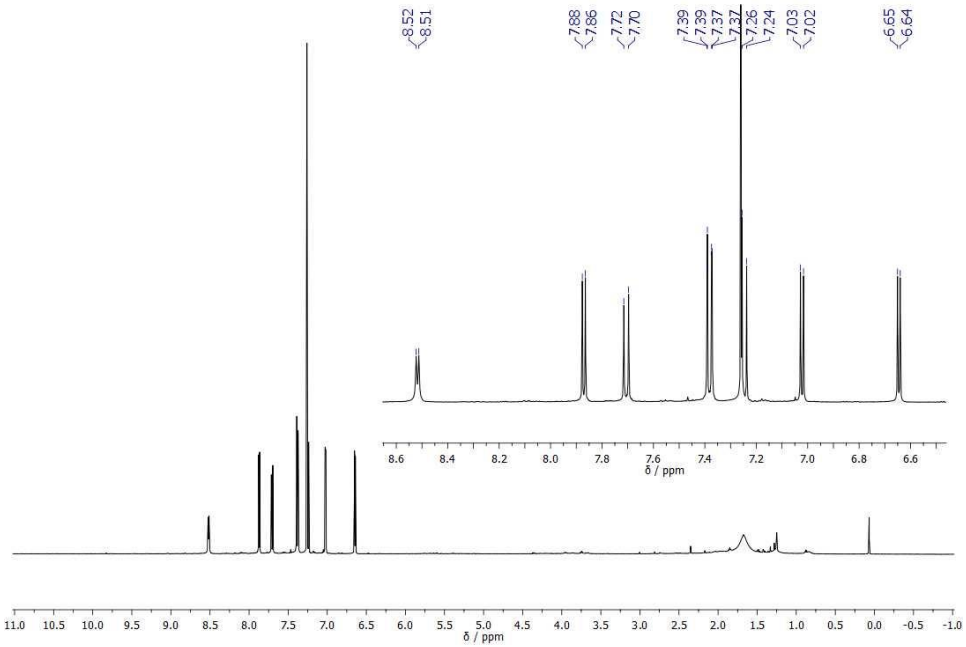

Figure A.53: ^{1}H-NMR, 500 MHz, $CDCl_3$

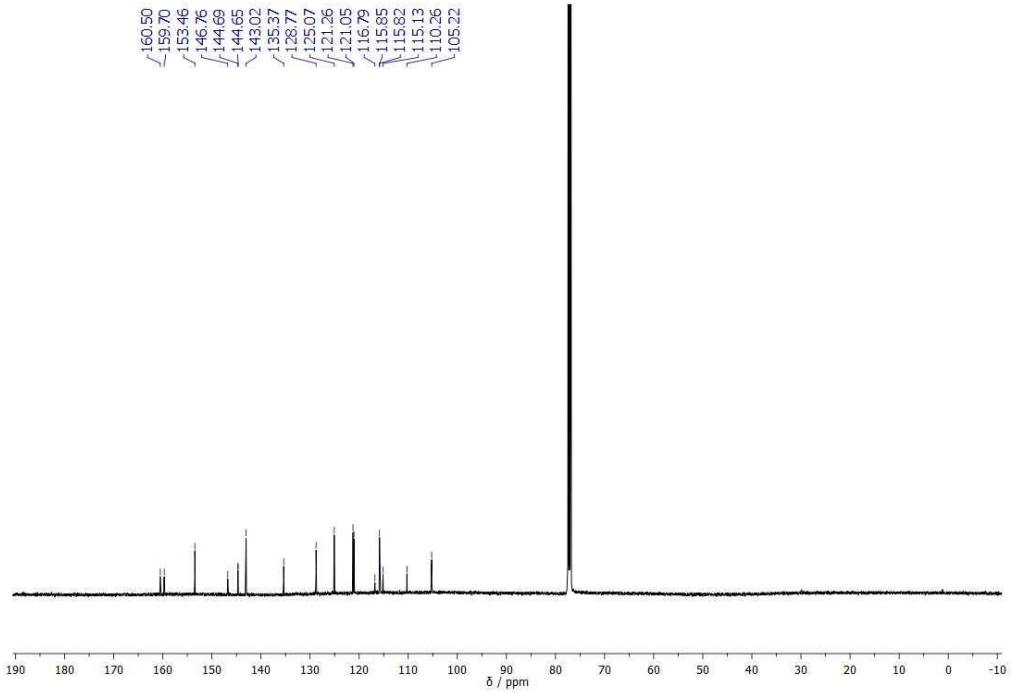

Figure A.54: ^{13}C-NMR, 125 MHz, $CDCl_3$

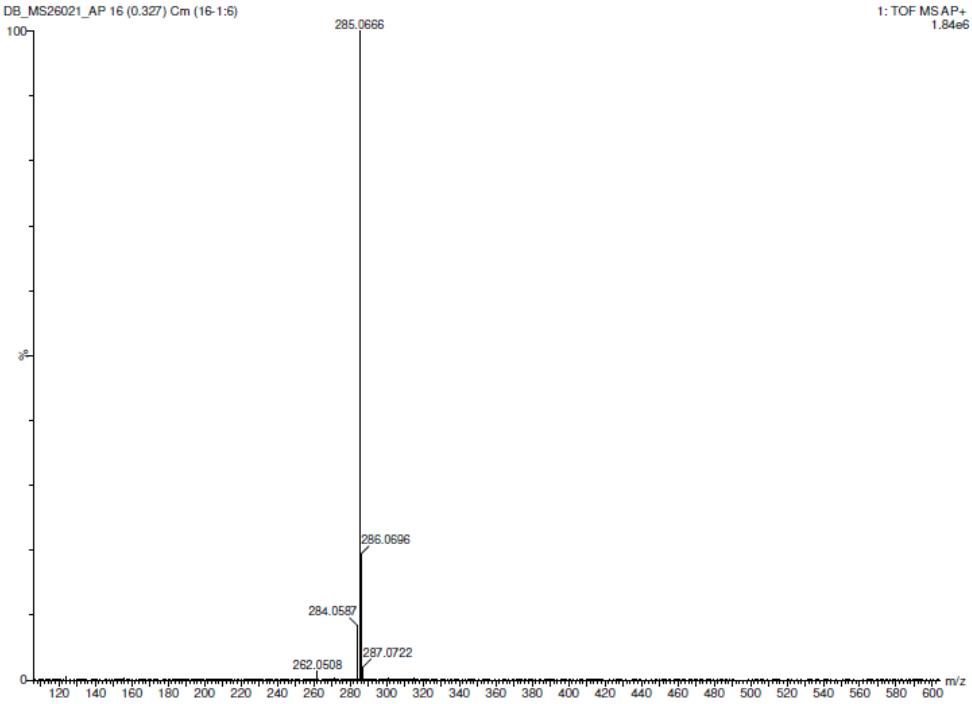

Figure A.55: HR-MS, AP-TOF.

Elemental Composition Report **Page 1**

Single Mass Analysis
Tolerance = 5.0 PPM / DBE: min = -1.5, max = 200.0
Element prediction: Off
Number of isotope peaks used for i-FIT = 3

Monoisotopic Mass, Odd and Even Electron Ions
4 formula(e) evaluated with 1 results within limits (up to 50 closest results for each mass)
Elements Used:
C: 0-18 H: 0-9 N: 0-2 O: 0-2

Minimum:				-1.5				
Maximum:		5.0	5.0	200.0				
Mass	Calc. Mass	mDa	PPM	DBE	i-FIT	Norm	Conf(%)	Formula
285.0666	285.0664	0.2	0.7	15.5	269.7	n/a	n/a	C18 H9 N2 O2

Figure A.56: Elemental Composition Report.

Characterization of methyl(naphthalen-2-yl)sulfane

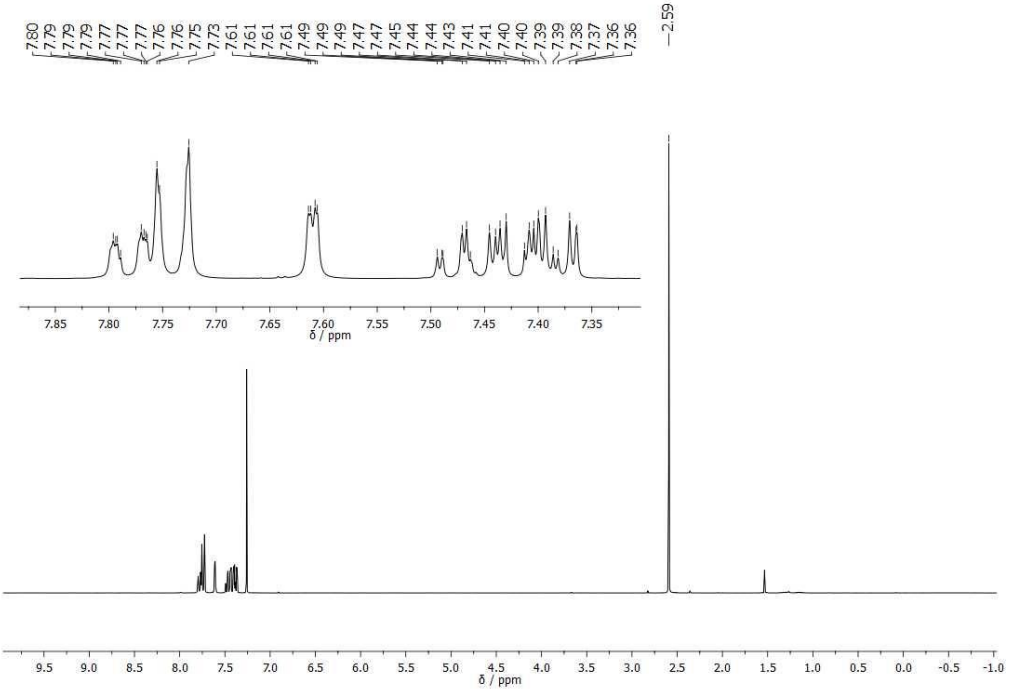

Figure A.57: ^{1}H-NMR, 500 MHz, $CDCl_3$

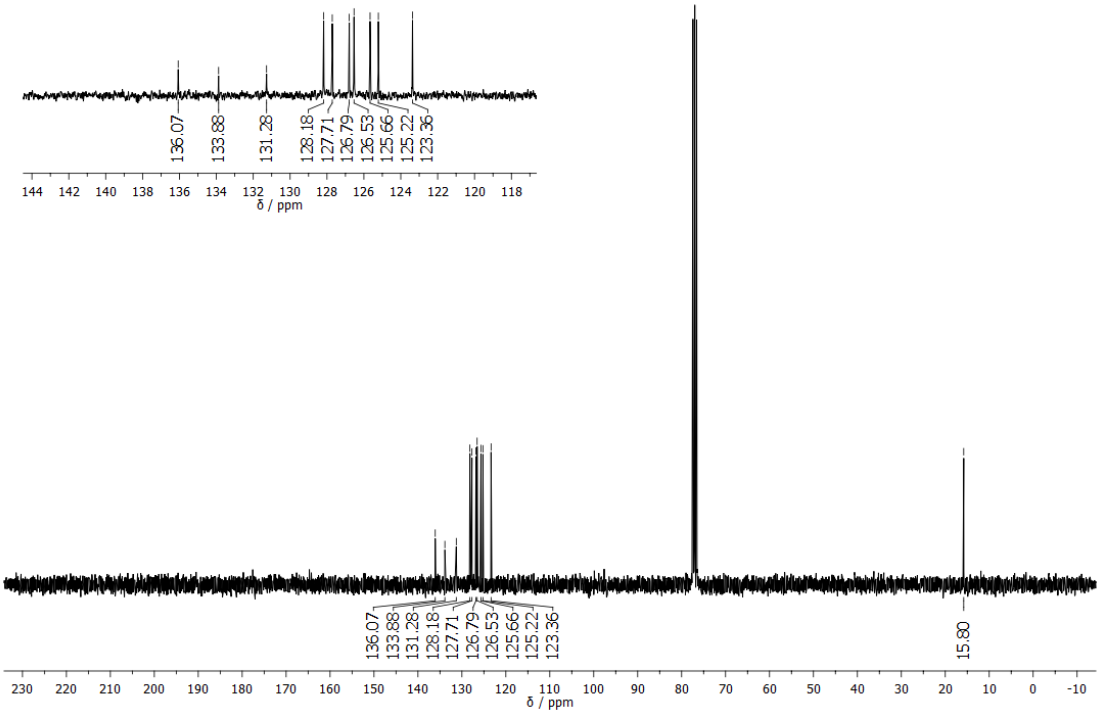

Figure A.58: ^{13}C-NMR, 125 MHz, $CDCl_3$

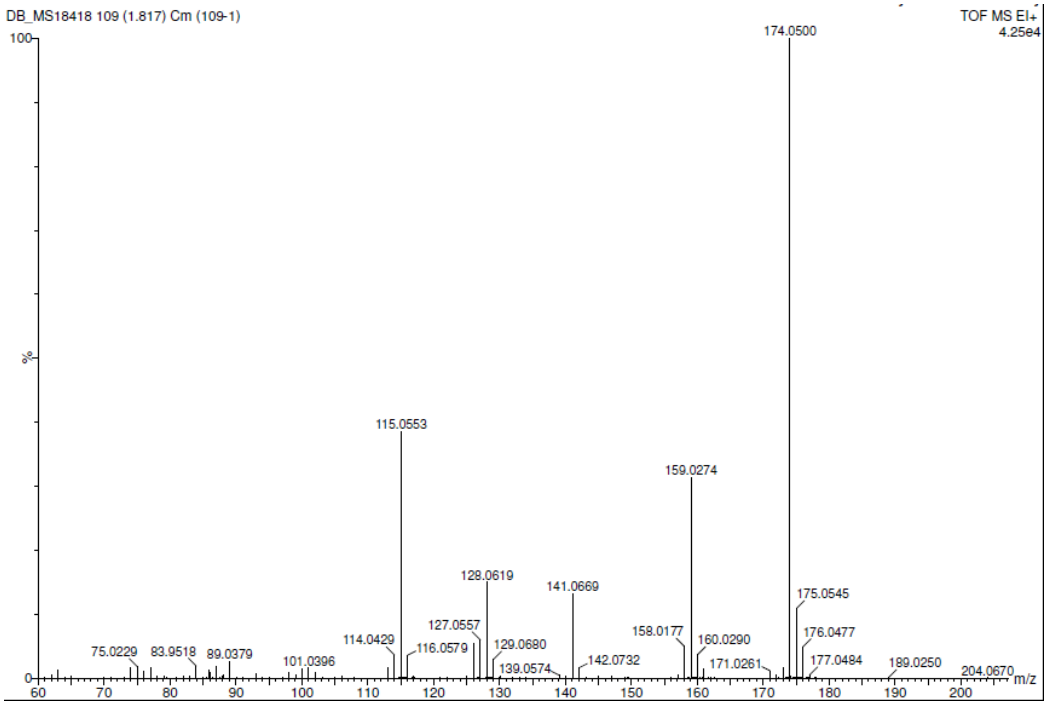

Figure A.59: HR-MS, EI-TOF.

Elemental Composition Report **Page 1**

Single Mass Analysis
Tolerance = 5.0 PPM / DBE: min = -1.5, max = 50.0
Element prediction: Off

Monoisotopic Mass, Odd and Even Electron Ions
2 formula(e) evaluated with 1 results within limits (all results (up to 1000) for each mass)
Elements Used:
C: 0-11 H: 0-10 S: 0-1

23-Jan-2018 BCV340 School of Chemistry Cardiff University
DB_MS18418 109 (1.817) Cm (109-1) TOF MS EI+
4.25e+004

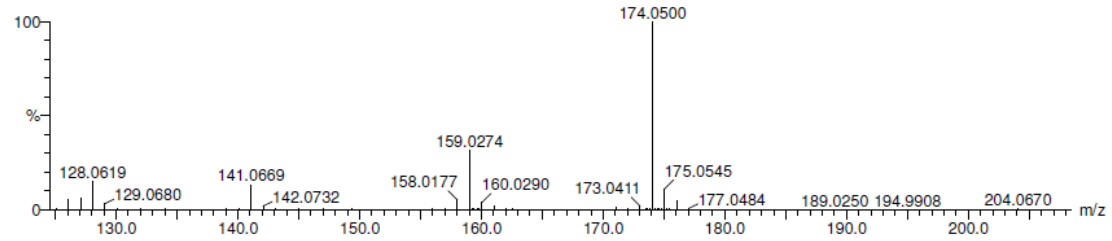

Minimum:				-1.5		
Maximum:		5.0	5.0	50.0		
Mass	Calc. Mass	mDa	PPM	DBE	i-FIT	Formula
174.0500	174.0503	-0.3	-1.7	7.0	94.2	C11 H10 S

Figure A.60: Elemental Composition Report.

Characterization of 2-(methylsulfinyl)naphthalene

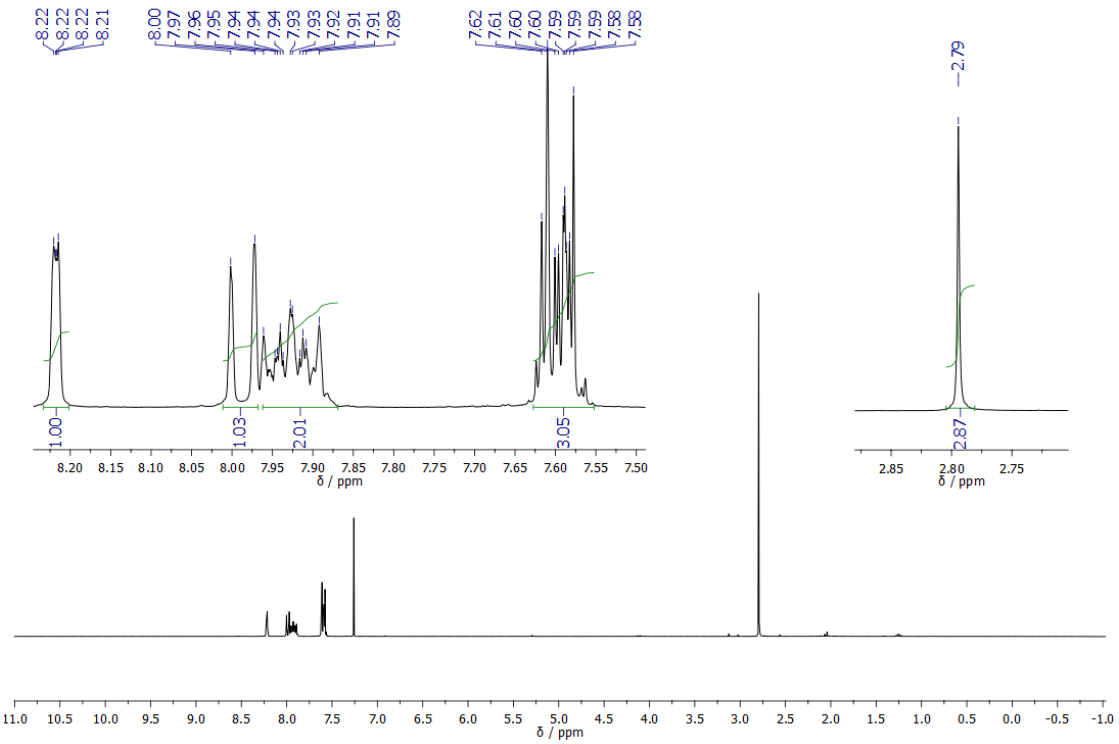

Figure A.61: ^{1}H-NMR, 300 MHz, $CDCl_3$

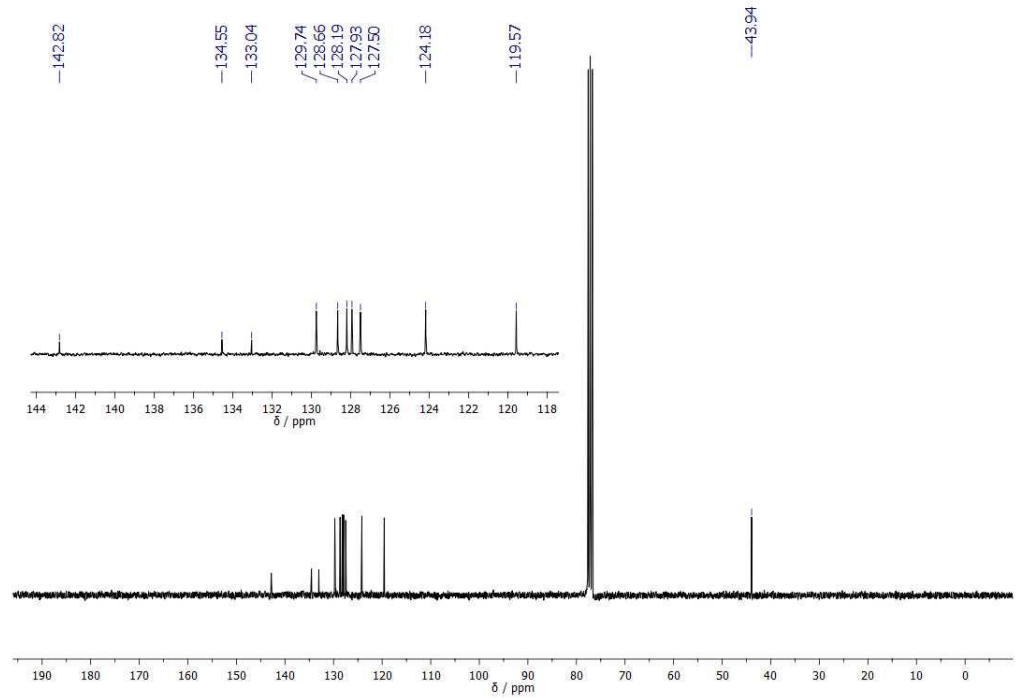

Figure A.62: ^{13}C-NMR, 500 MHz, $CDCl_3$

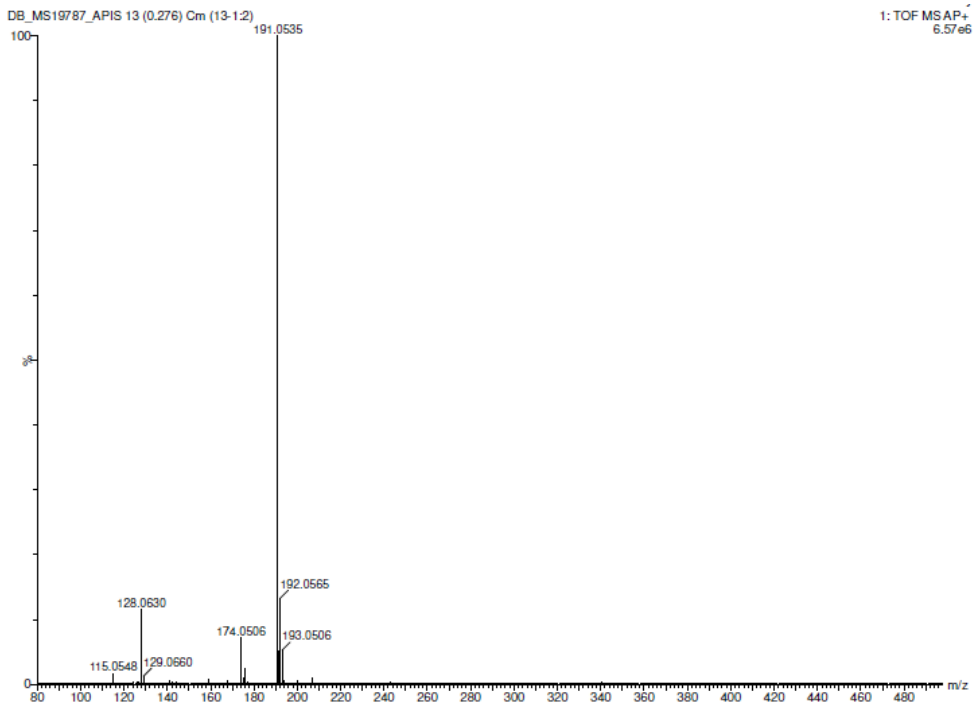

Figure A.63: HR-MS, AP-TOF.

Elemental Composition Report **Page 1**

Single Mass Analysis
Tolerance = 5.0 PPM / DBE: min = -1.5, max = 50.0
Element prediction: Off
Number of isotope peaks used for i-FIT = 3

Monoisotopic Mass, Odd and Even Electron Ions
3 formula(e) evaluated with 1 results within limits (up to 50 best isotopic matches for each mass)
Elements Used:
C: 0-11 H: 0-11 O: 0-1 S: 0-1

Minimum:				-1.5				
Maximum:		5.0	5.0	50.0				
Mass	Calc. Mass	mDa	PPM	DBE	i-FIT	Norm	Conf(%)	Formula
191.0535	191.0531	0.4	2.1	6.5	716.9	n/a	n/a	C11 H11 O S

Figure A.64: Elemental Composition Report.

Characterization of 2'-(methylthio)-[1,1'-binaphthalen]-2-ol

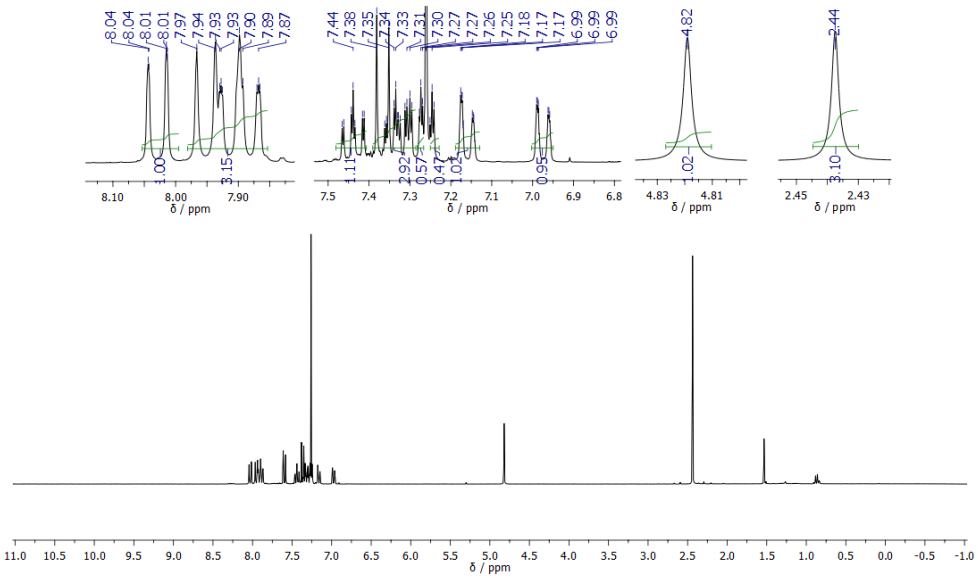

Figure A.65: ^{1}H-NMR, 300 MHz, $CDCl_3$

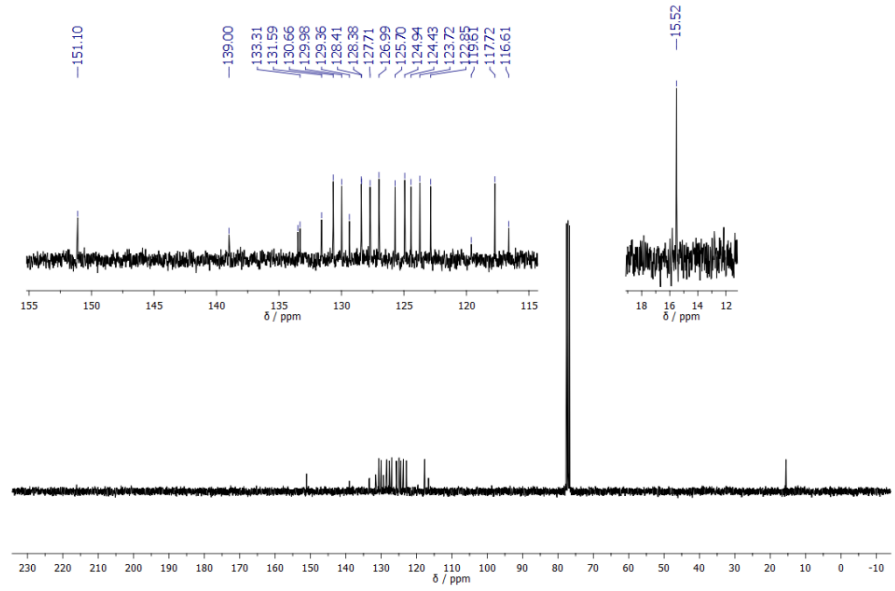

Figure A.66: ^{13}C-NMR, 75 MHz, $CDCl_3$

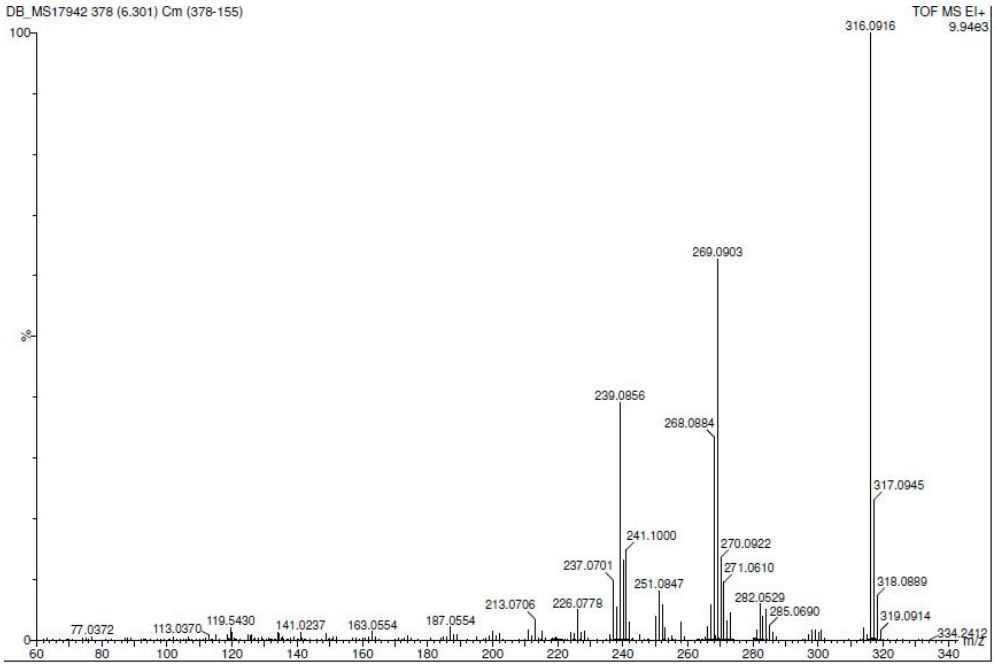

Figure A.67: HR-MS, EI-TOF.

Single Mass Analysis
Tolerance = 5.0 PPM / DBE: min = -1.5, max = 50.0
Element prediction: Off

Monoisotopic Mass, Odd and Even Electron Ions
2 formula(e) evaluated with 1 results within limits (all results (up to 1000) for each mass)
Elements Used:
C: 0-21 H: 0-16 O: 0-1 S: 0-1

04-Oct-2017
DB_MS17942 378 (6.301) Cm (378-155)

BCV305

School of Chemistry Cardiff University
TOF MS EI+
9.94e+003

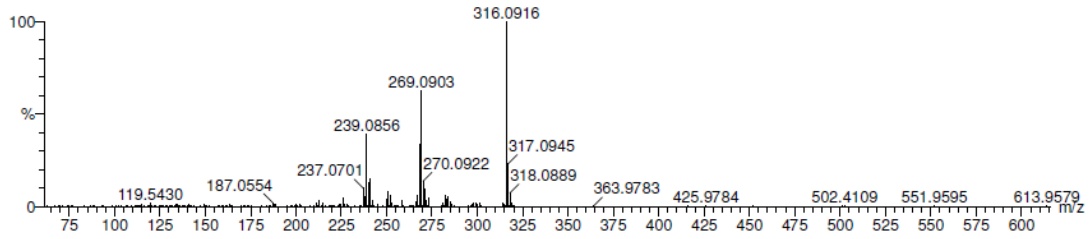

Minimum:				-1.5		
Maximum:		5.0	5.0	50.0		
Mass	Calc. Mass	mDa	PPM	DBE	i-FIT	Formula
316.0916	316.0922	-0.6	-1.9	14.0	3.6	C21 H16 O S

Figure A.68: Elemental Composition Report.

Characterization of 2'-(methylsulfinyl)-[1,1'-binaphthalen]-2-ol

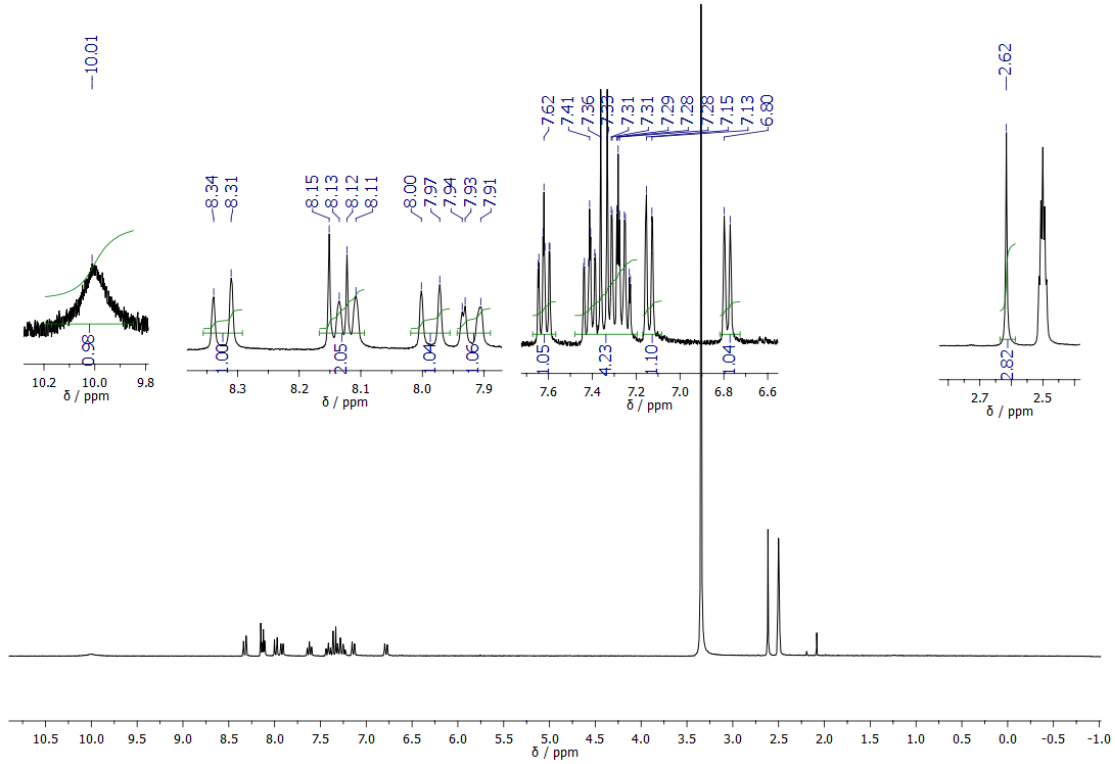

Figure A.69: ^{1}H-NMR, 300 MHz, DMSO-d_6

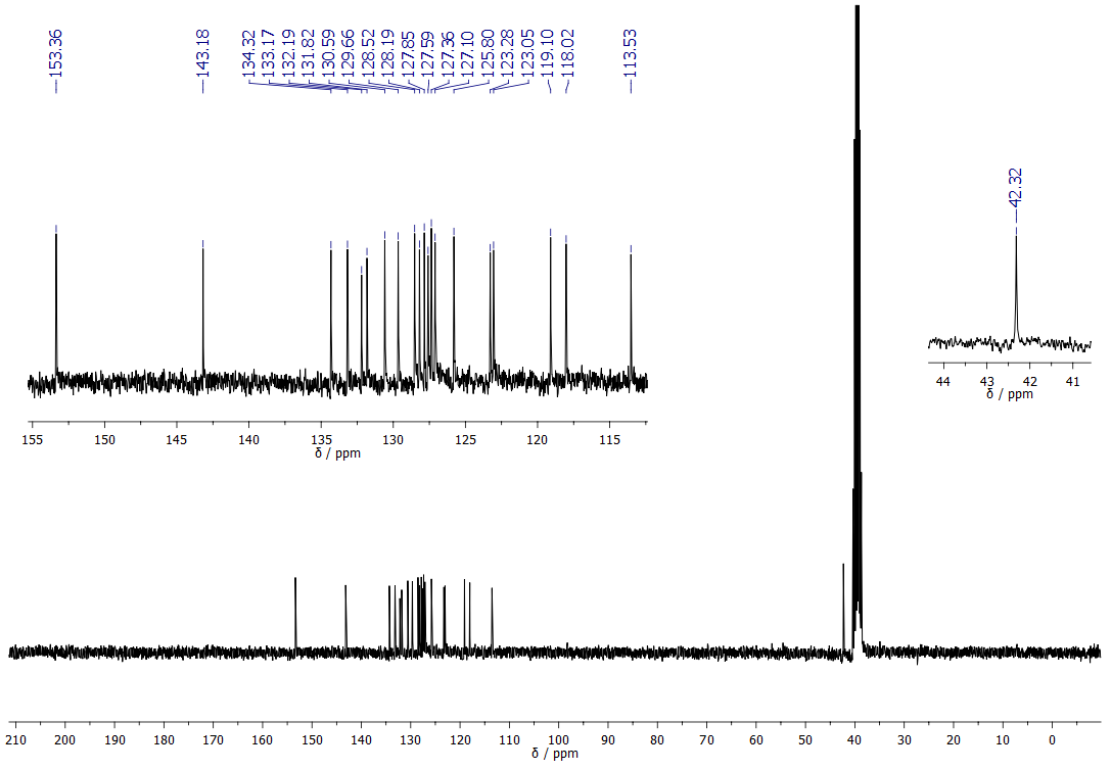

Figure A.69: ^{13}C-NMR, 75 MHz, DMSO-d_6

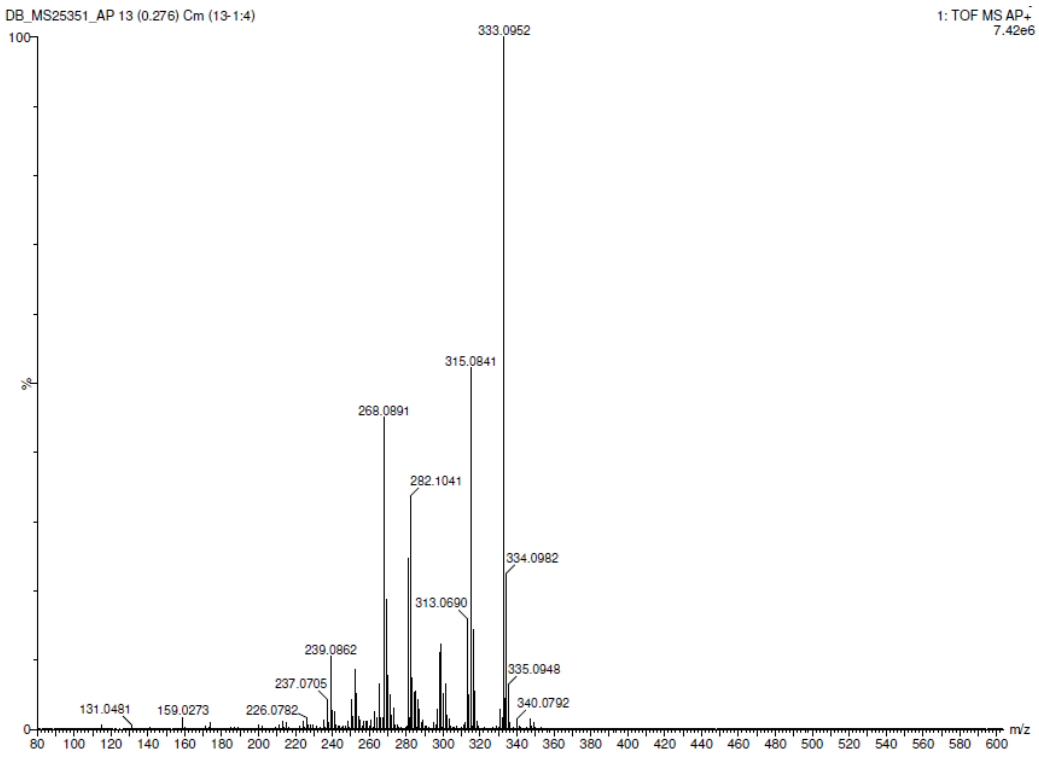

Figure A.70: HR-MS, AP-TOF.

Elemental Composition Report **Page 1**

Single Mass Analysis
Tolerance = 5.0 PPM / DBE: min = -1.5, max = 200.0
Element prediction: Off
Number of isotope peaks used for i-FIT = 3

Monoisotopic Mass, Odd and Even Electron Ions
3 formula(e) evaluated with 1 results within limits (up to 50 closest results for each mass)
Elements Used:
C: 0-21 H: 0-17 O: 0-2 S: 0-1

Minimum:				-1.5				
Maximum:		5.0	5.0	200.0				
Mass	Calc. Mass	mDa	PPM	DBE	i-FIT	Norm	Conf(%)	Formula
333.0952	333.0949	0.3	0.9	13.5	653.5	n/a	n/a	C21 H17 O2 S

Figure A.71: Elemental Composition Report.

Characterization of (2'-methoxy-[1,1'-binaphthalen]-2-yl)(methyl)sulfane

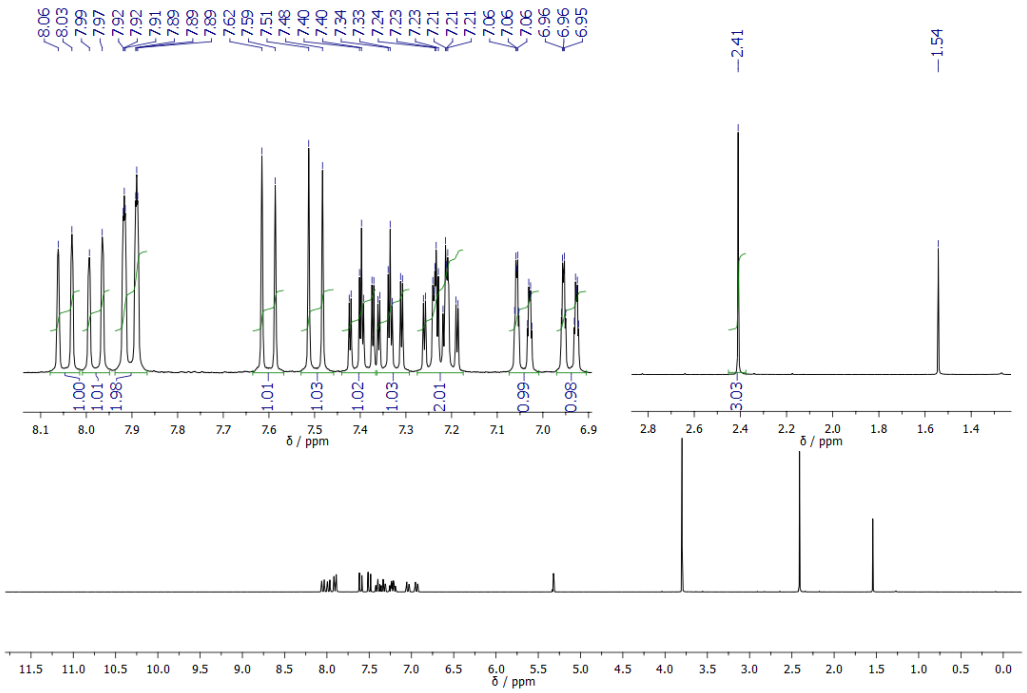

Figure A.72: ^{1}H-NMR, 300 MHz, CD_2Cl_2

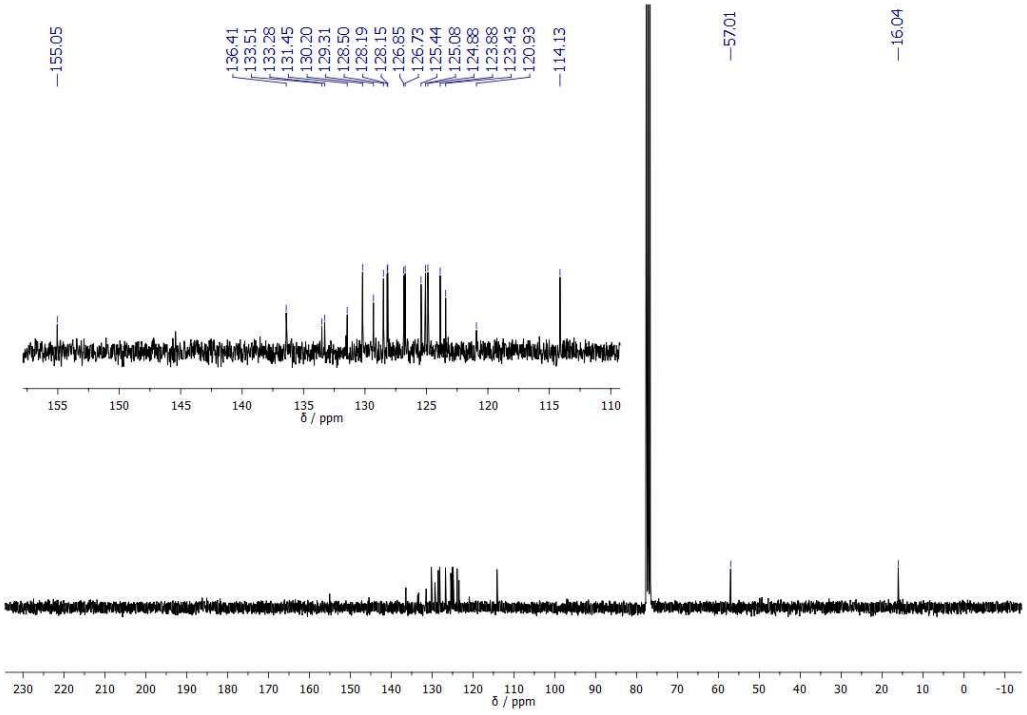

Figure A.73: ^{13}C-NMR, 75 MHz, $CDCl_3$

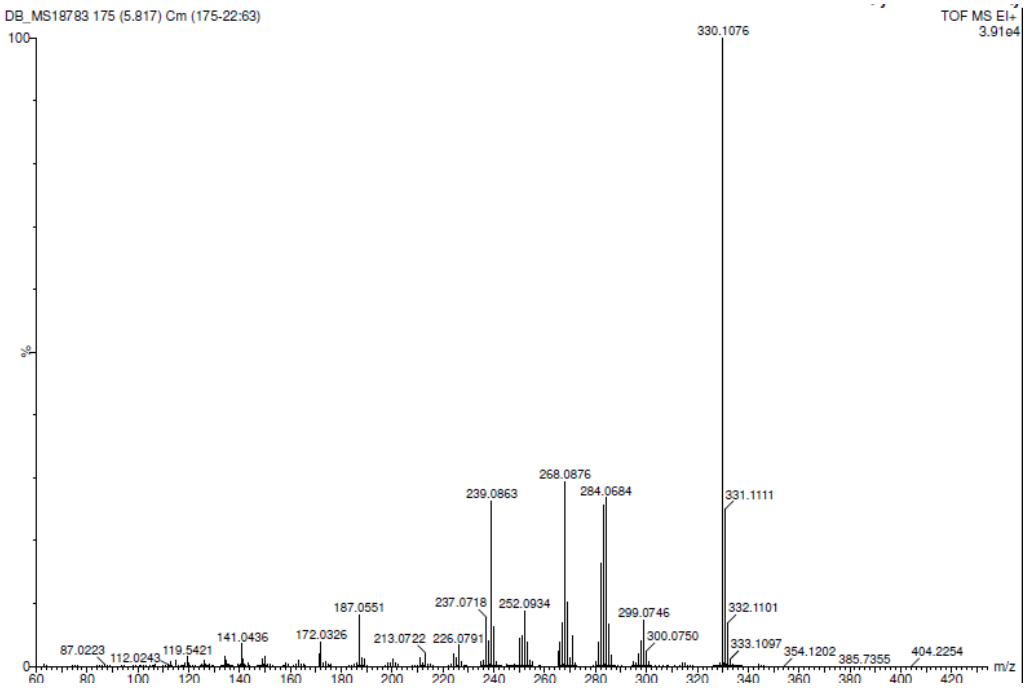

Figure A.74: HR-MS, EI-TOF.

Elemental Composition Report **Page 1**

Single Mass Analysis
Tolerance = 10.0 PPM / DBE: min = -1.5, max = 50.0
Element prediction: Off

Monoisotopic Mass, Odd and Even Electron Ions
10 formula(e) evaluated with 1 results within limits (all results (up to 1000) for each mass)
Elements Used:
C: 0-22 H: 0-18 O: 0-4 S: 0-1

28-Feb-2018 BCV351 School of Chemistry Cardiff University
DB_MS18783 175 (5.817) Cm (175-22:63) TOF MS EI+
3.91e+004

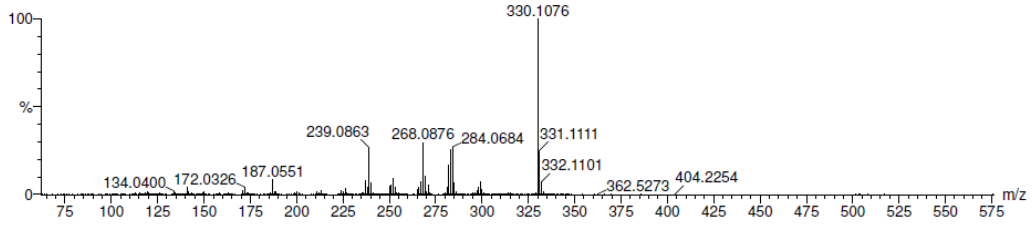

Minimum:				-1.5		
Maximum:		5.0	10.0	50.0		
Mass	Calc. Mass	mDa	PPM	DBE	i-FIT	Formula
330.1076	330.1078	-0.2	-0.6	14.0	17.6	C22 H18 O S

Figure A.75: Elemental Composition Report.

Characterization of 2-methoxy-2'-(methylsulfinyl)-1,1'-binaphthalene

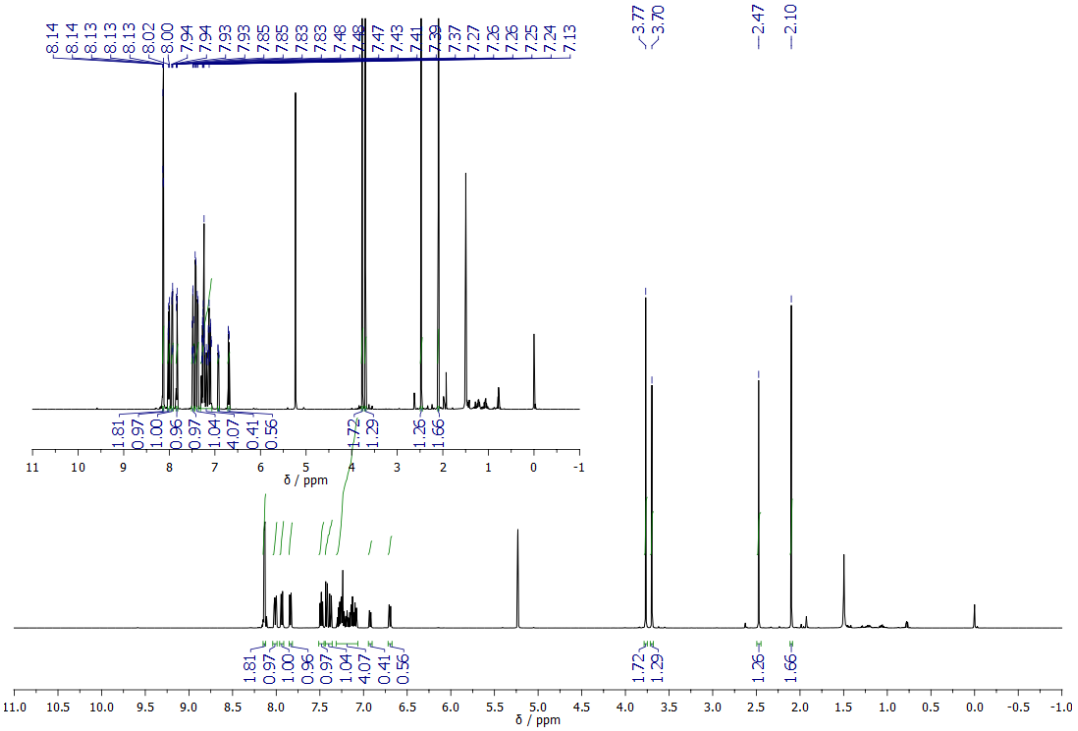

Figure A.76: ^{1}H-NMR, 300 MHz, CD_2Cl_2

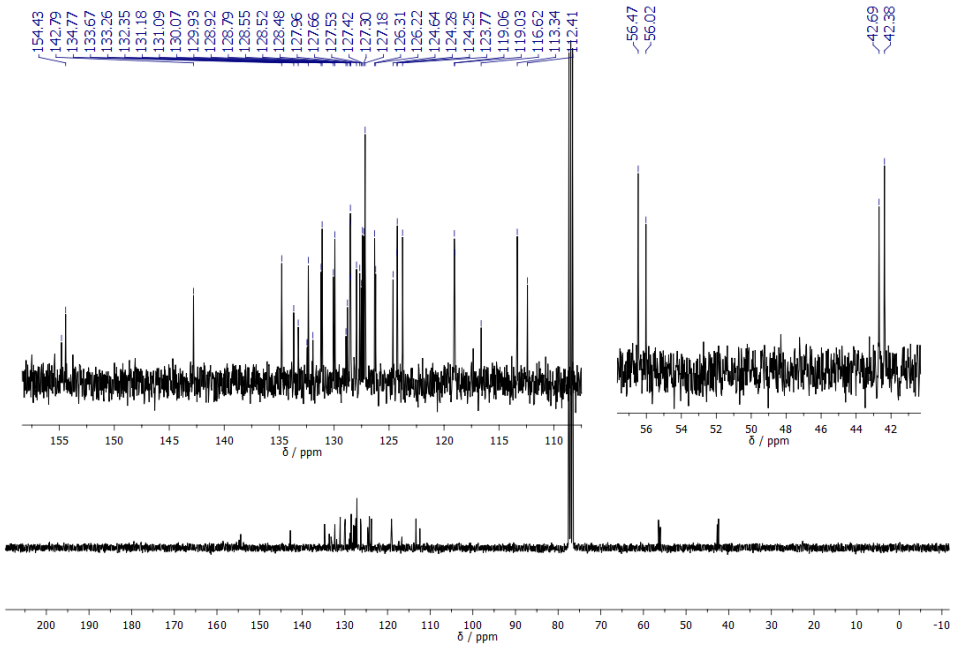

Figure A.77: ^{13}C-NMR, 75 MHz, $CDCl_3$

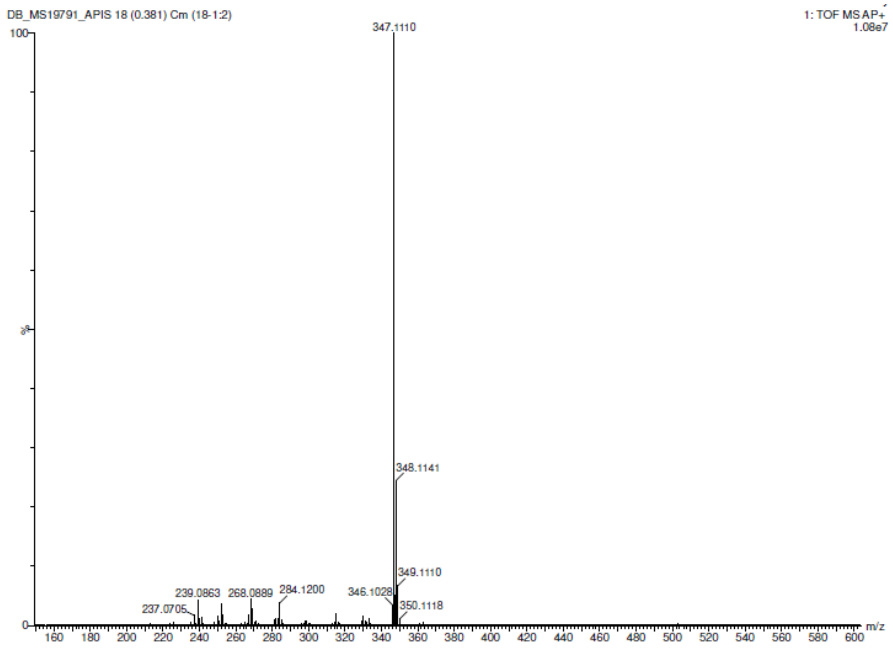

Figure A.78: HR-MS, AP-TOF.

Elemental Composition Report **Page 1**

Single Mass Analysis
Tolerance = 5.0 PPM / DBE: min = -1.5, max = 50.0
Element prediction: Off
Number of isotope peaks used for i-FIT = 3

Monoisotopic Mass, Odd and Even Electron Ions
3 formula(e) evaluated with 1 results within limits (up to 50 best isotopic matches for each mass)
Elements Used:
C: 0-22 H: 0-19 O: 0-2 S: 0-1

Minimum:				-1.5				
Maximum:		5.0	5.0	50.0				
Mass	Calc. Mass	mDa	PPM	DBE	i-FIT	Norm	Conf(%)	Formula
347.1110	347.1106	0.4	1.2	13.5	810.2	n/a	n/a	C22 H19 O2 S

Figure A.79: Elemental Composition Report.

Characterization of 1-methoxydibenzo[a,kl]thioxanthene

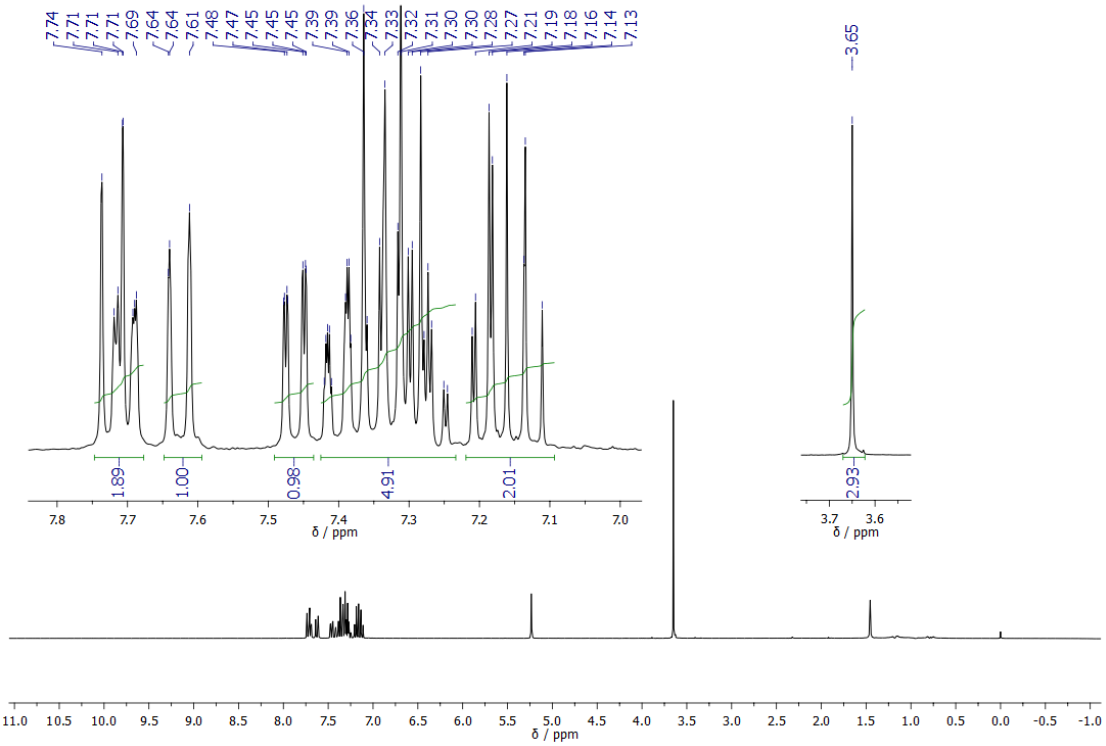

Figure A.80: ^{1}H-NMR, 500 MHz, CD_2Cl_2

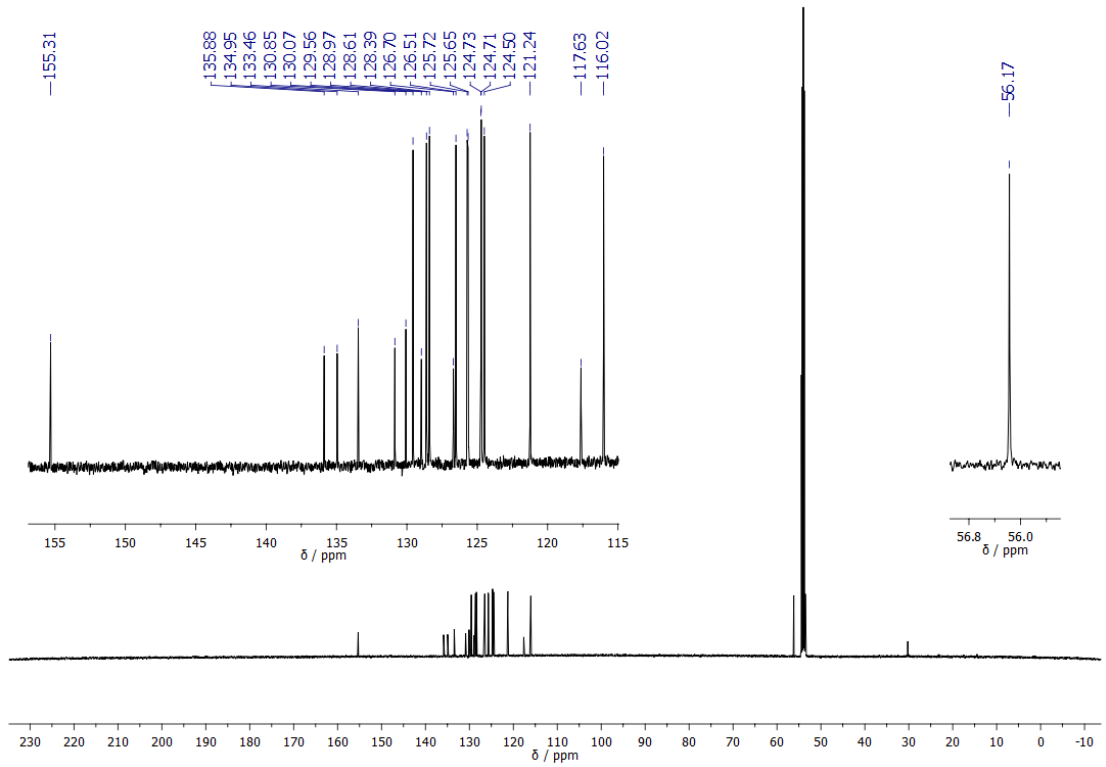

Figure A.81: ^{13}C-NMR, 125 MHz, CD_2Cl_2

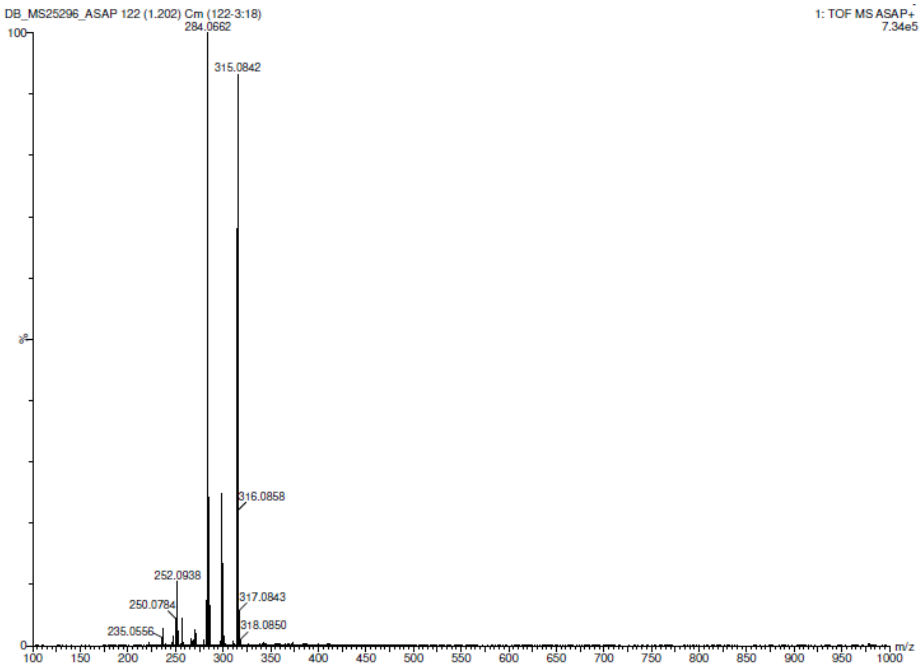

Figure A.82: HR-MS, ASAP-TOF.

Elemental Composition Report **Page 1**

Single Mass Analysis
Tolerance = 5.0 PPM / DBE: min = -1.5, max = 200.0
Element prediction: Off
Number of isotope peaks used for i-FIT = 3

Monoisotopic Mass, Odd and Even Electron Ions
2 formula(e) evaluated with 1 results within limits (up to 50 closest results for each mass)
Elements Used:
C: 0-21 H: 0-15 O: 0-1 S: 0-1

Minimum:				-1.5				
Maximum:		5.0	5.0	200.0				
Mass	Calc. Mass	mDa	PPM	DBE	i-FIT	Norm	Conf(%)	Formula
315.0842	315.0844	-0.2	-0.6	14.5	1106.6	n/a	n/a	C21 H15 O S

Figure A.83: Elemental Composition Report.

Characterization of 1-methoxydibenzo[a,kl]thioxanthene 7,7-dioxide

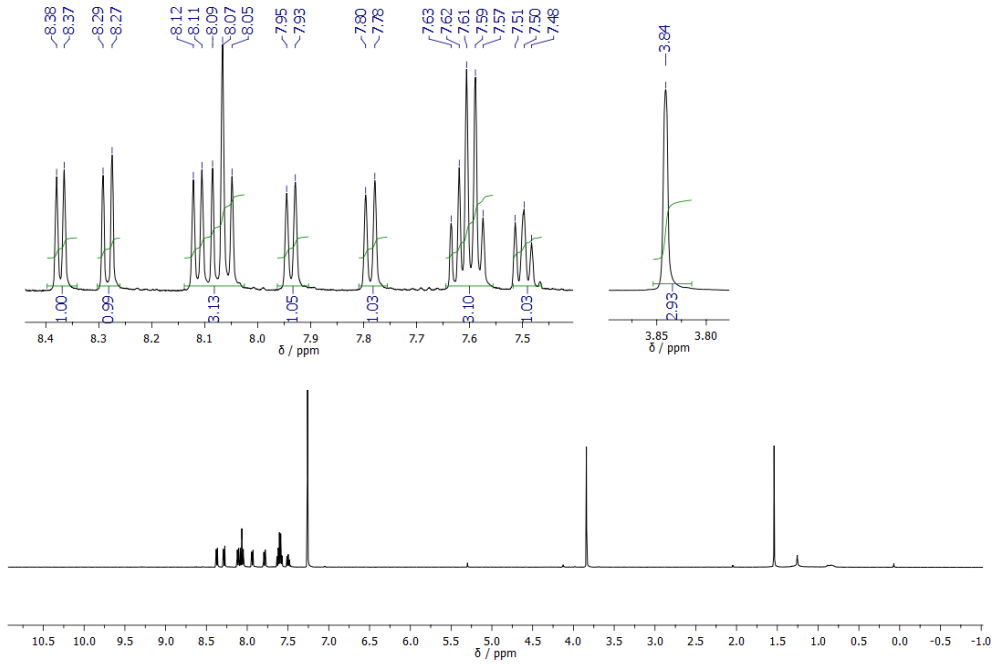

Figure A.84: ^{1}H-NMR, 500 MHz, $CDCl_3$

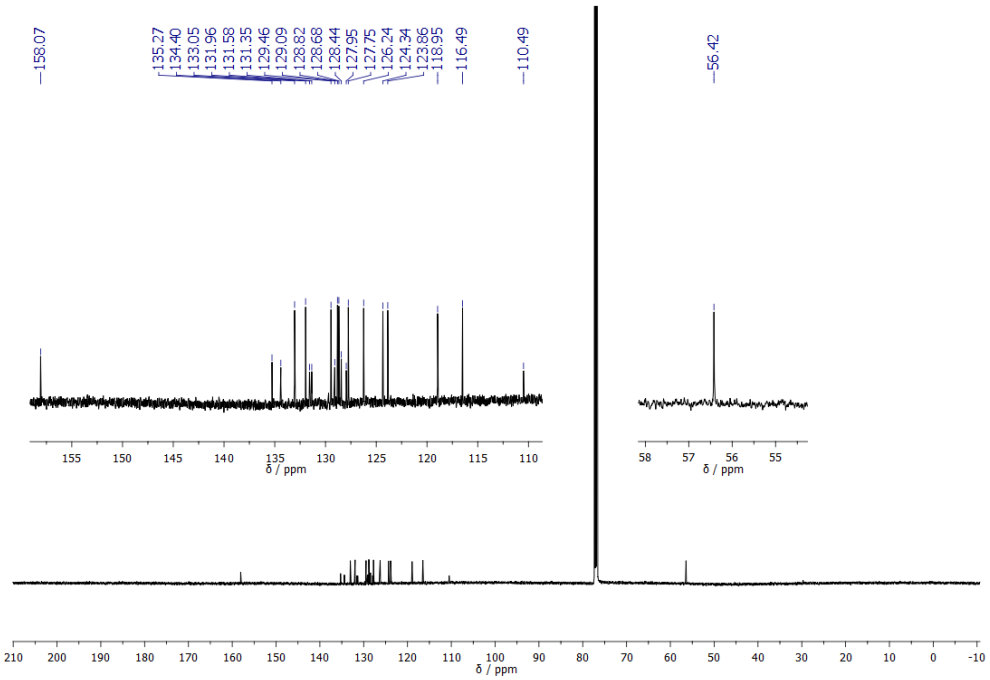

Figure A.85: ^{13}C-NMR, 125 MHz, $CDCl_3$

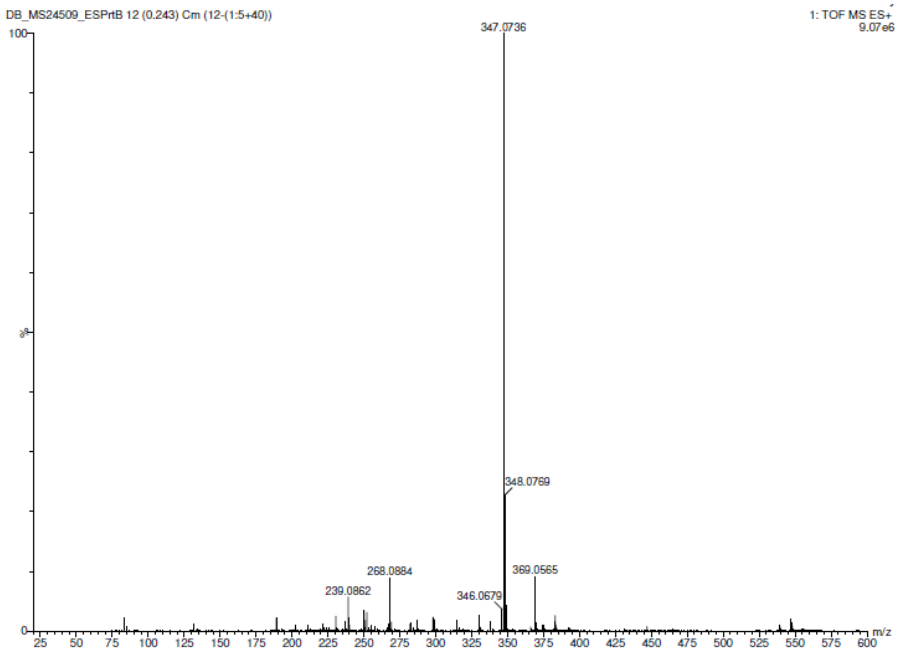

Figure A.86: HR-MS, ES-TOF.

Elemental Composition Report **Page 1**

Single Mass Analysis
Tolerance = 30.0 PPM / DBE: min = -1.5, max = 180.0
Element prediction: Off

Monoisotopic Mass, Odd and Even Electron Ions
5 formula(e) evaluated with 1 results within limits (up to 50 closest results for each mass)
Elements Used:
C: 0-21 H: 0-15 O: 0-3 S: 0-1

Minimum:				-1.5	
Maximum:		5.0	30.0	180.0	
Mass	Calc. Mass	mDa	PPM	DBE	Formula
347.0736	347.0742	-0.6	-1.7	14.5	C21 H15 O3 S

Figure A.87: Elemental Composition Report.

Characterization of 1-hydroxydibenzo[a,kl]thioxanthene 7,7-dioxide

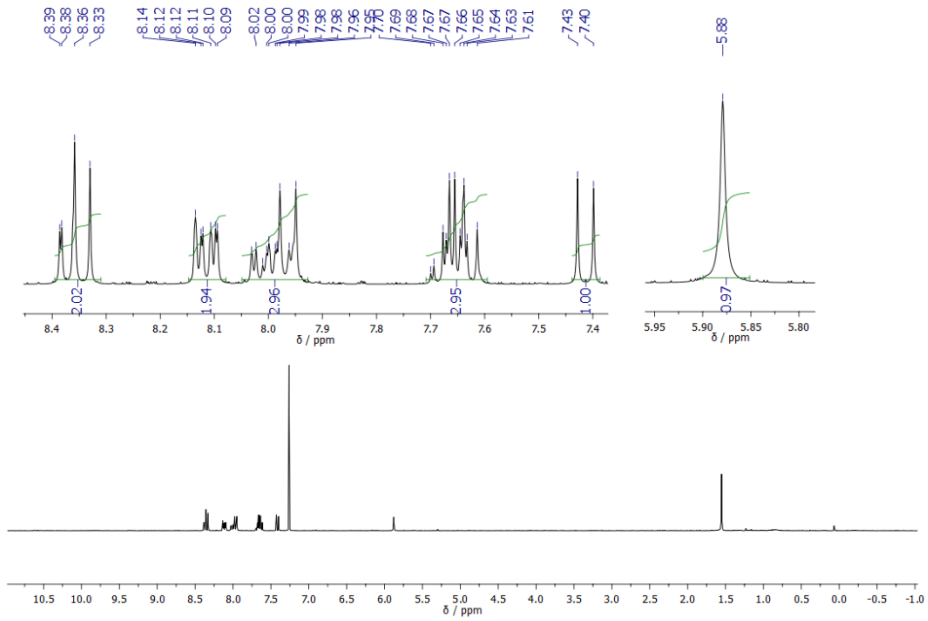

Figure A.88: ^{1}H-NMR, 300 MHz, $CDCl_3$

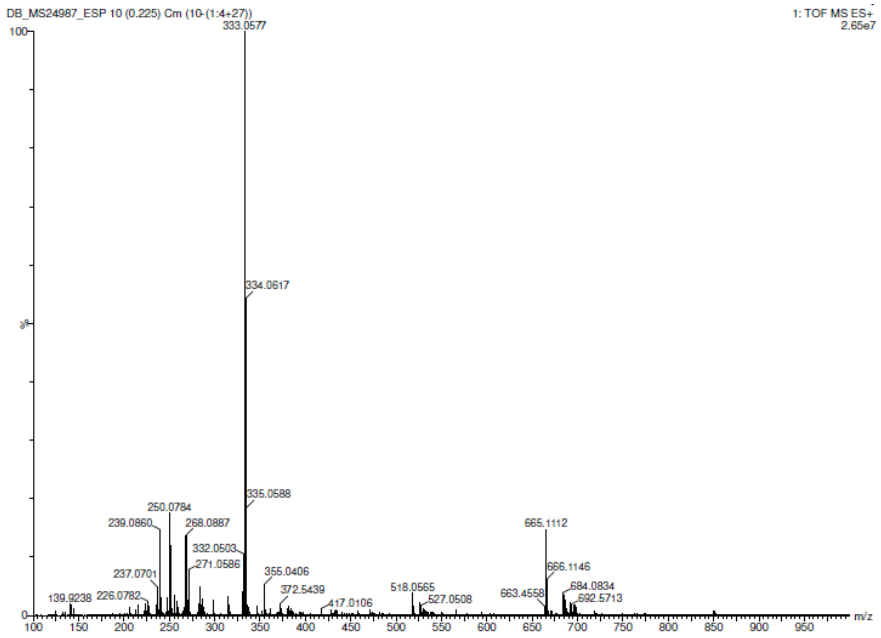

Figure A.89: HR-MS, ES-TOF.

Elemental Composition Report **Page 1**

Single Mass Analysis
Tolerance = 5.0 PPM / DBE: min = -1.5, max = 180.0
Element prediction: Off
Number of isotope peaks used for i-FIT = 3

Monoisotopic Mass, Odd and Even Electron Ions
5 formula(e) evaluated with 1 results within limits (up to 50 closest results for each mass)
Elements Used:
C: 0-20 H: 0-13 O: 0-3 S: 0-1

Minimum:				-1.5				
Maximum:		5.0	5.0	180.0				
Mass	Calc. Mass	mDa	PPM	DBE	i-FIT	Norm	Conf(%)	Formula
333.0577	333.0585	-0.8	-2.4	14.5	854.4	n/a	n/a	C20 H13 O3 S

Figure A.90: Elemental Composition Report.

Characterization of thioxantheno[2,1,9,8-klmna]xanthene 12,12-dioxide

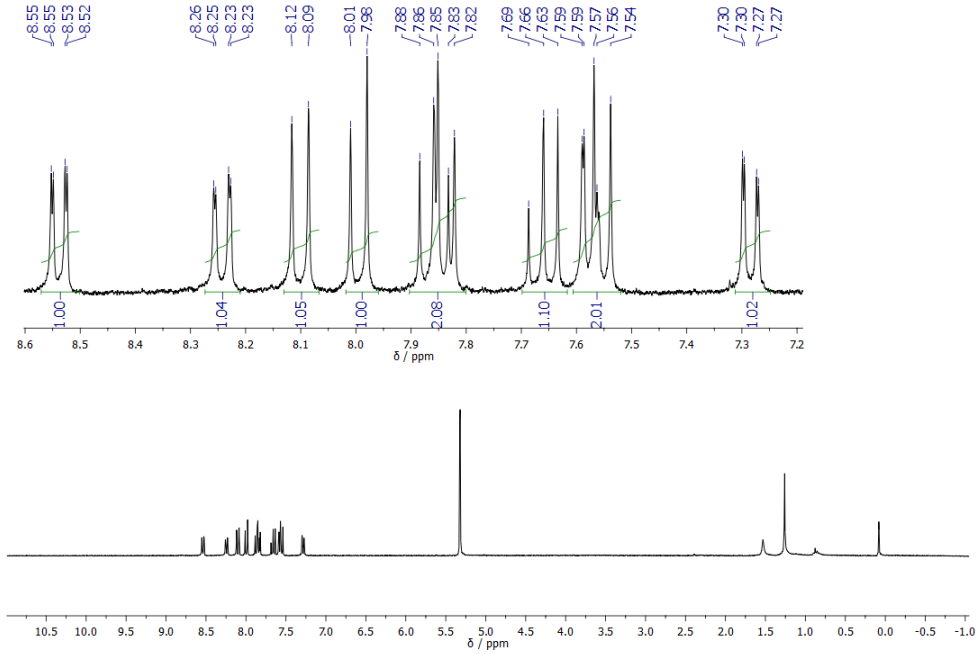

Figure A.91: ^{1}H-NMR, 300 MHz, CD_2Cl_2

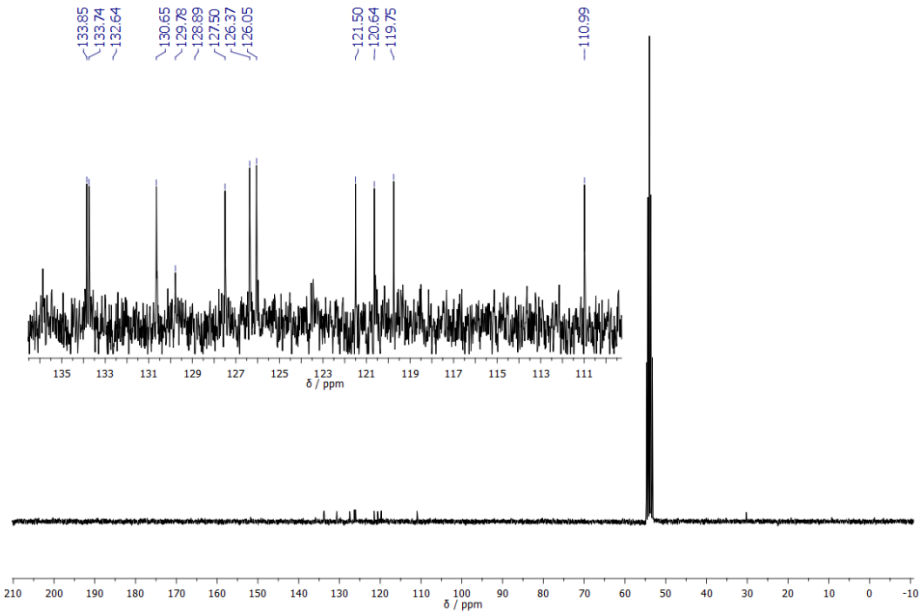

Figure A.92: ^{13}C-NMR, 125 MHz, CD_2Cl_2

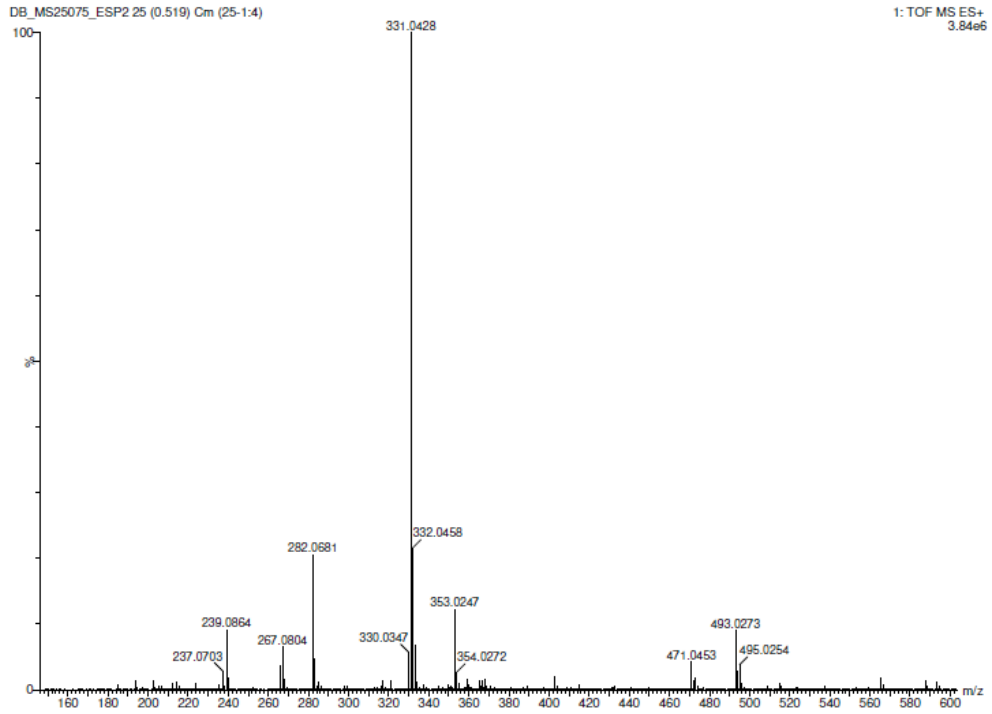

Figure A.93: HR-MS, ES-TOF.

Elemental Composition Report **Page 1**

Single Mass Analysis
Tolerance = 5.0 PPM / DBE: min = -1.5, max = 180.0
Element prediction: Off
Number of isotope peaks used for i-FIT = 3

Monoisotopic Mass, Odd and Even Electron Ions
5 formula(e) evaluated with 1 results within limits (up to 50 closest results for each mass)
Elements Used:
C: 0-20 H: 0-11 O: 0-3 S: 0-1

Minimum:				-1.5				
Maximum:		5.0	5.0	180.0				
Mass	Calc. Mass	mDa	PPM	DBE	i-FIT	Norm	Conf(%)	Formula
331.0428	331.0429	-0.1	-0.3	15.5	251.1	n/a	n/a	C20 H11 O3 S

Figure A.94: Elemental Composition Report.

Characterization of N,N-dimethyl-1,7-diaza peri-xanthenoxanten

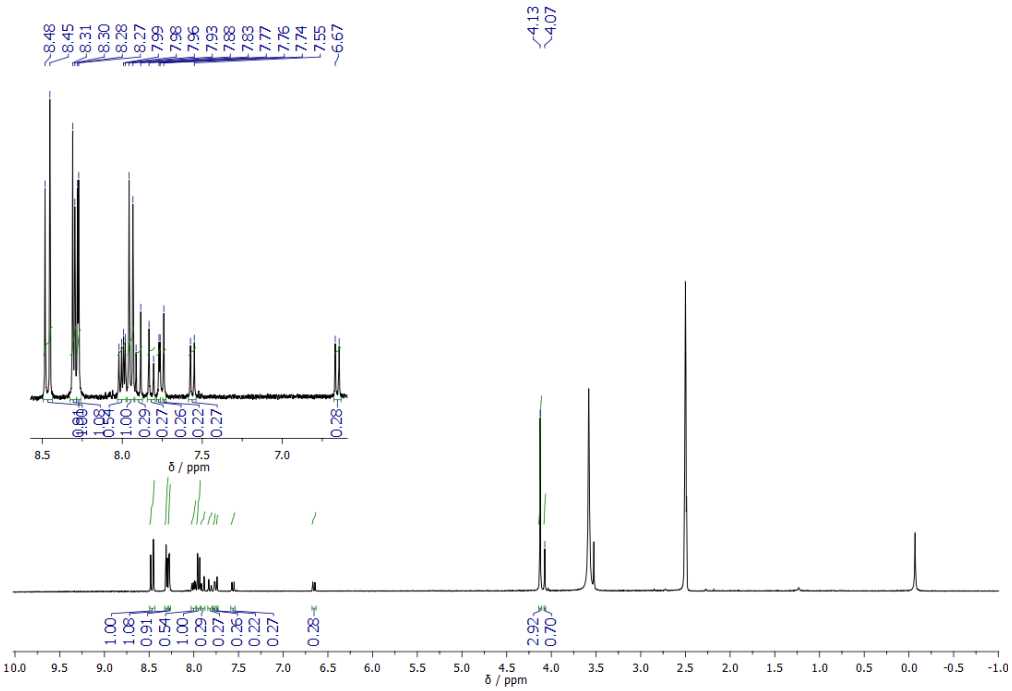

Figure A.95: ^{1}H-NMR, 300 MHz, DMSO-d_6

Characterization of N,N-dimethyl-3,9-diaza peri-xanthenoxanten

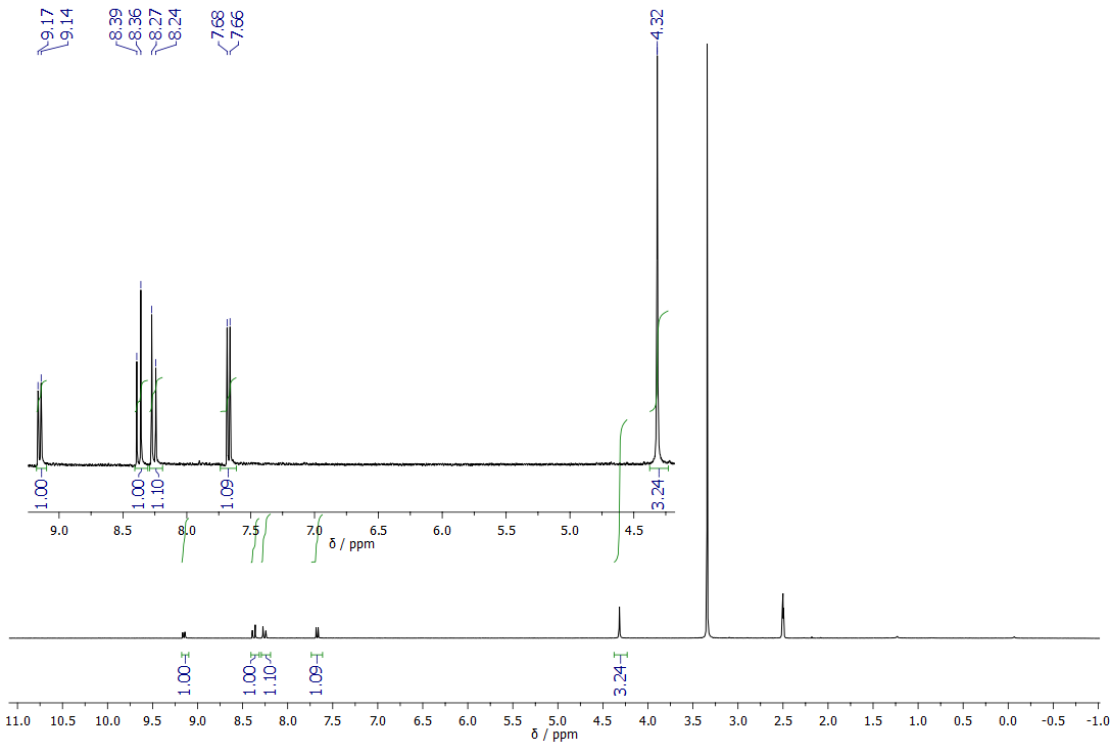

Figure A.96: ^{1}H-NMR, 300 MHz, DMSO-d_6

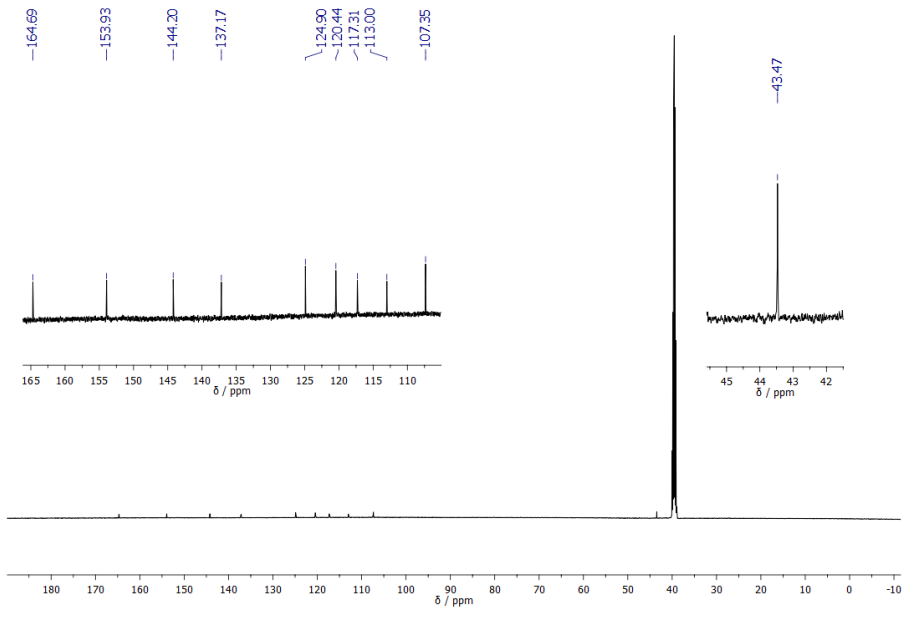

Figure A.97: ^{13}C-NMR, 125 MHz, DMSO-d_6

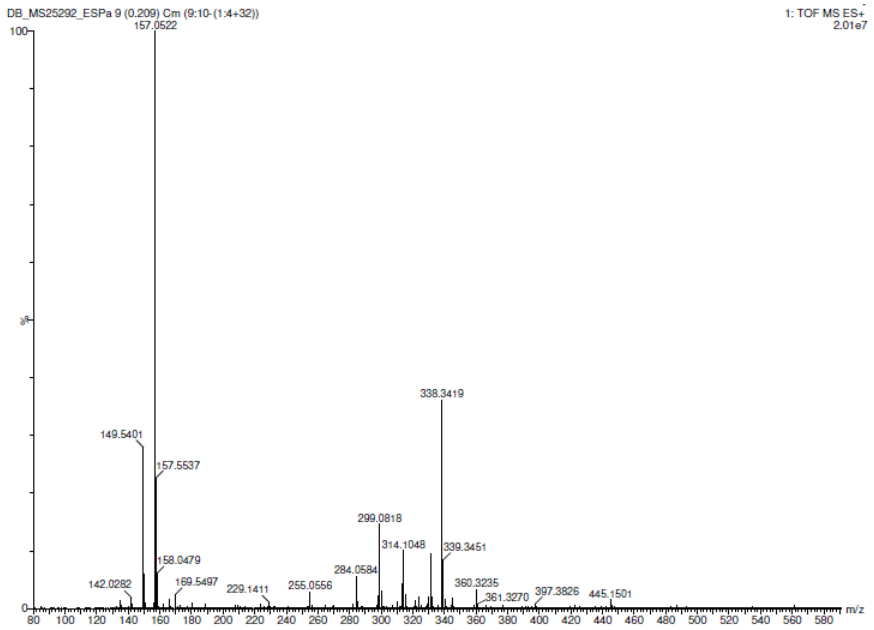

Figure A.98: HR-MS, ES-TOF.

Characterization of N,N-dimethyl-4,10-diaza peri-xanthenoxanten

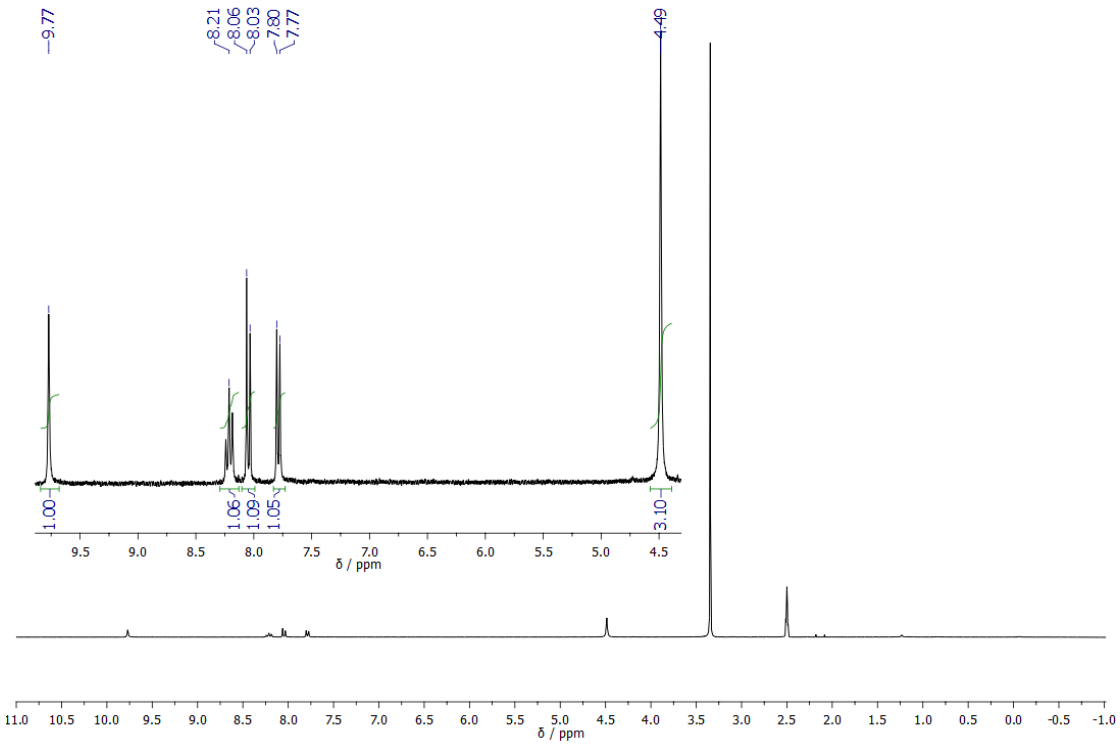

Figure A.99: ^{1}H-NMR, 300 MHz, DMSO-d_6

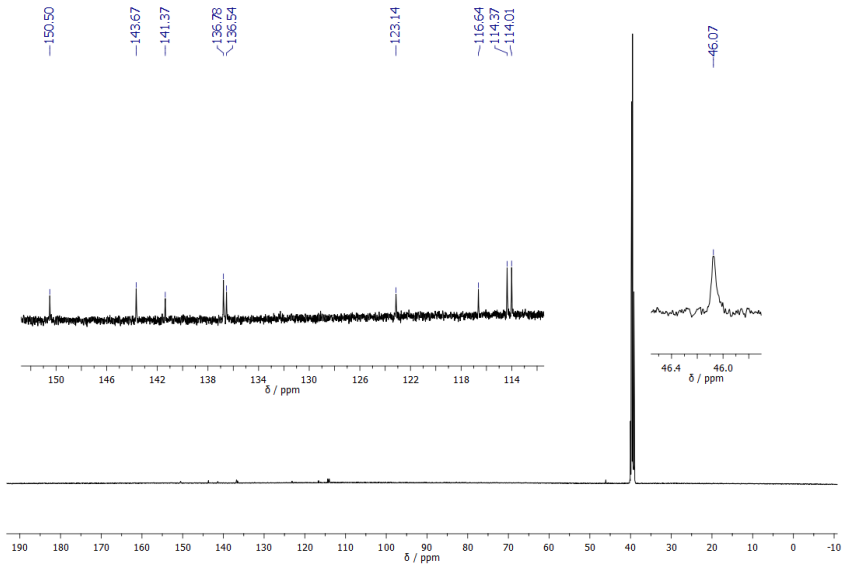

Figure A.100: ^{13}C-NMR, 125 MHz, DMSO-d_6

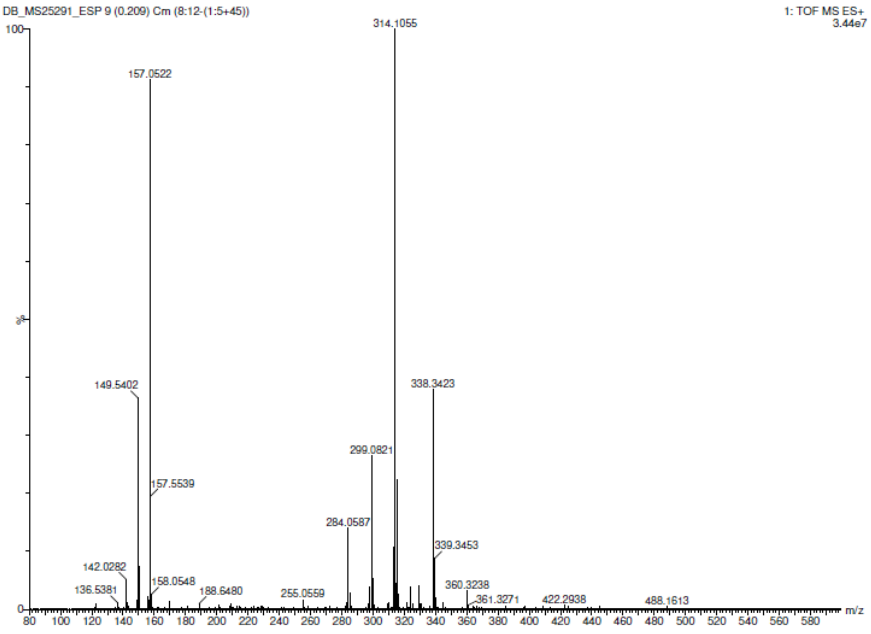

Figure A.101: HR-MS, ES-TOF.

Elemental Composition Report **Page 1**

Single Mass Analysis
Tolerance = 5.0 PPM / DBE: min = -1.5, max = 200.0
Element prediction: Off
Number of isotope peaks used for i-FIT = 3

Monoisotopic Mass, Odd and Even Electron Ions
4 formula(e) evaluated with 1 results within limits (up to 50 closest results for each mass)
Elements Used:
C: 0-20 H: 0-14 N: 0-2 O: 0-2

Minimum:				-1.5				
Maximum:		5.0	5.0	200.0				
Mass	Calc. Mass	mDa	PPM	DBE	i-FIT	Norm	Conf(%)	Formula
314.1055	314.1055	0.0	0.0	15.0	857.5	n/a	n/a	C20 H14 N2 O2

Figure A.102: Elemental Composition Report.